



Exposure

Dosimetry of exposure to electromagnetic fields
in daily life and medical applications

Jurriaan Bakker

Dosimetry of Exposure to Electromagnetic Fields in Daily Life and Medical Applications

Jurriaan Bakker

Colofon:

The investigations presented in this thesis were carried out at the Department of Radiation Oncology, Erasmus MC - Daniel den Hoed Cancer Center, Rotterdam.

This research was financially supported by The Netherlands Organization for Health Research and Development (ZonMw) and the Dutch Cancer Society (KWF Kankerbestrijding). Financial support for the printing of this thesis was provided by ZonMw and the Erasmus University Rotterdam.

Address for correspondence:

J.F. Bakker, Department of Radiation Oncology: Unit Hyperthermia, Erasmus MC Daniel den Hoed Cancer Center, PO box 5201, 3008AE Rotterdam, The Netherlands.
j.bakker@erasmusmc.nl

ISBN: 978-90-8891-457-7

Printed by: Proefschriftmaken.nl, Uitgeverij BOXPress

Copyright: © 2012 J.F. Bakker

All rights reserved. No part of this thesis may be reproduced, stored in a retrieval system of any nature, or transmitted in any form by any means, electronic, mechanical, photocopying, recording or otherwise, included a complete form or partial transcription, without the permission of the copyright owners.

Dosimetry of Exposure to Electromagnetic Fields in Daily Life and Medical Applications

Dosimetrie van blootstelling aan elektromagnetische velden in het dagelijkse
leven en medische toepassingen

Proefschrift

ter verkrijging van de graad van doctor aan de
Erasmus Universiteit Rotterdam
op gezag van de
rector magnificus

Prof. dr. H.G. Schmidt

en volgens besluit van het College voor Promoties.

De openbare verdediging zal plaatsvinden op
vrijdag 26 oktober 2012 om 13:30 uur

door

Jurriaan Fokke Bakker

geboren te Schagen



Promotiecommissie

Promotoren: Prof. dr. ing. G.C. van Rhoon

Overige leden: Prof. dr. P.C. Levendag
Prof. dr. ir. A. Burdorf
Prof. dr. ir. A.P.M. Zwamborn

Copromotor: Dr. ir. M.M. Paulides

Contents

	Page
1 Introduction	9
2 3D models of adults and children	17
Part I: Exposure in daily life	24
3 EMF exposure guidelines	25
4 EMF sources and dosimetry	29
5 Exposure to ELF fields	35
6 Exposure to RF fields: SAR assessment	51
7 Exposure to RF fields: temperature assessment	67
Part II: Exposure in medical applications	90
8 2D validation of RF models	91
9 3D validation of RF models	113
10 Virtual prototyping of hyperthermia applicators	129
11 RF dosimetry in patients and medical staff	141

12 General discussion and perspectives	151
Summary	159
Samenvatting	163
PhD portfolio	167
Curriculum Vitae	177
Dankwoord	179
References	181

1. Introduction

1.1 Background

Humans are continuously exposed to electromagnetic fields (EMF). These EMF are for example generated by domestic devices, telecommunication systems, the transmission of electric power, but also in medical applications such as Magnetic Resonance Imaging (MRI) and hyperthermia treatments of cancer.

During the last century, numerous new electronic devices and technologies have been developed leading to an exponential increase in exposure to EMF. Especially the exposure to GSM and UMTS base stations and to other wireless technologies has led to a growing concern among the public about potential adverse health effects.

To avoid such adverse health effects, a number of national and international organizations have formulated guidelines containing limits for general public and occupational exposure. Safety or reduction factors are applied in these exposure limits to assure that threshold dose levels, at which biological effects have been established, are not exceeded. These factors and exposure limits have been derived from assessments that approximated the human anatomy by simple shapes and homogeneous materials and for a limited amount of exposure scenarios. Since individual anatomy and exposure conditions are highly diverse, it is questionable if the applied reduction factors are sufficient to keep the exposure under the threshold dose levels in all cases.

Exposure assessment or “dosimetry” is not only an integral part of health risk characterization for everyday situations, but also an important issue in medical applications. Medical exposure assessments can be used for example to assess the risk of wearing pacemakers in an Magnetic Resonance (MR) scanner, to target the heat in hyperthermia treatments and to estimate the exposure of medical staff. As a consequence, there is a mutual benefit in advanced electromagnetic models for both health risk assessments and medical applications.

1.2 Electromagnetic spectrum

The name “electromagnetic spectrum” describes a collection of different forms of electromagnetic (EM) radiation (Figure 1.1). EM radiation is emitted energy that travels through a medium or space with wave-like and particle-like properties. Radio waves, microwaves, infra-red, visible light, ultraviolet, X-rays and gamma-rays are fundamentally all electromagnetic radiation. The only difference is the frequency and hence the amount of energy of the photons. The word “radiation” is commonly used for ionizing radiation only, i.e. where the photons contain sufficient energy to ionize atoms or molecules. The work described in this thesis is limited to non-ionizing electromagnetic fields with frequencies lower than 300 GHz.

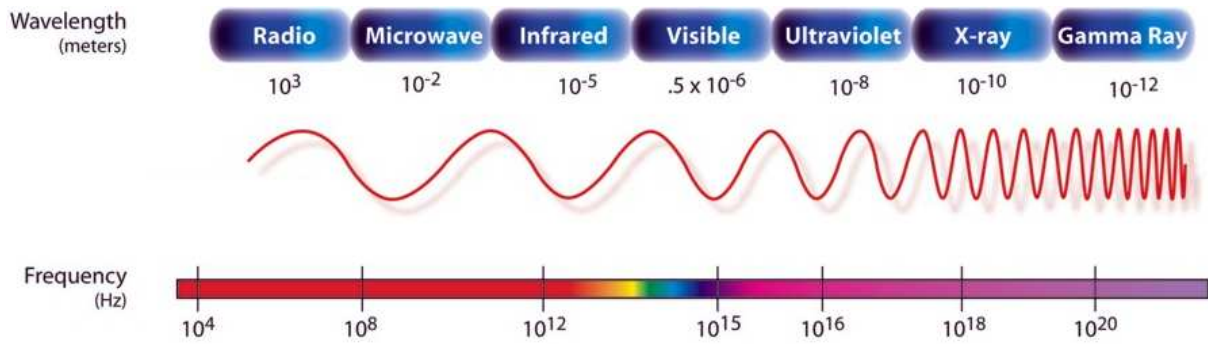


Figure 1.1: Visualization of the electromagnetic spectrum. www.wikipedia.org

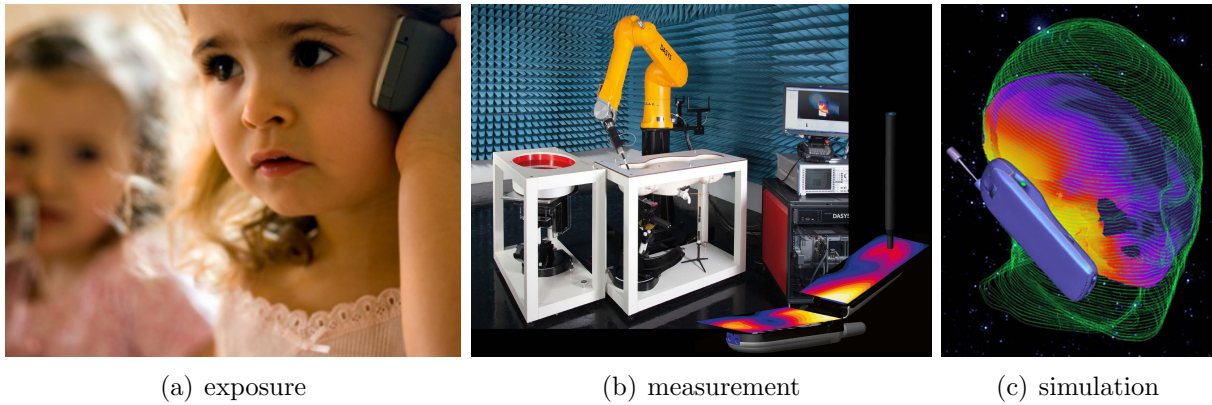


Figure 1.2: Example of dosimetry of a typical exposure configuration (a) using phantom measurements (b) or numerical simulations (c).

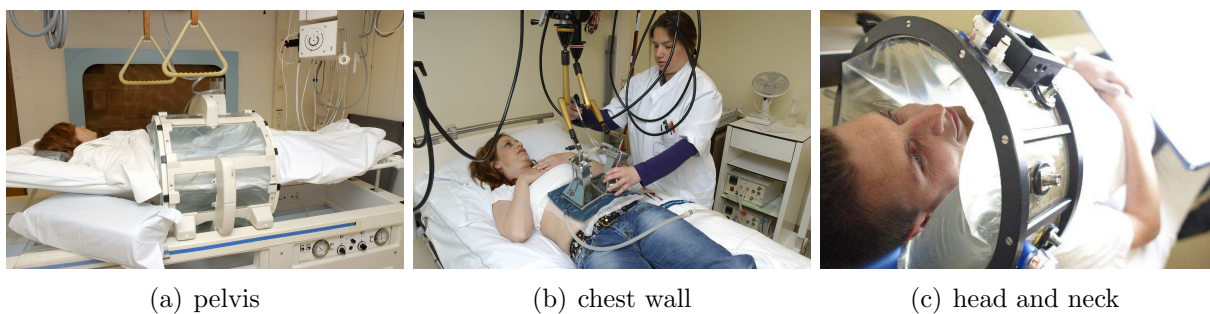


Figure 1.3: Hyperthermia applicators used at the Erasmus MC - Daniel den Hoed Cancer Center for various treatment sites.

1.3 Interaction of EMF with human tissues

Electric and magnetic fields exert forces on charges in materials, e.g. human tissues. However, these charges also produce electric and magnetic fields. Human tissues have dielectric (insulating) properties, i.e. when they are placed in an electric field electric charges do not flow through the material, as in a conductor, but only slightly shift from their average equilibrium positions causing dielectric polarization.

Interactions of the electric and magnetic fields with tissues are too complex to describe in terms of individual charges on a microscopic scale. Therefore, macroscopic material parameters, such as the permittivity, are used for these interactions. Maxwell's equations describe how electric charges and electric currents act as sources for the electric and magnetic fields. A detailed description can be found for example in Jackson¹⁰⁷. The interaction of EMF with materials depends on their frequency. For human tissues, three ranges can be distinguished that lead to different dominant biological and health effects:

- 1Hz-100kHz. Current densities, J (Am^{-2}) and internal electric fields, E_i (Vm^{-1}) can stimulate the nervous system.
- 100kHz-10GHz. Absorbed electromagnetic energy, expressed in SAR (Wkg^{-1}), is converted into heat that can cause tissue damage.
- 10GHz-300GHz. Superficially absorbed electromagnetic energy in the skin, expressed in S (Wm^{-1}) is converted into heat that can cause damage of skin tissue.

A detailed description of bio-electromagnetics can be found for example in Durney⁴⁶.

1.4 Dosimetry

Dosimetry is the assessment, by measurement or calculation, of the absorbed dose in matter and tissue resulting from the exposure to EMF. Dosimetry is required in epidemiological and biological studies for the development of dose-response models determining “safe” and “hazardous” levels.

The dose is usually reported in quantities such as electric fields, current densities, specific absorption rate and temperature increase, which must be assessed inside the body. Measurements in “phantoms” or numerical calculations are commonly used instead to determine the absorbed dose from a known source of exposure. Figure 1.2a shows a typical example of mobile phone exposure. The dose from a mobile phone (a) is either measured inside a phantom mimicking the brain, using an electric field monitor attached to a robotic arm (b)²⁸, or predicted by simulation software such as SEMCAD X (c)¹⁶⁷.

1.5 Topics addressed in this thesis

The goal of this thesis is to report several aspects of dosimetry in humans exposed to electromagnetic fields, by means of modelling, experiments and data analysis. Within the scope of this thesis, the research effort was focused on two main themes:

Part I. Exposure in daily life In the past, exposure guidelines were developed to restrict exposure of the general public. These guidelines approximated the human anatomy by simple shapes and homogeneous materials. Due to a lack of anatomically correct models of children, most studies on e.g. cell phone exposure and whole-body absorption used adult models that were scaled down to match the body dimensions of children. This approach has been disputed heavily and the World Health Organization (WHO) has recognized the importance for further research on children's exposure to EMF.

In response to increasing public concern over possible health hazards from electromagnetic fields, Erasmus MC and the IT'IS Foundation* started a joint project†. This project was aimed at providing a comprehensive assessment of the exposure in children to different field sources at a range from several Hz up to GHz frequencies, and to use the detailed dosimetry results to investigate how the guidelines from simple models translate to the dose in complex anatomies in various population groups.

Within the joint project, detailed anatomical models of adults and children were developed in combination with efficient algorithms to predict the complex propagation of electromagnetic waves. These state-of-the-art electromagnetic models were then used for detailed dosimetry in humans exposed to specific sources, such as mobile phones, induction cookers, trains and electronic article surveillance (EAS) systems.

For this thesis, the models of adults and children were exposed to uniform waves with various incidences and polarizations, such that the results are generic and can be used for a widespread of applications. First, the internal electric field were assessed for magnetic fields exposures at Extremely Low Frequencies (ELF). Second, the specific absorption rates were assessed for radio frequencies (RF). Third, the worst-case RF exposure scenarios were selected to assess also the local temperature increase.

Part II. Exposure in medical applications Hyperthermia (HT), an increase of the temperature towards 40 to 44°C, is a powerful modality to improve the clinical outcome of radiotherapy and chemotherapy. In the Erasmus MC - Daniel den Hoed Cancer Center, HT is applied for tumours at various treatment sites, such as the pelvic area, the chest wall and the head and neck (Figure 1.3). HT applicators use ultrasound (US) or electromagnetic (EM) waves to direct energy to the tumour region. Patient-specific treatment planning is used to obtain the correct treatment settings leading to an optimum heating strategy.

*Foundation for Research on Information Technologies in Society, Switzerland

†supported by the Netherlands Organization for Health Research and Development (ZonMw)

In 2003, a project[‡] was started to develop a head and neck HT applicator, including a high-power amplifier system. In this project the predicted SAR patterns were verified by measurements. This thesis shows that state-of-the-art validated electromagnetic models provide a better understanding of the complex interaction between electromagnetic fields and the human anatomy. Further, these models can be used to maximize treatment quality for patients while minimizing unwanted exposure of medical staff. However, when used in clinical routines, it is crucial to verify these models by measurements to guarantee patient safety and optimum treatment quality. Therefore, 2D verifications of the predicted SAR were performed in a prototype head and neck HT applicator, by using electric field sensors, an infra-red camera and fibre-optic temperature probes. 3D validation of the models is explored using a 7T Magnetic Resonance Imaging (MRI) scanner. Next, it is demonstrated that the mathematical models can be used as “virtual prototyping” tools to design new medical equipment, i.e. a phased-array HT applicator for heating deeply located tumours in the intact breast. Finally, it is demonstrated that detailed anatomical models and electromagnetic simulations provide a better understanding of counter intuitive hot-spots in the feet during hyperthermia treatments and that these models allow predicting the exposure in medical staff.

1.6 Outline of this thesis

Figure 1.4 illustrates the framework of this thesis. The exposure to EMF was computed for the general public, medical staff and patients and the computations were validated for hyperthermia treatments.

Chapter 2 demonstrates the detailed anatomical models of adults and children which were used in the various exposure assessments in this thesis.

Chapter 3 describes the guidelines and shows that the exposure levels are based on simple models.

Chapter 4 provides an overview of relevant sources that can emit electromagnetic fields during daily life scenarios.

Chapter 5 describes the assessment of the exposure of adults and children to uniform magnetic fields at extremely low frequencies (ELF).

Chapter 6 describes the simulation study to assess the exposure of adults and children to uniform electromagnetic fields at radio frequencies (RF).

Chapter 7 describes simulations to assess the worst-case local temperature increase in adults and children, when exposed to uniform electromagnetic fields at the maximum permitted levels.

[‡]supported by the Dutch Cancer Society (KWF)

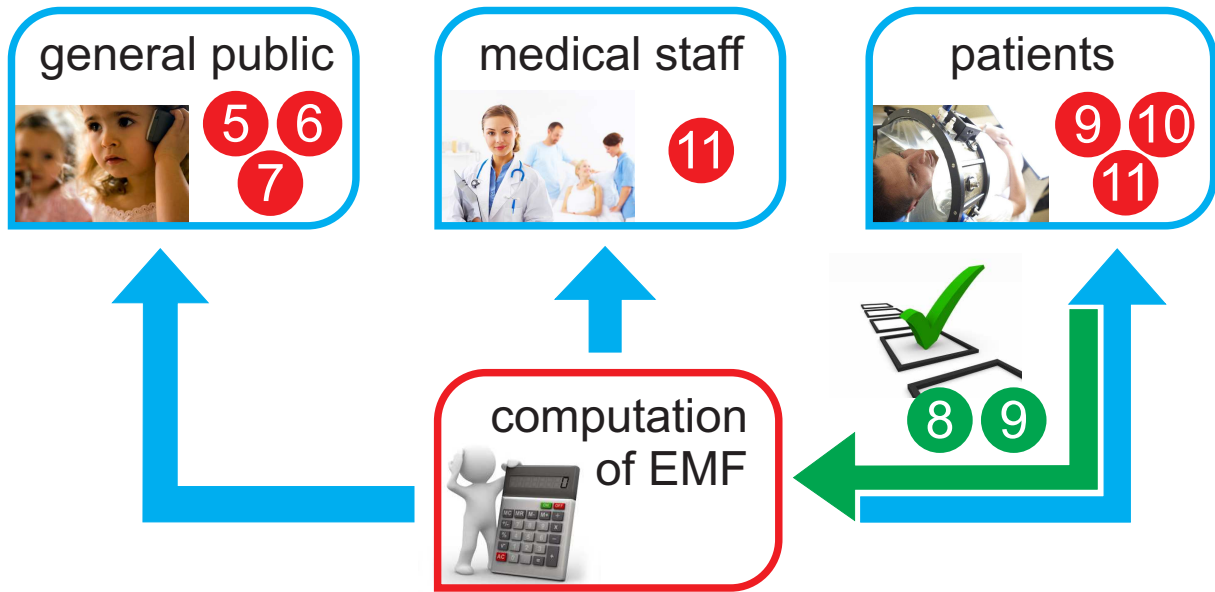


Figure 1.4: The framework of this thesis consists of three clusters: computations for 1) the general public in daily life exposure scenarios, 2) medical staff and 3) patients during hyperthermia treatments. The computations (blue arrows) are validated (green arrow) for hyperthermia treatments. The chapters are indicated by the numbers in the dots.

Chapter 8 demonstrates 2D validation of the electromagnetic model by infra-red, electric field and temperature measurements to verify the predicted SAR in a prototype head and neck hyperthermia applicator.

Chapter 9 explores if 3D validation of the electromagnetic model is feasible using a 7T MRI to verify the predicted RF excitation fields (B_1^+) in a modified prototype hyperthermia applicator.

Chapter 10 shows that detailed anatomical models and electromagnetic simulations can be used to design focussed heating applicators for hyperthermia treatments of tumours in intact breast.

Chapter 11 shows that detailed anatomical models and electromagnetic simulations can be used to provide a better understanding of the whole-body exposure of both patients and medical staff during hyperthermia treatments.

Chapter 12 provides the general conclusions and future perspectives.

2.

3D models

3D models of adults and children

2.1 Generation of numerical models of children of different age groups

Exposure assessments using numerical simulations require detailed models of the human anatomy. These anatomical models are created by delineating various tissues from Magnetic Resonance Imaging (MRI) scans and by using a literature database of physical tissue properties. For exposure assessments in children, anatomical models of adults have been scaled to the anatomical dimensions of children. This scaling introduces anatomical errors due to the strong changes of the body proportions during adolescence, leading to incorrect exposure assessments for children.

Therefore, several numerical body models, based on high-resolution MR-scans of children between 5 and 14 years of age, have been developed at the IT'IS Foundation (Figure 2.1). Approximately 80 organs and tissues are represented by three-dimensional CAD objects yielding a high level of detail. The models have a body mass and height which is typical for their age range (Table 2.1). The fidelity of the child models were reviewed and improved by medical doctors from the Erasmus MC - Daniel den Hoed Cancer Center. More information on the development of the models can be found in Christ et al.²³, and the regularly updated “Virtual Population” is freely available for scientific purposes*.

2.2 Development of methods and algorithms to change the posture of the model

To enhance the applicability of the models, dedicated software has been developed to change the posture in a natural fashion while maintaining the integrity of the inner organs, the skin and the outer tissue layers (Figure 2.2). Advanced deformation techniques¹⁶⁵ are

*<http://www.itis.ethz.ch/vip>

Table 2.1: Characteristics of the anatomical models, ordered according to the line-up in Figure 2.1. BMI is the Body Mass Index.

Name	Sex	Age (y)	Height (m)	Weight (kg)	BMI (kg/m ²)
Duke	male	34	1.77	72	23.1
Ella	female	26	1.63	59	22.0
Billie	female	11	1.47	35	16.5
Thelonious	male	6	1.17	19	14.0
Louis	male	14	1.69	50	17.7
Eartha	female	8	1.36	31	16.7
Dizzy	male	8	1.39	26	13.4
Roberta	female	5	1.09	18	14.9

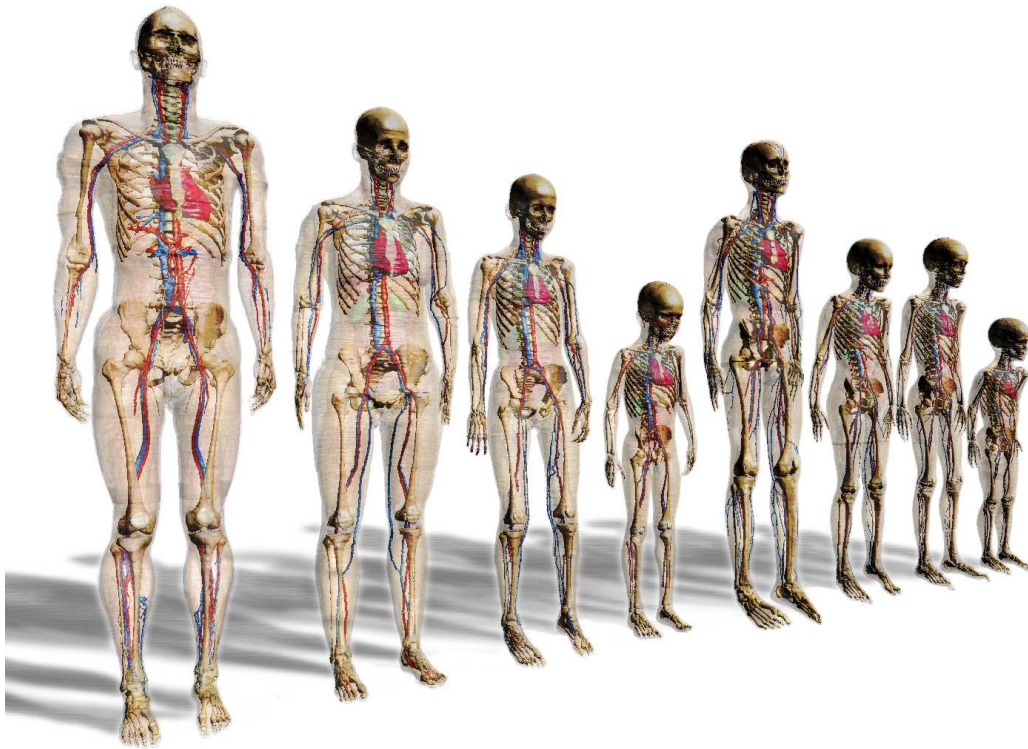


Figure 2.1: Virtual Family models used. From left to right: Duke, Ella, Billie, Thelonious, Louis, Eartha, Dizzy and Roberta.

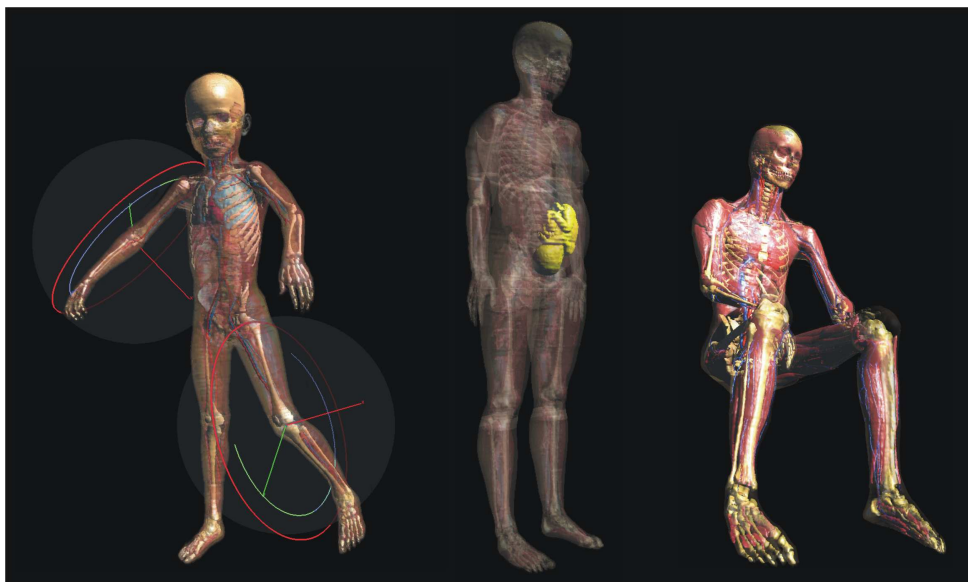


Figure 2.2: Examples of the poser tool: articulation of the joints (left), integration of a foetus in the Ella model (center), and a typical position (right).

used for easy articulation of joints in their physiological ranges, deformation of the soft tissue without loss of connectivity and without changes in the total tissue volume.

2.3 Online database of tissue properties

For the numerical models, both dielectric and thermal properties of the various tissues are required. The thermal tissue properties are based on an extensive literature study, containing more than 150 references. The dielectric properties in the database have been obtained by fitting a 4-Cole-Cole dispersion model on measurements using human cadavers and animals⁷⁴. This model allows obtaining the tissue properties for each frequency. Differences between the measurements of several references are used to estimate uncertainties in the tissue properties. In addition, age-dependent dielectric properties are available for a selection of tissues^{152,153}. Since the anatomical models contain more delineated tissues than defined in the dispersion models, a “recommended tissue properties table” was developed for dielectric and thermal properties assignments (Table 2.2)⁷.

Both the electromagnetic and thermal tissue properties are joined in an online[†] material parameter database⁸⁷, providing an up-to-date and comprehensive estimation of tissue material parameter values. In addition, the database contains the standard deviation and spread per tissue for the different thermal parameters.

Table 2.2: Virtual Family tissue parameters. ϵ_r is the relative dielectric permittivity, σ is the effective electric conductivity (Sm^{-1}), ρ is the volume density of mass (kgm^{-3}), c is the specific heat capacity ($\text{Jkg}^{-1} \text{ }^\circ\text{C}^{-1}$), k is the thermal conductivity ($\text{Wm}^{-1} \text{ }^\circ\text{C}^{-1}$), ω is the volumetric blood perfusion rate ($\text{mlmin}^{-1}\text{kg}^{-1}$) and Q is the metabolic heat generation rate (Wkg^{-1}).

Tissue	ϵ_r, σ (corresponding tissue in Gabriel et. al ⁷⁴)	ρ	c	k	ω	Q
Adrenal Gland	Gland	1025	3400	0.39	3060	61.0
Air Internal	Air Internal	1	1006	0.03	0	0
Aorta	Aorta	1060	3824	0.51	10^4	0
Artery	Blood	1060	3824	0.51	10^4	0
Bladder	Bladder	1040	3900	0.56	78	1.5
Blood	Blood	1060	3824	0.51	10^4	0
Cortical Bone	Cortical Bone	1990	1300	0.39	12	0.3
Cancellous Bone	Cancellous Bone	1920	1613	0.39	30	0.3
Bone Marrow Not Infiltr.	Bone Marrow Not Infiltr.	980	3120	0.32	450	5.8
Grey Matter	Grey Matter	1039	3675	0.57	671	6.8
White Matter	White Matter	1043	3621	0.50	237	6.8
Breast	BreastFat	928	2524	0.50	27	0.3
Bronchi	Blood Vessel	1063	3456	0.46	39	1.4
Bronchi Lumen	Air	1	1006	0.03	0	0
Cartilage	Cartilage	1100	3664	0.47	50	1.5
Cerebellum	Cerebellum	1040	3640	0.53	560	6.8
Cerebro Spinal Fluid	Cerebro Spinal Fluid	1007	4191	0.60	0	0
Cervix	Cervix	1013	3700	0.56	700	1.5
Commissura Anterior	White Matter	1043	3621	0.50	237	6.8
Commissura Posterior	White Matter	1043	3621	0.50	237	6.8
Connective Tissue	Tendon	1013	3035	0.37	39	1.4
Cornea	Cornea	1076	3793	0.52	38	0
Diaphragm	Muscle	1041	3546	0.53	28	0.5
Dura	Dura	1013	2947	0.35	38	0
Ear Cartilage	Cartilage	1100	3664	0.47	50	1.5
Epididymis	Gland	1050	3761	0.53	1697	61.0
Esophagus	Esophagus	1040	3500	0.53	383	1.4

[†]<http://www.itis.ethz.ch/vip>

Tissue	ϵ_r, σ (corresponding tissue in Gabriel et. al ⁷⁴)	ρ	c	k	ω	Q
Esophagus Lumen	Air	1	1006	0.03	0	0
Eye Lens	Lens Nucleus	1090	3664	0.40	38	0
Eye Sclera	Eye Sclera	1032	3000	0.40	38	0
Eye Vitreous Humor	Eye Vitreous Humor	1009	3932	0.59	0	0
Fat Average Infiltr.	Fat Average Infiltr.	916	2524	0.25	27	0.3
Fat Not Infiltr.	Fat Not Infiltr.	916	2524	0.25	27	0.3
Gall Bladder	Gall Bladder	1040	3900	0.55	78	1.6
Heart Lumen	Blood	1060	3824	0.51	10 ⁴	0
Heart Muscle	Heart	1060	3720	0.54	900	9.1
Hippocampus	Grey Matter	1039	3675	0.57	671	6.8
Hypophysis	Gland	1066	3761	0.53	1697	61.0
Hypothalamus	Gland	1050	3761	0.53	1697	61.0
Intervertebral Disc	Cartilage	1100	3664	0.47	50	1.5
Kidney Cortex	Kidney	1049	3745	0.52	4500	45.9
Kidney Medulla	Kidney	1044	3745	0.52	725	45.9
Large Intestine	Colon	1044	3653	0.56	752	9.1
Large Intestine Lumen	Muscle	1000	4000	0.20	0	0
Larynx	Cartilage	1028	3664	0.47	50	1.5
Lens Cortex	Lens Cortex	1090	3664	0.40	38	0
LensNucleus	LensNucleus	1090	3664	0.40	38	0
Liver	Liver	1050	3600	0.51	1007	11.4
Lung (Inflated)	Lung (Inflated)	655	3625	0.44	400	2.6
Lung (Deflated)	Lung (Deflated)	655	3625	0.44	400	2.6
Mandible	Cortical Bone	1990	1300	0.39	12	0.3
Red Marrow	Bone Marrow Infiltr.	1027	3120	0.32	219	5.6
Medulla Oblongata	White Matter	1039	3648	0.53	435	6.8
Meniscus	Cartilage	1098	3664	0.47	50	1.5
Midbrain	White Matter	1039	3648	0.53	435	6.8
Mucosa	Skin (Wet)	1100	3250	0.40	120	1.5
Muscle	Muscle	1041	3546	0.53	28	0.5
Nerve	Nerve	1038	3664	0.46	549	6.8
Ovary	Ovary	1048	3600	0.53	3059	62.4
Pancreas	Gland	1045	3452	0.49	625	22.0
Patella	Cortical Bone	1990	1300	0.39	12	0.3
Penis	Blood	1060	3824	0.51	10 ⁴	0
Pharynx	Air	1	1006	0.03	0	0
Pineal Body	Gland	1050	3600	0.53	3059	61.0
Pons	White Matter	1039	3648	0.53	435	6.8
Prostate	Prostate	1045	3761	0.53	1697	61.0
SAT	Fat Average Infiltr.	916	2524	0.25	27	0.3
Skin	Skin (Dry)	1100	3437	0.35	97	1.5
Skull	Cortical Bone	1990	1300	0.39	12	0.3
Small Intestine	Small Intestine	1044	3653	0.56	1000	12.5
Small Intestine Lumen	Muscle	1000	4000	0.20	0	0
Spinal Cord	Nerve	1038	3664	0.46	549	6.8
Spleen	Spleen	1054	3603	0.54	1142	14.3
Stomach	Stomach	1050	3553	0.53	374	5.0
Stomach Lumen	Muscle	1000	4000	0.20	0	0
Teeth	Cortical Bone	2160	1200	0.06	0	0
Tendon Ligament	Tendon	1110	3500	0.50	50	1.4
Testis	Testis	1044	3746	0.53	93	3.3
Thalamus	Grey Matter	1039	3675	0.57	671	6.8
Thymus	Thymus	1026	3960	0.52	1697	61.0
Thyroid Gland	Gland	1050	3553	0.53	9938	61.0
Tongue	Tongue	1041	3546	0.53	28	0.5
Trachea	Trachea	1100	3664	0.47	50	1.5
Trachea Lumen	Air	1	1006	0.03	0	0
Ureter Urethra	Blood Vessel	1056	3456	0.46	39	1.4
Uterus	Uterus	1052	3580	0.50	37.66	0.5
Vagina	Colon	1044	3653	0.56	752	9.1
Vein	Blood	1060	3824	0.51	10 ⁴	0
Vertebrae	Cortical Bone	1990	1300	0.39	12	0.3

Part I

Exposure in daily life

3.

Guidelines

Guidelines to restrict exposure to EMF

3.1 EMF exposure guidelines

Various organisations have proposed guidelines for limiting exposure to electromagnetic fields for protection against all established adverse health effects. The limits defined by ICNIRP* are used in many countries, including The Netherlands. In North America, the limits defined by IEEE† are used.

The limits are based on established evidence regarding acute effects shown in biological and epidemiological studies. Protection against acute health effects is assured if the dose *inside* the human body does not exceed “basic restrictions”. In general, dose assessment inside the human body is difficult and cannot be performed for all types of exposures. Therefore, practical “reference levels” for the external exposure are defined that can be used to determine whether exposure limits are met (Figure 3.1).

Reduction factors are applied to the basic restrictions to avoid acute biological and health effects during exposure. For example, a whole-body temperature increase of 1°C in 30 minutes was observed⁹⁹ in an RF exposure experiment at a whole-body averaged specific absorption rate (SAR_{wb}) of 4 Wkg⁻¹. In establishing the basic restrictions, reduction factors are used to account for both uncertainties in the scientific data and differences in sensitivity between various population groups, see Figure 3.2 for RF and Figure 3.3 for ELF.

The reference levels in the RF guidelines have been derived to translate the external exposure into internal dose levels, by using simple models developed in the early eighties. These models approximate the human anatomy by prolate spheroid bodies or homogen-

*International Commission for Non-Ionizing Radiation Protection

†Institute of Electrical and Electronics Engineers

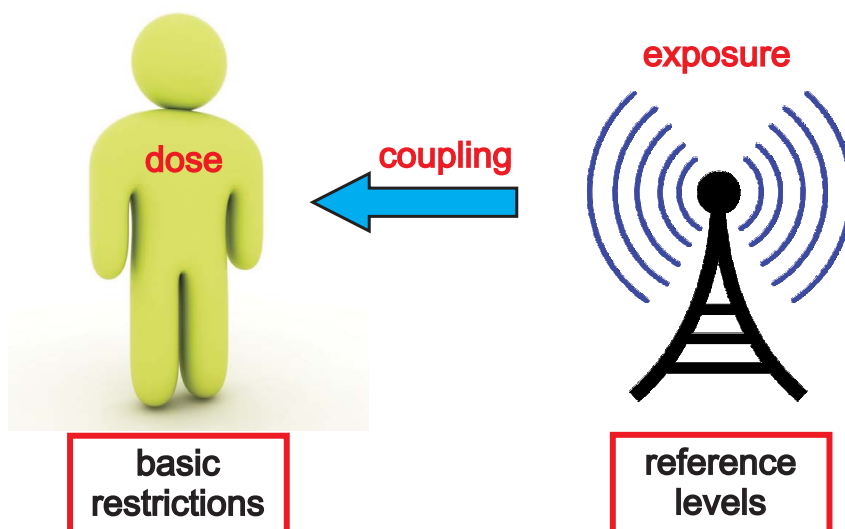


Figure 3.1: Quantities in de guidelines: basic restrictions on the internal dose and reference levels for the external exposure.

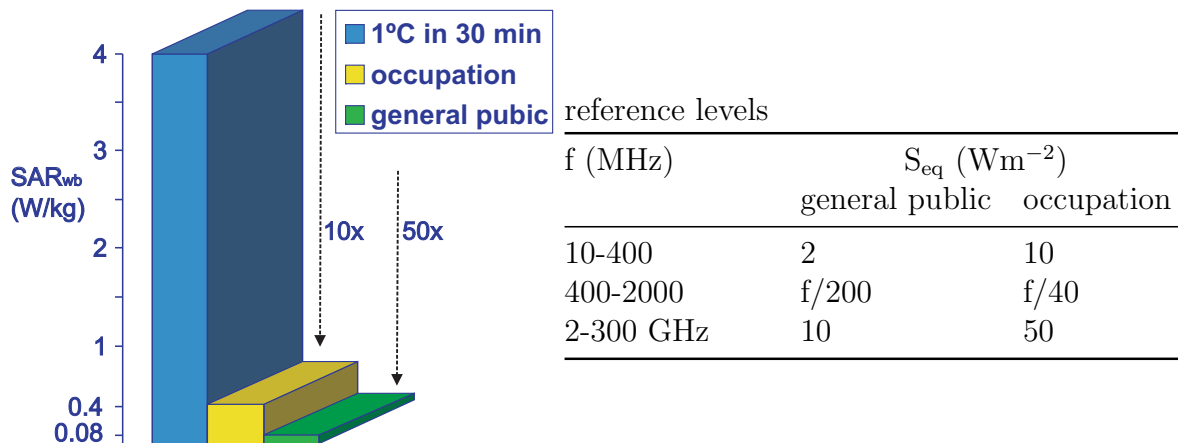


Figure 3.2: Basic restrictions on whole-body averaged specific absorption rate (SAR_{wb}) (left) and general public reference levels for the plane wave power density S_{eq} (right).

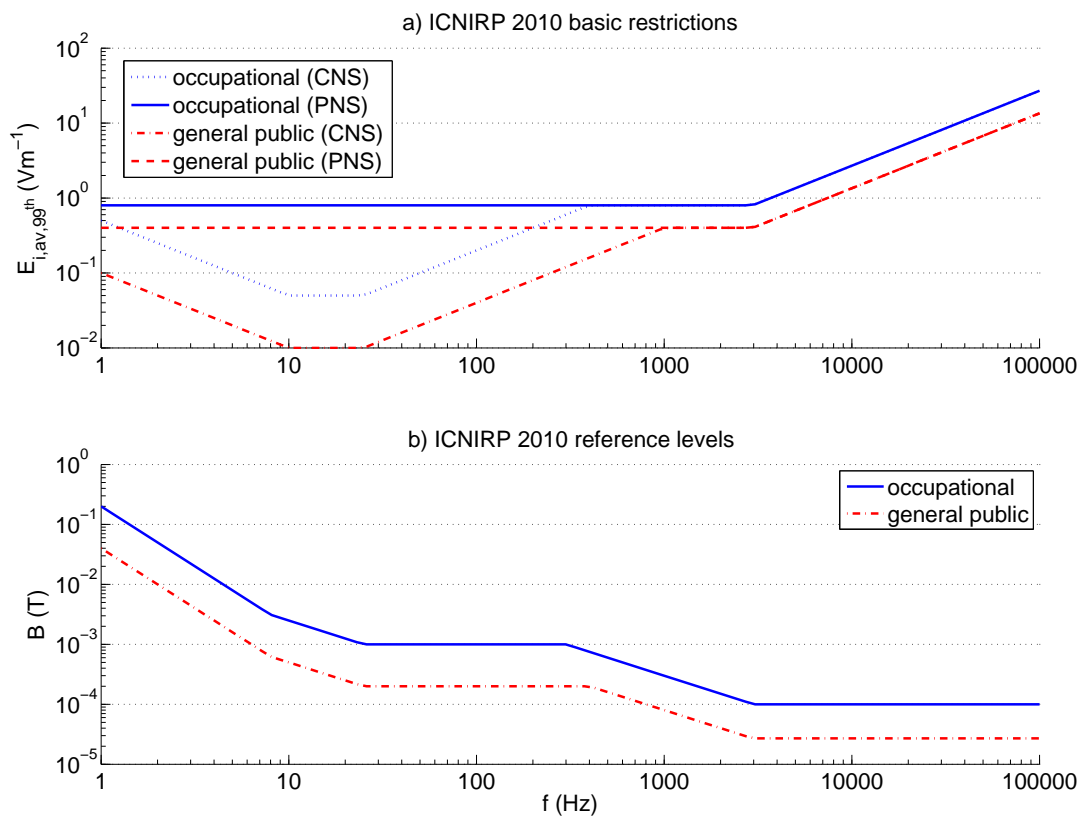


Figure 3.3: Basic restrictions on the averaged induced electric field strength (E_{i,av,99th}) (a) and reference levels for exposure to time-varying magnetic fields (b). The restrictions are specified separately for tissues of the central (CNS) and peripheral (PNS) nerve system.

eous blocks for which analytical solutions can be derived. The reference levels in the ELF guidelines have been derived from a limited set of exposure assessments in adult models. Today, detailed anatomical models and sufficient computational resources are available for precise and tissue specific dosimetry. Hence, the following question is investigated in this thesis:

Question: how do the reference levels from simple models translate into the dose in complex anatomies in various population groups?

More details can be found in the guidelines for low^{101,103} and for high frequencies^{99,103}. Note that for medical applications, such as Magnetic Resonance Imaging (MRI), special guidelines have been developed to protect patients¹⁰⁰.

4.

Dosimetry

EMF sources and dosimetry

4.1 Sources that emit electromagnetic fields

Electromagnetic fields are generated for example by domestic devices, telecommunication systems and the transmission of electric power. In literature, information is available on sources types and their characteristics, such as power, frequency, measured electric or magnetic field etc. Table 4.1 lists a number of sources that can emit strong electromagnetic fields, i.e. at field strengths above the ICNIRP reference levels. For these sources, the general public might be exposed to EMF above the recommended ICNIRP reference levels. However, (numerical) dosimetry is required to determine whether also the basic restrictions are exceeded.

In general, the exposure to EMF depends on time and location. For example, the exposure from Wi-Fi antennas in laptops reduces very rapidly with increasing distance and depends on internet traffic. Hence, it is difficult to assess the absorbed dose for all possible exposure scenarios, i.e. all possible locations of the exposed subject at all times. Since source-specific dosimetry is impossible for all scenarios, we distinct between exposure in the near-field or in the far-field and between exposure at extremely low (ELF) or radio frequencies (RF). This distinction allows major simplifications, such that we can perform human-specific dosimetry for “generic sources”, such as plane wave approximation in the radio frequency

Table 4.1: Examples of strong electromagnetic fields compared to the reference levels for the general public (% ICNIRP) at a distance (d) from the source.

EMF source	frequency	% ICNIRP	d (m)	reference
WLAN	2.4-17.3GHz	100	0.03-0.09	14,48
GSM	824-849MHz	238-386	0.05	9,128
GSM base station	880-1880MHz	100	3	14,47
EAS	218-58kHz	115-5851	0-0.2	61,76,86
energy transport	50Hz	100-220	7.6	12,51,142,202
induction cooker	800Hz	448-19100	0.1-1.5	61
microwave oven	2.45GHz	230	0.05	128,133
can opener	50Hz	150	0.15	51,88,142
power saw	50Hz	100	0.15	51,142
vacuum cleaner	50Hz	840	0.15	77,115
hair dryer	50Hz	2110	0.03	77,115
shaver	50-130Hz	165-1560	0-0.05	14,77,88,115
tag deactivator	1kHz	1625-1720	0-0.5	76
hand-held speedradar	10.5-24GHz	197-205	0.1	128,204
weather radar NL	5.7GHz	131	1000	14
radio navigation	10.2-100kHz	3253-5057	3-12	81,128
radio broadcasting	205kHz-164MHz	6-5000	0-30	1,14,24,50,85,123 128,134,158,178,181

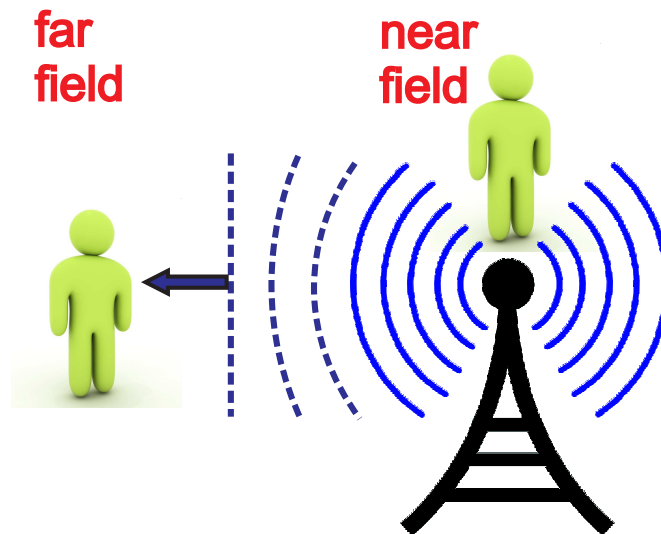


Figure 4.1: Field regions of a radiating antenna. In the near-field, inductive and capacitive effects are influenced by the anatomy. In the far-field region, i.e. at a few wavelengths distance, the wave fronts are uniform and the anatomy does not influence the antenna properties.

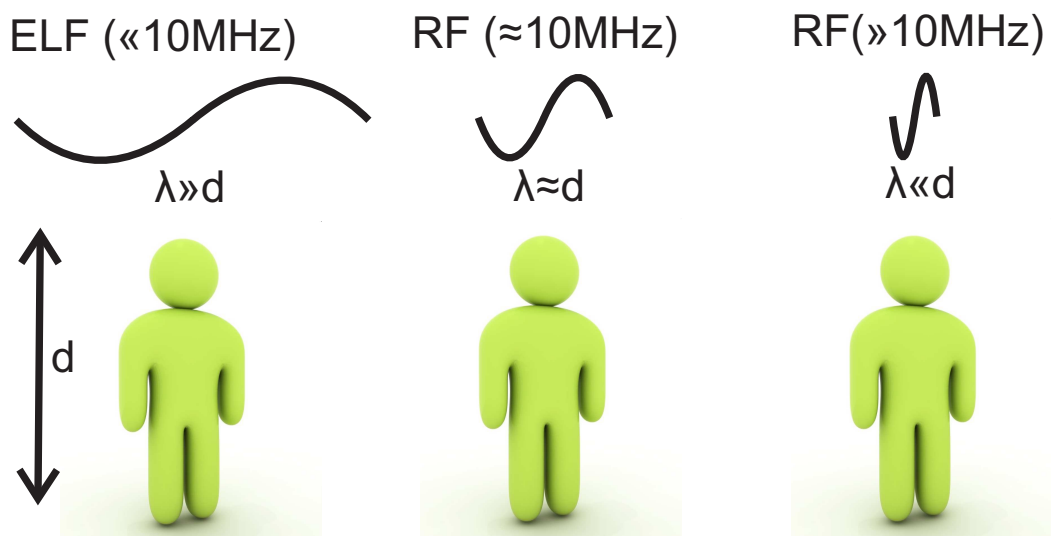


Figure 4.2: Size of the anatomy (d) versus wavelength. For extremely low frequencies (ELF), the anatomy is small compared to the wavelength. For high frequencies (RF), the anatomy is relatively large.

range and uniform exposure from ELF magnetic fields. However, for non-uniform exposure scenarios in the near field, such as a mobile-phone (RF) and induction cookers (EL), a full dose assessment including an accurate source description is still required.

4.2 Near-field and far-field region

EMF sources can be located nearby the human body, e.g. a mobile phone during a phone call, or far away, e.g. an FM radio station at a distance of 50 kilometres. However, more important than the physical distance is the ratio between the physical distance and the wavelength. For example, the wavelength is approximately 13 centimetres for mobile phone UMTS frequencies, while it is three meters for a radio FM antenna.

A distinction between “near-field” and “far-field” region is commonly made in exposure assessments. The near-field is a region generally in close proximity to an antenna or radiating structure, i.e. where the electric and magnetic field vary considerably from point to point. In the far-field, the electric and magnetic fields are uniform and have a plane wave character.

For near-field assessments, detailed knowledge about the antenna or radiating structure is required to accurately predict the complex wave patterns near the antenna. In addition, the presence of any dielectric material in the proximity of the antenna influences the antenna characteristics. For example, the radiation pattern and coupling of energy of a mobile phone is sensitive to various positions and geometry of the human head.

In the far-field, there is no influence of the human anatomy on the antenna characteristics. Consequently, exposure assessment in the far-field has the great advantage that detailed knowledge on the antenna radiation characteristics and relative position are not required.

4.3 Exposure at ELF or RF

The characteristic behaviour of electromagnetic fields in and around objects differs with its size compared to the wavelength. Figure 4.2 distinguishes three different cases: the wavelength is much bigger, similar or smaller than the outer anatomy dimensions. For each wavelength or frequency range, specific assumptions can be applied.

For extremely low frequencies, the magnetic and electric fields are said to be “uncoupled”, because they do not act as sources of each other. Propagation effects are negligible and quasi-static approximations allow fast numerical computations.

For radio frequencies, the magnetic and electric fields are “coupled”. A time-changing magnetic field acts as a source of an electric field and vice versa. Hence, neither the electric or magnetic fields exists alone. Propagation effects dominate and electromagnetic field theory is used to describe the propagating waves.

Resonance effects might be observed for wavelengths comparable to the size of the anatomy, i.e. the human anatomy can radiate due to external field excitation.

4.4 Generic and specific exposure assessments

Since it is impossible to assess the dose for all exposure scenarios and all human anatomies, the general public exposure in this thesis is restricted to generic exposure conditions.

Hereto, the exposure to uniform magnetic fields at extremely low frequencies and plane waves at radio frequencies was investigated.

Within the ZonMw project, the dose was assessed also for specific sources, such as induction cookers, mobile phones, trains and electric cars. Furthermore this thesis demonstrates that the same electromagnetic simulation models can be used also for specific exposure conditions. Hereto the dose was assessed in patients and medical staff during hyperthermia treatments, for which the exposed subjects are in the proximity of the radiating sources.

5. ELF

Exposure to extremely low frequency magnetic fields

This chapter is based on:

JF Bakker, MM Paulides, A Christ, XL Chen, N Kuster and GC van Rhoon. "Children and adults exposed to low frequency magnetic fields at the ICNIRP reference levels: theoretical assessment of the induced electric fields".

Phys Med Biol, Vol. 57, No. 7, pp. 1815-1829, 2012.

Abstract

Purpose: To avoid potentially adverse health effects, the International Commission on Non-Ionizing Radiation Protection (ICNIRP) has defined reference levels for time varying magnetic fields. Restrictions on the electric fields induced in the human body are provided based on biological response data for peripheral nerve stimulation and the induction of phosphenes. Numerical modelling is commonly used to assess the induced electric fields for various exposure configurations. The objective of this study was to assess the variations of the electric fields induced in children and adults and to compare the exposure at reference levels with the basic restrictions as function of anatomy. **Materials and methods:** We used the scalar potential finite element (SPFE) method to calculate the induced electric fields in six children and two adults when exposed to uniform magnetic fields polarized in three orthogonal directions. **Results:** We found that the induced electric fields are within the ICNIRP basic restrictions in nearly all cases. In PNS tissues, we found electric fields up to 95% (upper uncertainty limit due to discretization errors, $k=2$) of the ICNIRP basic restrictions for exposures at the general public reference levels. For occupational reference levels, we found an over-exposure of maximum 79% ($k=2$) in PNS tissues. We further found that the ICNIRP recommendations on spatial averaging in $2 \times 2 \times 2$ mm³ contiguous tissue volumes and removal of peak values by the 99th percentile cause the results to depend strongly on the grid discretization step (i.e. an uncertainty of more than 50% at 2 mm) and the number of distinguished tissues in the anatomical models. **Conclusions:** The computational results obtained by various research institutes should be robust for different discretization settings and various anatomical models. Therefore, we recommend considering alternative routines for small anatomical structures, such as non-contiguous averaging without taking the 99th percentile in future guidelines leading to consistent suppression of peak values amongst different simulation settings and anatomical models. The peak electric fields depends on the local tissue distribution in the various anatomical models and we could not find a correlation with the size of the anatomy. Therefore, we recommend extending the evaluation using a sufficient set of anatomies including other than standing postures, to assess the worst-case exposure setting and correspondence to the basic restrictions.

5.1 Introduction

Public concern over health effects of electromagnetic fields has increased, due to the exponential increase in electric power consumption²⁰³. In the past, exposure guidelines have

been developed to provide protection against all established adverse health effects^{99,101}. For the radio frequency (RF) range, these guidelines are based on keeping the temperature increase under 1 °C^{64,191,207}. In the early guidelines, restrictions on exposure of people to low frequency (1 Hz to 100 kHz) magnetic fields were based on limiting the current densities that are induced in the human body⁹⁹. The induction of currents was considered as the major mechanism for biological and health effects such as the excitation of muscle and central nervous tissues, as most experimental data at that time were based on this metric. Today, guidelines are based on biological response data of induced electric field thresholds for peripheral nerve stimulation and the induction of magnetic phosphenes¹⁰¹. While limits on induced currents and electric fields are useful for theoretical analyses, reference levels for the incident electric and magnetic fields are derived to enable fast assessments. In the original guidelines⁹⁹, these reference levels were determined by mathematical modelling of exposure conditions by using simple geometric models. The new guidelines¹⁰¹ are based on computational simulations using anatomically detailed models of an average adult male and female^{37,38}. As individual anatomy is highly diverse, it is difficult to generalize the results from only two models to the entire human population. Therefore, subsequent studies were used to investigate the induced currents and electric fields^{29,34,37–39,90,175}. Only adult models were used for these investigations in the majority of the cases.

Some studies examined the exposure of children to the non-uniform fields generated by electronic article surveillance (EAS) devices¹¹². Gandhi and Kang⁷⁶ assessed the induced current densities for down-scaled 10-year-old and 5-year-old child models exposed to EAS devices operating at 1 and 30 kHz. Bahr et al.⁴ used the down-scaled 5-year-old exposed to 50 Hz uniform electric and magnetic fields. Martinez-Burdalo et al.¹²⁹ is an exception as they calculated the induced current densities of EAS devices operating at 10 MHz, by using down-scaled 10-year-old and 5-year-old child models, and also two anatomically correct models of 11-year-old and 6-year-old children from the Virtual Family project²³. Overall, the majority of these studies used approximated down-scaled models, leading to non-realistic assessments and therefore, further research is required to fill this gap²⁰⁰. Hence, an extended evaluation using a sufficient set of anatomies, for both uniform and non-uniform exposures and various frequencies, is necessary to verify the suitability of the reference levels for children.

The main interaction of low frequency magnetic fields with humans is the Faraday induction of electric fields leading to currents in tissues. Humans do not significantly perturb the low frequency magnetic fields, since the permeability of tissue is the same as that of air. Therefore, the induced electric fields and the currents are defined by the orientation of the external field and the conductivity distributions in a human body. The induced quantities are not independent as the induced electric field and the current density in the body are linearly related through Ohm's law. The peak current densities are not necessarily located at the same spatial locations as the peak electric fields, due to the contrast in conductivity. Faraday's law states that the induced electric fields and circulating currents in homogeneous materials are proportional to the radius of the loop (i.e. the cross-section of the body), the frequency, the conductivity and the magnitude of the

magnetic flux density. Hence, in general the highest electric fields and currents will be induced if the magnetic field is oriented from front-to-back. However, other field orientations might induce the highest electric fields and currents in the individual organs and specific tissues. Most of the current literature has studied only three orthogonal orientations of the magnetic flux density vector: side-to-side, front-to-back and head-to-feet.

The objective of this study was to assess the variations of the electric fields induced in children and to compare exposure at reference levels with the basic restrictions as function of anatomy. In a brute-force approach, we assessed the induced electric fields in anatomical models of six children and two adults exposed to uniform magnetic fields. The anatomical models were exposed to fields with various field orientations and frequencies in the range of 1 Hz to 100 kHz. Additional simulations with altered settings were used to assess the dependence of the results on grid discretization and on polarization direction to find the worst-case values. We used the anatomical models of the Virtual Family in standing position and we did not investigate the electric fields for other anatomical postures.

5.2 Methods

5.2.1 Numerical model

The electric fields induced in the human body by magnetic fields were analyzed using the Magneto Quasi Static low frequency solver of SEMCAD X¹⁶⁷, which uses a Biot-Savard solver and is based on the Scalar Potential Finite Element (SPFE) method. Uniform rectilinear meshes were applied to easily discretize the complex anatomical models. The code implementation of the SPFE method is validated by comparing its results to analytical solutions for simple geometries. The validation scenario consisted of an ungrounded uniform ellipsoidal object exposed to uniform magnetic fields at different polarizations and the maximum difference between the numerical and analytical solutions was within 1%. A description of the methods and validation of the low frequency solver can be found in Chen²⁰.

5.2.2 Contiguous tissue evaluations

The dosimetric results were assessed in terms of the induced electric fields per specific tissue. ICNIRP¹⁰¹ recommends determining the induced electric field at any location \mathbf{r}_0 as a vector average of the electric field within a small cubic volume of $2 \times 2 \times 2 \text{ mm}^3$ of contiguous tissue, i.e. tissue-specific. More specifically,

$$\langle \mathbf{E}(\mathbf{r}_0) \rangle_V = \frac{1}{V} \int_V \mathbf{E}(\mathbf{r}) dv, \quad (5.1)$$

where $0 < V \leq 8 \text{ mm}^3$ is the volume of the selected tissue within the cube. The averaging is performed on a cube centered at each tissue voxel. The integration of the electric fields

within this volume is obtained by summing up the contribution of each voxel as follows:

$$\langle \mathbf{E}(\mathbf{r}_0) \rangle_V \approx \frac{1}{V} \sum_n \mathbf{E}(\mathbf{r}_n) f_n V_n, \quad (5.2)$$

where V_n is the volume of the n^{th} voxel within the cube and $0 < f_n \leq 1$ is the filling factor accounting for the partial volume of the outermost voxels of the averaging cube. For a specific tissue, the 99th percentile value of the averaged electric field is the relevant value to be compared with the basic restriction. In addition, ICNIRP¹⁰¹ states as a general rule that the averaging volume should not extend beyond the boundary of the tissue except for tissues such as the retina and skin, which are too thin to cover the whole averaging cube. For the skin, the averaging volume may extend to the subcutaneous tissue. For the retina it may extend to the tissues in front and behind it.

Following these guidelines, we implemented an algorithm using the SEMCAD X v14 Python scripting interface, that calculates the 99th percentile of the average induced electric field ($E_{i,\text{av},99^{\text{th}}}$) for each specific tissue in peripheral (PNS) tissues of the whole-body and central nerve system (CNS) tissues of the head. The maximum value of the PNS and CNS tissues, is reported as the peak average induced electric field ($E_{i,\text{av},99^{\text{th}},\text{max}}$).

5.2.3 Human models and dielectric properties

We used eight human models (Figure 2.1), which have been developed from high-resolution MRI data and are known as the “Virtual Family” and the “Virtual Classroom”^{5,23}. They consist of models of six children and two adults of both genders with various body dimensions (Table 2.1). A 4-Cole-Cole dispersion model for each tissue type was used to assign the frequency dependent effective conductivity (σ), according to the commonly used database from Gabriel et al.⁷⁴. We assigned dielectric properties according to the “recommended tissue properties”⁷, since the models contain more delineated tissues than defined in the dispersion model. We do note that the dispersion model below 1 MHz is based on sparse measurements and that more accurate dielectric properties can be found for selected tissues and frequencies⁷².

5.2.4 Exposure configurations

We selected three orthogonal polarizations of the incident magnetic field vector: B_x , B_y and B_z . Two opposing current lines (length = 10 mm) were placed in the x, y, or z-direction at a distance of 100 m from the body, leading to an homogeneity in the magnetic field above 99.99%. Note that the induced magnetic fields in the body are neglected by the quasi-static approximation. In addition we investigated also non-orthogonal fields for the Roberta model, by varying the inclination between the magnetic field vector and the x, y, or z axis in steps of 5° between -90° and 90°.

The external magnetic fields at the human body were normalized to the reference levels and the induced electric fields were normalized to the basic restrictions (Figure 3.3) and

we extracted the peak of all PNS or CNS tissues such that,

$$E_{i,\text{av},99^{\text{th}},\text{max}} (\%) = \frac{\max(E_{i,\text{av},99^{\text{th}}})}{E_{i,\text{av},99^{\text{th}},\text{basic restriction}}} \frac{B_{\text{reference level}}}{B_{\text{body}}} 100 \%. \quad (5.3)$$

5.2.5 50 Hz and 60 Hz

Humans in most countries have been exposed to low-frequency electric and magnetic fields at power-line frequencies (50 or 60 Hz) for more than a century. This exposure is associated with transmission and distribution of electricity and the use of various electrical and electronic devices at home and work^{110,175}. Therefore, we decided to point out the results of our study in more detail for the frequencies of both 50 Hz and 60 Hz.

5.2.6 Grid discretization error

The effect of the spatial resolution in the model discretization was investigated by repeating the simulations at grid discretization steps (Δ_{grid}) between 0.75 (computational limit) and 3 mm (arbitrarily chosen). Hereto, we exposed the Roberta model to each of the three orthogonal uniform magnetic fields at 50 Hz and 100 kHz. We used the maximum deviation u from the center of the dynamic range between 0 to 2 mm, and since we do not have data between 0 and 0.75 mm, we assume that this represents one standard deviation of a normal (Gaussian) distribution. We used a coverage factor ($k=2$) to obtain the expanded uncertainty in the 95% confidence interval. For simplicity, we report only the maximum discretization errors observed for the three polarizations and the two frequencies.

5.3 Results

5.3.1 Orthogonal polarized magnetic fields

To investigate if the induced electric fields remain below the ICNIRP basic restrictions, we exposed the adult and child models to uniform magnetic fields at the reference levels and at frequencies in the range of 1 Hz to 100 kHz. Figure 5.1 shows the maximum induced electric fields for the general public. Maximum 52% of the basic restriction on the electric field is induced for CNS tissues and 62% for PNS tissues. Due to the grid discretization uncertainty, this maximum extends to 80% (CNS) and 95% (PNS) for the upper limit of the 95% confidence interval ($k = 2$).

Figure 5.2 shows that maximum 52% (85%, $k = 2$) of the basic restriction is induced for CNS tissues at the occupational reference levels. For PNS tissues at the occupational reference levels, the maximum fraction is 116% (179%, $k = 2$) in the frequency range of 400 Hz to 65 kHz, i.e. an overexposure of maximum 79% for the Thelonious child model. We detected an over-exposure also for adult models at the occupational levels, i.e. 149% ($k = 2$) for the adult woman and 141% ($k = 2$) for the adult man.

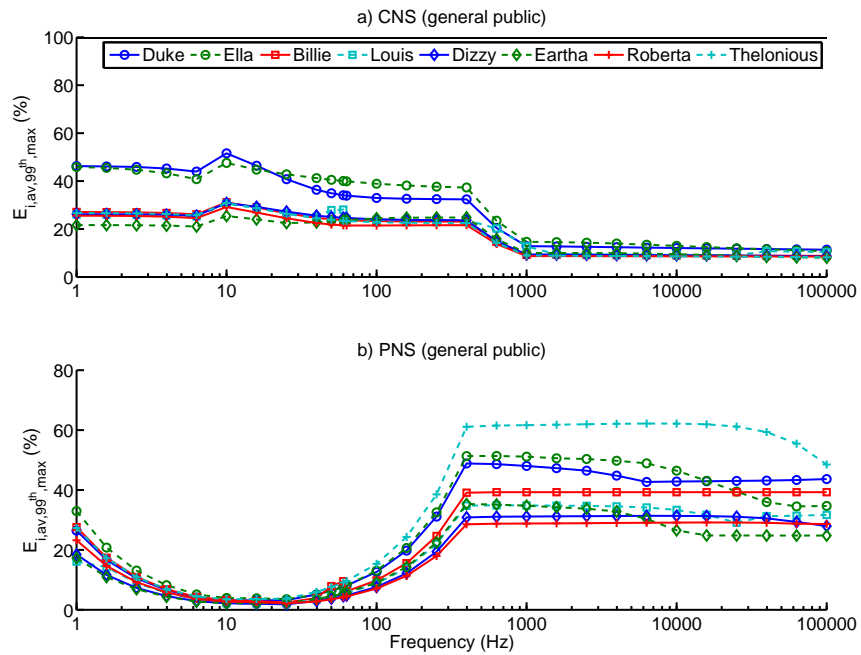


Figure 5.1: Maximum fraction of the ICNIRP basic restriction ($E_{i,av,99th,max}$) for exposure of the **general public** to magnetic fields at the reference levels.

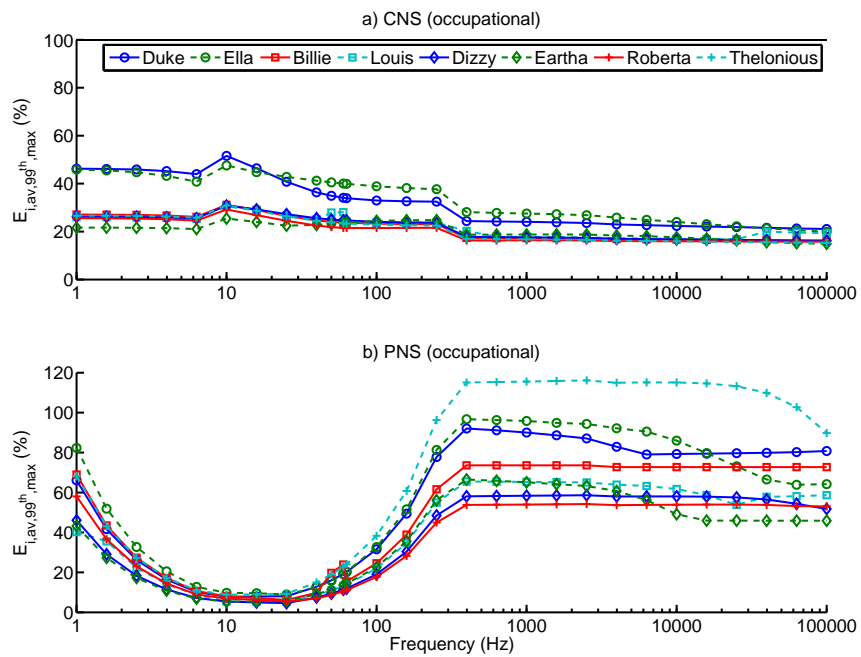


Figure 5.2: Maximum fraction of the ICNIRP basic restriction ($E_{i,av,99th,max}$) for **occupational** exposure to magnetic fields at the reference levels.

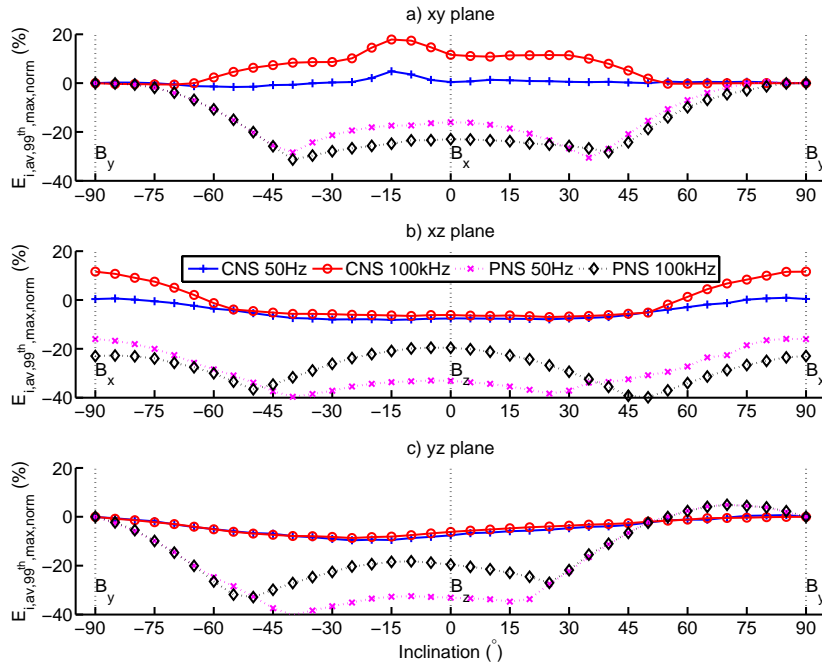


Figure 5.3: Influence of the inclination of the magnetic field vector on the peak averaged induced electric field in the Roberta model. The inclination is varied for polarizations in a) the xy plane, b) the xz plane and c) the yz plane. The horizontal dashed lines indicate the inclinations with orthogonal polarization in either the x, y or z direction. The magnetic fields are normalized to the ICNIRP reference levels. The induced electric fields are normalized to those at B_y polarization and specified separately for 50 Hz/100 kHz and CNS/PNS tissues

5.3.2 Non-orthogonal polarized magnetic fields

We investigated non-orthogonal polarized magnetic fields for the Roberta model by varying the inclination in the xy, yz and xz planes and normalizing the electric fields to those for B_y polarization. Figure 5.3 shows that the maximum electric fields are not necessarily obtained for orthogonal polarizations of the uniform magnetic field. The inclination at the maximum electric fields depends on the tissue type, i.e. CNS or PNS and on the frequency for this specific model in this position. The maximum variations in the peak electric fields ($E_{i,av,99th,max}$) due to polarization changes in the xy, xz or yz plane, is restricted to the range between -40 and 18%.

5.3.3 50 Hz and 60 Hz

Table 5.1 lists the peak electric fields ($E_{i,av,99th}$) in both CNS and PNS tissues for frequencies of 50 Hz and 60 Hz. The values demonstrate that grey matter and nerve tissues

Table 5.1: Peak electric fields ($E_{i,av,99th}$) normalized to the magnetic field exposures at a frequency of 50 Hz or 60 Hz ($Vm^{-1}T^{-1}$). The magnetic field polarization is parallel to either the x ($E@B_x$), y ($E@B_y$) or z axis ($E@B_z$). The text behind the value indicates the tissue where the peak induced electric field is located. Note that “grey m.” is brain grey matter, “large int.” is large intestines and “vert.” is vertebrae.

CNS tissues						
Name	50 Hz			60 Hz		
	$E@B_x$	$E@B_y$	$E@B_z$	$E@B_x$	$E@B_y$	$E@B_z$
Duke	35 grey m.	27 grey m.	24 grey m.	41 grey m.	32 grey m.	28 grey m.
Ella	41 nerve	24 grey m.	23 nerve	48 nerve	29 grey m.	28 nerve
Billie	24 grey m.	24 grey m.	23 grey m.	29 grey m.	28 grey m.	27 grey m.
Thelonious	24 grey m.	23 grey m.	21 grey m.	28 grey m.	27 grey m.	25 grey m.
Louis	25 grey m.	28 nerve	21 grey m.	29 grey m.	34 nerve	25 grey m.
Eartha	23 nerve	19 grey m.	19 grey m.	28 nerve	23 grey m.	23 grey m.
Dizzy	23 grey m.	24 grey m.	25 grey m.	27 grey m.	29 grey m.	30 grey m.
Roberta	22 grey m.	22 grey m.	20 grey m.	26 grey m.	26 grey m.	24 grey m.

PNS tissues						
Name	50 Hz			60 Hz		
	$E@B_x$	$E@B_y$	$E@B_z$	$E@B_x$	$E@B_y$	$E@B_z$
Duke	129 mucosa	93 skin	65 vert.	154 mucosa	112 skin	79 vert.
Ella	127 mucosa	117 vagina	67 vert.	154 mucosa	129 vagina	82 vert.
Billie	56 large int.	158 skin	38 vert.	65 skull	191 skin	46 vert.
Thelonious	70 mucosa	152 skin	44 skin	85 mucosa	183 skin	53 skin
Louis	88 mucosa	66 bone	57 vert.	105 mucosa	81 bone	69 vert.
Eartha	91 mucosa	60 skin	47 vert.	109 mucosa	73 skin	57 vert.
Dizzy	62 skull	75 skin	46 vert.	75 skull	90 skin	56 vert.
Roberta	59 mucosa	70 skin	47 vert.	70 mucosa	84 skin	57 vert.

are the CNS tissues where the maximum peak electric fields are located. For PNS tissues, the tissue where peak electric fields are induced depends on the magnetic field polarization, i.e. mucosa for B_x , skin for B_y and vertebrae for B_z . The peak electric fields are not only found for front-to-back (B_y) but also for side-to-side (B_x) polarizations. Due to small changes in tissue conductivity between 50 Hz and 60 Hz, the peaks are located in the same tissues and the values can be obtained using the fraction ‘60/50’, as can be expected from Faraday’s law.

5.3.4 Dependence on cross-section of the body

In general, the amount of induced electric fields is correlated to the radius of the loop, i.e. the cross-section of the body. However, the local peak averaged electric fields ($E_{i,av,99th}$) are not necessarily related to the size of the Virtual Family models. Therefore, we displayed the peak averaged electric fields as a function of the length, as a surrogate for the cross-section, of the Virtual Family models at two frequencies (50 Hz and 100 kHz) and at three orthogonal polarizations. Figure 5.4 demonstrates that there is no clear correlation, i.e. the highest local peak values are not necessarily found for the anatomical models with

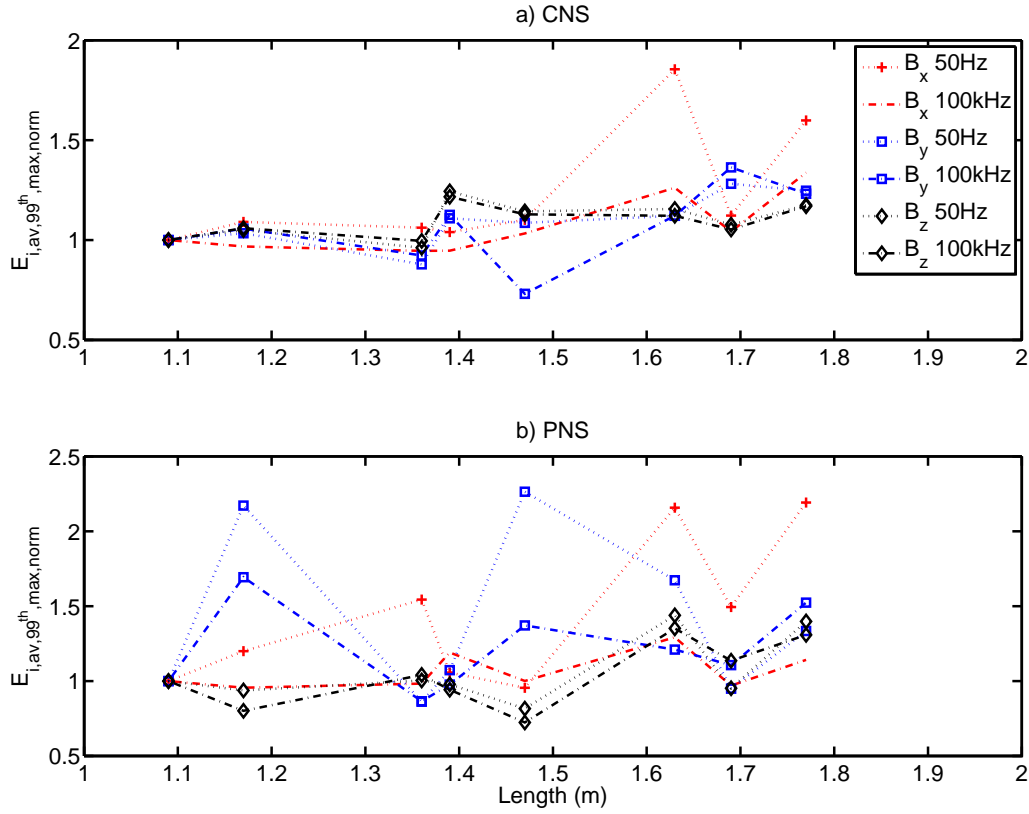


Figure 5.4: Peak averaged induced electric field ($E_{i,av,99^{th},norm}$) as a function of the anatomical length, normalized to the value at the smallest Virtual Family model (Roberta is 1.09m).

the highest body cross-sections.

5.3.5 Grid discretization error

Figure 5.5 shows the peak averaged induced electric fields (max and 99th percentile) as a function of the grid discretization step. The dashed lines indicate the dynamic range of the electric fields between 0 and 2 mm. The maximum deviation u from the center of the dynamic range is indicated in the legend. The values do not yet converge for decreasing discretization steps. As a consequence, we could not estimate a converged value at zero discretization and compute the error at the discretization of 2 mm used in this study. Since no data between 0 and 0.75 mm is available, we assume that the maximum deviation between 0 and 2 mm, i.e. 27% (99th) and 29% (max), represents one standard deviation of a normal (Gaussian) distribution. The expanded uncertainty ($k=2$) is thus 54% (99th) and 58% (max).

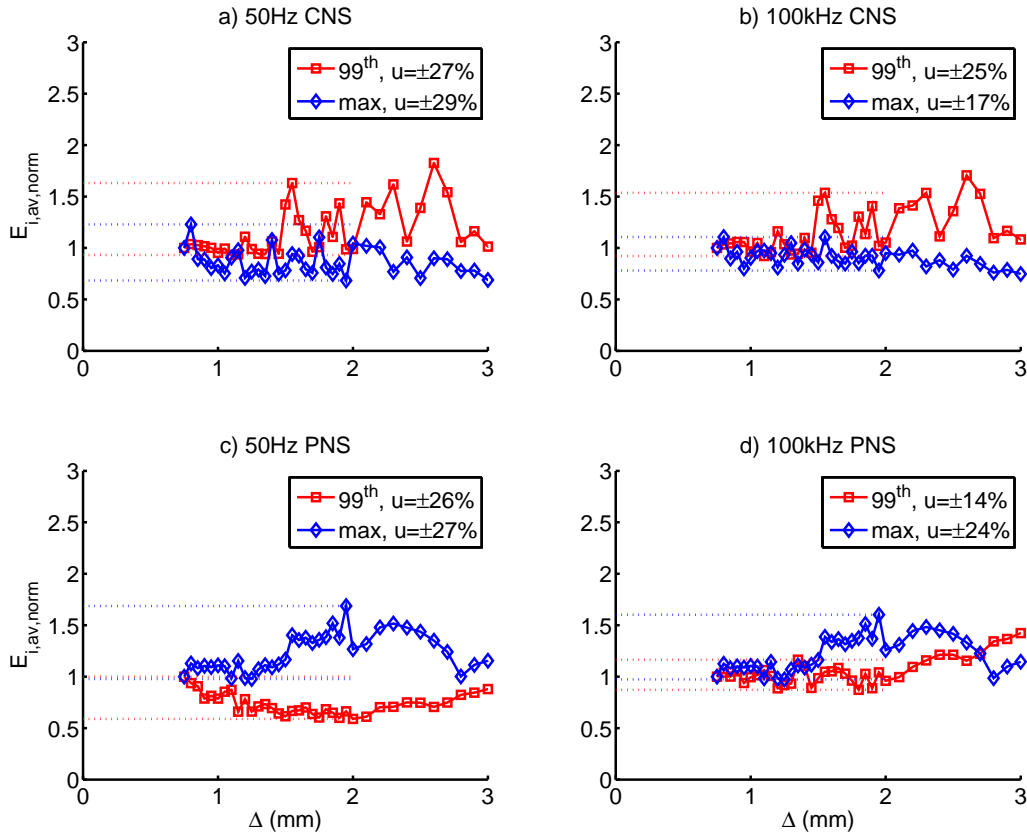


Figure 5.5: Peak averaged induced electric field ($E_{i,av,norm}$) in the Roberta model as a function of grid discretization step (Δ_{grid}), normalized to the value at the smallest Δ_{grid} of 0.75 mm. The values are specified separately for CNS (a,b) or PNS (c,d) tissues at 50 Hz or 100 kHz. For simplicity the peak values of all tissues and three orthogonal polarizations are reported. The dashed lines indicate the dynamic range of the electric fields between 0 and 2 mm. In the legend, u indicates maximum deviation from the center of the dynamic range for the maximum (max) and 99th percentile of the averaged electric fields. Note that electric fields are spatially averaged in $2 \times 2 \times 2$ mm³ contiguous tissue volumes, hence for discretizations larger than 2 mm it equals the voxel maximum.

5.4 Discussion

5.4.1 Evaluation of the results

In this study, we investigated the induced electric fields in anatomical models of six children and two adults in straight position exposed to uniform magnetic fields. In PNS tissues, we found electric fields up to 95% ($k = 2$) of the ICNIRP basic restriction on

the electric field for exposures at the general public reference levels. For occupational reference levels, we found an over-exposure of maximum 79% ($k = 2$) for PNS tissues for one model in the frequency range of 400 Hz to 65 kHz.

We do note that this over-exposure is detected for a 1.17 m tall 6-year-old child model (Thelonious) exposed to occupational reference levels, and that it is questionable if a child can be exposed to occupational levels. However, we detected over-exposures also for adult models at the occupational levels, i.e. 149% ($k = 2$) for the adult woman and 141% ($k = 2$) for the adult man. Closer analysis at the 6-year-old child model revealed that the peak is located at the skin of the ear, which is too thin to cover the entire volume of the contiguous averaging cube and has only few voxels such that the 99th percentile is removing only a small amount of peak values.

The ICNIRP basic restrictions at higher frequencies are based on an ad hoc extrapolation of biological data from much lower frequencies, i.e. the induction of magnetic phosphenes at 20 Hz¹⁰¹. Therefore, we do note that the biological significance of the modest over-exposure at frequencies above 400 Hz is unclear.

The induced electric fields (Figures 5.1 and 5.2) show a typical non-smooth frequency dependence between 2% and 116% due to the frequency-dependent dielectric properties, reference levels and basic restrictions. The difference between the maximum and minimum induced field between the anatomical models is approximately a factor two. The highest electric fields are expected to be induced for the anatomical models with the largest cross-section of the body perpendicular to the magnetic field. However, the results are very sensitive to local peak values and discretization. Therefore, the maximum is not necessarily found at the largest models (Figure 5.4).

As expected from Faraday's law maximum electric fields are induced if the magnetic field is oriented from front-to-back (B_y). However, we found that other polarizations can induce increased electric fields (18%) in specific organs and tissues. Hence it is not sufficient to look only at the "worst-case" B_y polarization for exposure assessments.

ICNIRP states that the most useful dosimetric results have been obtained from high resolution calculations of induced electric fields with voxel sizes below 4 mm^{4,37,96,136}. The dosimetry described in^{4,37,96} is restricted to 50 Hz, and Nagaoka et al.¹³⁶ was not studying the ELF range at all. Our results are consistent with the results mentioned by ICNIRP at 50 Hz, i.e. we found maximum local peak electric fields in CNS tissues of 22-41 mVm⁻¹ per mT (ICNIRP: 23-33), depending on field orientation and body model. We found electric fields in the skin of approximately 44-158 mVm⁻¹ per mT (ICNIRP: 20-60), which is relatively high. These differences are explained by both the grid-discretization uncertainty and the relatively low electrical conductivity of skin tissues, i.e. we used the Gabriel values ($\sigma=0.0002$ at 50 and 60 Hz) while Dimbylow³⁷ used a higher value ($\sigma=0.1$) corresponding to moist skin due to sweating. Hence, we have a larger contrast in conductivity between the skin and its neighbouring tissues, possibly leading to increased induced electric fields.

5.4.2 Uncertainty evaluation

Discretization We estimated an expanded uncertainty of 54% due to grid discretization at the fixed discretization of 2 mm used in this study. Minor changes in the grid discretization step can have a strong effect on the discretized tissue distribution. Consequently, the maximum values of a specific contiguous tissue are highly sensitive to the grid discretization step and the gridding algorithm. The discretization error did not converge to a stable value for the smallest grid step investigated, i.e. 0.75 mm. Consequently, it is difficult to estimate the “converged” value at $\Delta_{\text{grid}} = 0$ mm. We believe that we did not reach convergence due to the fact that the Virtual Family has features in the order of the minimum grid size, i.e. 0.75 mm. Hence, we expect “numerical” convergence for grid steps smaller than 0.75 mm. The strong impact of the discretized tissue distribution emphasizes the possible effect on the results due to the limited accuracy of the tissue delineation. The precision of the human models is affected by the quality of the MRI data (i.e. geometrical distortion errors and the limited voxel size from 0.5 to 2 mm) and inter-person variations in the tissue delineations.

We found that the 99th percentile equals the maximum value for small tissue volumes and therefore, it does not provide a stable measure. The grid discretization error depends on the tissues considered in the contiguous averaging procedure. The errors reported in Figure 5.5 are valid only for the tissues where we found the maximum electric fields. Consequently, we might underestimate the error for exposure configurations where the peaks are located at other tissues.

In other words, the effect of small anatomical details are important for the induced fields. Consequently, the reference values of a sound standard must have sufficient margins to be conservative with respect to the basic restrictions to account for the uncertainties in modelling small anatomical structures. Further, to obtain convergence for small grid steps, we recommend to investigate if numerical artefacts can be compensated for by sufficient oversampling, i.e. ten times smaller discretization than the finest details in the anatomical models.

Dielectric tissue properties In our study, we assessed the influence of discretization and field polarization on our obtained peak electric fields. However, there are also other parameters that can influence the results. The uncertainty of our results depends for a large amount on the reliability and availability of the literature values of the electromagnetic tissue parameters⁷⁴. The parametric Cole-Cole type dispersion models can be used with confidence for frequencies above 1 MHz. However, at lower frequencies where the literature values are sparse and have larger than average uncertainties, the dispersion model should be used with caution⁷². If all the conductivities of the body are multiplied by a constant factor, then the induced electric field will remain unchanged, while the induced current density is increase by the same constant factor. However, tissue specific uncertainties and heterogeneous conductivities in tissues will have an impact also on the induced electric field. Bahr et al.⁴ showed in a conductivity sensitivity analysis using uniform magnetic field exposure oriented from front-to-back at 50 Hz, that the maximum

sensitivity for the averaged current density is 122% (grey matter), i.e. “a 100% increase of the conductivity for grey matter leads to a 122% increase of the corresponding current density. The maximum sensitivity for the induced electric field amounts to -20% (white matter)”. Hence, more literature values for the dielectric properties of tissues at frequencies below 1 MHz are required to estimate the uncertainty of the results. In addition, the dielectric properties of tissues are age-dependent¹⁵²⁻¹⁵⁴, which has been characterized for the radio frequency range, but unfortunately it is not available for low frequencies. We assumed isotropic properties for all tissues, while some tissues can have increased conductivity components in the direction parallel to fibres in, e.g., the cerebellar cortex and muscle tissues. Anisotropies of a factor 10 are demonstrated for the conductivity along and across the fibres in white matter⁷². Although we did not investigate the impact of such anisotropies, we expect a linear increase in local induced current densities and electric fields for worst-case polarizations of the magnetic field. We used the literature parameters, which represents an average of heterogeneous tissues. However, tissues are not homogeneous, e.g. different muscles can have different infiltrations of fatty tissues and vessels. MRI maps can be used in future models to account for such heterogeneous tissue distributions. Hence, for a better understanding of the uncertainties of our results, more detailed knowledge on the tissue conductivity at low frequencies is required. Since the variations in dielectric properties are at least partly tissue specific, we recommend to then use a Monte Carlo analysis to assess the uncertainty of the results as in Bakker et al.⁷.

Anatomical posture We limited our analysis to eight human models in straight position. In literature, only small effects on the induced current density have been shown for applied magnetic fields⁴¹. However, the effect on induced electric fields was not considered. We did not investigate postures with electrical loops potentially leading to higher induced electric fields. The peak electric fields depend on the local tissue distribution in the various anatomical models and in our analysis we could not find a correlation with the size of the anatomy. Therefore, we recommend extending the evaluation using a sufficient set of anatomies including postures with electrical loops, to determine the exposure envelope of the entire population.

5.5 Conclusions

In this study, we exposed anatomical models of six children and two adult models in standing position to uniform magnetic fields at the ICNIRP reference levels. We found that the induced electric fields are within the ICNIRP basic restrictions in nearly all cases. In PNS tissues, we found electric fields up to 95% ($k = 2$) of the ICNIRP basic restriction on the electric field for exposures at the general public reference levels. For occupational reference levels, we found an over-exposure of maximum 79% ($k = 2$) for PNS tissues. The peak electric fields depend on the local tissue distribution in the various anatomical models and we could not find a correlation with the height of the anatomy. We have

identified the following items of the ICNIRP guidelines that should be improved. First, the reference levels do not have sufficient margins to be conservative or compliant with the basic restrictions as the induced electric fields strongly depend on small anatomical features. Second, spatial averaging in $2 \times 2 \times 2 \text{ mm}^3$ contiguous tissue volumes and removal of peak values by the 99th percentile cause the results to depend strongly on the grid discretization step (i.e. an uncertainty of more than 50% at 2 mm) and the number of delineated tissues in the anatomical models. We recommend to investigate if the percentile can be replaced with the peak averaged value of the electric field, under the condition that sufficient oversampling of the anatomy is obtained to avoid errors by numerical artefacts. Third, for small averaging volumes the requirements for contiguous tissue averaging could be dropped for the benefit of easier evaluations. Fourth, the numerical evaluation procedure should be rigorously defined in the guidelines, such that the results obtained by various research institutes are robust for different simulations settings and various models. Fifth and finally, we recommend extending the evaluation using a sufficient set of anatomies including other than standing postures, to assess the worst-case envelope for defining conservative reference levels that are compliant with the basic restrictions.

6. RF: SAR

Exposure to radio frequency fields:
SAR assessment

This chapter is based on:

JF Bakker, MM Paulides, A Christ, N Kuster and GC van Rhoon. "Assessment of induced SAR in children exposed to electromagnetic plane waves between 10 MHz and 5.6 GHz". *Phys Med Biol*, Vol. 55, No. 11, pp. 3115-3130, 2010.

Abstract

Purpose: To avoid potential adverse health effects of Electromagnetic Fields (EMF), the International Commission on Non-Ionizing Radiation Protection (ICNIRP) has defined EMF reference levels from the basic restrictions on the induced whole-body-averaged Specific Absorption Rate (SAR_{wb}) and the peak 10g spatial-averaged SAR (SAR_{10g}). The objective of this study is to assess if the SAR in children remains below the basic restrictions upon exposure at the reference levels. **Materials and methods:** Finite Difference Time Domain (FDTD) modelling was used to calculate the SAR in six children and two adults when exposed to all twelve orthogonal plane wave configurations. A sensitivity study showed an expanded uncertainty of 21% (SAR_{wb}) and 23% (SAR_{10g}) due to variations in simulation settings and tissue properties. **Results:** In this study, we found that the basic restriction on SAR_{wb} is occasionally exceeded for children, up to a maximum of 45% in small children. The maximum SAR_{10g} values, usually found at body protrusions, remain under the limit for all scenarios studied. **Conclusions:** Our results are in good agreement with literature suggesting that the recommended ICNIRP reference levels may need fine tuning.

6.1 Introduction

Due to the exponential increase in wireless applications, public concern over their potentially adverse health effects has also increased. In the past, safety guidelines have been developed to restrict exposure to Electromagnetic Fields (EMF). For the radio frequency (RF) range of 100kHz-300GHz, these guidelines are based on keeping the body temperature rise under 1°C, which has been correlated to a maximum SAR_{wb} of $4Wkg^{-1}$ for 30 minutes in adults¹⁹⁹. To account for sensitive subpopulations such as children and the elderly, this threshold is reduced to $0.08Wkg^{-1}$ for the general public. While SAR limits are useful for theoretical analyses, reference levels for the incident electromagnetic (EM) field are more commonly used for practical exposure assessments^{99,103}. These reference levels have been derived from the SAR limits through simulations modelling the human anatomy as prolate spheroid bodies⁷⁵ or homogeneous blocks⁴⁵. As individual anatomy is highly diverse, it is difficult to generalize the results from these simplistic models to the entire human population. Therefore, various anatomical models have been used in several studies to investigate the SAR_{wb} for plane wave exposure at the reference levels.^{26,35,36,57,92,95,137,162,197} These previous studies also examined the exposure of children by using approximated models, leading to simulation inaccuracies. According to the World Health Organization (WHO), correct anatomical models of children have been insufficiently examined, and further research is required to fill the gap in numerical

modelling of children exposure assessments²⁰⁰.

Most of the previous studies use child models that are derived from down-scaling adult models, through either homothetic transformations or piecewise reductions²⁶. However, due to anatomical changes that occur during adolescence, this scaling leads to inaccuracies, particularly in the skin thickness and proportions of the head and brain²⁶. For tissue interfaces with high dielectric contrast, this might influence the accuracy of the SAR_{wb} and SAR_{10g} predictions²¹. Only a limited number of studies have used anatomically correct models. Dimbylow and Bolch⁴⁰ calculated the SAR_{wb} in five child models in the range of nine months to 14 years and Kuhn et al.¹¹⁹ used child models of six and eleven years old. Although the SAR_{wb} results are in good agreement with the down-scaled models, large differences were found for the SAR_{10g}. Hence, an extended evaluation using a sufficient set of anatomies is necessary to determine the exposure envelope for the entire population¹¹⁹. Typically, peaks in both the SAR_{wb} and SAR_{10g} are present in two distinguishable frequency regions. The “primary” peak $f_{\text{res,peak1}}$ in the 50-150MHz region is related to the physical phenomenon of whole-body resonances occurring when the electric field is parallel to the main body axis. The “secondary” peak f_{peak2} in the GHz band is related to the definition of the frequency dependent ICNIRP reference levels (Figure 3.2).

Most of the current literature has studied frontal vertically aligned plane waves, as it was expected that the SAR_{wb} is maximum at this polarization at $f_{\text{res,peak1}}$.

Recent studies, including both scaled and anatomically correct models, have shown that SAR_{wb} can also peak at f_{peak2} for other incidences and polarizations^{43,95,119,137,182}. The peaks of SAR_{wb} at $f_{\text{res,peak1}}$ and at f_{peak2} are highly dependent on body size and anatomical structures. Therefore, existing data should be rigorously verified at all incidences and polarizations, as well as for a variety of anatomically correct child models.

The objective of this study was to assess if the induced SAR in children remains below the ICNIRP basic SAR restrictions for incident EMF exposure at the reference levels. In a brute-force approach, we assessed the induced SAR in anatomical correct models of six children by using twelve plane wave configurations, i.e. all orthogonal incidences and polarizations and frequencies in the range of 10MHz to 5.6GHz. For comparison, we also assessed the exposure for two adult models. Additional simulations with altered settings were used to assess the expanded uncertainty of the numerical results. SAR distributions of configurations, from which the recommended reference levels are not consistent with the SAR restrictions, have been analysed to understand mechanisms in the spatial peak locations. Finally, we verified the consistency of our results by comparing them to previously published exposure data.

6.2 Methods

First, we assessed the induced whole-body-averaged SAR (SAR_{wb}) and peak 10g spatial-averaged SAR (SAR_{10g}) in six child and two adult models. Second, we analysed the SAR distributions and SAR_{10g} locations for configurations where restrictions are exceeded. Third, we assessed the uncertainty and finally we compared the results to existing data.

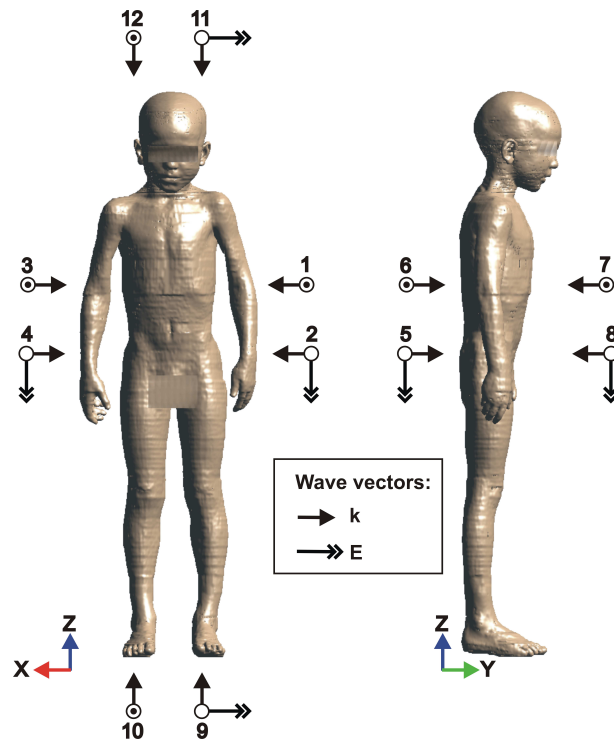


Figure 6.1: Visualization of the twelve orthogonal plane wave exposure configurations.

6.2.1 Human models

Figure 2.1 shows the eight models used in our dosimetric simulations. The models have been developed from high resolution MRI data²³ and are known as the “Virtual Family” and “Virtual Classroom”. They consist of six child and two adult models from both genders and with different body dimensions (Table 2.1). The method of selecting tissue properties used in the models is explained in section 6.2.4.

6.2.2 Plane wave configurations

Plane waves were used with incident directions of the six major sides, i.e. frontal, dorsal, left, right, bottom and top (Figure 6.1). In addition, we used two orthogonal polarizations of the electric field per incident direction. We used frequencies in the range of 10MHz to 5.6GHz, with specific refinements at $f_{res,peak1}$ and at f_{peak2} to find the peak values. The frequency dependent ICNIRP reference levels for the general public (Figure 3.2) were used for the plane wave power density S_{eq} , to enable evaluation if the basic SAR restrictions are exceeded. Including additional simulations for assessing the numerical uncertainty, the twelve plane wave configurations at 20 frequencies and eight human models resulted in more than 2200 scenarios.

Table 6.1: Number of grid-steps in tissues Δ_{tissue} per wavelength at the tissue with maximum relative dielectric permittivity $\lambda_{\epsilon_{r,max}}$. Note that we used $\Delta_{\text{tissue}}=2\text{mm}$ for $f < 2400$ and $\Delta_{\text{tissue}}=1\text{mm}$ for $f \geq 2400\text{MHz}$.

f (MHz)	$\epsilon_{r,max}$	tissue $_{\epsilon_{r,max}}$	$\lambda_{\epsilon_{r,max}}/\Delta_{\text{tissue}}$
10	488	small intestine	680
100	98	kidney cortex	150
1000	70	gallbladder	18
1800	69	gallbladder	10
2400	69	gallbladder	15
3200	68	eye vitreous humor	11
5600	65	eye vitreous humor	6

6.2.3 Numerical model

SEMCAD X¹⁶⁷ was used for the modelling, simulation and analysis of the plane wave configurations. Its Finite Difference Time Domain (FDTD) solver was used to numerically evaluate the electromagnetic wave propagation and interaction with the body¹⁷⁶. A rectangular Huygens surface with electromagnetic sources¹³² was used to produce the correct total field inside and the scattered field outside the surface, also known as the total-field scattered-field (TFSF) technique. A minimum separation of five mesh cells between the human models and the Huygens surface was used to avoid intersection and to describe the plane waves accurately.

Uni-axial Perfectly Matched Layers (UPML), at a 20mm distance from the Huygens surface were applied to avoid reflections back into the computational domain. A UPML efficiency of $\geq 95\%$ was used to automatically generate the layers and its absorbing profile, based on modified geometrical progressions¹⁶⁷. As a result, the number of UPML layers was in the range of seven at 5.6GHz to 14 at 10MHz.

To ensure steady state EM fields, the number of harmonic periods corresponds to a propagation distance of at least two times the maximum diameter of the computational domain. Another restriction is a minimum of two periods, since we used one period to ramp the envelope of the sinusoidal excitation waveform. This ramp function was used to minimize the generation of other frequency components outside the main carrier at the start of the pulse train.

To obtain adequate sampling, the maximum grid-step in tissues Δ_{tissue} allowed is $\lambda_{\text{tissue}}/10$, based on tissues with the maximum dielectric permittivity ($\epsilon_{r,max}$) (Table 6.1). Outside the body, the grid step was gradually increased by a factor 1.3 to maximum $\lambda/15$ in free space.

SAR_{wb} and SAR_{10g}

The SAR in a single FDTD cell and the localized peak SAR are calculated based on Annex E of IEEE C95.3¹⁰². To compute the SAR for a single FDTD cell, the complex vector components of the electric field at each individual cell edge is averaged into the voxel center using linear interpolation¹⁹. The absorption rate in all cells is summed and then divided by the mass of the whole body, to obtain the whole-body-averaged SAR (SAR_{wb}).

A special “fast” strategy is used to find the overall maximum of the peak localized SAR, averaged over a 10g cube (SAR_{10g}), as required in the current IEEE guidelines. Although this strategy does not calculate the peak SAR at full resolution in the regions with lower absorption, the overall maximum is identical to the peak SAR defined in the IEEE standard.

6.2.4 Numerical uncertainty

To investigate the overall uncertainty^{105,177} of the numerical modelling, we determined the influence of various modelling parameters on the obtained results, i.e. SAR_{wb} and SAR_{10g}. The investigated modelling parameters were 1) model discretization, 2) absorbing boundary conditions, 3) deviations from steady state, 4) plane wave homogeneity, and 4) tissue properties.

Model discretization

The effect of the spatial resolution in the model discretization was investigated by simulating grid steps (Δ) between 0.7mm and 10mm for the Thelonious model. Although both SAR_{wb} and SAR_{10g} converge for decreasing Δ , rate of convergence depends on frequency, wave incidence, and polarization. Therefore we evaluated this convergence for all twelve plane wave configurations and for the frequencies 10, 100, 1000, 1800, 3200 and 5600MHz. To estimate the converged value for $\Delta \rightarrow 0$, we fitted a quadratic curve to the data in the range of 0.7 to 3mm. The analysis was simplified by using the maximum error of the twelve plane wave configurations. We used $\Delta=2$ for $f < 2000$ and $\Delta=1$ mm for $f \geq 2000$ MHz, since we allowed a maximum SAR_{wb} error of $\pm 5\%$ due to the discretization. The effect of using a uniform expanding grid step is investigated by using additional simulations with a uniform spaced grid. For this analysis, we assumed that the induced dispersion error becomes maximum for smallest grid step, i.e. 1mm and for maximum frequency, i.e. 5.6GHz.

Absorbing boundary conditions and deviations from steady state

We estimated the uncertainty contribution of deviation from steady state fields and imperfect ABC's simultaneously. We increased the efficiency of the UMPL by using additional absorbing layers. In addition we increased the distance from the Huygens surface to the

ABC's from 20mm to $\lambda_{\text{air}}/2$. Also additional time steps were used to increase the number of periods of the harmonic wave in order to propagate at least two times through the computational domain, applying a maximum ϵ_r of tissue instead of air, to calculate the wave speed. As a result the number of periods was increased from 2 to 2.5 at 10MHz and from 20 to 170 at 1800MHz.

Since these uncertainties depend on frequency, incidence, polarization and human model, we investigated the uncertainty for both 10MHz and 1.8GHz, two incidences and polarizations (cases 8 and 12) to all models. Due to limitations in memory resources of our simulation hardware, we were not able to estimate the ABC's and steady state uncertainty for $f \geq 1800\text{MHz}$. We simplified the analysis by using the maximum error of both frequencies and both plane wave configurations.

Plane wave homogeneity

The incident plane waves are excited by a rectangular Huygens surface¹³² and the maximum error in the electric field amplitude is obtained for smallest λ/Δ at 5.6GHz. By using field sensors, we determined the maximum deviation in the homogeneous wave front. Since the SAR is quadratically related to E, the uncertainty in SAR is doubled.

Tissue properties

A 4-Cole-Cole dispersion model for each tissue type was used to assign the frequency dependent relative permittivity (ϵ_r) and effective conductivity (σ), according to the commonly used literature review^{71,73,74}. For the "mass" specific-absorption-rate (SAR), we assigned the volume density of mass (ρ) according to the mean literature values of Duck⁴⁴. For individuals however, the tissue properties deviate from the mean literature values, which influences the values for SAR_{wb} and $\text{SAR}_{10\text{g}}$.

Volume density of mass There is a variation in the measured ρ of $\pm 10\%$ in most of the tissues, while up to $\pm 50\%$ is reported for the lungs¹³⁰. These variations directly affect the SAR values, however we excluded the variation in the lungs, since we assume that the influence on SAR_{wb} and $\text{SAR}_{10\text{g}}$ are negligible due to the low fields at this location.

Permittivity and conductivity There is a 90% maximum age-dependent decline in dielectric properties of tissues with low water content, such as fat and bone^{69,153}. The influence of this decline on SAR_{wb} and $\text{SAR}_{10\text{g}}$ was investigated by applying the changes to the Theloniou model for exposure configuration eight at 900 and 1800MHz²².

Additionally, assumptions were made to assign literature values to tissues where either no data or multiple data was available. For example, we use dry and not wet skin and fat that is average infiltrated instead of not infiltrated by blood. The influence of these choices on SAR_{wb} and $\text{SAR}_{10\text{g}}$ for exposure configuration eight at $f=1800\text{MHz}$ is 10.7%⁴². For other configurations and frequencies, the influence is unknown.

Further, the 4-Cole-Cole parameters provide only a “best estimate”, due to measurement uncertainties and variations in literature⁷⁰. Although the influence of these dielectric changes on SAR_{wb} and SAR_{10g} is unknown, we do know that the variations are much smaller than the age-dependent dielectric changes. Therefore, we estimated the influence of dielectric measurement uncertainties on SAR_{wb} and SAR_{10g} by a 25% fraction of the influence caused by age-dependent dielectric changes.

Finally, the dielectric properties are mostly obtained from excised tissue, while post-mortal changes up to 18% occur immediately after death, as a consequence of stopped circulation^{17,163,164}. Although the influence on SAR_{wb} and SAR_{10g} is unknown, these changes are much smaller than the age-dependent changes, and therefore we use a 25% fraction of the age-dependent result.

6.3 Results

We first analysed the SAR_{wb} and SAR_{10g} data for the eight human models exposed to the twelve plane wave configurations. The worst-case summary for models is shown in Figure 6.3. We then focused on the SAR distributions where ICNIRP basic restrictions were exceeded. Finally, we provide an example to demonstrate the typical SAR_{10g} locations for the Thelonious model.

6.3.1 Comparison of calculated SAR to basic restrictions

Figure 6.2 shows the SAR_{wb} and SAR_{10g} for all frequencies and exposure configurations in the Thelonious model. We visualize this only, since we observed similar trends for the other models. Figure 6.3 shows the worst-case maximum exposure scenarios, highlighting which model and frequency combinations where exposure at ICNIRP reference levels leads to exposure above the basic restrictions.

These figures confirm that the SAR_{10g} is increased at two frequency bands, i.e. at $f_{res,peak1}$ and at f_{peak2} . Figure 6.3 shows over-exposure of SAR_{wb} at $f_{res,peak1}$ for the small models, i.e. Billie, Thelonious, Eartha, Dizzy and Roberta. Closer analysis reveals that this occurs only for configurations with the electric field aligned parallel to the main body axis, i.e. configurations two, four, five and eight. Note that the ratio between body height and wavelength in air at $f_{res,peak1}$ is 0.4 ± 0.02 for all models.

At f_{peak2} , SAR_{wb} over-exposure of max 45% occurs also for the same small models for configuration with maximum body surface illumination, i.e. configurations five, six, seven and eight.

For SAR_{10g} the same tendencies are observed as for SAR_{wb} . Note that for some frequencies, the SAR_{10g} limits for head and trunk were exceeded. Closer analysis revealed that this high SAR_{10g} was confined to the limbs, for which a higher limit is defined. Hence, the SAR_{10g} is within the limits for all cases.

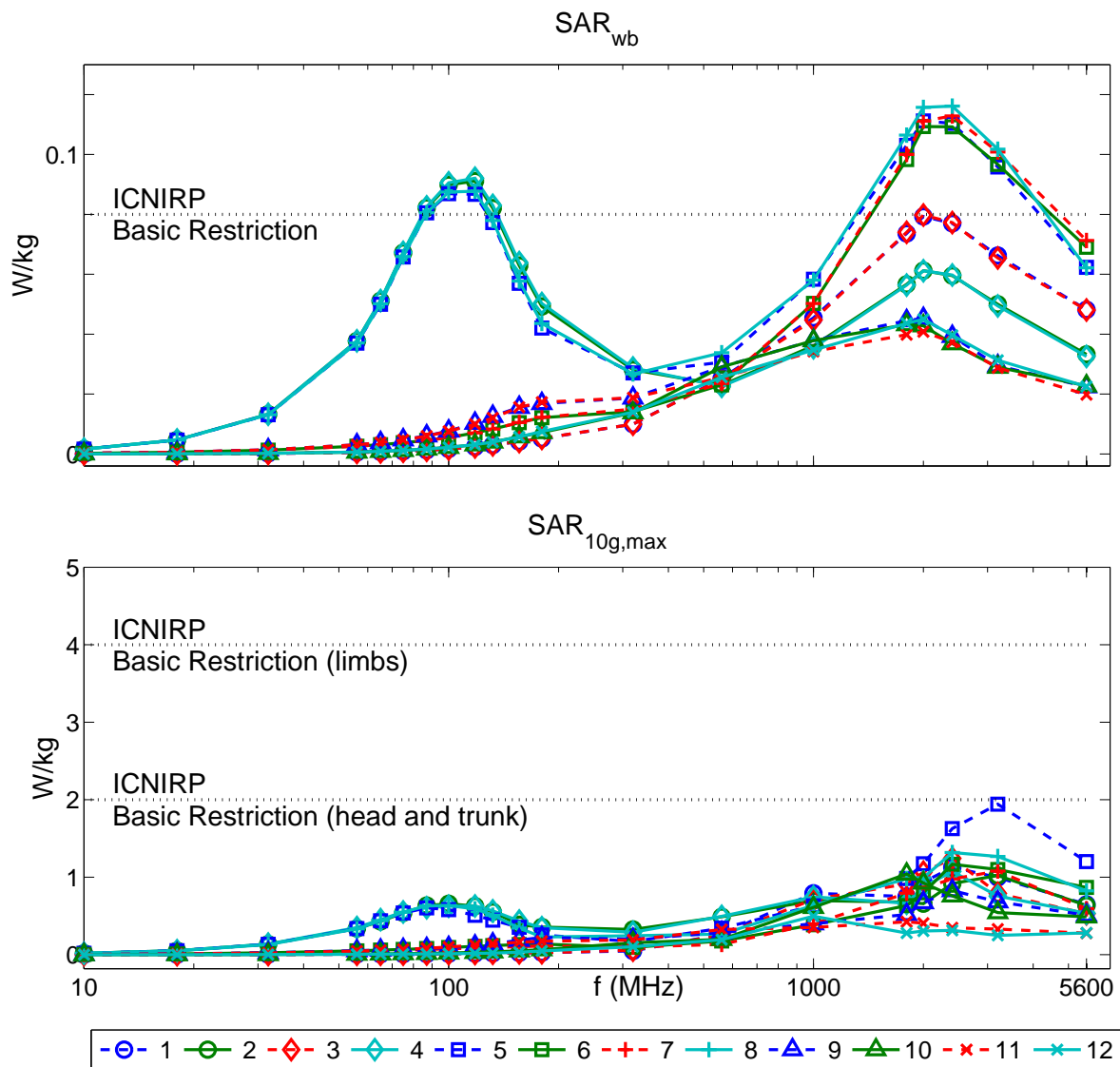


Figure 6.2: SAR_{wb} (top) and SAR_{10g} (bottom) for exposure at the ICNIRP reference level in the Thelonious model for twelve plane wave configurations.

Numerical uncertainty To determine the expanded uncertainty U of the numerical modelling with 95% confidence, we assessed the influence of various modelling parameters on the simulation results. Table 6.2 shows that U is 21% for SAR_{wb} and 23% for SAR_{10g} .

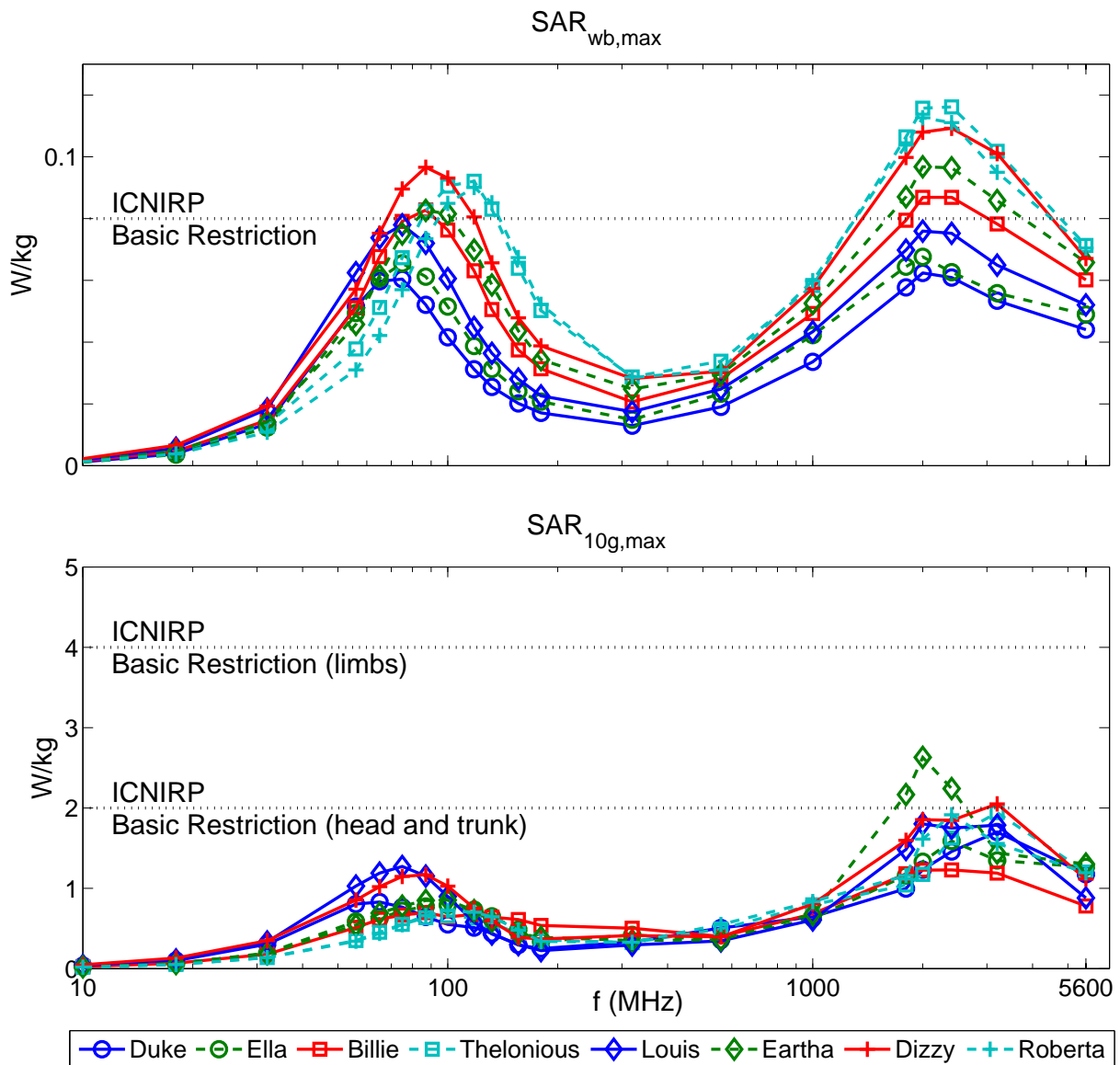


Figure 6.3: Worst case SAR_{wb} (top) and peak SAR_{10g} (bottom) in the eight human models for twelve plane wave configurations. Note that the locations where the SAR_{10g} restrictions for head and trunk are exceeded, are all located in the limbs.

6.3.2 Closer analysis of SAR distributions at configurations which exceed the basic restrictions

To assess thermal relevance, we analysed the SAR distributions and peak locations for configurations that exceeded the basic restrictions. In addition, we also examined typical peak SAR_{10g} locations.

Table 6.2: Evaluation of the standard combined uncertainty u_c and the expanded uncertainty U of the whole-body (wb) or spatial averaged over 10g tissue (10g) SAR. Div. is the division factor to obtain the standard uncertainty (std. unc.) and k is the coverage factor. The sensitivity coefficients c_i equals one for all uncertainty contributions.

	SAR unc.			Div.	SAR std. unc.	
	%		Prob. distr.		%	
	wb	10g			wb	10g
Discretization						
a) spatial resolution	5.0	11.9	Normal	2	2.5	5.5
b) non-uniform grid	1	1	Normal	2	0.5	0.5
ABC + steady state dev.	6.0	3.5	Rect.	$\sqrt{3}$	3.5	2.0
Wave homogeneity	1.0	1.0	Normal	1	1.0	1.0
ρ	10.0	10.0	Normal	2	5.0	5.0
ϵ_r, σ						
a) Age-dependency	5.8	6.5	Normal	1	5.8	6.5
b) Tissue assignment	10.7	10.7	Normal	2	5.4	5.4
c) 4-Cole-Cole	1.5	1.6	Normal	1	1.5	1.6
d) Post-mortal changes	1.5	1.6	Normal	1	1.5	1.6
u_c ($k=1$)					11	12
U ($k=2$)					21	23

Example SAR distributions in Thelonious at $f_{\text{res,peak1}}$ and f_{peak2}

Figure 6.4 demonstrates for exposure configuration eight, the SAR distributions at the frequencies where the basic restrictions were exceeded, i.e. at $f_{\text{res,peak1}}$ (a,b) and at f_{peak2} (c,d). Note that the color scaling is very sensitive to peak values, since spatial averaging is not used.

At $f_{\text{res,peak1}}$, high SAR values are shown at the ankles, knees and the neck and high SAR values for both superficial and deep locations.

At $f_{\text{res,peak2}}$, the illuminated sides of the model show high SAR values, while the “shadow” sides have a low SAR. Although not shown here, this applies also for the other exposure configurations and models. Peak SAR values are observed at body protrusions such as the nose, chin, fingers and toes.

Figure 6.5 shows that similar distributions are obtained at $f_{\text{res,peak1}}$ for the other exposure configurations where the basic restrictions are exceeded, i.e. configurations two, four, five. At f_{peak2} , the “shadowing” effect due to low penetration is also shown for the other peak configurations, i.e. five, six, and seven. Although not shown here, this applies also for the other exposure configurations and models.

Peak SAR_{10g} locations are mostly at the body protrusions such as the nose, chin, fingers, toes, shoulders, armpits, wrists, ankles, male organ and the tail bone. For the frequencies

below 1000MHz, these peak locations are “grouped” by the field polarization. Although not shown here, these typical locations and polarization dependency are also present at other frequencies and in other models.

6.4 Discussion

In this study, we investigated the SAR_{wb} and SAR_{10g} in anatomical models of six children and two adults when exposed to all orthogonal plane wave configurations at frequencies in the range of 10MHz-5.6GHz. In this study we found that for worst-case exposure scenarios, the ICNIRP basic restrictions on SAR_{wb} are exceeded for small children by maximum 45%, which is in agreement with existing data that used both scaled and anatomically correct models. The result of the expanded uncertainty analysis (21% for $k=2$) revealed that the over-exposure is limited to 120% for these generic plane wave scenarios.

Evaluation of the methods In our opinion, a rigorous uncertainty assessment should be included when testing the consistency of the ICNIRP reference levels. Although various studies have tested the validity of their code and the influence of various modelling parameters on the results, a complete uncertainty evaluation is usually not included. The validity of the FDTD implementations is usually tested by comparison to an analytical Mie series solution for a homogeneous sphere¹³⁹. The influence of the distance from the human model to the absorbing boundaries is investigated in e.g.⁵⁸ and the influence of discretization and deviation from steady state signals in¹¹⁹. Fortunately, recent advances^{69,153} made it possible to estimate the influence of age-dependent tissues. In addition, we assessed the uncertainty of volume mass density and variation in dielectric properties due to tissue assignment, 4-Cole-Cole dispersion model and post-mortal changes. Although we provided an extensive uncertainty analysis with our results, it is recommended to further investigate the influence on SAR_{wb} and SAR_{10g} for more plane wave configurations. Standardized techniques are required for the validation of an FDTD code and for the assessment of the uncertainty of numerical results.

In this study we compared the peak localized SAR averaged over a 10g cube (SAR_{10g}) with the ICNIRP guidelines. However, contiguous region averaging is required in these guidelines and therefore a direct comparison to the ICNIRP guidelines of $2Wkg^{-1}$ (head and trunk) and $4Wkg^{-1}$ (limbs) can not be made. Contiguous averaging is more conservative (up to a factor of 2.5) than averaging over a cube⁵⁹. Our results are consistent when comparing to IEEE guidelines¹⁰³ which prescribes 10g cube averaging to restrict the localized SAR to $2Wkg^{-1}$ (localized) and $4Wkg^{-1}$ (extremities and pinnae). However, for contiguous averaging, the SAR_{10g} might exceed the ICNIRP basic restriction on localized SAR in the head and trunk.

In this study, the human models were exposed to plane waves under free-space conditions. The introduction of a ground plane leads to several differences, i.e. scattering effects and body resonance changes. When an electromagnetic field is normal or oblique incident to a ground plane, the combination of the original plane wave and its’ reflection cause an

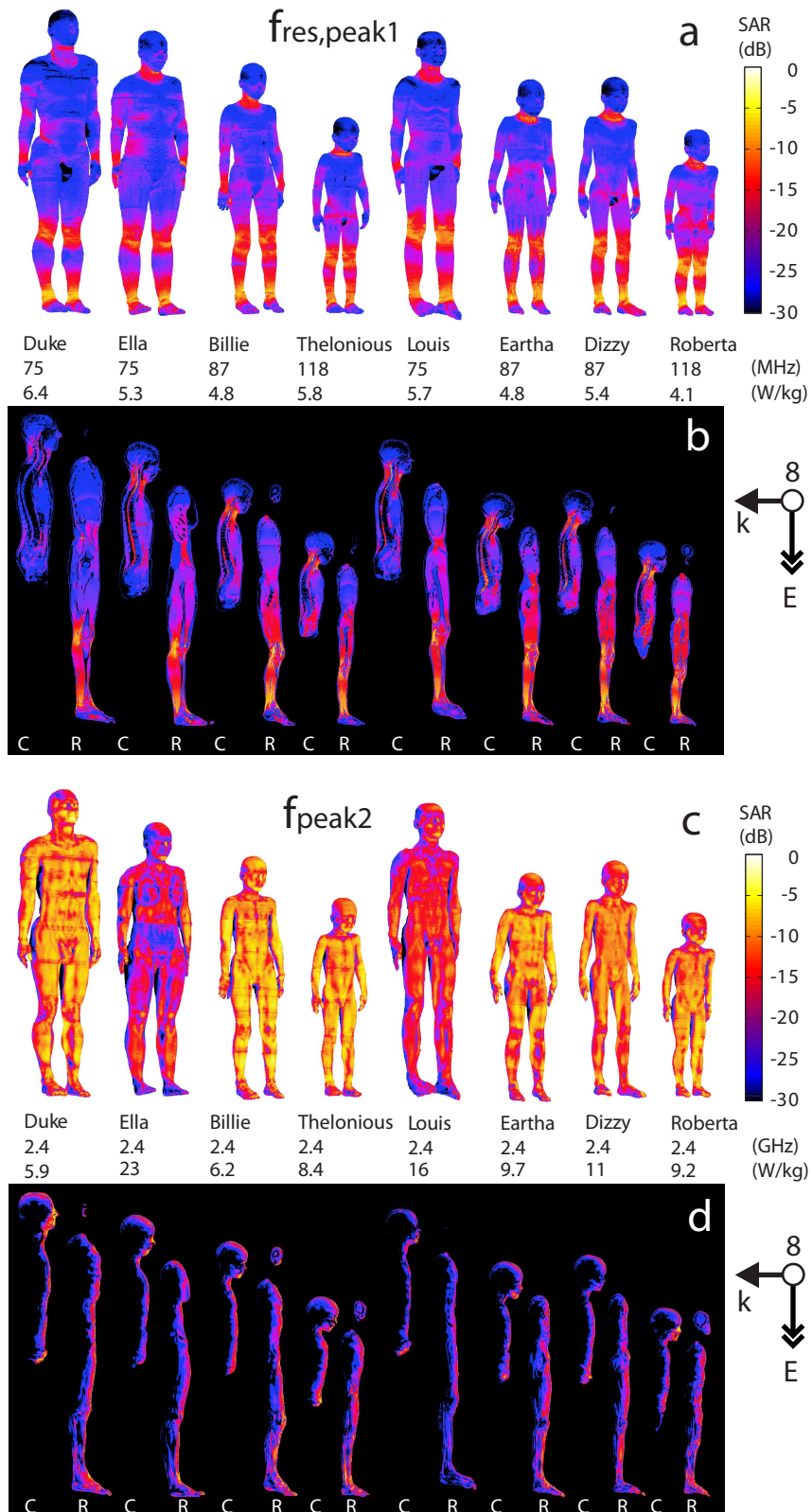


Figure 6.4: Surface SAR and SAR in slices through the central body axis (C) and right leg (R) in all models at $f_{res,peak1}$ (a,b) and at f_{peak2} (c,d) for plane wave configuration eight. The SAR values indicate the maximum SAR in the model.

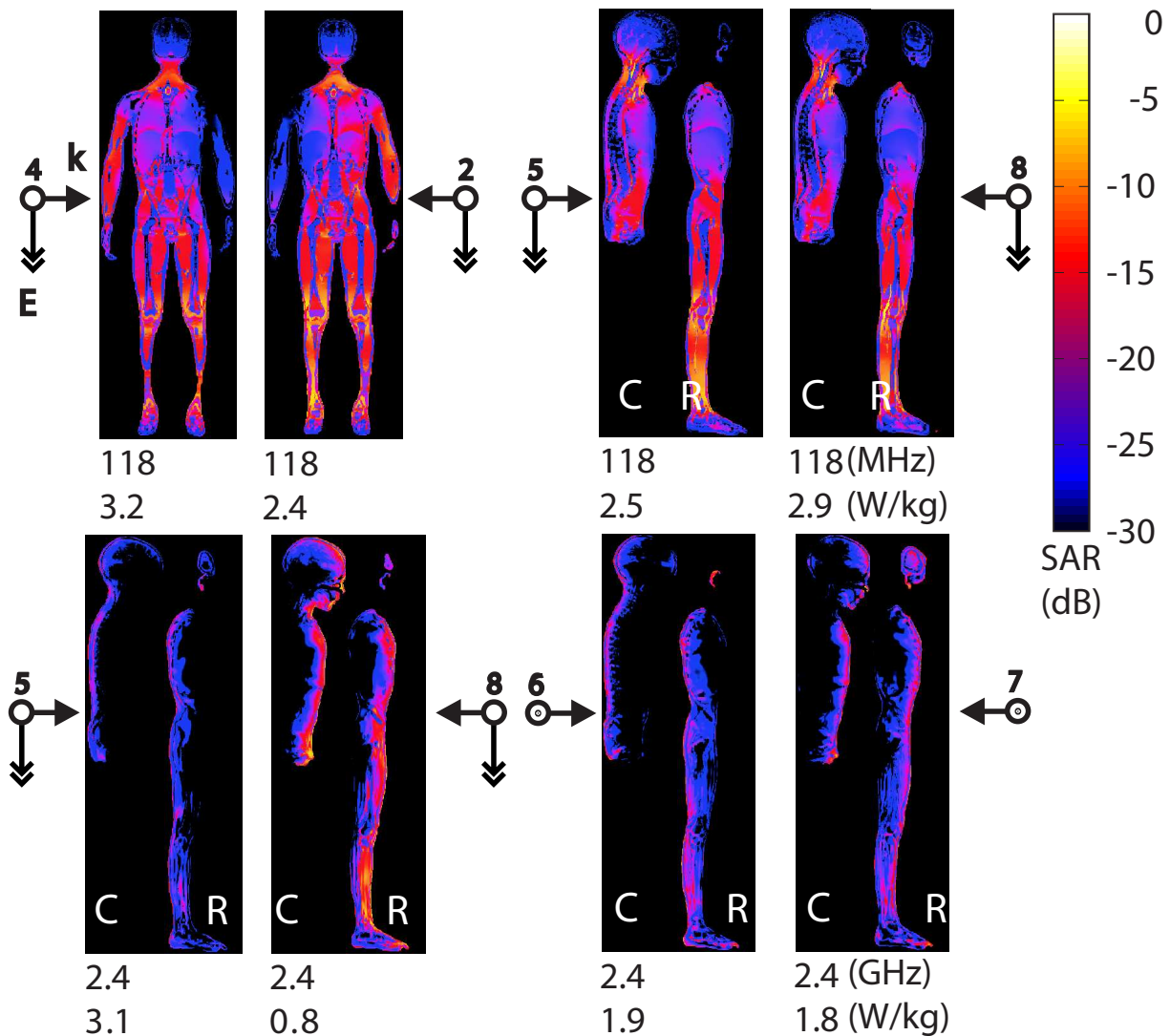


Figure 6.5: SAR in slices through the central body axis (C) and right leg (R) of Thelionious exposed to the worst-case plane wave configurations at $f_{\text{res,peak1}}$ (top) and at f_{peak2} (bottom).

inhomogeneous exposure in the vertical direction. However, when normalizing the total exposure to the spatially averaged field, the locally increased field values does not induce higher exposures with respect to the free-space plane wave^{59,119}. For frontal and vertical aligned electric fields, i.e. configuration eight, the ground plane causes the body's resonant frequency $f_{\text{res,peak1}}$ to shift approximately to $f_{\text{res,peak1}}/2$, but no increase in exposure^{33,36}. It was recommended¹¹⁹ to extend the frequencies below 50MHz and above 2.45GHz to determine the exposure envelope. Our results demonstrate that the SAR values are not increased for frequencies below 50MHz. The envelope of the second peak extends to 4GHz for the small children, i.e. Thelionious, Roberta and Dizzy. These findings are in agreement

with existing data^{26,40,43,60,95,182}.

Evaluation of the results The ICNIRP reference levels for the high-frequency incident EM fields have been derived by using simulations with humans modelled as a prolate spheroid body^{75,99}. In this derivation, a SAR_{wb} of 4Wkg^{-1} induces a body temperature increase of less than 1°C . A safety factor of 50 is applied to the basic SAR restriction to avoid excessive heating for the general public. Additional factors are used also in the reference levels to account for “differences in absorption by individuals of different sizes and different orientations relative to the field”. Despite these additional factors, we have demonstrated that for children smaller than 1.48m, the basic SAR_{wb} restrictions of 0.08Wkg^{-1} are exceeded at the EMF reference levels. Note that we used standing models, while the SAR values can be averaged over six minutes and it is unlikely that small children can stand straight for this length of time.

Previous studies have applied mainly frontal vertically aligned plane waves, i.e. configuration eight, since SAR_{wb} is maximum for this configuration at $f_{\text{res,peak1}}$. Analysis of our results reveals that SAR_{wb} is maximum also for other incidences with similar polarizations, i.e. configurations two, four and five. At $f_{\text{res,peak1}}$, the basic restrictions on SAR_{wb} are exceeded by maximum 20% (Dizzy), 15% (Thelonious and Roberta) and 10% (Billie, Louis and Eartha). These findings are consistent (5%) with existing data obtained using the Thelonious model¹¹⁹. Note that deviations might be caused by a small difference in $f_{\text{res,peak1}}$.

At f_{peak2} , the SAR_{wb} is maximum for configurations with maximum body surface illumination, i.e. configurations five, six, seven and eight. The basic restrictions on SAR_{wb} are exceeded by maximum 45% (Thelonious), 41% (Roberta), 37% (Dizzy), 21% (Eartha) and 9% (Billie). The restrictions are not exceeded for the taller models, i.e. Duke, Ella and Louis. These findings are consistent (10%) with existing data obtained using the Thelonious model^{119,182}.

Figure 6.6 demonstrates that our SAR_{wb} results of configuration eight are in good agreement with previously published data, which includes both scaled and anatomically correct models^{26,33,35,40,42,43,60,119,137,182}. Note that we sorted the results by body mass index (BMI) to distinct between the models. Differences in the results are explained by the various human models. Further confounding factors are uncertainties of the simulations and small differences in frequency, because not all authors provide data from simulations precisely at $f_{\text{res,peak1}}$ and f_{peak2} .

Typical locations of the $\text{SAR}_{10\text{g}}$ peaks are found at body protrusions, which is in agreement with previously published data¹¹⁹. The exact location and value is strongly dependent on the model geometry, hence it is highly sensitive to the segmentation of the tissues and it is favourable to use realistic rather than scaled anatomies. We found that the probability of the peak locations is related to the polarization of the electric field rather than to the incidence direction, which might be clarified by partial body resonances. In this study we used orthogonal field polarizations, which are a good approach to assess the worst-case SAR_{wb} ¹⁸². However, this publication further shows that for $\text{SAR}_{10\text{g}}$, the maximum values

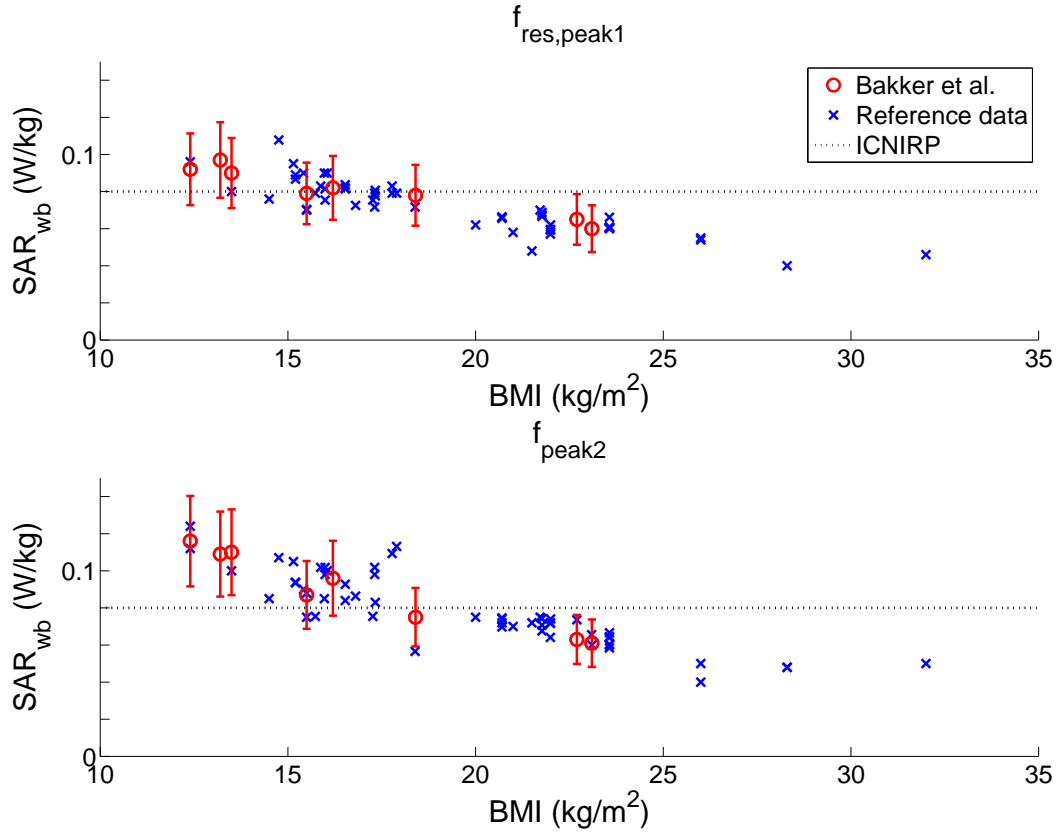


Figure 6.6: Comparison with reference data of the SAR_{wb} at $f_{res,peak1}$ (top) and f_{peak2} (bottom) for plane wave configuration eight. The error bars indicate the expanded uncertainty U with a coverage factor $k = 2$.

can also be obtained for oblique incidences and polarizations.

For all anatomical models, we observed that $f_{res,peak1}$ is related to the body height by a factor of 0.4, which is also found by⁴². Our results show also a secondary peak at f_{peak2} , for plane waves incident to the front or back, since it corresponds to the largest illuminated cross-section.

6.5 Conclusions

In this study, we investigated the SAR_{wb} and SAR_{10g} in anatomical models of six children and two adults that are exposed to twelve orthogonal plane wave configurations at the ICNIRP reference levels for the EMF. The ICNIRP basic restrictions on SAR_{wb} are exceeded for small children by maximum 45%. We do note that this is a very minor over-exposure when compared to the safety factor of 50.

7.

RF: temperature

Exposure to radio frequency fields:
temperature assessment

This chapter is based on:

JF Bakker, MM Paulides, E Neufeld, A Christ, N Kuster and GC van Rhoon. "Children and adults exposed to electromagnetic fields at the ICNIRP reference levels: theoretical assessment of the induced peak temperature increase".

Phys Med Biol, Vol. 56, No. 15, pp. 4967-4989, 2011.

Abstract

Purpose: To avoid potentially adverse health effects of Electromagnetic Fields (EMF), the International Commission on Non-Ionizing Radiation Protection (ICNIRP) has defined EMF reference levels. Restrictions on induced whole-body-averaged Specific Absorption Rate (SAR_{wb}) are designed to keep the whole-body temperature increase ($T_{body,incr}$) under $1\text{ }^{\circ}\text{C}$ during 30 minutes. Additional restrictions on the peak 10g spatial-averaged SAR (SAR_{10g}) are provided to prevent excessive localized tissue heating. The objective of this study is to assess the localized peak temperature increase ($T_{incr,max}$) in children upon exposure at the reference levels. **Materials and methods:** Finite-difference time-domain (FDTD) modelling was used to calculate the $T_{incr,max}$ in six children and two adults exposed to orthogonal plane wave configurations. We performed a sensitivity study and Monte Carlo analysis to assess the uncertainty of the results. **Results:** Considering the uncertainties in the model parameters, we found that a peak temperature increase as high as $1\text{ }^{\circ}\text{C}$ can occur for worst-case scenarios at the ICNIRP reference levels. **Conclusions:** Since the guidelines are deduced from temperature increase, we used $T_{incr,max}$ as being a better metric to prevent excessive localized tissue heating instead of localized peak SAR. However, we note that the exposure time should also be considered in future guidelines. Hence, we advise to define limits on $T_{incr,max}$ for specified durations of exposure.

7.1 Introduction

Due to the exponential increase in wireless applications, public concern over their potentially adverse health effects has increased^{201,203}. In the past, safety guidelines have been developed to restrict exposure to electromagnetic fields (EMF)^{99,103}. For the radio frequency (RF) range, these guidelines are based on keeping the body temperature increase under $1\text{ }^{\circ}\text{C}$, which has been correlated to a maximum whole-body-averaged specific absorption rate (SAR_{wb}) of 4 Wkg^{-1} for 30 minutes in adults, under moderate environmental conditions¹⁹⁹. A SAR_{wb} of 0.4 Wkg^{-1} has been chosen as the restriction that provides adequate protection for occupational exposure. An additional safety factor of five is introduced for exposure of the public, giving a SAR_{wb} limit of 0.08 Wkg^{-1} . To prevent excessive localized tissue heating, additional restrictions on the localized (peak spatial-average) SAR_{10g} are provided, i.e. 4 Wkg^{-1} for the limbs⁹⁹ or pinnae and extremities (arms and legs distal for the elbows and knees)¹⁰³ and 2 Wkg^{-1} for the other parts. Note that the ICNIRP prescribes to average over any 10 g of contiguous tissue, while the IEEE prescribes to use 10g of tissue volume in the shape of a cube.

Frequency dependent reference levels for the incident EMF (Figure 3.2) have been derived

from the SAR limits to allow practical exposure assessments. These reference levels have been derived through simulation studies, using prolate spheroid bodies as approximation for the human anatomy⁷⁵. It is difficult to generalize the results from these simplistic models, because the individual anatomy is highly diverse. Over the last decade, more sophisticated anatomical models have been used to assess the induced SAR for exposure at the reference levels. These studies show that absorption of EMF in the human body for exposures at the specified reference levels peaks at two frequency regions^{5,26,43,95,119}. Of these, the first peak “ $f_{\text{res,peak1}}$ ” is in the 50-150 MHz region and is caused by electrical resonances of the body. The second peak, “ f_{peak2} ”, shows up at frequencies close to 2 GHz and is caused by the slope discontinuity of the reference levels at this frequency. In Bakker et al.⁵, we showed that the basic restriction on SAR_{wb} is exceeded in children up to 45% for specific exposure scenarios. In contrary, the $\text{SAR}_{10\text{g}}$ values remain under the limits for all scenarios studied, although partial body resonances have not been systematically reviewed. The observation of peak SAR values raises further questions about the induced body temperature increase $T_{\text{body,incr}}$ and potentially excessive localized tissue heating for children exposed to various EMF scenarios at the reference levels.

There are few studies addressing the temperature increase (T_{incr}) for exposure of children. Bernardi et al.¹⁰ and Hirata et al.⁹⁴ have demonstrated negligible induced $T_{\text{body,incr}}$ for worst-case SAR_{wb} exposure scenarios at $f_{\text{res,peak1}}$ and f_{peak2} . Localized peak temperature increase $T_{\text{incr,max}}$ of 0.2-0.7 °C in adults and 0.2 °C in a 3-year-old child were shown for scenarios with ventral (frontal) and dorsal exposure using parallel aligned electric fields. The objective of this study was to assess the peak localized temperature increase in children and adults exposed to EMF at the ICNIRP reference levels. Since it is impossible to assess all possible exposure scenarios for the entire population, we restricted our analysis to worst-case $\text{SAR}_{10\text{g}}$ scenarios found in a previous study⁵ at $f_{\text{res,peak1}}$ and f_{peak2} , in which we studied twelve orthogonal plane-waves and eight models of the Virtual Family²³. In addition, we investigated the required EMF values that can induce a peak temperature increase of 1 °C to determine the level of protection for localized heating effects in the ICNIRP guidelines⁹⁹. Hereto, we scaled the ICNIRP reference levels (Figure 3.2) such that $T_{\text{incr,max}}$ is 1 °C. Next, we calculated the corresponding localized peak over 1 or 10g tissue and whole-body-averaged SAR values for these scaled EMF values. Further, we correlated the peak temperature increase to $\text{SAR}_{1\text{g,max}}$, $\text{SAR}_{10\text{g,max}}$ and SAR_{wb} to determine the appropriate metric for protecting against RF heating effects. Finally, we performed an extensive uncertainty analysis by a sensitivity study of the modelling input parameters and a Monte Carlo uncertainty analysis.

7.2 Methods

This section starts to introduce the applied bio-heat equations, modelling input parameters and the human models used in the exposure assessments. Secondly, we describe the parameter sensitivity study and Monte Carlo analysis to assess the uncertainty of the results. Third, we describe the worst-case SAR exposure scenarios extracted from Bakker

et al.⁵. Then, we describe the simulations to obtain the required incident EMF and related SAR values to induce a peak temperature increase of 1 °C and finally, we describe how we tested the correlation of $T_{\text{incr,max}}$ to $\text{SAR}_{1\text{g,max}}$, $\text{SAR}_{10\text{g,max}}$ and SAR_{wb} .

We have separated the electromagnetic and thermal evaluations to reduce the amount of computations. Hence we used the electromagnetic source power (SAR) as input source in the thermal simulations.

7.2.1 Thermal simulations using human models

We used eight human models (Figure 2.1), which have been developed from high-resolution MRI data and are known as “the Virtual Family” and the “Virtual Classroom”^{5,23}. They consist of six child and two adult models from both genders and with different body dimensions (Table 2.1). They consist of models of six children and two adults of both genders with various body dimensions. The models contain more than 80 tissue types that we assigned thermal properties according to an in-house developed database of literature values, which are provided with the human models as “recommended tissue properties” (Table 2.2). A 4-Cole-Cole dispersion model for each tissue type was used to assign the frequency dependent relative permittivity (ϵ_r) and effective conductivity (σ), according to the commonly used literature review^{71,73,74}.

Pennes Bioheat Equation

SEMCAD X v14¹⁶⁷ was used to calculate the SAR induced temperature increase. We used the improved Finite Difference Time Domain (FDTD) implementation equivalent to Neufeld et al.¹⁴⁰ to numerically evaluate the temperature according to the Pennes Bioheat Equation¹⁵¹,

$$\rho c \frac{\partial T}{\partial t} = \nabla \cdot (k \nabla T) + \rho Q + \rho S - \rho_b c_b \rho \omega (T - T_b), \quad (7.1)$$

where T is the temperature, t is the time, ρ is the volume density of mass, c is the specific heat capacity, k is the thermal conductivity, ω is the volumetric blood perfusion rate, Q is the metabolic heat generation rate, S is the specific absorption rate (SAR) and the subscript _b denotes a blood property. For clarity we omitted the parameter dependencies on T , t and spatial position \mathbf{r} . To account for energy losses at tissue-air interfaces, we applied a mix of convective and Neumann (fixed flux) boundary conditions,

$$k \frac{dT}{dn} + h(T - T_{\text{outside}}) = F, \quad (7.2)$$

where T is the tissue temperature, n is the direction normal to the surface, T_{outside} is the temperature outside the boundary, h is the heat transfer coefficient due to convective and radiative losses and F is the fixed heat flux due to perspiration.

When investigating the temperature increase (T_{incr}) due to the induced SAR, a first simulation is required to determine the steady state base temperature distribution (T_{base}) in the absence of any EM induced heating⁹⁴. However, for small temperature increases (T_{incr}

$\leq 1^\circ\text{C}$), tissue parameters can be considered time and temperature independent^{10,94,196}, i.e.

$$\max(T_{\text{incr}}) \leq 1^\circ\text{C} \rightarrow \rho, c, k, \omega, Q, T_{\text{b}}, h, F \neq f(t, T) \quad (7.3)$$

Now, substitution of

$$T = T_{\text{base}} + T_{\text{incr}}, \quad (7.4)$$

into equations (7.1) and (7.2), results in a simplified equation for the temperature increase T_{incr}

$$\rho c \frac{\partial T_{\text{incr}}}{\partial t} = \nabla \cdot (k \nabla T_{\text{incr}}) + \rho S - \rho_{\text{b}} c_{\text{b}} \rho \omega T_{\text{incr}}, \quad (7.5)$$

with boundary condition

$$k \frac{dT_{\text{incr}}}{dn} + h T_{\text{incr}} = 0. \quad (7.6)$$

This new set of equations for T_{incr} has several advantages. First, knowledge about Q , F , T_{b} and T_{outside} is not required anymore. Secondly, this method omits the first simulation to determine the base temperature distribution in the absence of any EM induced heating. Finally, use of relative instead of absolute temperatures, reduces numerical rounding errors. This allows faster computations by using single instead of double precision memory. We reduced stair-casing artefacts¹⁶¹ by a conformal correction scheme for the fluxes through the boundaries¹⁴⁰.

7.2.2 Sensitivity study and combined uncertainty

We investigated the influence of the individual modelling parameters (Table 7.1) on the results and applied the square-root of the sum-of-the-squares of the individual standard uncertainties (u_i) to obtain the combined standard uncertainty (u_c). The sensitivity of the results was obtained by repeating exposure scenarios $S1$ to $S4$ for the Roberta model, while altering the input modelling parameters in at least 13 linear steps between the ranges as indicated in Table 7.1.

We applied a linear regression between \pm one standard deviation to obtain the individual standard uncertainty (u_i). A coverage factor k of two is used to obtain the expanded uncertainty U within the 95% confidence interval^{105,177}. For the standard uncertainty of the source power, we used the uncorrelated combined standard uncertainty of 11% from our previous assessment of the induced SAR in children exposed to plane waves⁵. This uncertainty includes variations in model discretization, absorbing boundaries and dielectric properties of (age-dependent) tissues.

The effect of the spatial resolution in the model discretization was investigated by simulating the grid steps (Δ_{grid}) between 0.7 (computational limit) and 20 mm (arbitrary chosen) for the Roberta model exposed to plane waves at both 118 MHz ($f_{\text{res,peak1}}$) and 2 GHz (f_{peak2}). To estimate the converged value for $\Delta_{\text{grid}} \rightarrow 0$, we used linear extrapolation of the values at 0.7 and 1 mm. We assumed that the extrapolated discretization error at $\Delta_{\text{grid}} \rightarrow 0$ represents the value within one standard deviation.

Table 7.1: Thermal modelling parameters. μ indicates the average value and σ indicates the standard deviation as used in the Monte Carlo analysis. The range studied indicates the values used in the sensitivity study.

Parameter	μ	$\pm\sigma$	range studied	SI unit
Source Power				
a) $S_{\text{eq}} @ f_{\text{res,peak1}}$	2	0.22	1.34-2.66	Wm^{-2}
b) $S_{\text{eq}} @ f_{\text{peak2}}$	10	1.1	6.7-13.3	Wm^{-2}
Discretization	2	-*	0.7-20	mm
Boundaries				
a) $h_{\text{cornea-air}}$	20	6.0	14-26	$\text{Wm}^{-2} \text{ } ^\circ\text{C}^{-1}$
b) $h_{\text{skin-air}}$	8.0	2.4	5.6-10.4	$\text{Wm}^{-2} \text{ } ^\circ\text{C}^{-1}$
c) $h_{\text{lung-internal air}}$	50	15	35-65	$\text{Wm}^{-2} \text{ } ^\circ\text{C}^{-1}$
Local tissue parameters				
a) ρ	Table 2.2	10%	-30-30%	kgm^{-3}
b) c	Table 2.2	10%	-30-30%	$\text{Wm}^{-1} \text{ } ^\circ\text{C}^{-1}$
c) k	Table 2.2	10%	-30-30%	$\text{Jkg}^{-1} \text{ } ^\circ\text{C}^{-1}$
d) ω	Table 2.2	50%	-50-50%	$\text{mlmin}^{-1}\text{kg}^{-1}$
Blood parameters				
a) ρ_b	1060	10%	-30-30%	kgm^{-3}
b) c_b	3824	10%	-30-30%	$\text{Wm}^{-1} \text{ } ^\circ\text{C}^{-1}$

* constant parameter in the Monte Carlo analysis.

We estimated the standard deviation in heat transfer coefficients by using the variations in a number of studies and assuming a normal (Gaussian) distribution^{83,84,94,95,120,44,55,80,91,93,10,195,196,205,62,63,121,126,127,157,174}. We estimated the standard deviation of the local tissue and blood parameters by using the variations in the in-house and comprehensive tissue database of McIntosh and Anderson¹³⁰, based on 140 original sources. Hereto, we assumed a normal probability distribution of the reported values, equal for all tissues.

7.2.3 Monte Carlo uncertainty analysis

In the previous combined uncertainty u_c analysis, the influence of the modelling parameters on the results was assumed to be independent. However, the existence of correlation can affect the uncertainty estimation. Therefore, we evaluated the influence of such correlations by an additional analysis to obtain the Monte Carlo uncertainty (u_{MC})¹¹⁴ for all models exposed to scenarios $S1$ to $S4$. Hereto, we used normally distributed pseudo-random modelling parameters, with one standard deviations as listed in Table 7.1 and we repeated the simulations 400 times to obtain the 95% confidence interval. We performed an additional Monte Carlo analysis with 1200 samples, to test the convergence at 400 samples. Hereto, we used only the Roberta model and exposure scenario $S1$.

7.2.4 Assessment of the peak temperature increase for exposure at the ICNIRP reference levels

In Bakker et al.⁵, we used plane waves with incident directions of the six major sides, i.e. ventral (frontal), dorsal, left, right, bottom and top. In addition, we investigated two orthogonal polarizations of the electric field per incident direction (Figure 7.1a). Frequencies in the range of 10-5600 MHz with specific refinements at “ $f_{\text{res,peak1}}$ ” and “ f_{peak2} ” were used to find the peak values. At “ $f_{\text{res,peak1}}$ ”, SAR values are maximum for scenarios with vertically aligned electric fields. At “ f_{peak2} ” SAR values are maximum for scenarios with maximum body surface illumination. In this study, we restricted the thermal analysis to four plane wave scenarios (Figure 7.1b), with the electric field polarization parallel to the main body axis, that were previously distinguished for leading to the highest SAR exposure⁵.

- scenario $S1$: left incidence at the whole-body resonance frequency ($f_{\text{res,peak1}}$)
- scenario $S2$: ventral incidence at the whole-body resonance frequency ($f_{\text{res,peak1}}$)

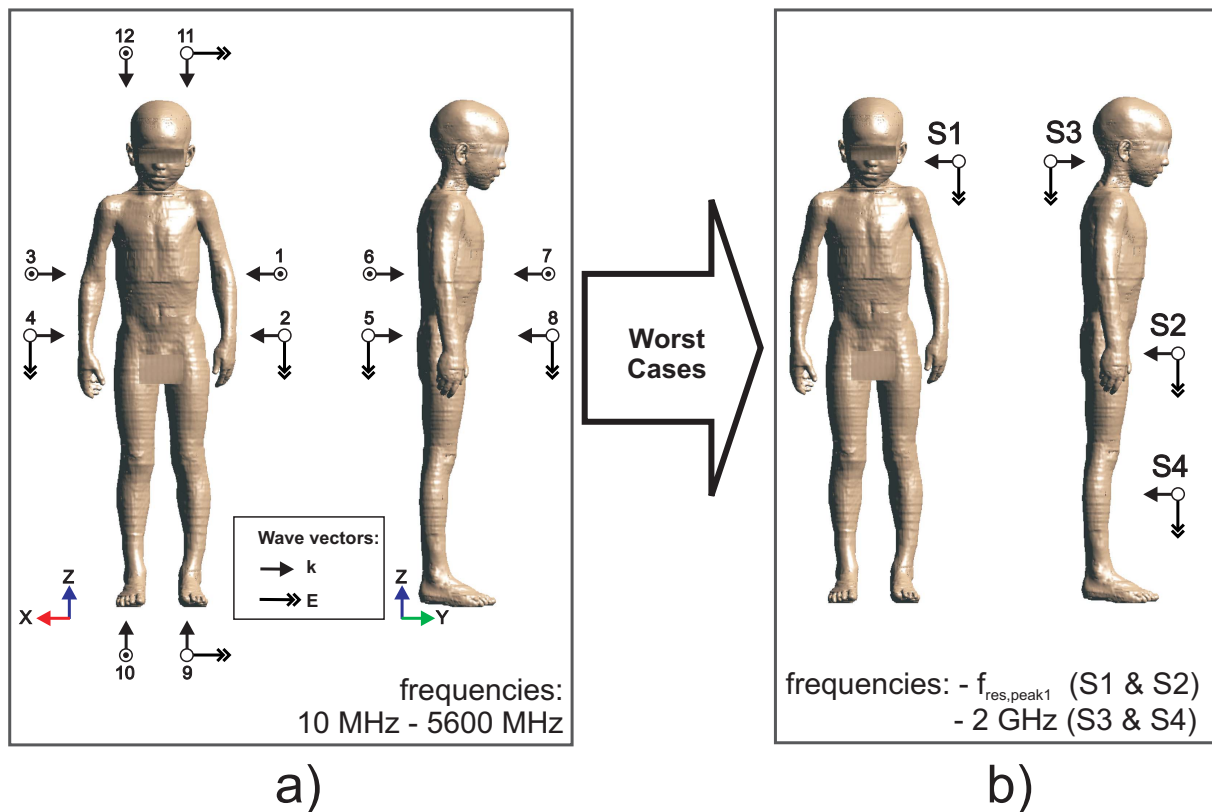


Figure 7.1: Visualization of (a) the twelve orthogonal plane wave exposure configurations at the full frequency range of 10 MHz to 5600 MHz and (b) the selected worst-case SAR scenarios $S1$ to $S4$ ⁵.

- scenario *S3*: dorsal incidence at 2 GHz (f_{peak2})
- scenario *S4*: ventral incidence at 2 GHz (f_{peak2})

The plane wave power density S_{eq} was set to the ICNIRP reference levels for the general public (Figure 3.2), i.e. 2 Wm^{-2} at $f_{\text{res,peak1}}$ and 10 Wm^{-2} at f_{peak2} .

We assessed $T_{\text{incr,max}}$ at exposure times $\Delta t = 0.5\text{h}$ and also at steady state temperatures, i.e. $\Delta t = 2\text{h}$.

7.2.5 Required incident EMF and SAR values to induce a peak temperature increase of 1 °C

To determine the level of protection for localized heating effects at the ICNIRP guidelines, we scaled the equivalent plane wave power densities to the value required to induce a peak temperature increase of 1 °C. Next, we calculated the corresponding $\text{SAR}_{1\text{g,max}}$, $\text{SAR}_{10\text{g,max}}$ and SAR_{wb} for these incident field levels, by using the electromagnetic results obtained previously⁵. We used average modelling parameters (Table 7.1) and we estimated the uncertainties by using the results of the Monte Carlo analysis.

7.2.6 Correlation of the peak temperature increase to SAR

From hyperthermia treatment planning we already know that high SAR levels are strongly correlated to high temperature levels^{18,149}. To verify the validity of this finding for our exposure scenarios and to determine the appropriate metric for protecting against RF heating effects, we used the Roberta model to assess $T_{\text{incr,max}}$ for all twelve orthogonal plane wave scenarios and for frequencies between 10 and 5600 MHz. First we compared the peak temperature increase to $\text{SAR}_{1\text{g,max}}$, $\text{SAR}_{10\text{g,max}}$ and SAR_{wb} as a function of frequency and exposure scenario. To simplify the correlation analysis, we computed the least-square regression coefficient (R^2) of the linear fits of $T_{\text{incr,max}}$ as a function of $\text{SAR}_{1\text{g,max}}$, $\text{SAR}_{10\text{g,max}}$ and SAR_{wb} . To determine the correlation of the peak location, we calculated the distance between the peak location of $T_{\text{incr,max}}$ to $\text{SAR}_{1\text{g}}$ and $\text{SAR}_{10\text{g}}$.

In addition, we determined the correlation also for all models, exposed to the worst-case scenarios *S1* to *S4*. The correlation depends strongly on frequency. Therefore, in our analysis we distinct between scenarios *S1* and *S2* at the resonance frequency, and scenarios *S3* and *S4* at 2 GHz.

7.3 Results

7.3.1 Sensitivity study

We assessed the sensitivity of the results to changes in the modelling parameters, such as the grid discretization step, source power, heat transfer coefficients, volume density of

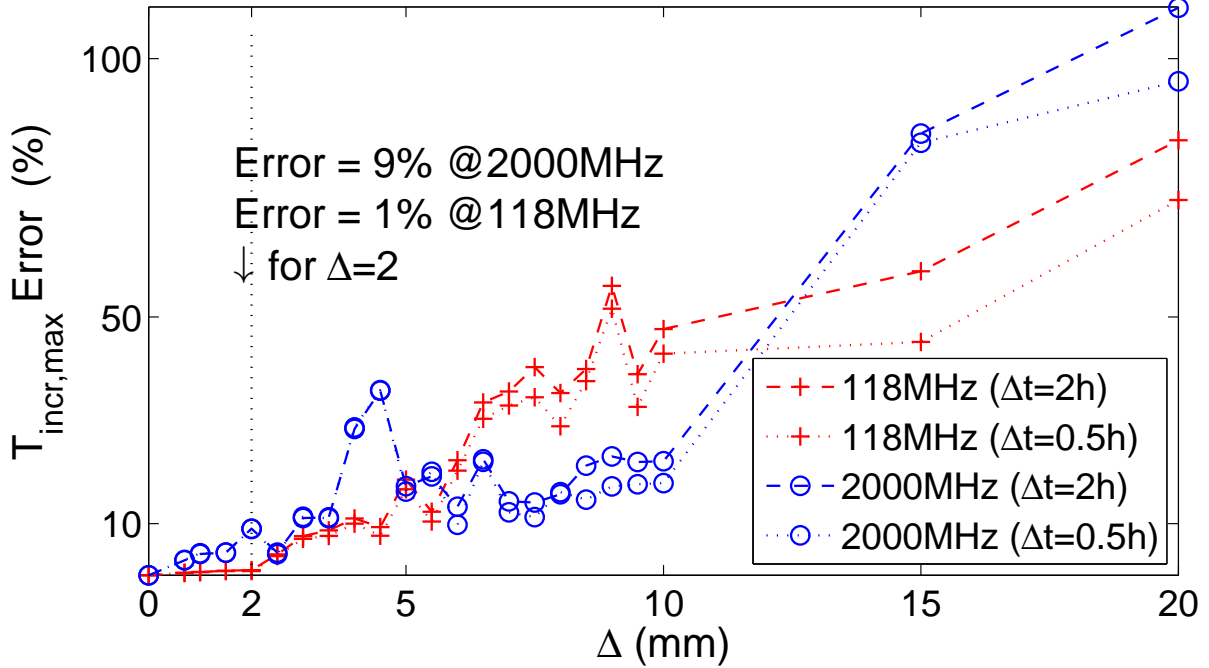


Figure 7.2: Error in peak temperature increase ($T_{\text{incr,max}}$) as a function of grid discretization step (Δ_{grid}) for the Roberta model exposed at the ICNIRP reference levels, i.e. 2 Wm^{-2} for scenarios $S2$ (118 MHz) and 10 Wm^{-2} for $S4$ (2 GHz). The exposure time Δt is either 0.5 or 2h.

mass, specific heat capacity, thermal conductivity, volumetric blood perfusion rate and the blood heat capacity.

Figure 7.2 demonstrates the relative error in the peak temperature increase as a function of the grid discretization step. In this study we used $\Delta_{\text{grid}} = 2 \text{ mm}$, at which the error is converged to 9% (2 GHz) or to 1% (118 MHz).

Figure 7.3 shows the relative change of the peak temperature increase as a function of relative changes (Δ) in the thermal modelling parameters. Since the peak temperature increase is not converged at $\Delta t = 0.5\text{h}$, there is a small dependency on the specific heat capacity. This dependency is omitted for steady state after two hours.

In the legend, “ $a_{\pm\sigma}$ ” indicates the derivative ($\%\%^{-1}$) of the linear regression over the range $\Delta = -\sigma$ to $+\sigma$, i.e. the standard deviation of the modelling parameters (Table 7.1). Table 7.2 shows the uncorrelated combined standard uncertainty of the peak temperature increase for half an hour and two hours of exposure.

7.3.2 Monte Carlo uncertainty analysis

To investigate the existence of correlation effects in the uncertainty estimation, we performed a Monte Carlo analysis for all models exposed to scenarios $S1$ to $S4$.

Table 7.3 demonstrates that the Monte Carlo standard uncertainty u_{MC} , i.e. the standard

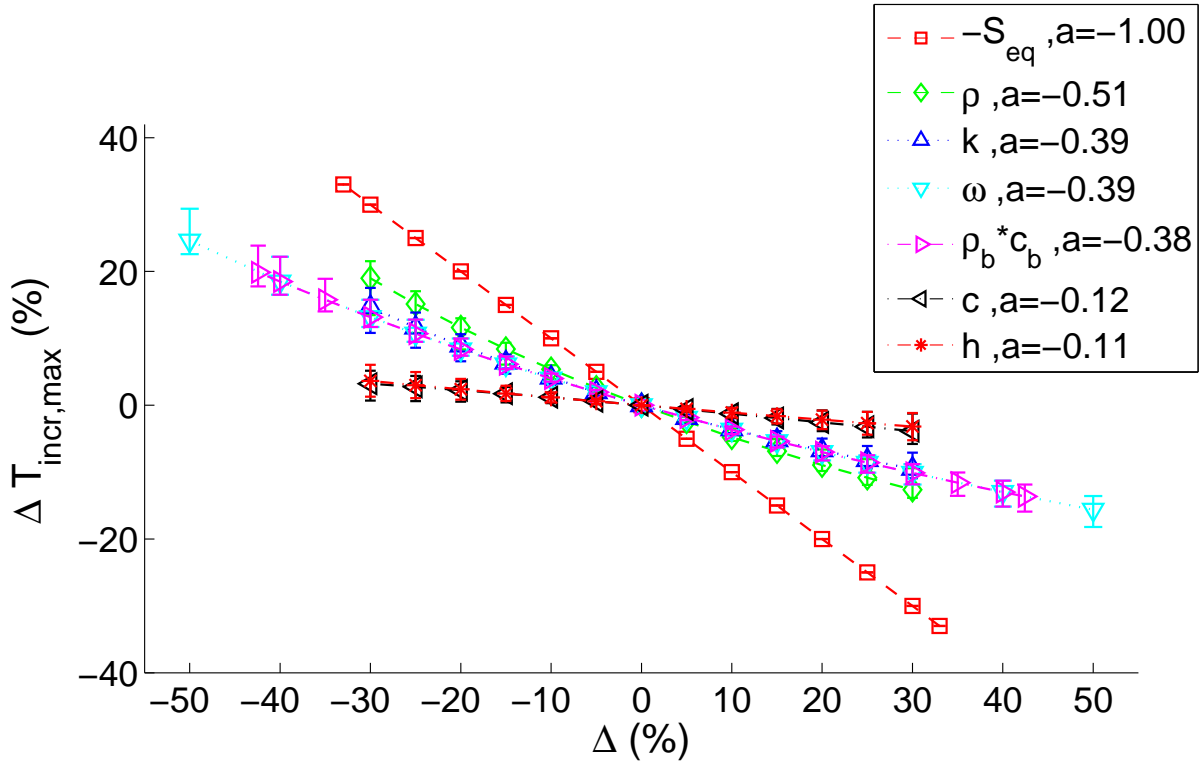


Figure 7.3: Sensitivity study of the relative change in peak temperature increase $\Delta T_{\text{incr,max}}$ as a function of the relative thermal parameter variation Δ . The error-bars indicate the minimum and maximum values found in the Roberta model exposed for half an hour to one of the four plane wave scenarios at the ICNIRP reference levels, i.e. 2 Wm^{-2} for scenarios $S1$ and $S2$ and 10 Wm^{-2} for $S3$ and $S4$. In the legend, “ $a_{\pm\sigma}$ ” indicates the slope ($\% \%^{-1}$) of the linear regression over the range $\Delta = -\sigma$ to $+\sigma$, i.e. the standard deviation of the modelling parameters (Table 7.1). We used “ $-S_{\text{eq}}$ ” for better comparison to the other parameters.

deviation of the 400 samples, is in the range of 14 to 37% and depends on the model and exposure scenario used. Hence, the expanded uncertainty U_{MC} ($k = 2$) of $T_{\text{incr,max}}$ is maximum 74%. To test the convergence at 400 samples, we repeated the Monte Carlo analysis with 1200 samples for the Roberta model and exposure scenario $S1$. We found a small difference of 1% in the mean and standard deviation of $T_{\text{incr,max}}$.

7.3.3 Assessment of the peak temperature increase for exposure at the ICNIRP reference levels

Figure 7.4 shows the calculated peak temperature increase for the models of six children and two adults exposed for half an hour to scenarios $S1$ to $S4$. The maximum peak temperature increase of $0.96 \text{ }^\circ\text{C}$ at the upper limit of the 95% confidence interval ($k=2$)

Table 7.2: Influence of the modelling parameters on the *uncorrelated* standard combined uncertainty (u_c) and the expanded uncertainty (U) of the peak temperature increase. We used normal (Gaussian) probability distributions and the uncertainties are obtained for only the Roberta model exposed to the worst-case scenarios $S1$ to $S4$ during 0.5h or 2h exposure time. k is the coverage factor.

	u_i (%)	
	0.5h	2h
Grid discretization Δ_{grid}		
a) $@f_{\text{res,peak1}}$	0.8	1.0
b) $@f_{\text{peak2}}$	9	9
Source power S_{eq}	11.0	11.0
heat transfer coefficient h	3.4	3.9
volume density of mass ρ	5.1	4.8
specific heat capacity c	1.2	0.0
thermal conductivity k	3.9	4.0
volumetric blood perfusion rate ω	19.7	25.8
blood heat capacity $c_b \cdot \rho_b$	5.5	6.9
u_c ($k=1$)	26	31
U ($k=2$)	51	62

Table 7.3: Influence of the modelling parameters on the *correlated* standard uncertainty u_{MC} (%) of the peak temperature increase, i.e. the standard deviation of the 400 Monte Carlo samples. Note that u_{MC} is obtained for all models exposed to the worst-case scenarios $S1$ to $S4$ during 0.5h or 2h exposure time (Δt).

Model Name	$\Delta t = 0.5\text{h}$				$\Delta t = 2\text{h}$				Average of the scenarios
	$S1$	$S2$	$S3$	$S4$	$S1$	$S2$	$S3$	$S4$	
Duke	17	18	25	17	20	21	30	21	21
Ella	16	15	24	22	18	18	27	26	21
Billie	14	18	31	28	17	21	37	32	25
Thelonious	20	14	25	26	24	19	32	32	24
Louis	15	16	26	21	21	19	31	29	22
Eartha	14	14	27	21	16	17	30	24	21
Dizzy	17	17	27	22	19	23	31	28	23
Roberta	16	17	24	25	19	20	26	24	21
Average of the models	16	16	26	23	19	20	30	27	

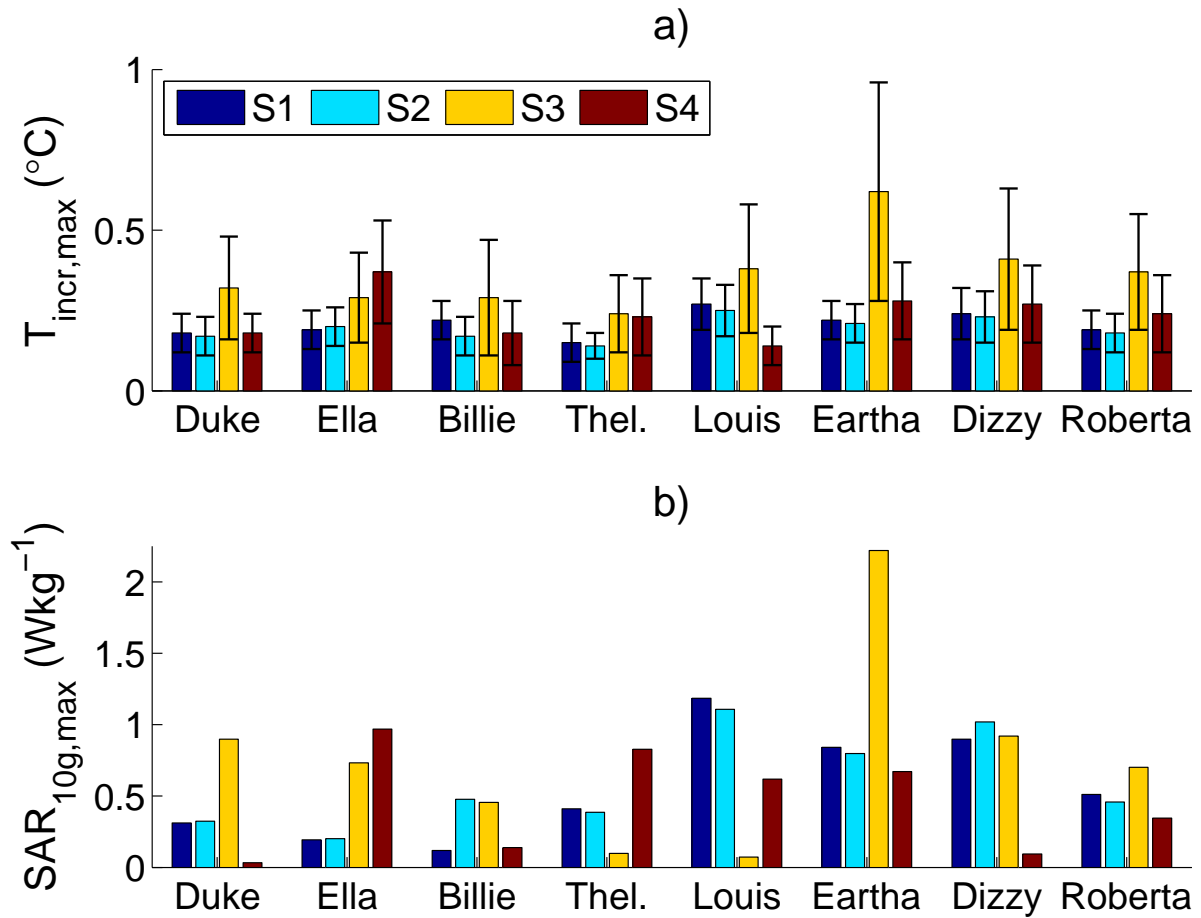


Figure 7.4: a) Peak temperature increase ($T_{\text{incr,max}}$) in the models of two adults (Duke and Ella) and six children exposed for half an hour to worst-case plane wave scenarios at the ICNIRP reference levels, i.e. 2 Wm^{-2} for scenarios $S1$ and $S2$ and 10 Wm^{-2} for $S3$ and $S4$ and b) the peak 10g spatial-averaged SAR ($\text{SAR}_{10\text{g,max}}$) at the location of $T_{\text{incr,max}}$. The error-bars indicate the expanded uncertainty U_{MC} ($k = 2$).

is found for the Eartha model exposed to scenario $S3$ for half an hour. For two hours exposure, this maximum is $1.01 \text{ }^{\circ}\text{C}$. Further analysis of the spatial distributions, revealed that this specific peak is located in the fingers of the right hand. In general, the peaks are located typically in the knees and ankles for scenarios $S1$ and $S2$, and in the fingers for $S3$ and $S4$ also for the other models. Figure 7.5 shows the $\text{SAR}_{10\text{g}}$ and the T_{incr} induced in the Eartha model exposed for half an hour to worst-case scenarios at the whole-body resonance peak $f_{\text{res,peak1}}$ ($S2$) and at the 2 GHz peak f_{peak2} ($S3$).

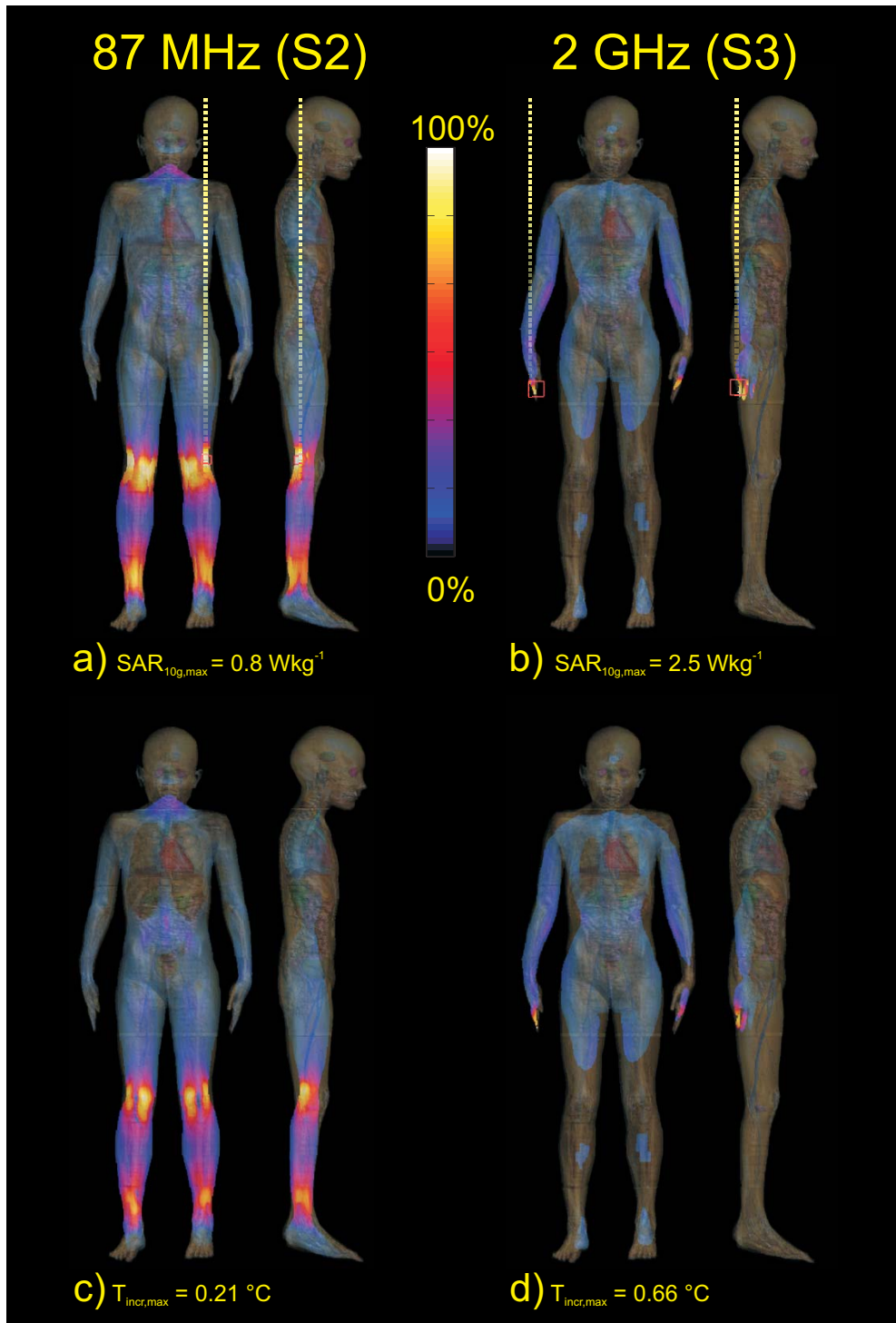


Figure 7.5: Transparent overlay of 2D SAR_{10g} (a,b) and T_{incr} (c,d) on top of the 3D Eartha model, for half an hour exposure at the ICNIRP reference levels. The cross-section locations are indicated by the dashed lines.

7.3.4 Required incident EMF and SAR to induce a peak temperature increase of 1 °C

To determine the level of protection against localized heating effects, we scaled the ICNIRP EMF levels of the exposure scenarios such, that the peak temperature increase is 1 °C.

Figure 7.6 demonstrates that the ICNIRP scaling factor is in the range of 1.0 to 12.2 (95% confidence, i.e. $\pm U_{MC}$). The peak SAR_{1g} values are in the range of 3.8 to 20.1 Wkg^{-1} and for SAR_{10g} the range is 2.2 to 11.7 Wkg^{-1} . The results are shown for an exposure time of half an hour. The scaling factors are on average 5% lower, with a maximum of 11%, for two hours exposure.

7.3.5 Correlation of the peak temperature increase to SAR

We determined the correlation of peak temperature increase (value and location) after half an hour exposure to localized peak SAR for the Roberta model exposed to all twelve orthogonal plane wave scenarios at frequencies between 10 and 5600 MHz. In addition, we determined this correlation for all human models exposed to the worst-case scenarios $S1$ to $S4$.

Figure 7.8 indicates a strong dependence of the peak temperature increase to SAR_{1g} and SAR_{10g} , which is confirmed by the goodness of fit R^2 in Figure 7.7. The location of the peak temperature increase is better correlated to the location of $SAR_{1g,max}$ (median distance d is 17 mm), than to $SAR_{10g,max}$ ($d=65$ mm).

Table 7.4 shows that for all human models exposed to the worst-case scenarios, the peak temperature increase correlates best to $SAR_{1g,max}$ for scenarios $S1$ and $S2$, i.e. the least-square regression coefficient (R^2) is highest and the median distance is smallest. For scenarios $S3$ and $S4$, R^2 is highest for $SAR_{1g,max}$ and $SAR_{10g,max}$. For scenarios $S1$ and $S2$ at $f_{res,peak1}$, the location of the peak temperature increase is best predicted by $SAR_{1g,max}$, i.e. the median distance is less than two voxels (3.4 mm). At 2 GHz ($S3$ and $S4$), the location of the maximum temperature is best predicted by the unfiltered SAR distribution.

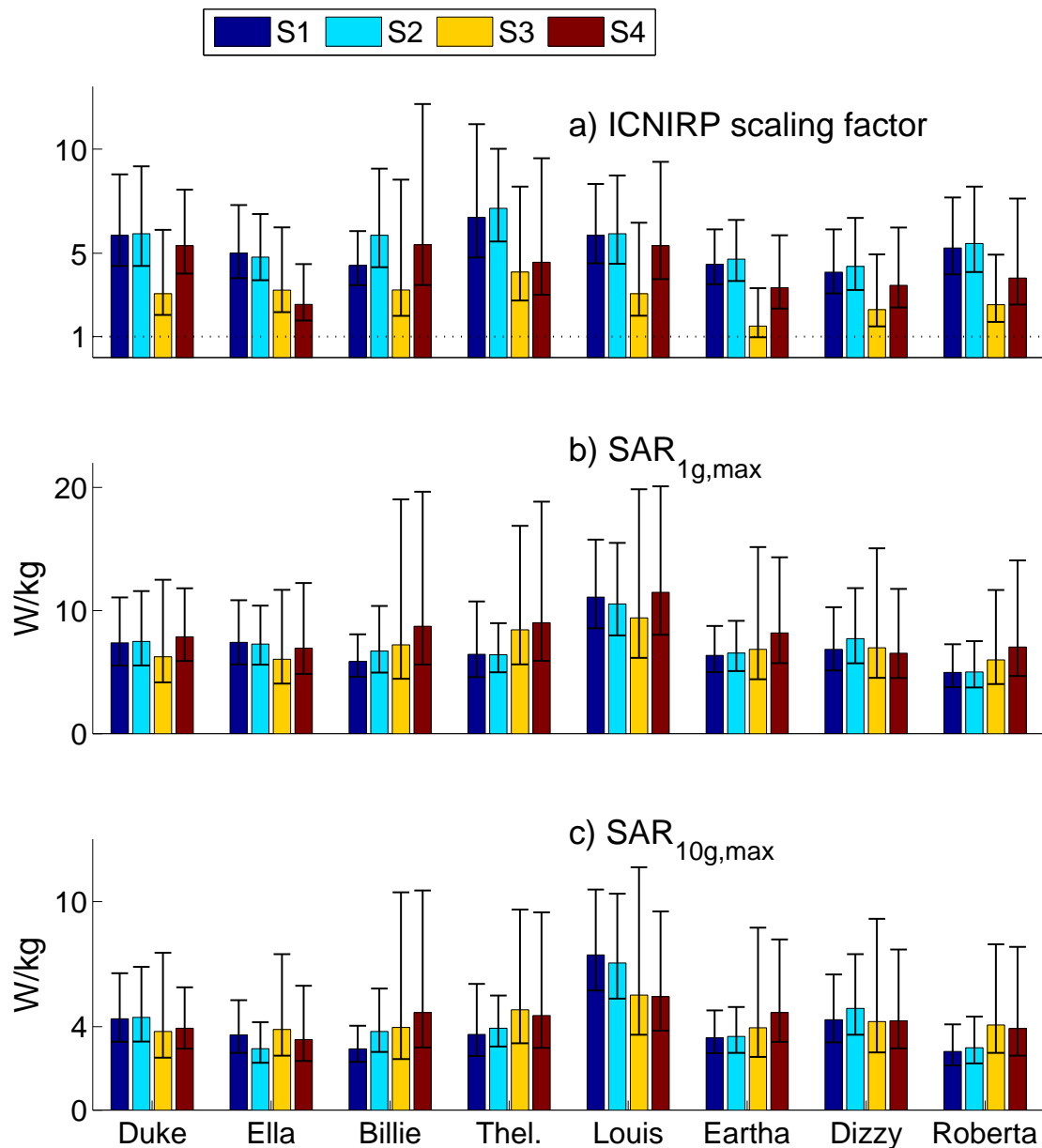


Figure 7.6: (a) Required scaling factors of the ICNIRP reference levels to induce a peak temperature increase of 1°C after half an hour exposure and (b) corresponding localized peak SAR averaged over 1g tissue ($SAR_{1g,max}$) and (c) localized peak SAR averaged over 10g tissue ($SAR_{10g,max}$). The results are for average modelling parameters and the error-bars indicate the expanded uncertainty U_{MC} ($k = 2$). The legend indicates the four plane wave scenarios $S1$ to $S4$. Note that the peak temperature increase location is not necessarily identical to the location of $SAR_{1g,max}$ (median distance is 6 mm) or $SAR_{10g,max}$ (median distance = 22 mm).

Table 7.4: Correlation of peak temperature increase with SAR, $SAR_{1g,max}$ and $SAR_{10g,max}$ for the eight human models exposed to the scenarios $S1$ to $S4$. The linear fit parameters are represented by the slope ($\Delta T/\Delta SAR$) and the goodness of the fit (R^2). The median distance to the peak temperature increase location is indicated by d .

Metric	$S1$ and $S2$ ($f_{res,peak1}$)			$S3$ and $S4$ (f_{peak2})		
	$\Delta T/\Delta SAR$	R^2	d	$\Delta T/\Delta SAR$	R^2	d
	$^{\circ}CkgW^{-1}$	-	mm	$^{\circ}CkgW^{-1}$	-	mm
SAR	-	-	76.9	0.11	0.69	4.9
$SAR_{1g,max}$	0.26	0.96	3.4	1.38	0.83	16.2
$SAR_{10g,max}$	0.27	0.73	104.0	2.27	0.84	18.7

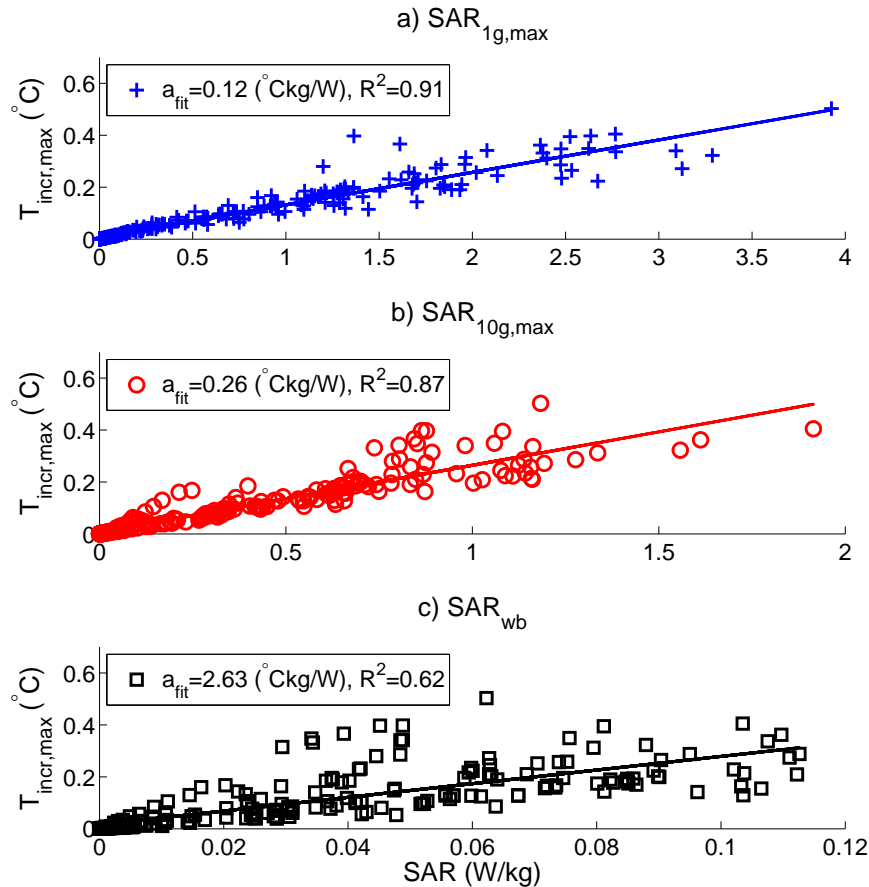


Figure 7.7: Correlation between $T_{incr,max}$ and $SAR_{1g,max}$ (a), $SAR_{10g,max}$ (b) and SAR_{wb} (c) for the Roberta model exposed to the twelve plane wave scenarios in the frequency range of 10 - 5600 MHz. a_{fit} is the derivative and R^2 is the coefficient of determination of the linear fits.

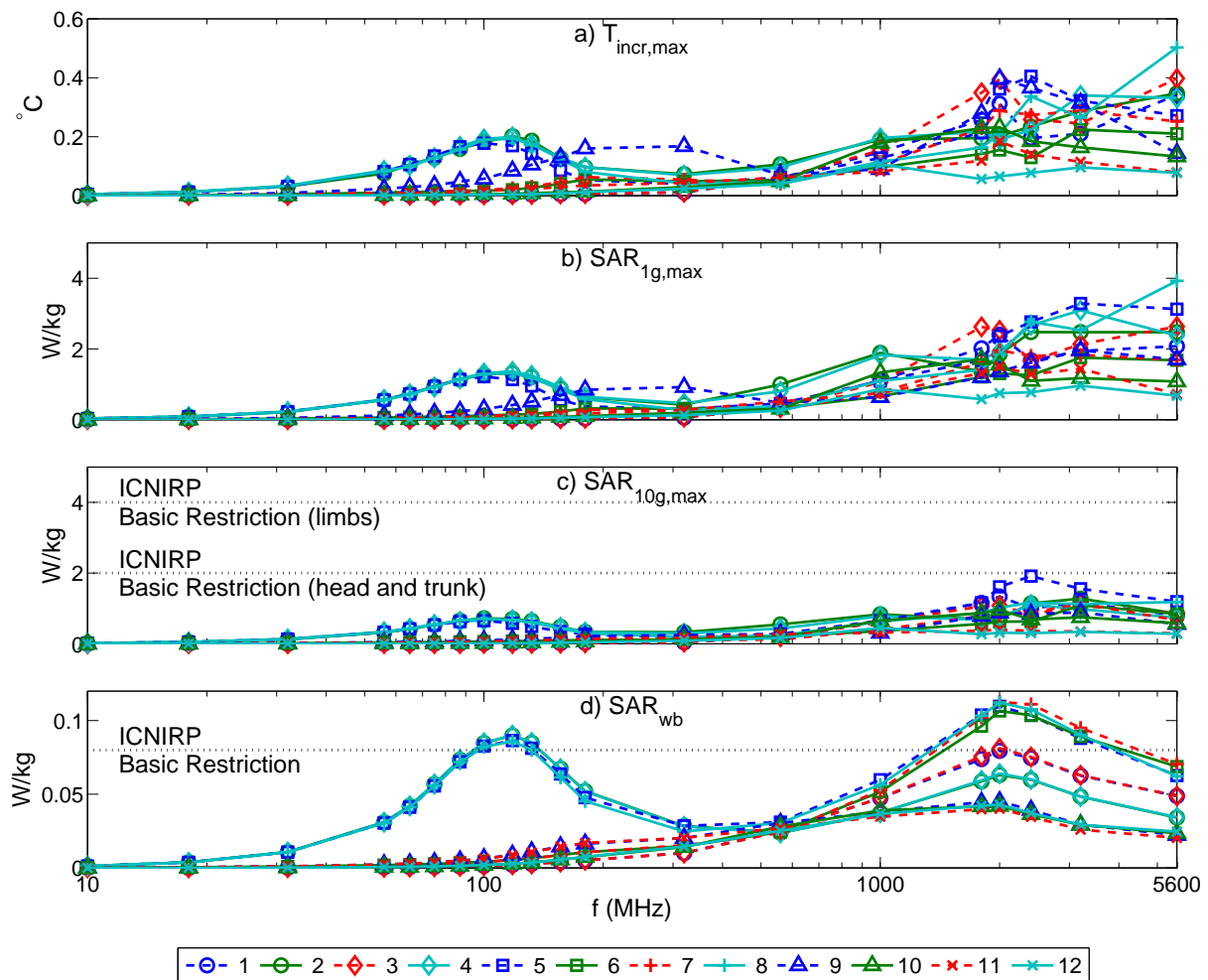


Figure 7.8: (a) Peak temperature increase ($T_{\text{incr,max}}$) after half an hour exposure, (b) localized peak SAR averaged over 1g tissue ($\text{SAR}_{1\text{g}}$), (c) localized peak SAR averaged over 10g tissue ($\text{SAR}_{10\text{g}}$) and (d) whole-body averaged SAR (SAR_{wb}) for the Roberta model exposed to twelve orthogonal plane wave scenarios in the frequency range of 10 - 5600 MHz at the ICNIRP reference levels. Note that only average values and not the expanded uncertainties are indicated.

7.4 Discussion

7.4.1 Evaluation of the results

In this study, we analysed the relevance in terms of the worst-case exposure conditions as defined in a previous study. The SAR distributions predicted for orthogonal plane-wave exposure scenarios, and models of adults and children, have been used to calculate the peak temperatures induced. Induced peak temperatures in the range of 0.1-1.0 °C have been obtained, which is consistent with Bernardi et al.¹⁰ and Hirata et al.⁹⁴ who found $T_{\text{incr,max}}$ in the range of 0.2-0.7 °C for ventral and dorsal exposure scenarios using parallel aligned electric fields. The temperature range in the current study is larger because we analysed more scenarios and we included a more advanced uncertainty analysis.

The current guidelines of ICNIRP aim at restricting excessive localized tissue heating by providing restrictions on SAR_{10g}. Since an absolute threshold temperature for such excessive heating is not given, we can not determine if these restrictions are compliant. In fact, besides the absolute temperature, thermal tissue damage is also determined by the exposure time^{64,67,191,207}. Therefore, we recommend defining a maximum peak temperature increase for a specific duration of exposure and more research into the correlation between tissue damage and thermal dose, i.e. temperature and time.

To determine the level of protection against localized heating effects, we scaled the ICNIRP reference levels that will lead to a 1 °C localized tissue temperature increase for worst-case scenarios. The required scaling factor is 1.0 to 12.2 (95% confidence interval) Assuming a maximum of 1 °C localized tissue temperature increase as acceptable and no additional safety factors, we found that the basic restrictions on SAR_{10g} should be lower than 2.2 Wkg⁻¹. The range of 2.2 to 11.7 Wkg⁻¹ is consistent with e.g. Anderson and McIntosh² and McIntosh and Anderson¹³¹ who found on average 3.6±2 Wkg⁻¹ in planar and 5±1 Wkg⁻¹ in complex human body models. The correlation between peak temperature increase and mass-averaged SAR has been studied previously by Anderson and McIntosh² and McIntosh and Anderson¹³¹ to determine the appropriate RF exposure metric for the range of 1 to 10 GHz. They found that the peak temperature increase is better correlated to SAR_{10g} at 1 and 3 GHz. Differences in tissue properties deteriorate the correlation between the peak temperature increase and SAR. Consequently, the peak temperature increase is not directly related to the peak SAR value and location. For example, a peak SAR values in the brain are usually cooled by the high perfusion levels and therefore the peak temperature located outside the brain.

We found that the peak temperature increase in the Roberta model correlates better to SAR_{1g} than to SAR_{10g}. Also the peak location is better predicted by SAR_{1g} than by SAR_{10g}. The correlation for the other models exposed to scenarios *S1* to *S4* depends on frequency: at the resonance frequency, the peak temperature increase value and location correlate best to SAR_{1g}. At 2 GHz, the peak values are best predicted by both SAR_{1g} and SAR_{10g}, while the location is best predicted by SAR. Finally, SAR_{1g} is much more restrictive ($a_{\text{fit}} = 1.38^\circ\text{CkgW}^{-1}$) than SAR_{10g} ($a_{\text{fit}} = 2.27$), for frequencies larger than 2 GHz. We assessed a limited amount of exposure scenarios with peaks at specific locations

and only the 1g or 10g averaging masses. The best exposure metric depends on the exposure scenario and on local tissue parameters. We used the peak temperature increase as being the best metric to prevent excessive localized tissue heating instead of localized peak SAR. Therefore, our rigorous analysis of the temperature distributions has improved the understanding about the correlation of simulated metrics (e.g., 1g/10g averaged SAR) and excessive localized tissue heating and the applicability of these metrics. This is a major step in tailoring the current restrictions for EMF exposure.

The peak temperature increase not only depends on frequency, it also depends on incident angle, field polarization, (age-dependent) electromagnetic and thermal tissue properties, the (reflecting) environment, and the human model geometries and postures. In this study, we limited our analysis to eight human models in straight position exposed to twelve orthogonal plane wave exposure scenarios. We did not analyse the effects of partial body resonances and effects due to other postures. Partial body resonances can result in increased SAR in thin structures close to the surface and need special considerations. Other postures change the local distribution of absorbed energy, but not the global distribution. In addition, note that we assumed exposure scenarios with subjects standing motionless in the field for half an hour, which is very unlikely to occur in real life. The peak locations and peak values in both $\text{SAR}_{10\text{g}}$ and temperature increase depend on the actual posture of the model. Therefore, the peak $\text{SAR}_{10\text{g}}$ locations might change as a function of time for moving subjects, leading to a lower time-averaged SAR and hence a lower peak temperature increases. Finally, the models in this study were positioned in free space, while the reflective environment such as a perfectly conducting ground or walls can have a major impact on the results^{111,193}.

7.4.2 Evaluation of the methods

Evaluation of the assumptions In this study, we simplified the Pennes Bioheat Equation by using an induced temperature increase equation. Although this method requires some assumptions, which are generally also present in absolute temperature simulations, major improvements on accuracy and computation speed are obtained. The first improvement is that the results are independent on poorly known thermal parameters, such as the metabolic heat generation rate, blood temperature, boundary heat flux and boundary temperature. Secondly, the simulation time is decreased due to the elimination of base temperature distributions and by reducing numerical rounding errors. This reduction allows faster computations by using single instead of double precision memory.

In this study, we assumed that the peak temperature increase is too low to activate changes in the thermo-regulation, i.e. the blood temperature, perfusion rate, metabolic heat generation rate, heat transfer coefficient and flux are temporally constant. Previous studies have shown a zero¹⁰ or negligible (0.03 °C)⁹⁴ influence on the increases in body temperature for various exposure scenarios at either the ICNIRP EMF reference levels or at the basic SAR_{wb} restriction of 0.08 Wkg^{-1} . Hirata et al.⁹⁴ showed that a much higher whole-body-averaged SAR is required to induce a body temperature increase of 1 °C, i.e. SAR_{wb} is 9 Wkg^{-1} for a three-year-old child and 6 Wkg^{-1} for an adult. The blood

circulates through the body a few times per minute and the time to reach steady state is four hours⁹⁴. Hence, we expect a negligible effect of blood heating on our results.

Temperature dependent changes in the thermal conductivity and perfusion are neglected. For the range of 37 to 38 °C, the change in conductivity is smaller than 1% and for the perfusion smaller than 5%¹¹. Note that these intrapersonal changes are much smaller than interpersonal changes and our sensitivity analysis shows that the effect of such small changes on the peak temperature increase can be neglected.

The values for the heat transfer coefficient between skin and air reported in literature show a standard deviation of 30% (Table 7.1). Our sensitivity analysis shows that such a variation has an effect of maximum 4% on the peak temperature increase. We do not expect that such changes in heat transfer coefficient between the cornea and air or between the lungs and air will have an effect on the peak temperature increase, since the peaks are not located near the eyes or lungs. In this study we assumed homogeneous heat transfer over the entire body surface and we did not investigate the effect of non-uniform clothing^{55,56}. Although such non-uniform insulation might have a major effect on the absolute temperatures of the subject, we expect from the sensitivity analysis a negligible effect on the induced temperature increase.

Validation of the code The finite-difference time-domain code to solve Pennes Bioheat Equation is implemented in SEMCAD X. Although we did not validate our simulations by measurements of the specific exposure scenarios, the code implementation of the conformal schemes is validated for both simple and complex cases¹⁴⁰. The simple, i.e. analytically solvable, cases consisted of square plates or hollow spheres¹⁶¹, with both Dirichlet and Neumann boundary conditions. The code is also validated for complex cases, such as the heating of tissues around implants during MRI¹⁴¹. In future work, we plan to validate the algorithms by interstitial and non-invasive thermometry using MRI for EMF induced heating techniques such as hyperthermia treatments^{18,149}.

Uncertainty evaluation In the sensitivity study, we investigated the influence of the modelling parameters, such as grid resolution and thermal tissue parameters on the results. We extracted the standard uncertainties of literature values for the thermal tissue and the boundary parameters to estimate the expanded uncertainty within the 95% confidence interval ($k=2$). A drawback of this approach is that we assumed that the reported literature values can be described by a normal (Gaussian) probability function. Since the available literature data is too sparse, we could not verify this assumption.

Table 7.2 shows that the expanded uncertainty at two hours exposure time is larger than at 30 minutes, due to the fact that steady-state is not yet reached at 30 minutes for lower perfusion rates. As expected we found larger grid discretization errors at 2 GHz than at the resonance frequency.

To reduce the amount of computations, we separated the electromagnetic from the thermal evaluations. The standard uncertainty in peak localized SAR found by Bakker et al.⁵, is used as a power density scaling factor in the thermal simulations. Hence, we assumed

that this uncertainty is equally distributed for the entire 3D distribution. In future Monte Carlo uncertainty investigations, we recommend to join the electromagnetic and thermal uncertainties per iteration.

To investigate the influence of correlation on the results, we compared the correlated standard uncertainty of Monte Carlo analysis (u_{MC}) of all human models to the uncorrelated standard uncertainty (u_c), which we obtained for only the Roberta model. Table 7.3 shows that for the Roberta model, the scenario-averaged correlated u_{MC} is lower than the uncorrelated u_c . Hence, the existence of correlation between thermal parameters might decrease the combined influence on the temperature. However, we also observed that these differences are due to the different method in the assignment of thermal properties. In the sensitivity study, we applied “bulk” scaling of the properties for all tissues together, while for the Monte Carlo analysis we applied “individual” scaling per tissue. For the perfusion variations, we found that “bulk” tissue scaling results in much higher deviations (std. unc. = 22%) than for “individual” tissue scaling (std. unc. = 9%).

In the Monte Carlo analysis, we did not account for discretization errors in the thermal computations. The maximum discretization error of 9% in the Roberta model was found at 2 GHz. If we add this error to the Monte Carlo uncertainty by the “square-root of the sum-of-the-squares” method, the uncertainties of Table 7.3 increases by a maximum of 2%.

In our analysis, we did not assess the uncertainty of the underlying thermal model. We used the Pennes Bio Heat Equation, which uses a homogeneous heat-sink term proportional to the tissue perfusion and the difference between local temperature and perfusing blood temperature. In this model, it is assumed that the heat exchange in the microvasculature equilibrates instantaneously and that infinitely small vessels are present at all locations. In reality however, large blood vessels (i.e. >5 mm) can significantly affect the temperature increase on a small scale. The most detailed modelling of individual blood vessels is obtained using the discrete vasculature (DIVA) model proposed by Kotte et al.¹¹⁷. Unfortunately, the human models used in this study contain only limited vascular information. Therefore, the validity of our temperature increase predictions in the direct neighbourhood (i.e. 1 cm) of large vessels is questionable. We found the worst-case peak temperatures typically in the fingers and in the ankles and knees (Figure 7.5). The peaks in the fingers are not located close to large vessels. However, the ankles and knees contain large vessels which might result in lower peak values when DIVA modelling would have been applied. In contrary, the heating patterns (Figure 7.5) shows a large volume containing a temperature increase close to the peak temperature. Hence, we expect negligible effect of the large vessel on the results for the worst-cases in this study.

In addition, we assumed isotropic properties for all tissues, while some tissues such as muscle fibres can have anisotropic dielectric and thermal properties. Although the modelling tools support such features, we did not use them in this study, since we could not find useful literature values.

We used the literature parameters, which represents the average of heterogeneous tissues. However, tissues are not discrete, e.g. different muscles can have different infiltrations of fatty tissues and vessels. We expect that heterogeneities lead to increased worst-case peak

temperature increases. In future research, we plan to use MRI maps to account for e.g. heterogeneous tissue perfusion.

The uncertainty of our results depends on the reliability and availability of the literature values of the thermal¹³⁰ and electromagnetic^{71,73,74} tissue parameters. We assumed that the variances in the literature values can be described by a normal (Gaussian) distribution. For future uncertainty assessments, we recommend to assess the shape of the distribution of the (age-dependent) tissue thermal properties of the entire human population.

Due to lack of knowledge of thermal tissue parameters, dosimetry studies should be accompanied by solid uncertainty assessments. We therefore recommend using Monte Carlo analysis standard in the assessment of EMF induced temperature elevations.

7.5 Conclusions

In this study, we investigated the peak localized temperature increase in six children and two adults exposed to orthogonal plane wave scenarios at frequencies in the range of 10 to 5600 MHz. Worst-case scenarios at the ICNIRP EMF reference levels can induce a peak temperature increase of more than 1 °C (upper limit of the 95% confidence interval). In addition, we found 2.2 Wkg⁻¹ as minimum peak 10g spatial-averaged SAR value that can induce a peak temperature increase of 1 °C (upper limit of the 95% confidence interval). The correlation between peak temperature increase and SAR, SAR_{1g} or SAR_{10g} was shown to depend on the frequency and the peak location is not necessarily identical to the peak SAR, SAR_{1g} or SAR_{10g} location. Therefore, the peak temperature increase is the best metric for protecting against RF induced localized heating effects. Hence in our view, for compliance testing, future guidelines require restrictions on peak temperature increase for specific duration of exposure instead of restrictions on SAR_{10g}.

Part II

Exposure in medical applications

8. 2D validation

2D validation of RF models
using electric field and
temperature sensors

This chapter is based on:

JF Bakker, MM Paulides, AH Westra, H Schippers and GC van Rhoon. "Design and test of a 434 MHz multi-channel amplifier system for targeted hyperthermia applicators". *Int J Hyperthermia*, Vol. 26, No. 2, pp. 158-170, 2010.

MM Paulides, JF Bakker and GC van Rhoon. "An electromagnetic head and neck hyperthermia applicator: experimental phantom verification and FDTD model". *Int J Rad Oncol Biol Phys*, Vol. 68, pp. 612-620, 2007.

Abstract

Purpose: Experimental verification of the feasibility of focussed heating in the neck region by an array of two rings of six electromagnetic antennas. We further measured the dynamic specific absorption rate (SAR) steering possibilities of this set-up and compared these SAR patterns to simulations. **Materials and methods:** By a specially constructed laboratory prototype head and neck applicator, including a neck mimicking cylindrical muscle phantom, we performed SAR measurements by electric-field Schottky-diode sheet measurements and, using the power-pulse technique, by fiberoptic thermometry and infra-red (IR) thermography. Using phase-steering, we also steered the SAR distribution in radial and axial directions. All measured distributions were compared to predictions by a finite-difference time-domain (FDTD)-based electromagnetic simulator. **Results:** A central 50% iso-SAR focus of 35 mm (± 3 mm) in diameter and around 100 mm (± 15 mm) in length are obtained for all investigated settings. Further, this SAR focus can be steered towards the desired location in radial and axial direction with an accuracy of ~ 5 mm. SAR distributions as measured by all three experimental methods are well predicted by the simulations. **Conclusions:** We conclude that focussed heating in the neck is feasible and that this focus can effectively be steered in both radial and axial direction. For quality assurance (QA) measurements we conclude that the Schottky-diode sheet provides the best compromise between effort, speed and accuracy, although a more specific and improved design is warranted.

8.1 Introduction

Loco-regional control of advanced carcinomas in the head and neck (H&N) region still poses a major therapeutic challenge^{49,155} and treatment related toxicity remains a major issue in this region¹⁷⁹. Combining hyperthermia (HT) with the current treatment modalities has a high potential to increase treatment outcome without increasing toxicity⁹⁷. Recent phase III trials have shown the benefit of the addition of HT to current treatment modalities for various tumour sites^{25,108,188}. Valdagni *et al.*^{183,184} have demonstrated that with a non-site-specific HT-applicator already a significant increase in local control (from 24% for radiotherapy (RT) alone versus 69% for RT plus HT) is achieved for metastatic lymph nodes in stage IV carcinoma of the H&N. Extension of the hyperthermia application to deeper located tumours is cumbersome with the available applicators and therefore requires a specific designed applicator that is also expected to contribute to a better treatment quality for this site^{206 172}.

In recent years, we have investigated the ability of a multi-element circumferential H&N HT applicator to deposit radiofrequency (RF) energy selectively in the center of the

neck¹⁴³. Suitable frequencies were shown to be in the frequency band between 300 and 600 MHz for all realistic target sizes therefore we selected 433 MHz* as operating frequency. Further, we found that eight antenna elements provide sufficient focussing for selective heating. Building on these findings, we analyzed the influences of the anatomy on the SAR pattern¹⁴⁴. In this study we found that the SAR patterns in a homogeneous muscle cylinder are predictive for the SAR pattern in inhomogeneous neck structures. Therefore muscle phantom measurements will be predictive for the SAR pattern that can be obtained in the middle of the neck. Due to the spine, the central SAR focus changes from a circular to a more donut shape but the central focus remains at its central position. Subsequently, research was conducted into possibilities of further improving the power absorption pattern by going from one to two or three antenna rings¹⁴⁸, which provides also axial steering possibilities. We established that heating at depth is highly correlated with the number of antennas arranged in multiple rings. Multiple rings enable steering in the direction of the patient axis, which is well validated for deep hyperthermia^{166 150} but needs confirmation for the head and neck application. This work resulted in a final set-up design: a set-up with two rings of six antennas each operating at 433 MHz. As radiators, we selected a patch antenna set-up that is simple, low-cost, efficient and small and we designed it specific for the head and neck applicator¹⁴⁵. Another major advantage of this antenna design is that no matching network is required, which facilitates a better control of the input parameters of the set-up and hence provides better possibilities to create a representative model. Subsequently, the latter improves the reliability and accuracy of numerical predictions.

The aim of the present study was to experimentally verify the feasibility of focussed heating in the head and neck region using an array of two rings of six antennas by the split-phantom technique. Simultaneously, we established the accuracy of the predictions of our electromagnetic simulation model. Finally, we explored the dynamic SAR steering behavior of the antenna array. Hereto we constructed a laboratory prototype applicator consisting of twelve patch antenna elements and a muscle-equivalent neck phantom. We performed measurements with this set-up and compared them to predicted SAR patterns.

8.2 Materials and methods

8.2.1 Multi-channel amplifier system

An amplifier system with full amplitude and phase-control to deliver the radio frequency signals, was not available. We therefore designed and tested a 433.92MHz multi-channel amplifier system.

System description Figure 8.1 provides a schematic overview of the amplifier system designed and shows the relationship between its elements. The path of the signals

*433 MHz is an ISM frequency: a frequency available for Industry Science and Medicine

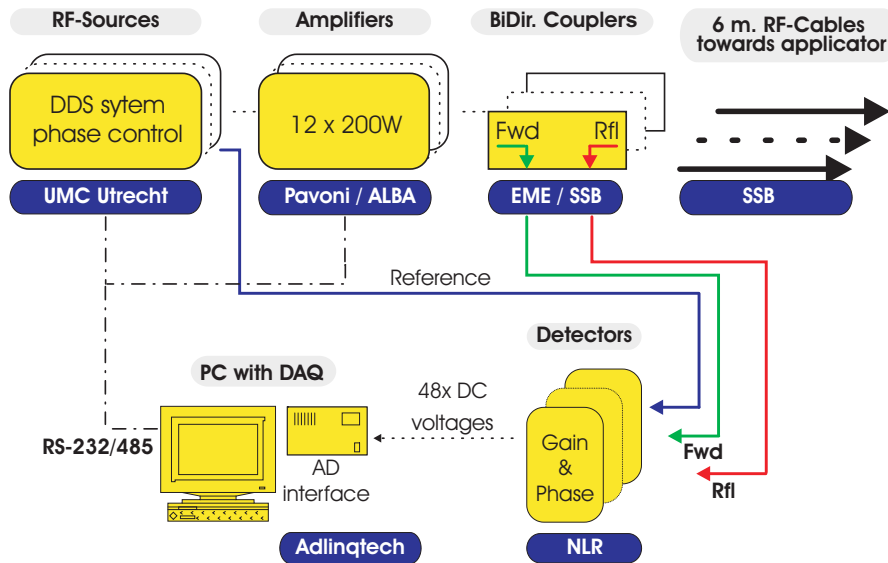


Figure 8.1: Schematic overview of the designed amplifier system. Fwd is the forward and Rfl is the reflected signal.

are visualized clockwise. A Direct Digital Synthesizer (DDS) system[†], which is designed around the AD9954 (Analog Devices, USA) generates twelve coherent signals of 10mW, 433.92MHz and with individual phase settings. These signals are amplified by 200 W RF amplifiers[‡]. Low-loss ($<0.1\text{dB/m}$) RF-cables (Ecoflex 10 SSB, Germany) are used to direct the high power signals from the amplifiers to the applicators in the treatment room. Directional couplers (2320/30B, EME HF-Technik, Germany) are placed at the amplifiers to couple a small portion ($\approx 30\text{dB}$) of the amplified signals to newly-developed gains and phase detectors[§]. A data-acquisition system using the DAQ-2208 (Adlink Technology) collects the DC detector outputs and performs an analog-to-digital (AD) conversion at a rate of 100Hz per channel. The entire system is mounted in two 19" racks 2m in height and is installed in an air-conditioned chamber.

We measured the RF spectra of all amplifiers in the power-range of 20-200W. The spurious emission in a 100kHz bandwidth around the center frequency of 433.92MHz is lower than 60dBc. The second harmonic frequency of 867.84MHz is suppressed more than 45dB and the third harmonic at 1301.8MHz is lower than 70dB. Any other frequency is suppressed more than 70dB.

Feedback control Signal instabilities and inaccuracies, often depend on frequency, amplifier gain and temperature of operation. We implemented a Proportional-Integral-Derivative (PID) feedback control to match the power and phases measured to those requested. Since the clinical practice requires stable signals with zero probability for un-

[†]University Medical Center Utrecht (UMCU), the Netherlands

[‡]Pavoni Diffusion, Italy

[§]Dutch Aerospace Laboratory (NLR), the Netherlands

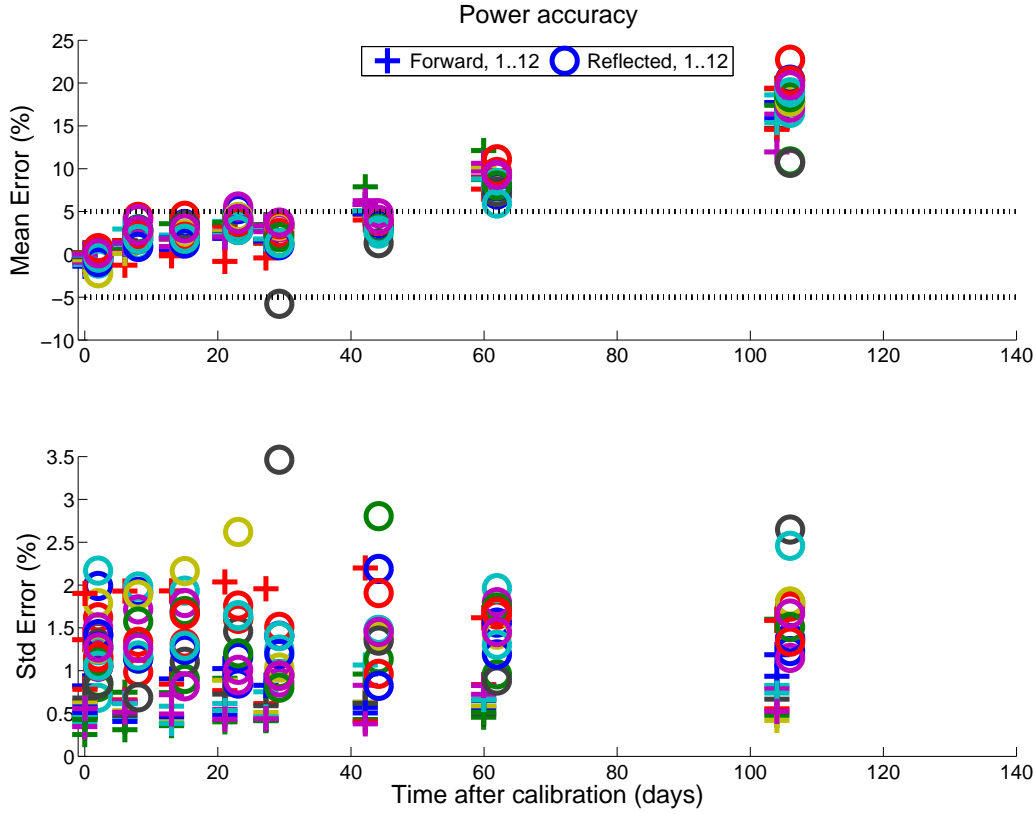


Figure 8.2: Forward and reflected power accuracy. The mean and std errors are the mean and standard deviations of the errors over the entire power range from 0 to 150W. The black dashed lines indicate the maximum errors according to the design criteria. Note that after the experiment, the powers are re-calibrated with an in interval period of one month.

stable loops, we used a simple feedback with only the proportional term. Although the sampling rate is 100Hz per channel, the update frequency of the feedback control is only 5Hz. In addition, the measurements are time-averaged over a period of one second for stability.

The settling time $t_{s,5\%}$, i.e. the time required for an output to reach and remain within a 5% error band is maximum eleven seconds for the power control and maximum nine seconds for the phase, without overshoot.

Accuracy of the power and phase measurements We used a digital power meter (EMP-442A, Agilent, USA), directional couplers (3020A, Narda, USA) and attenuators (R412720000, Radial, USA) to measure the accuracy of the power measurements provided by the amplifier system. We measured the total insertion loss of this path by using a network analyzer (8751A, Agilent, USA). We used 50 ohm terminations for the forward

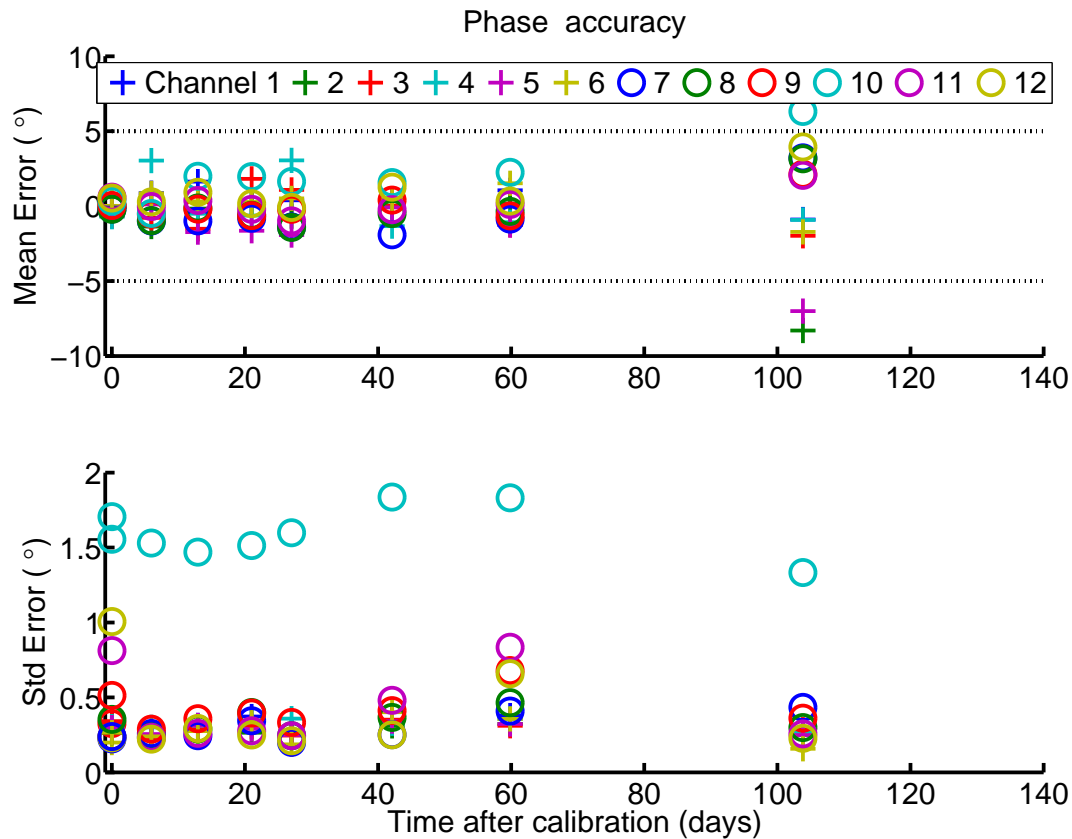


Figure 8.3: Phase accuracy as a function of the time after calibration. The mean and std errors are the mean and standard deviations of the errors over the entire phase range from -180 to 180° . The black dashed lines indicate the maximum errors according to the design criteria. Note that after the experiment, the phases are re-calibrated with an interval period of two months.

measurements and short terminations for the reflected ones. The power error is defined as the difference between the power readings of the accurate digital power meter and the readings provided by the amplifier system. We measured the forward power errors in 30 steps between 0 and 200W. For the reflected power errors we used 30 steps between 0 and 100W and one step of 200W. The time between each step was approximately 2.5 seconds, to provide sufficient settling time for both the amplifiers and the digital power meter. The channels were calibrated sequentially and the total time required for the calibration of both forward and reflected powers of all channels was approximately 30 minutes.

Figure 8.2 shows the mean and standard deviation of the power errors as a function of time after calibration. The mean error increased from 0% at the initial calibration to maximum 25% at 105 days after the calibration. The standard deviation of the power errors measured was smaller than 3.5% within the 105-day period.

We measured the phase accuracy by using a configuration that is almost similar to the power one: one DDS channel of the amplifier system provides the reference signal for measurements using a vector voltmeter (Agilent HP8508A). The forward power was set to 30W. Figure 8.3 shows the mean and standard deviation of the phase errors. The mean phase error increased from 0° at the initial calibration to maximum $\pm 8^\circ$ at 105 days after calibration. Within the 105-day period, the standard deviation of the measured phase errors is smaller than 2° .

Note that we performed the phantom experiment always within one week after calibration, i.e. the power error was smaller than 5% and the phase error was smaller than 5° .

8.2.2 Prototype design

Figure 8.4 shows a picture of the bottom half of the prototype applicator and Figure 8.5 visualizes an exploded view of its two parts. These parts can be separated to allow 2D IR measurements or positioning of measurement devices: glass fibre probes or electric (E)-field Schottky-diode sheet. Both parts of the applicator consist of a semi-circular PVC backplane (diameter = 30 cm, length = 60 cm: Figure 8.6) and PVC shields at both ends. Both half backplanes are covered, waterproof, with a $50\mu\text{m}$ thick ABS copolymer sheet that is glued on a frame that can be mounted on the backplanes (see Figure 8.5). Twelve antenna elements are mounted on the PVC backplanes in a 2x6 arrangement¹⁴⁸, i.e. two rings (distance = 8 cm, ring-radius = 30 cm: see Figure 8.6) of six equally spaced patch antennas. We defined the origin of the applicator between the rings so the antennas in these rings are located at $z = -4$ cm and $z = 4$ cm. The water in the prototype was circulated and temperature controlled by two E4850 refrigerated recirculators (Bio-Rad, Microscience Division).

Every patch antenna¹⁴⁵ consists of a, resonant, 2mm-thick brass patch (width = 12 mm, length = 25 mm) that is asymmetrically (the distance from the rod to the side of the patch is 0.5 mm) mounted on the extending conducting rod of a C-female receptacle connector. The conducting backplane required for the patch antenna design is formed by soft copper tape (thickness: $35\mu\text{m} + 25\mu\text{m}$ adhesive) that covers the inner side of both PVC backplanes (see Figure 8.4).

Two PVC semi-cylinders (muscle cylinder diameter = 11.6 cm, PVC thickness = 1.5 mm)[¶] filled with muscle equivalent material, representing the neck of a patient, are positioned at the center of the prototype. The muscle-equivalent material was created using a recipe described by Ito *et al.*¹⁰⁶ and had properties in accordance with Gabriel *et al.*⁷⁴ (see Table 8.1).

8.2.3 EM modelling

We predicted the SAR distributions in the prototype applicator using SEMCAD¹⁶⁷. SEMCAD has a FDTD kernel that can be used for dosimetric simulations. It includes a solid

[¶]The dimensions of the phantom approximately equal an average neck¹⁴⁴

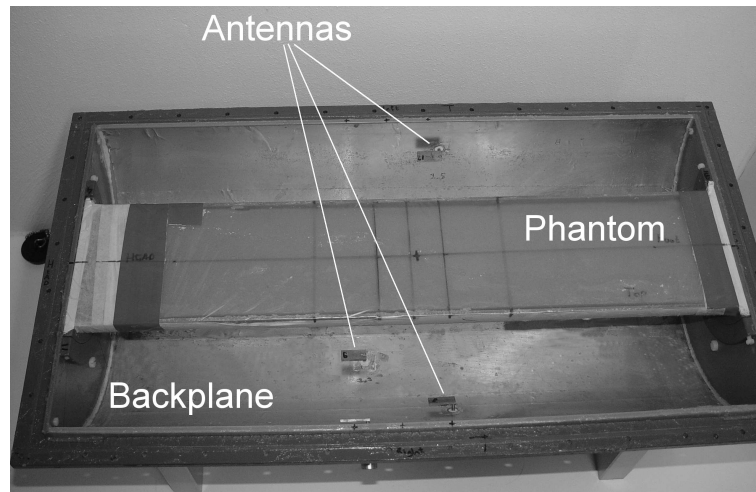


Figure 8.4: Picture of the bottom half of the prototype with the sheet and its frame excluded. Visible are the copper tape that covers the backplane, one half of the muscle phantom and multiple patch antennas

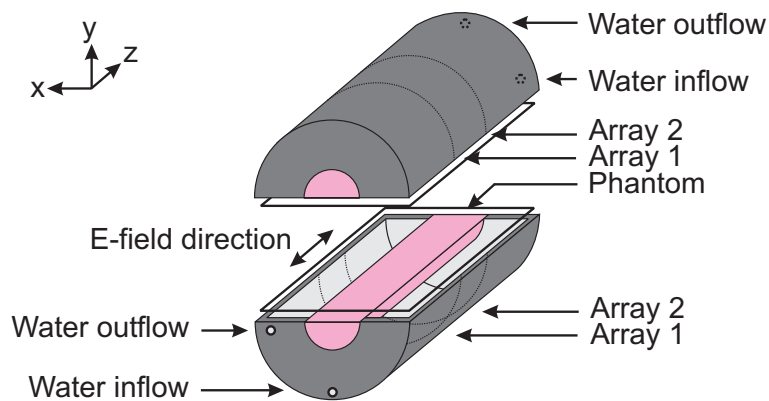


Figure 8.5: Exploded view of the prototype that is constructed in two parts for measurements (T-probes, E-field sheet, IR pictures). Visible are the phantom semi-cylinders (pink/light grey), the two frames spanning the sheet, the PVC backplanes (dark grey) and the copper tape on the inside of the backplanes (light grey).

modeling kernel in which we created a full 3-D model using the exact dimensions of the applicator prototype and muscle phantom. The sheets between the semi-cylinders could be neglected for calculations since they were very thin. Further, instead of modeling the complete connector and the transmission line, we used the commonly accepted approach to apply a voltage source at the gap between the conducting backplane and the rod of the patch antenna¹⁵⁹, which provides accurate field distributions³⁰. This solid model was converted automatically into a grid implementation with maximum gridsteps of $\lambda/15$ and

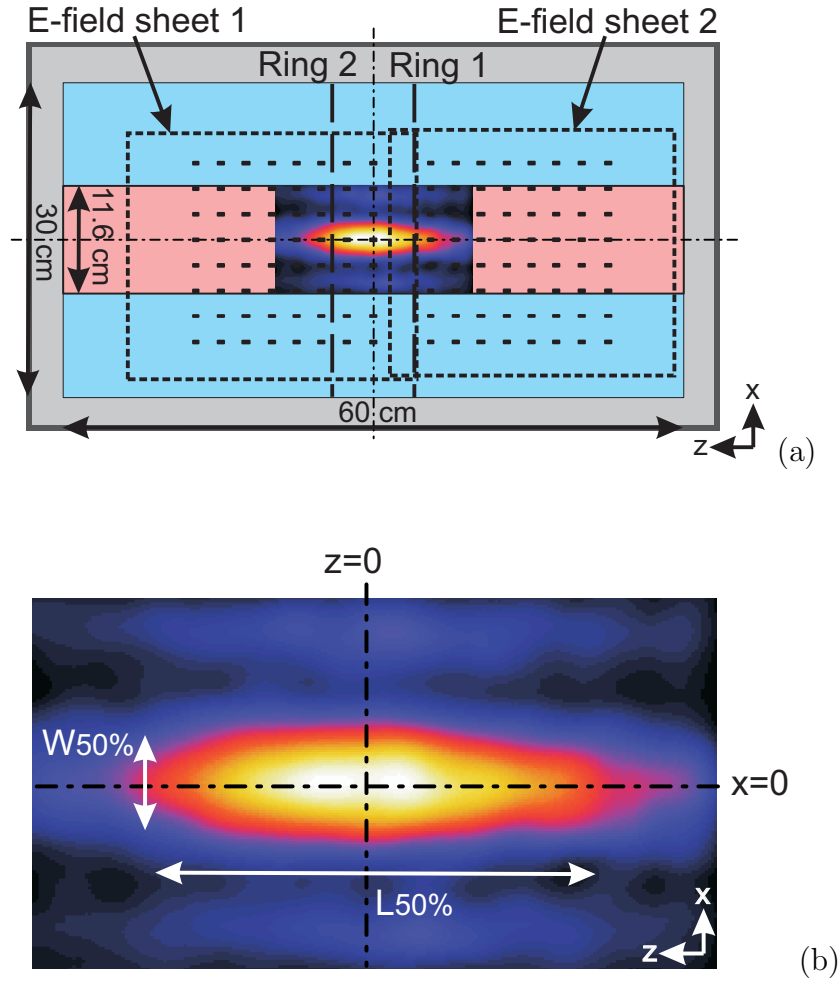


Figure 8.6: Cross-section through the prototype at $y = 0$ cm with a SAR distribution obtained from two IR pictures (before and after heating) for central settings (a) and a zoomed version of this SAR distribution (b). In (a), the location of the Schottky diodes (E-field sheet 1 and 2) is indicated by the black rectangles and the boundaries of the sheets by the dotted lines. Further, the location of the antenna rings and the main dimensions of prototype and phantom are indicated. T-probe measurements are taken at locations on the lines indicated by “ $x=0$ ” and “ $z=0$ ”. In (b) the color scale is from black (0%) to white (100%) and the length ($L_{50\%}$) and width ($W_{50\%}$) of the focus, i.e. the 50% iso-SAR contour, are indicated.

grid refinements at the locations of the antennas ($\lambda/250 < \Delta < \lambda/80$), i.e. a total of ~ 5 million cells. The grid refinements at the antennas were required to accurately model the (important) small dimensions of the antenna and the non-orthogonal placement in the grid, at the location of the feeding rod. Table 8.1 lists the properties of all the materials used in the simulation. Properties of demineralized water (salinity = 0.04 g/l, $T = 25^\circ\text{C}$) were found in a publication of Stogryn¹⁷³. We exited the voltage sources at all gaps at

Table 8.1: Properties of the materials at 433 MHz

Material	ρ (kg/m ³)	ϵ_r (-)	σ_{eff} (S/m)
Muscle phantom	900	56	0.8
PVC	1350	2.2	0.004
Demineralized water	1000	78	0.04

433 MHz and steady state was obtained after 10 periods (1% variation).

8.2.4 Measurements

Three SAR pattern measurement methods were used because they all have their own features: their major strengths are either accuracy (fibreoptic thermometry), resolution (IR thermography) or speed (E-field Schottky diode sheet). These measurement methods and their results were compared to establish the optimum method for quality assurance. Waterbolus temperatures were chosen such that mean temperatures in the prototype were around 22°C, at which the phantom properties are reported, i.e. the waterbolus temperatures was 18-19°C for the power-pulse measurements (T-probes and IR) and 22°C for the E-field measurements. Figure 8.6 shows a cross-section through the applicator at $y=0$ cm and a zoomed version of the SAR distribution obtained by taking IR pictures before and after heating.

Fibreoptic thermometry

Temperatures were measured with 24 Takaoka FTP1 standard sensor probes (accuracy = 0.1°C, precision = 0.1°C), which are read with a Takaoka FT1310 fibre thermometer (Takaoka Electric MFG Co. Ltd., Japan) with a refresh rate of 3s. These non-metallic probes were positioned at the main axes between both halves of the prototype. The local SAR was measured using the power pulse method: the change of temperature (3-10°C) in a phantom is measured while applying a high power (300-600W) for a short time (90-300s) at the antennas of the applicator¹⁶⁰ (see Figure 8.8). To reduce influences of heat conductivity a short heating time is required, therefore we used a high power to obtain accurately measurable temperature changes. The local SAR is calculated from the temperature rise via:

$$\text{SAR}(x, y = 0, z) = c \cdot \frac{\Delta T(x, y = 0, z)}{\Delta t}, \quad (8.1)$$

where c is the specific heat capacity of the muscle phantom material (3.63 kJ kg⁻¹ K⁻¹), ΔT is the local temperature rise [K] and Δt is the corresponding heating time [s]. We assumed no electric field disturbing effect of the fibre probes.

IR thermography

We used IR thermography to visualize the temperature (rise) pattern at a high resolution (320x236 pixels). Pixel size was determined by taking an IR picture of a hot object with known dimensions: for our set-up the dimensions were 0.5x0.5 mm². After application of power, the top half was removed and IR pictures were taken using a TVS-600 infrared camera (Nippon Avionics Co. Ltd., Japan) that was mounted on a solid framework. From the IR picture before and after heating we calculated the SAR pattern using equation 8.1. The inevitable time between end of heating and first IR picture was kept as short as possible (typically $\sim 10s$) in an attempt to reduce influences of heat conduction.

E-field Schottky-diode sheet

For fast measurements, which also enables studying the prototypes dynamic behavior, we performed SAR measurements also with the E-field Schottky diode sheet, that is described in Kaatee *et al.*¹¹³ and Van Rhoon *et al.*¹⁸⁹. Hereto, two diode sheets were positioned between both halves of the prototype (Figure 8.6). To avoid a decrease in sensitivity caused by overlapping sheets at the location of the diodes¹⁹⁰, we used a distance between both sheets such that one row of measurement points was absent. SAR values can be calculated from the amplitude of the measured E-field values, using the effective conductivity (σ_{eff}) and mass-density (ρ), according to:

$$SAR(x, y = 0, z) = \sigma_{eff} \cdot \frac{|E(x, y = 0, z)|^2}{2\rho}. \quad (8.2)$$

The E-field sheet directly measures real-time the axial (z) component of the E-field. Also, variations in dielectric properties of the phantom materials are much lower because measurements can be performed at low power (120W). Further, no manipulation of the set-up is required for multiple measurements, i.e. all distributions can be measured using one single disposition of the experimental set-up. Without calibration the accuracy of the sheets is 6%¹⁸⁹, however when airgaps are present close to the diodes this accuracy is reduced due to lower sensitivity. A main disadvantage of the current design of the sheet is its poor spatial resolution for measurements at 433 MHz, i.e. the distance between two diodes is 2.5 cm ($\sim \lambda/4$).

Measurement procedures and phase settings

As a first step we measured impedance characteristics of the antennas using an 8751A network analyzer (Agilent Technologies, USA) to verify that they were sufficiently resonant. As a side step we also assessed the amount of cross-coupling using the network analyzer. Fibreoptic and IR measurements were conducted simultaneously. Hereto we positioned an IR camera above the prototype and positioned the probes between both halves of the prototype. High power was applied and simultaneously we measured temperatures with the fibre probes (see Figure 8.8). After the required maximum temperature change

was obtained, we opened the applicator and took IR pictures. We used a cooling time of typically 2 hours between subsequent measurements to obtain a homogeneous thermal distribution. E-field sheet measurements were performed separately at low power to avoid variations in dielectric properties of the phantom due to temperature differences. To check for measurement errors, all measurements were conducted multiple times in a time period of a year and the muscle phantom was newly constructed two times.

To obtain a central focus for each antenna (i) on each ring (j) we used central power (P) and phase (φ) settings ($P_{j,i} = 25\text{W}$ and $\varphi_{j,i} = 0$). Subsequently, we investigated the possibilities of SAR steering in radial and axial direction by using a phase-steering method in analogy to the method that is used in the BSD2000 Sigma-60 system¹⁶¹⁸⁰. For each antenna, we analytically calculated the required phase delays ($\varphi_{i,j}$), using the difference in wave velocity in muscle and water, such that maximum interference occurs at the desired Target Center Point (TCP). For this analytical model we assumed a muscle cylinder (radius is 5.8 cm) and two circumferential arrays (radius = 14.15 cm) of six point sources at $z = -4$ cm and $z = +4$ cm and we neglected the PVC phantom-shell.

8.3 Results

8.3.1 Reflection and cross-coupling

After one year, reflection coefficients had increased due to degradation (oxidation) of the set-up (mainly the copper tape of the groundplane). Figure 8.7 shows the typical reflection coefficients of all antennas in the array at 23°C and 25°C halfway during our measurement period. This figure clearly shows that the reflection coefficient is influenced by the temperature of the water in the waterbolus. For both temperatures these reflection coefficients are all beneath -10dB ($\sim 6\%$ reflection on average) so efficiency of the antennas was sufficient for the purposes of our measurements. For the clinical applicator, however, we constructed a redesign that has somewhat improved reflection characteristics¹⁴⁵. For this qualitative analysis we neglected the influences of the variations in efficiency ($\sim 6\%$) for the antennas of the prototype. We further found low cross-coupling between the antennas: maximum -22dB (0.6%) and on average -27dB (0.2%). The lowest values were obtained for neighboring antennas while the highest values were found for antenna pairs with around one quadrant inner antenna spacing. This effect is related to the radiation pattern of the antennas combined with the distance through a lossy medium.

8.3.2 SAR tracks

Figure 8.8 visualizes an example of the measured temperatures with the fibre probes and the corresponding measured powers and phases. It shows the length of the power pulse and the corresponding temperature rise from which we calculated the local SAR values. In this example case, the upper halve of the prototype was removed approximately 160s after Power On and 10s later the IR picture was taken. The corrections by the control

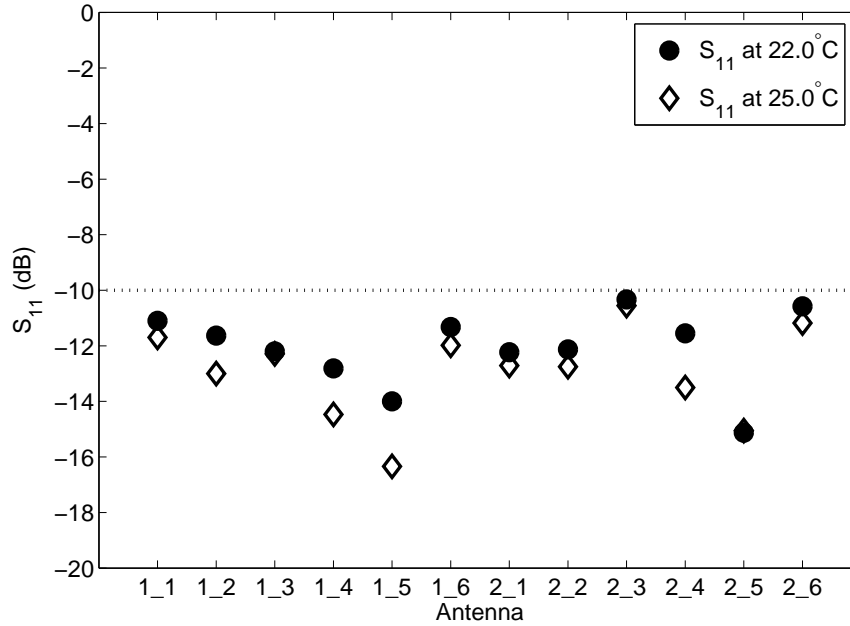


Figure 8.7: Reflection coefficients at 433.92 MHz for each antenna of both arrays, e.g. 1_2 is the second antenna of the first antenna ring.

loop that are required to keep the power at the set value (25W) are clearly visible in the power curves. At the start of the power pulse, the phases were influenced somewhat by the increase in power level, but these were automatically adjusted. The figure also shows that two amplifiers were leaking some power after power-off but this influence was relatively small (power-on: 300W vs power-off: ~ 5 W leakage). We found an almost perfect correlation between the measured temperatures and a linear fit, for all spatial locations ($r^2 = 1.0$), so we concluded that the influence of heat conduction on the SAR measurements was negligible.

Comparing measurements and simulation

Figure 8.9 shows SAR values as function of the x -coordinate for TCP-based x -steering, i.e. for $x = -30$ mm, $x = 0$ mm and $x = +30$ mm. Similarly, Figure 8.10 shows SAR values as function of the z -coordinate for TCP-based z -steering, i.e. for $z = -50$ mm, $z = -25$ mm and $z = 0$ mm. For all IR thermography tracks we averaged over 10 pixels (one pixel was 0.7×0.7 mm²) to reduce noise. The tracks were normalized to their own maximum (IR thermography) or their own maximum of a spline-fit through the measurement points (T-probes and E-field sheet measurements). For central steering this maximum was typically around 0.6 W/kg (normalized to 1W total input power). The desired focus point (TCP) is always indicated with the dashed line.

All measurements and predictions show that a central focus is obtained. As shown by these

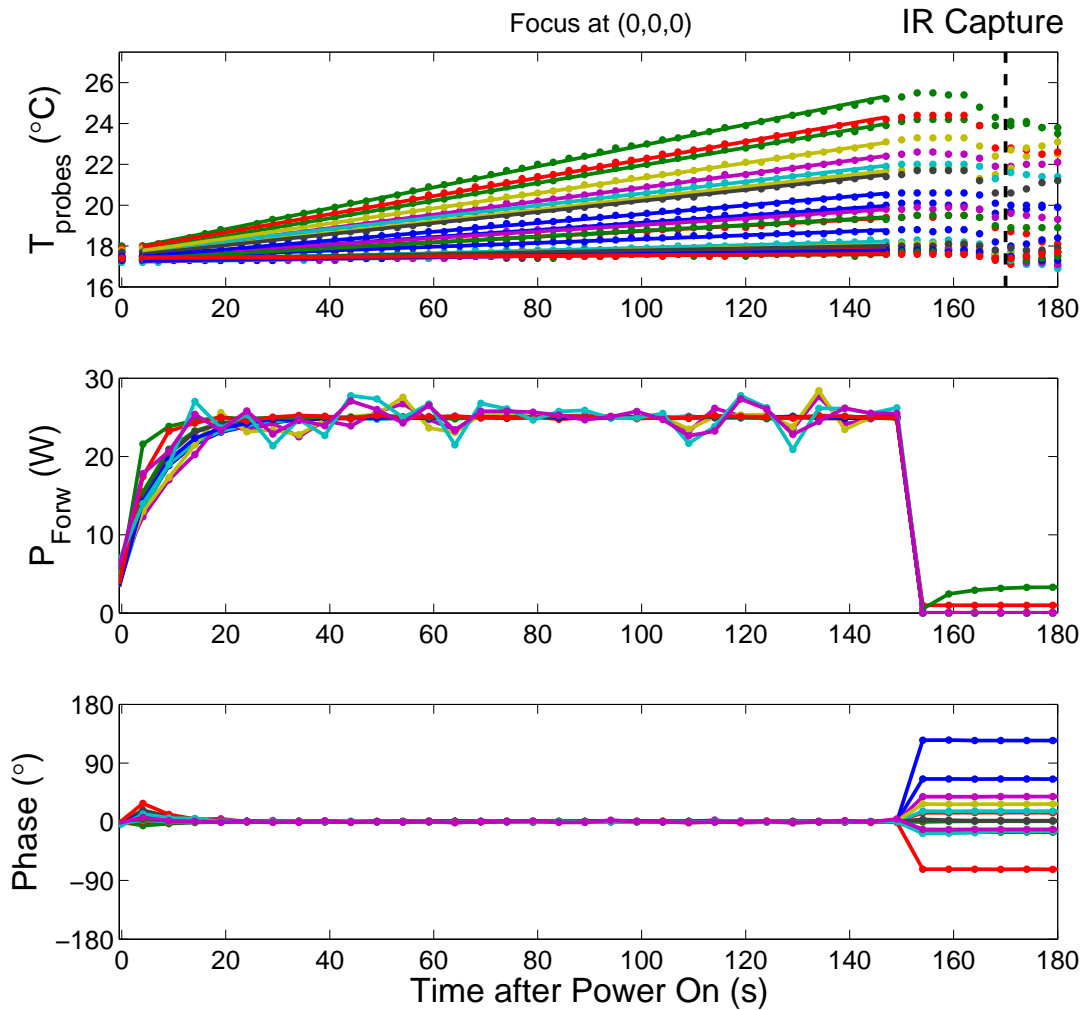


Figure 8.8: Temperature (T_{probes}) values and corresponding powers (P_{Forw}) and phases as function of time during an example powerpulse measurement. For the fibre probe temperature measurements (visualized in dots) we created linear fits (solid lines) and calculated the local SAR values from the slopes. IR pictures were captured before Power On and after Power Off (shown in the figure).

figures, this focus can be changed in the radial (x) and axial (z) directions. Comparing the results of the three measurement methods, we found a good qualitative agreement. Comparison of the simulations to these measurements reveals good agreement at central positions but discrepancies for more radial positions close to the PVC phantom border. The reason for this difference may lie in: 1) wrong dielectric properties of muscle phantom (lower conductivity) or 2) air-gaps at the connection between both halves of the set-up. In the axial direction, there is an unexpected small asymmetry in the FDTD results for

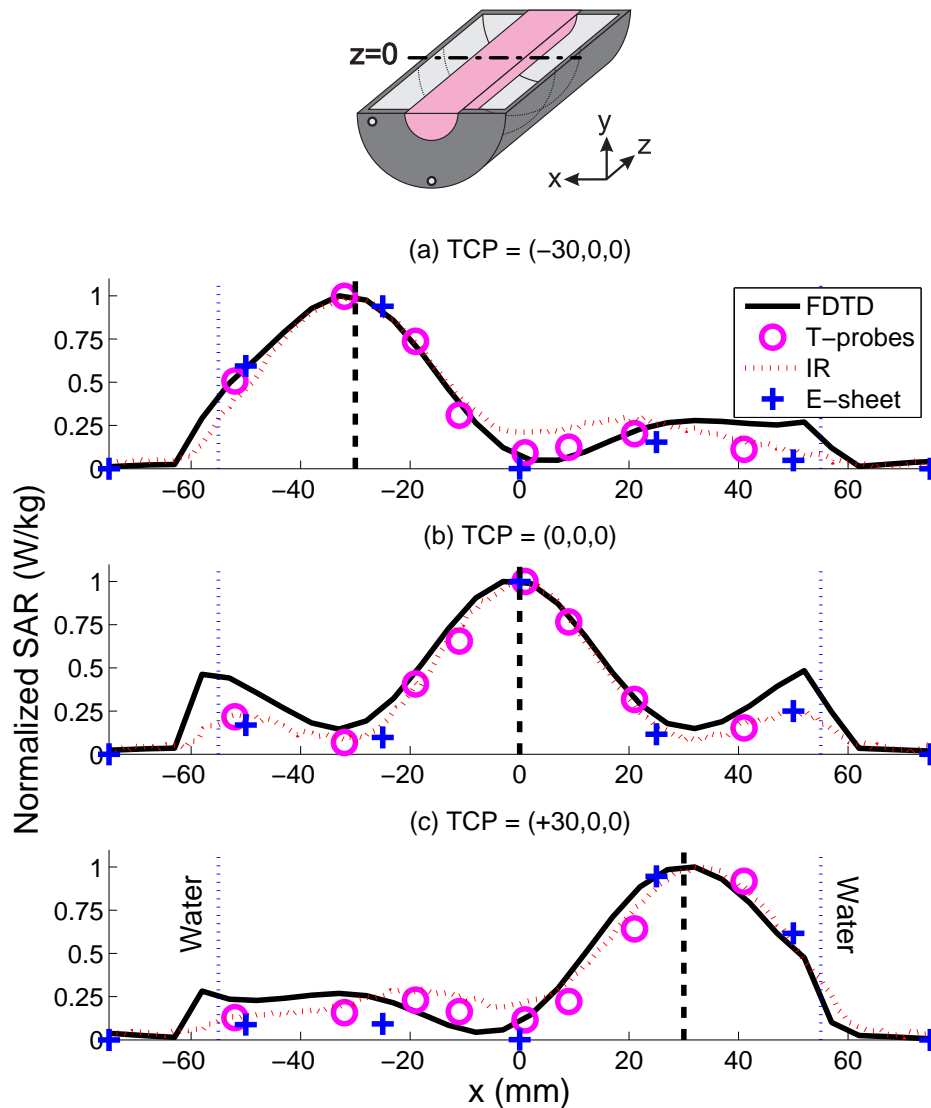


Figure 8.9: Simulated (FDTD) and measured (T-probes, IR and E-field sheet) SAR values at $y = 0$ mm and $z = 0$ mm for steering in the x -direction. The measurement values of all tracks are normalized to their own respective maximum value.

central settings (Figure 7a), this is probably caused by the asymmetry in the feeding of the antennas¹⁴⁵.

In radial direction, where the SAR patterns are the steepest, the IR thermography curves show a somewhat flattened profile compared to the FDTD tracks. This flattening is caused by thermal conduction during opening of the two halves after power application. After

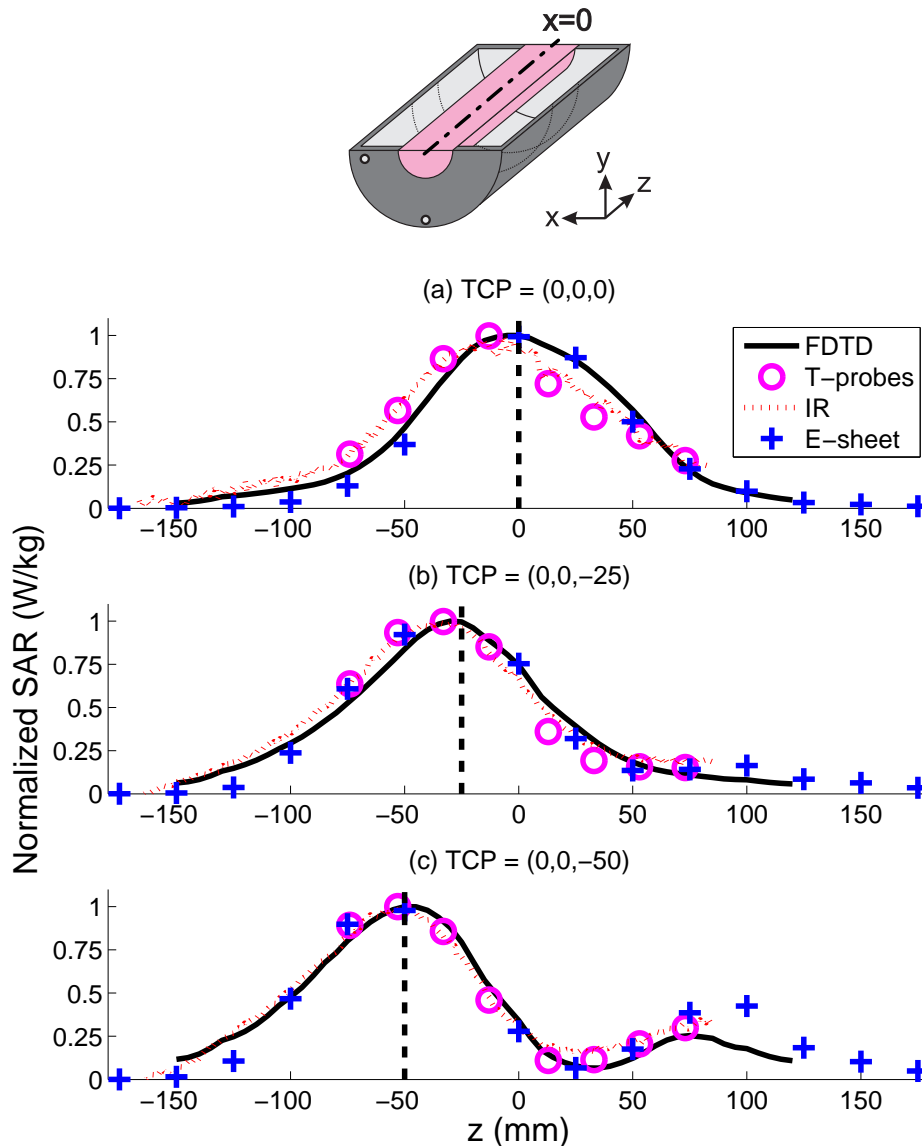


Figure 8.10: Simulated (FDTD) and measured (T-probes, IR and E-field sheet) SAR values at $x = 0$ mm and $y = 0$ mm for steering in the z -direction. The measurement values of all tracks are normalized to their own respective maximum value.

normalization this results in relatively higher values in the valleys of the curves because the maximum value is reduced. In axial direction this effect is less prominent because SAR curves are less steep. Further, the SAR values are decreased by the circulated water of the waterbolus of a stable temperature.

Table 8.2: SAR steering (TCP setting (mm) and location of SAR_{max} (mm)) and corresponding focus-size (length $L_{50\%}$ (mm) and width $W_{50\%}$ (mm) of the 50% iso-SAR contour) parameters for the simulated (FDTD) and measured (IR thermography) tracks.

TCP setting	Method	SAR_{max}	$L_{50\%}$	$W_{50\%}$
Central	FDTD	(0,-,-1)	103	35
(0,0,0)	IR	(0,-,-5)	112 (+9%)	34 (-3%)
X-steering	FDTD	(31,-,0)	96	39
(+30,0,0)	IR	(32,-,0)	103 (+7%)	37 (-5%)
Z-steering	FDTD	(0,-,-50)	82	37
(0,0,-50)	IR	(0,-,-51)	87 (+6%)	38 (+3%)

Determination of the focus-size

Table 8.2 summarizes the most important parameters from Figure 8.9 and Figure 8.10. This table shows the SAR steering and corresponding focus-size parameters for the simulated (FDTD) and measured (IR thermography) tracks. The simulated SAR distribution for central settings and the focus-size parameters ($L_{50\%}$, $W_{50\%}$) are visualized in Figure 8.6. IR measurements were used for verification of the predicted focus-size due to its superior resolution and because its values correlated well with the T-probe measurements, which we assume to be more accurate. Table 8.2 shows that, using the TCP based phases, the obtained SAR focus can be steered towards the desired location with a reasonable accuracy, i.e. ~ 5 mm. Further, it indicates that the corresponding focus-lengths ($L_{50\%}$) are in the range of 87-112 mm and the focus-widths $W_{50\%}$ are around 35 mm.

8.3.3 Dynamic SAR steering

We used measurements with the E-field sheet to investigate the dynamic steering possibilities of the focus since no cooling down period is required for this method. We measured the location of maximum SAR and correlated this position to the TCP settings, which is visualized in Figure 8.11 (a,b). In this figure we show the maximum SAR location for x and z -steering along several tracks. These curves show a staircase shape due to the spatial resolution of the E-field sheet and because the use of a spline-fit to find the location of the maximum was omitted. We indicated the location of the E-field sheet diodes by the horizontal dotted lines and the identity curve, indicating a perfect match, by the vertical dotted line. Both figures show a linear relation and a high correlation between TCP location and location of maximum SAR, in both radial (x , and y due to symmetry) and axial (z) direction. This means that the focus can be accurately steered by using the TCP method to the desired location in the neck-equivalent muscle phantom. We further found that steering in the radial plane is possible in the entire phantom. In the z -direction,

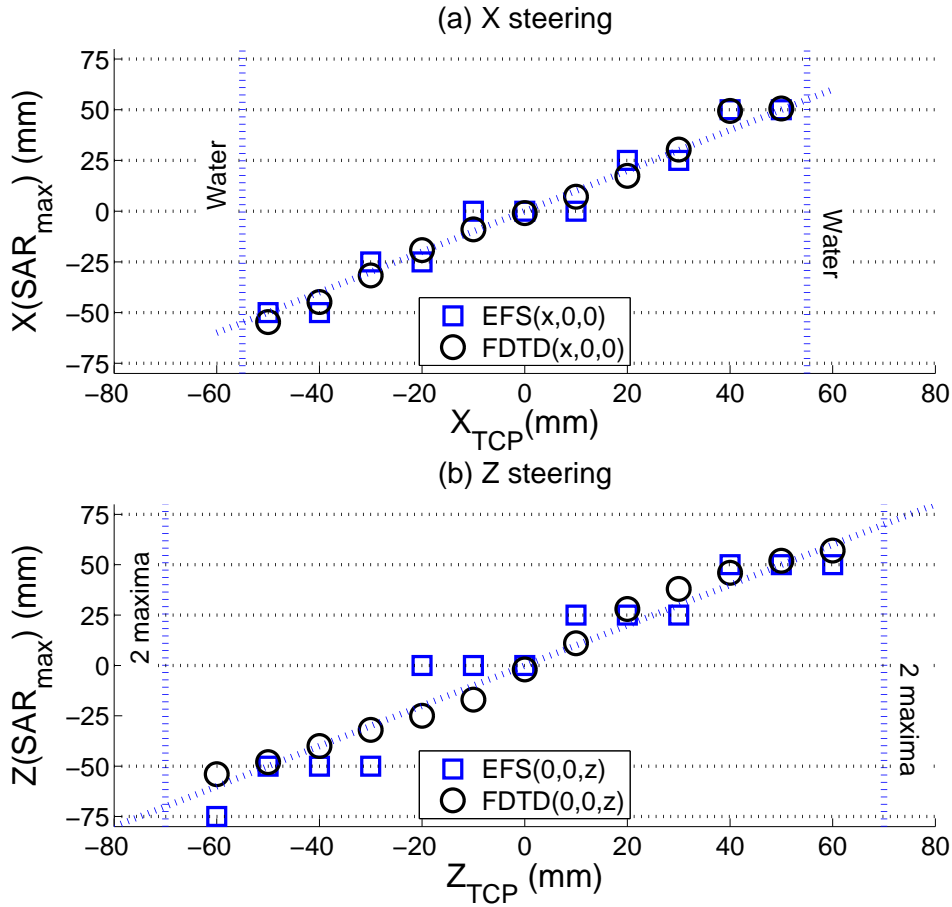


Figure 8.11: Measured maximum SAR point as function of TCP for SAR-steering in radial (a) and axial (b) directions. Locations of E-field sheet measurement points are indicated by the horizontal dotted lines and the unity curve by the diagonal dotted line. At $z=-25$ mm no E-fields were measured because of the design of the E-field sheets.

the focus can be steered up to 60 mm from the center. From this location a double focus distribution is obtained, i.e. the secondary focus becomes more than 50% of the maximum.

8.4 Discussion

8.4.1 Evaluation of the materials and methods

For this work we constructed a split-phantom set-up consisting of two semi-cylinders that are closed with polymer sheets. In this way the set-up provided the versatility that enabled measurements between two parts with several measurement devices and IR measurements by opening the set-up. The drawback of our approach is the possibility of air-gaps between

the sheets which, especially for these high frequencies, can have a large effect on the local SAR and on the measurement accuracy. We have tried to decrease these influences by inserting some water between the sheets and some additional water pressure while the halves of the prototype are clamped together.

For the measurements we have used a muscle phantom recipe of Ito *et al.*¹⁰⁶. Amounts of ingredients were used for muscle-equivalent properties ($\epsilon_r = 56$, $\sigma_{eff} = 0.8$ S/m) at 22°C. These properties, however, vary with temperature and are very sensitive to small variations in salinity. Due to the required interference of multiple sources, these SAR values depend upon the conductivity in a non-linear fashion. By carrying out simulations with different conductivity values, we found that the SAR tracks in the x -direction are strongly dependent on conductivity, i.e. the lateral normalized SAR values are decreased by 30% for a 20% decrease in conductivity. Therefore, in future measurements we expect to improve the predictability of the measurements by measuring the properties of the phantom before each measurement.

8.4.2 Evaluation of the results

Electromagnetic models are used more and more for HT treatment planning and there is a growing use of EM models to perform parameters studies for the optimization of HT applicators^{118,135,169}. While the accuracy of EM modelling has increased dramatically and high resolution simulations have become possible, up to now this has not led to higher standards concerning model validations. Such a validation is a crucial step to assess dosimetry accuracy and will reduce the need for verification measurements for new applicators. For a superficial antenna, recently, a first attempt of such a quantitative validation by high resolution 3D measurements was presented by De Bruijne *et al.*³⁰. This validation, however, was for a single antenna set-up and should be confirmed for the SAR distributions with higher gradients that are typically obtained with array set-ups. For high accuracy SAR dosimetry validations of array set-ups, accurately on-site measured dielectric properties of all (phantom) materials are required. Further, an accurate measurement device is required, which in general is very expensive.

For our approach we used the availability of more accurate modelling for optimizing the entire HT applicator. To our knowledge, we were the first to use EM modelling to design an HT applicator from scratch by detailed parameter studies at frequencies above 400 MHz. In a previous publication we have explained our work dedicated to the design of an optimized antenna positioning. Further, we used EM modelling to fully optimize the reflection characteristics of a single element of the antenna array. In the present paper we have experimentally verified the feasibility of focussed heating in the neck, which has been predicted earlier^{143,148}, and as such to validate our approach. We further assessed the dimensions of the focus and verified the possibilities of dynamic steering. By comparing measurements to simulation we performed a qualitative verification of the predicted SAR patterns in a muscle phantom.

In this study we verified that a central focus can be obtained with two rings of six antennas each. For central settings, we determined the width of this focus as 34 mm (IR) and 35

mm (FDTD) and the length as 112 mm (IR) and 103 mm (FDTD). This difference might be due to thermal conduction, which results in an overestimation of the EFS by IR thermography. In the radial direction this size is usually $\lambda/3$ ^{144,190}, which means ~ 31 mm in a muscle phantom, and correlates well with the values in this study. In axial direction this focus is determined by a combined effect of the distance between the antenna rings, the radius of the antenna rings, and the operating frequency¹⁴⁸, i.e. the wavelength in muscle. The obtained focus can be steered in radial directions towards every point in the muscle phantom. In the axial direction $(-z, z)$, extreme focus center point location is a 60 mm off-center position.

For verification of the SAR profiles we used the split-phantom technique in combination with 1) glass-fibre thermometer probe measurements, 2) IR thermography using a high resolution IR camera, and 3) measurements using our Schottky diode E-field sheet. Local SAR values are determined for the first two (fibre-probes, IR) by using the power-pulse technique⁸², which means that high power is required. The latter (E-field) measurements were carried out at low power. The fibre-probe measurements have the advantage of a high accuracy and they provide the possibility to monitor temperatures during heating. Further, they are non-metallic and very thin thus field disturbances are negligible. The disadvantage of this method is the required cooling time after measurement (1-2 hours) due to the high temperature gradients required. Further, multiple (multi-sensor) probes are required for a high resolution and positioning multiple probes in the split-phantom is cumbersome. IR thermography measurements with the most recent IR cameras have a high resolution, which enables to investigate, besides the size of the focus, also the shape of the focus. IR measurements share the disadvantage of long cooling times. Further, for these measurements it is required to open up the set-up for taking an IR picture, i.e. measurements were taken typically 10s after power off. According to Samaras *et al.*¹⁶⁰, for effective field size (EFS) measurements, this is sufficiently short for an accurate measurement. Compared to flat-phantom EFS measurements, the distributions obtained in this publication show much higher SAR gradients and therefore heat conduction might have somewhat more influence. By comparing the thermography results to the fibre probe measurement we could show that the influence of heat conduction remains low. By using the Schottky-diode E-field sheet^{113,189} we performed E-field measurements that can be performed at low power thus dynamic SAR steering with the prototype can be assessed. A major drawback of this equipment is its low resolution because it was designed for superficial hyperthermia applicator assessments in flat phantoms where the fields are more gradual. Further, in this split-phantom set-up, air-gaps may be present that considerably decrease the sensitivity of the diodes. The measured SAR values close to water from both power-pulse based methods further might have been hampered by the active water-cooling of the sides of the phantom. By the resemblance between the SAR derived from the E-field and temperature measurements, we conclude that this influence is low.

8.4.3 Quality assurance

Currently, no specific QA guidelines have been defined for our application or for newly developed applicators. Within the framework of ESHO, guidelines for ESHO protocols have been defined 1) for treatment of superficial tumours⁸², i.e. locally advanced breast carcinoma, advanced neck nodes, malignant melanoma, and 2) for regional hyperthermia in the pelvic area by radiofrequency equipment¹²². In terms of (regular) assessment of the SAR pattern of an applicator, clearly different approaches are suggested. For superficial QA guidelines and assessment of applicator performance, the effective field size (EFS) and penetration depth (PD) are defined, which “should be determined by measuring the changes in temperature resulting from a brief pulse of high power”⁸². In these guidelines, the necessity for an additional characterization of the SAR pattern corresponding to a multi-element array of applicators is recognized. Further, it is mentioned that if “non-perturbing E-field probes, thermographic imaging or liquid-crystal sheet imaging” are used, they should be corroborated by measurements obtained using the power pulse technique. A requirement for using this technique is that 60s after power-on the EFS and PD should be determined. However, by finding perfect linear temperature curves, we showed that longer heating periods can be used. In the guidelines for regional hyperthermia¹²², it is required for SAR distribution characterization of equipment to perform system performance regularly using the LED matrix/lamp phantom using different phase/amplitude settings, different phantom positions and different bolus configurations. The E-field Schottky-diode sheet system is compliant to all requirements but a higher resolution is required so the focus size and shape can be determined as well, i.e. $\sim \lambda/10$ instead of $\sim \lambda/4$ (at 433 MHz). Further, to obtain a more homogeneous temperature distribution, an improvement would be to use a liquid phantom material. The required new E-field sheet system, however, requires additional research since it must be designed specifically.

The applicator performance is related to the hardware performance. In this paper, we designed and characterized a 12-channel 433.92 MHz amplifier system. We showed that the required measurement accuracy for the power ($\pm 5\%$) is valid for at least 20 days after calibration and for the phase ($\pm 2^\circ$) it is at least two months. Recent improvements on malfunctioning 10 mW RF amplifiers on the DDS printed circuit-boards has led to more robust and stable power measurements over time. The system is being used for daily-routine HT treatments of both superficial and head-and-neck tumours, and it is calibrated at a one month interval.

8.5 Conclusions

In this paper we analysed the ability of using a phased array hyperthermia applicator for focussed heating in the head and neck region. Firstly, we conclude that the early design of the patch antenna, in a well controlled water environment, provides an average efficiency of 94%, which is highly sufficient for our investigations. Secondly, we measured low cross-

coupling between antennas in the array (maximum -22dB). Thirdly, we conclude that, using the analysed set-up of two rings of six antennas, focussed heating in the head and neck is feasible. By IR thermography we measured a central 50% iso-SAR focus of 112 mm in axial and 34 mm in radial direction in a muscle phantom. This radial dimension is sufficiently small to allow targeted heating of advanced tumours and by de-focussing also good SAR coverage of larger tumours should be possible. The axial length of this focus is somewhat large for tumour-specific heating. However, this can result in some blood pre-heating because vessels are mainly oriented in this direction. The focus can be steered in axial (cranial-caudal) direction to maximum 6 cm from the center in the phantom. Combined with the focus size of 10 cm in axial direction, this indicates that 50% SAR coverage may be possible up to 11 cm from a central location. The actual extent of heating in a patient remains to be determined.

We found little differences between the predictions of the SAR distribution by the three investigated measurement methods. Therefore, as best system for regular quality assurance we suggest the Schottky-diode E-field sheet system. This device enables quick measurements and better control of the temperatures resulting in more predictable di-electric properties of the phantom materials. However, a modified design of the Schottky-diode E-field sheet system is required that provides a higher resolution.

9. 7T MRI

Exploring 7T MRI
for 3D validation of RF models

This chapter is partly based on:

RF Verhaart, JJ Bluemink, JF Bakker, P Togni, AJ Raaijmakers, GC van Rhoon, CAT van den Berg and MM Paulides. "Validation of the predicted B_{1+} of a radiofrequency hyperthermia applicator using a 7T MR scanner". 29th Annual Scientific Meeting of the European Society for Magnetic Resonance in Medicine and Biology, Lisbon, Portugal, 2012.

Abstract

Purpose: At the Erasmus Medical Center in Rotterdam, the HYPERCollar, i.e. an electromagnetic applicator for heating tumours in the head and neck region has been developed and clinically integrated. This phased-array applicator incorporates twelve antennas excited by independently controlled 434 MHz signals. Treatment planning simulations are applied pre-treatment and during treatment to maximize thermal dose delivery. Magnetic Resonance Imaging (MRI) is of great interest since it provides high resolution 3D image data of tissue dielectric and thermal properties, and non-invasive thermometry. MR scanners provide the option of 3D validations of hyperthermia planning tools by measuring the propagated electromagnetic fields. In this study, we explored the feasibility of validation the electromagnetic modelling of the HYPERCollar by using B_1^+ measurements of the MR scanner. The second objective was to investigate if the HYPERCollar can be used in conjunction to the MR imaging. **Methods and Results:** We redesigned the patch dimensions for 298 MHz and integrated the laboratory prototype applicator, i.e. the LABproto, into a 7T MR scanner. Simulations and measurements show that the reflection coefficient (S_{11}) of the redesigned patch antenna is lower than 14dB (<4%) and the cross coupling (S_{21}) is lower than 15.3dB (<3%). We compared the predicted B_1^+ fields to those measured by the MR scanner. A good qualitative agreement was found in a muscle-equivalent phantom, i.e. the acceptance criteria of the gamma evaluation are met for a dose difference of 6% at a distance to agreement of 2 mm. However, we found large differences in the absolute values between the model predictions and MR measurements likely caused by an inaccurate estimation of the applied powers. In a theoretical study, we redesigned the patch antennas of the HYPERCollar for 298 MHz such that it can be used as both a heating device and as a transmit/receive imaging “coil” for the 7T MR scanner. Electromagnetic simulations show that this applicator, i.e. the 7Tcollar provides both intense B_1^+ maps and focussed SAR distributions for larynx and nasopharynx tumours. **Conclusions:** B_1^+ MR interferometry is a promising technique to validate the predictions of hyperthermia treatment planning tools. However, more work is required to monitor the applied RF signals during the experiment to enable accurate and absolute validations. Theoretical simulations showed that a phased array of patch antennas, i.e. the 7Tcollar can be used effectively to both image and heat tumours in the head and neck region.

9.1 Introduction

Hyperthermia, an increase of the temperature towards 40 to 44 °C, is a powerful modality to improve the clinical outcome of radiotherapy (RT) and chemotherapy. Several clinical Phase-III trials have demonstrated that addition of hyperthermia to radiotherapy results in improved clinical outcome. Good examples are: the long-term survival for advanced cervical cancer is doubled^{65,188} and also the local control rate is doubled for recurrent breast cancer in previously irradiated areas¹⁹⁴. Because the clinical outcome is related to the thermal dose^{66,108}, a controlled delivery of heat in the tumour is required.

Heat is often applied using electromagnetic radiation generated by either a single antenna or antenna arrays. To ensure treatment quality, the thermal dose delivery should preferably be verified by accurately measuring temperatures at a high spatial resolution³. In the clinic however, interstitial thermometry provides only sparse data. We therefore focus our efforts on enhancing treatment quality by improving the accuracy of the specific absorption rate (SAR) deposition.

At the Erasmus Medical Center in Rotterdam, a clinical electromagnetic applicator, i.e. the *HYPERcollar* (Figure 1.3c) has been developed for the treatment of tumours in the head and neck region^{6,146}. The SAR is controlled by characterizing the radiation patterns of our applicators^{31,54,146} and by using state-of-the-art hyperthermia planning tools¹⁸⁷. The predicted SAR distributions have been verified experimentally in a two-dimensional (2D) plane using a laboratory prototype hyperthermia applicator (*LABproto*)¹⁴⁷. The *HYPERcollar* is currently being used in clinical treatments¹⁴⁹.

Magnetic Resonance Imaging (MRI) is of great interest for hyperthermia applications since it provides high resolution three-dimensional (3D) image data of e.g. tissue dielectric properties, blood perfusion levels and non-invasive thermometry^{78,79}. MR scanners measure the strength of the transmitted electromagnetic fields, also referred to as the B_1^+ field. Van den Berg et al.¹⁸⁶ showed that MR B_1^+ imaging can be used to obtain quantitative information about the transmitted RF field inside phantoms and human anatomies for a 3T MR scanner, of which the Larmor frequency of 128MHz is within the range of indicated frequencies for regional hyperthermia. 7T (298 MHz) MR scanners are in range with superficial and head and neck hyperthermia applicators (434 MHz). Combining MR scanners and hyperthermia applicators that can work on the same frequency, i.e. an “hybrid” MR/HT applicator, has the great advantage that it might work with the existing RF amplifiers and electronics of the MR scanner. When other than Larmor frequencies are used for the heating part, special RF heating equipment, shielding and filtering of the different RF signals is required.

In this study, we explored if MR B_1^+ mapping at 7T can be used to validate electromagnetic modelling tools of deep local hyperthermia applicators. The second objective was to investigate if an hyperthermia phased-array applicator can be used simultaneously as an heating device and as an effective transmit and receive MR imaging device. Hereto, we redesigned the *LABproto*, used previously for 2D verification¹⁴⁷, and integrated this new

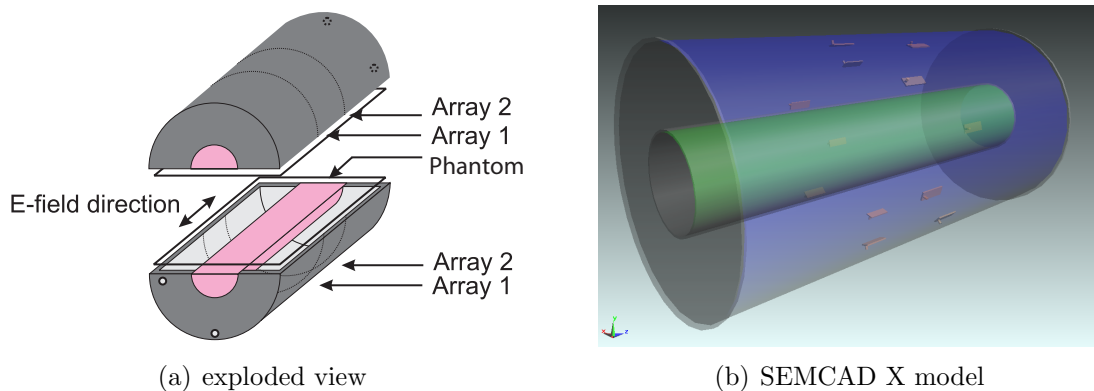


Figure 9.1: Exploded view (a) and SEMCAD X model (b) of the LAB*proto* applicator that consists of two phantom semi-cylinders filled with water and muscle-equivalent material and two rings with six patch antennas.

design (7T*proto*) into a 7T MR scanner*. The predicted B_1^+ maps of the phased-array antennas operating at a frequency of 298 MHz are compared to those measured by the MR scanner. In addition, we modified the HYPER*collar* such that it can be used in a 7T MR scanner. For this 7T*collar*, we investigated if adequate image quality and heating can be obtained, indicated by predicted B_1^+ maps and specific absorption rate (SAR) profiles.

9.2 Materials and methods

9.2.1 Redesign of the LAB*proto* and integration into a 7T MR scanner

We redesigned the LAB*proto*, used previously for 2D validation¹⁴⁹ (Figure 9.1), such that it can be used in the 7T MR scanner. Hereto, the dimensions of the original patch-antenna¹⁴⁵ are re-designed to 40.6×18.5 mm such that it is resonant at 298 MHz. We measured the antenna characteristics of all twelve antennas using a network analyser[†]. Figure 9.2 demonstrates that the reflection coefficient (S_{11}) was always lower than 14 dB (<4%) for both the simulations and measurements. The cross coupling (S_{21}) was always lower than 15.3 dB (<3%).

The ferromagnetic parts of the water filling connectors were removed to prevent safety issues and imaging artefacts. The Erasmus MC LAB*proto* was installed in the UMC Utrecht Philips Achieva 7T MR scanner (Figure 9.3). We used an in-house developed eight-channel transmit and receive (T/R) electronics box to interface the phased array applicator with the Philips system. Six amplifiers with a maximum power of 1 kW and a

*Philips Achieva 7T MR scanner, University Medical Center Utrecht

†Agilent 8751A, USA

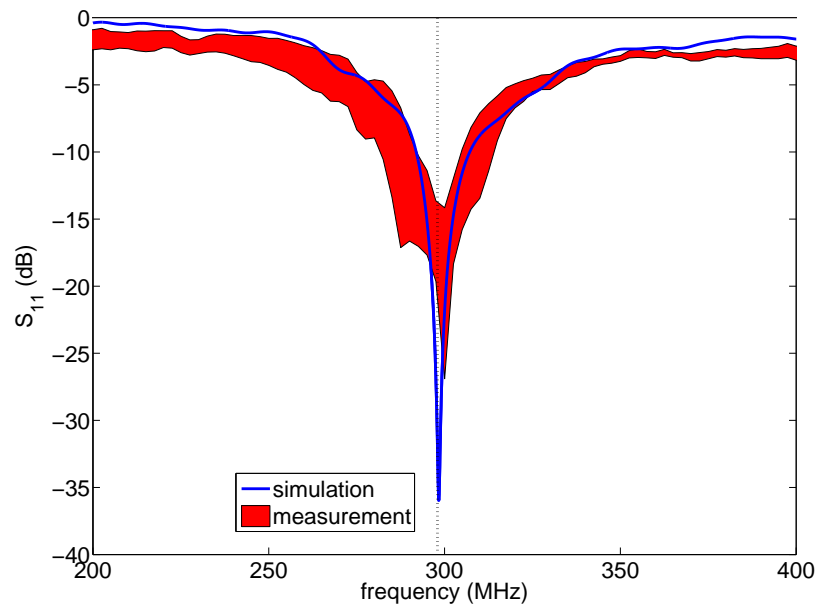


Figure 9.2: Calculated (a) and measured (b) reflection coefficient (S_{11}) of the re-designed patch antenna. The filled area shows the variation (min-max) in measured S_{11} of the twelve antennas. The black dotted line indicates the frequency at 298 MHz.

maximum duty cycle of 10% are connected to one antenna ring of the *LABproto*. Reflected powers are circulated to 50 ohm loads. Unused antennas were terminated using 50 ohms loads. Coaxial cables of approximately 15 m were required to connect the amplifiers outside the MR scanner room (Faraday cage) to the connector box. The total insertion loss of the path from the amplifiers to the RF connectors of the *LABproto* was approximately 75%. The power at the antennas was measured before the experiments using an oscilloscope[‡] and a network analyser[§] to measure the insertion loss of the measurement cables.

Electromagnetic modelling

The electromagnetic propagation in the *LABproto* were predicted using SEMCAD X¹⁶⁷. Modelling parameters, such as simulation grid settings were equal to those in Paulides et al.¹⁴⁹. Table 9.1 lists the dielectric properties of the materials at 298 MHz. A phantom was used based on a receipt of Ito et al.¹⁰⁶, providing muscle-equivalent dielectric properties at 434 MHz instead of 298 MHz. Therefore, we verified these properties of the

[‡]Tektronix, TDS 3064B

[§]Rhode & Schwarz ZVL 9

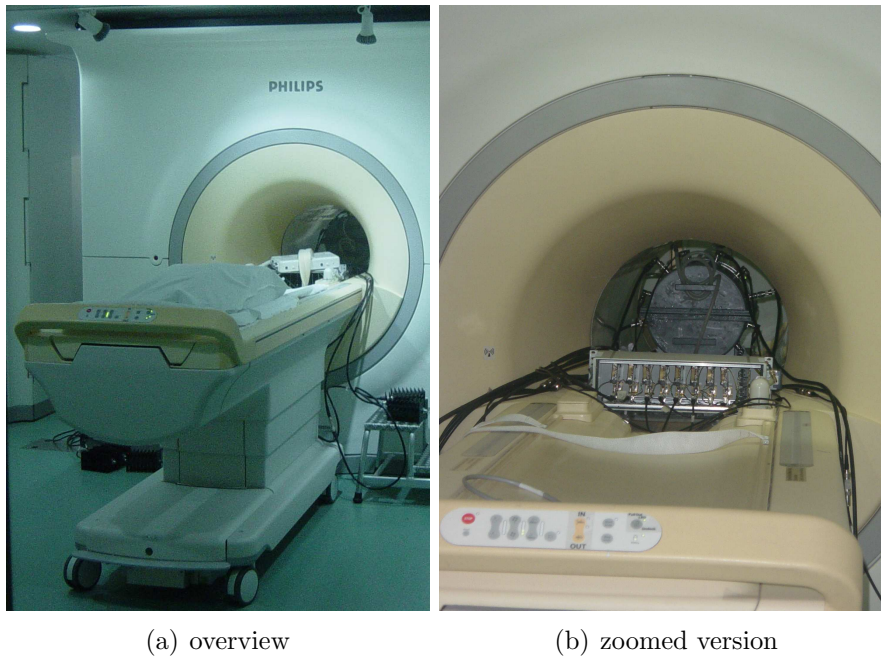


Figure 9.3: Photograph of the Erasmus MC LAB*proto* integrated in the UMC Utrecht Philips Achieva 7T MR scanner.

Table 9.1: Dielectric properties of the materials at a frequency of 298 MHz. ρ is the volume density of mass, ϵ_r is the dielectric permittivity and σ_{eff} is the effective electric conductivity. The relative magnetic permeability μ_r equals 1 for all materials.

	ρ (kgm ⁻³)	ϵ_r (-)		σ_{eff} (S/m)	
		model	measurement	model	measurement
de-mineralized water	1000	78	n.a.	0.04	n.a.
PVC	1350	2.2	n.a.	0.004	n.a.
muscle-equivalent	900	57	53	0.8	0.93

prepared phantom with a coaxial probe[¶] and a network analyser^{||} at 298 MHz.

Geometrical errors in the electromagnetic model and the MR images

For constructing a numerical model from the existing LAB*proto*, we assumed that 1) the applicator consists of perfectly shaped cylinders, and 2) that the de-mineralised water and muscle-equivalent phantom were homogeneous. A high resolution (1 mm) Computed

[¶]Agilent Technologies 85070E

^{||}Agilent Technologies 8712ET

Table 9.2: Maximum geometrical errors (\pm mm) in the SEMCAD X dielectric model and magnetic resonance (MR) images of the laboratory prototype applicator (LAB*proto*). Note that we used the high-resolution computed tomography (CT) scan as reference.

	CT vs SEMCAD X	CT vs MR
phantom	0.1	2
de-mineralized water	1.2	2
antenna	1.5	-

Tomography (CT) scan was acquired to investigate these assumptions.

Figure 9.4 demonstrates that in reality, the cylinders are slightly flattened due to the weight of the water-filled split cylinders and limited strength of the polyvinyl chloride (PVC) material. Air gaps exist between the two split cylinders, on top of the upper half and inside the muscle phantom. To estimate the maximum geometrical errors of the SEMCAD X model and the MR images, we compared the Hounsfield Units (HU) of the CT and the gray values of the MR images using iSeg¹⁰⁴. Table 9.2 lists the maximum geometrical errors found from this analysis. Note that comparisons of antenna positions were impossible due to susceptibility artefacts from the highly conductive antenna structures.

9.3 Results

9.3.1 3D validation of RF modelling tools using B_1^+ MR interferometry

The B_1^+ fields were obtained by an improved B_1^+ mapping method for multi RF transmit systems¹³⁸. This method is optimized for maps that have a large dynamic range by using super-positioning of antenna elements to improve the quality of the noisy B_1^+ maps. Complementary B_1^+ maps $\underline{m}_i(x, y)$ are acquired where all antennas, but one (i), are enabled. The B_1^+ map for channel i $m_i(x, y)$ is reconstructed via

$$m_i(x, y) = \frac{1}{N-1} \sum_{j=1}^N \underline{m}_j(x, y) - \underline{m}_i(x, y), \quad (9.1)$$

where N is the number of antennas. The predicted and measured B_1^+ maps are compared by the gamma evaluation method³¹, in which the gamma index (Γ) is calculated at each MR voxel for pre-defined acceptance criteria. These criteria consists of the distance to agreement (δd , mm) and the dose difference (δD , %) between the predicted and measured values. The predictions are considered accepted if the 95th percentile of all measurement points have a gamma index smaller than one, i.e. $\gamma_{95} < 1$.

Figure 9.5 shows an example of the predicted and measured B_1^+ map of channel one. We found differences up to a factor 2.8 in the absolute B_1^+ values between the predictions and

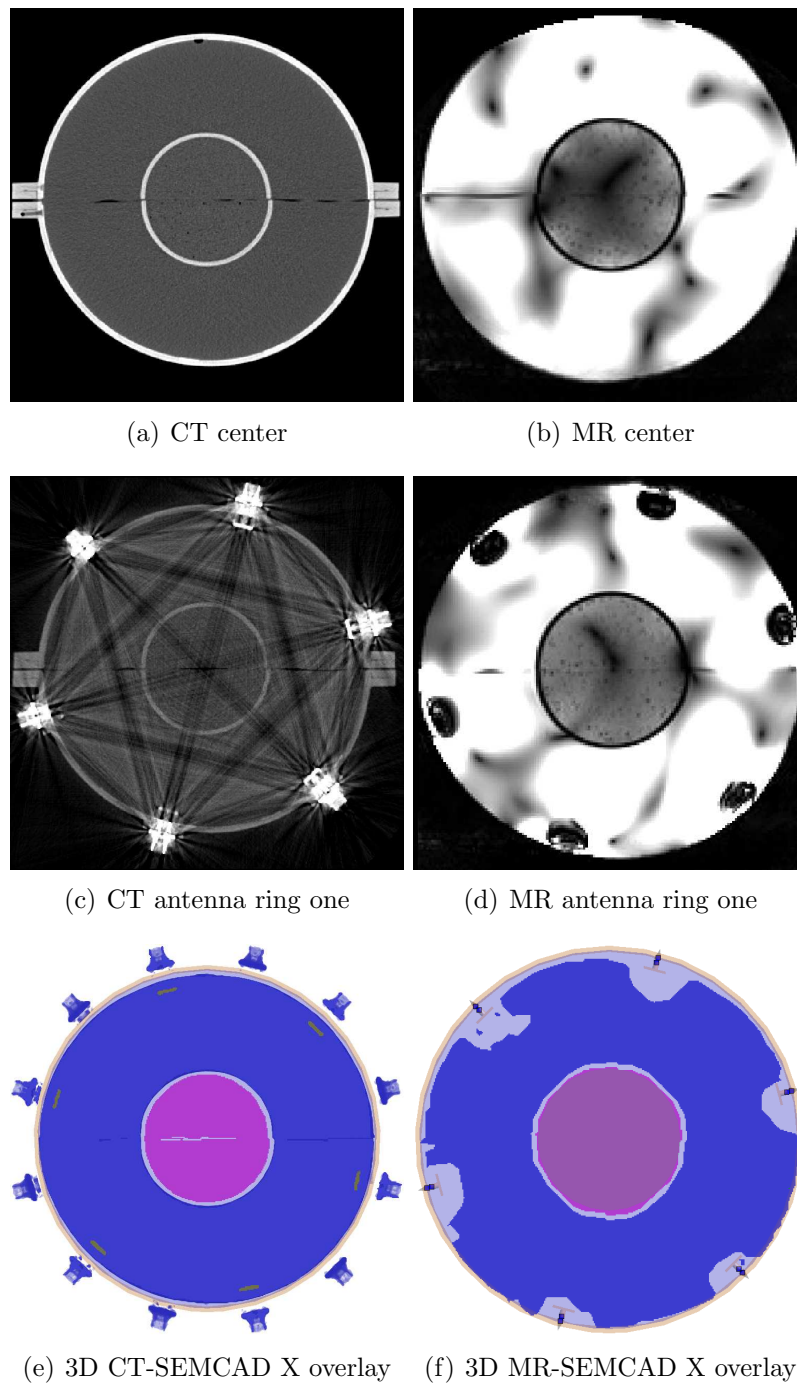


Figure 9.4: Cross-section of the CT (a) and MR (b) at the center of the LAB_{proto} applicator or at patch antenna ring one (c,d) and a transparent overlay of the 3D segmentation (e,f) on top of the SEMCAD X model.

Table 9.3: Ratios of the measured (MR) and predicted (SEMCAD X) $|B_1^+|$ in a square of 20×20 mm² in the centre of the muscle phantom in the LAB*proto* applicator. P_{pk} is the peak value of the measured powers at the applicator RF connectors.

antenna number	1	2	3	4	5	6
MR B_1^+ / model B_1^+	2.7	2.5	2.6	2.4	2.2	2.8
P_{pk} (W)	22	36	16	33	28	34

the measurements (Table 9.3). Therefore, the measurements were scaled such that the average B_1^+ of the muscle phantom equals the predicted value. The acceptance criteria $\delta D/\delta d$ of 6%/2 mm were met for the measurements inside the muscle phantom ($\gamma_{95}=0.9$) for the muscle phantom. Measurements close to the antenna's do not meet this acceptance criterion ($\gamma_{95}=4.1$), probably due to clipping of the data, i.e. the measured values are at the upper detection limit of the MR scanner. Note that the accuracy of the B_1^+ dual TR mapping method²⁰⁸ is restricted to a limited B_1^+ , which was chosen to be optimum for the muscle equivalent phantom. Although we show the results for antenna one only, we found similar results for the other antennas due to symmetry. Figure 9.6 explains the choice for $\delta D/\delta d=6\%/2$ mm, i.e. the acceptance criterion is not met for smaller dose differences or smaller distances to agreements.

9.3.2 B_1^+ optimization in an homogeneous muscle phantom

In ultra-high field MRI, the improved signal to noise ratio (SNR) is accompanied by higher B_1^+ field inhomogeneities and increased specific absorption rates, leading to a limited image quality at the acceptable exposure limits¹⁰⁰. To overcome these problems, parallel transmit arrays are used together with fast B_1^+ mapping routines to calibrate the transmit antenna arrays and to correct for B_1^+ inhomogeneities. The amplitude and phase of the pulses are chosen to maximize the B_1^+ field over the region of interest (ROI). The required value of B_1^+ depends on the flip angle θ and the time interval τ of the RF excitation pulse. For a square pulse this relates according to:

$$\Delta\theta = \gamma B_1^+ \tau, \quad (9.2)$$

where γ is the gyromagnetic ratio, i.e. for Hydrogen (one proton) it is $2.675 \cdot 10^8$ (rad/s/T) or 42.58 (MHz/T).

To investigate the potential imaging capabilities of the LAB*proto*, we optimized the RF phases for maximum B_1^+ value at the deepest voxel location, i.e. at the center of the muscle phantom. For simplicity and to obtain symmetric distributions, we used only one ring of six channels to create a focussed B_1^+ map.

Figure 9.7 demonstrates that the LAB*proto* provides good penetration and focussing possibilities, i.e. a B_1^+ of $0.34 \mu\text{T}$ per 1 W peak input power. For these specific focussing amplitude and phase settings, the corresponding peak localized $\text{SAR}_{10\text{g,max}}$ is 0.3 Wkg^{-1} .

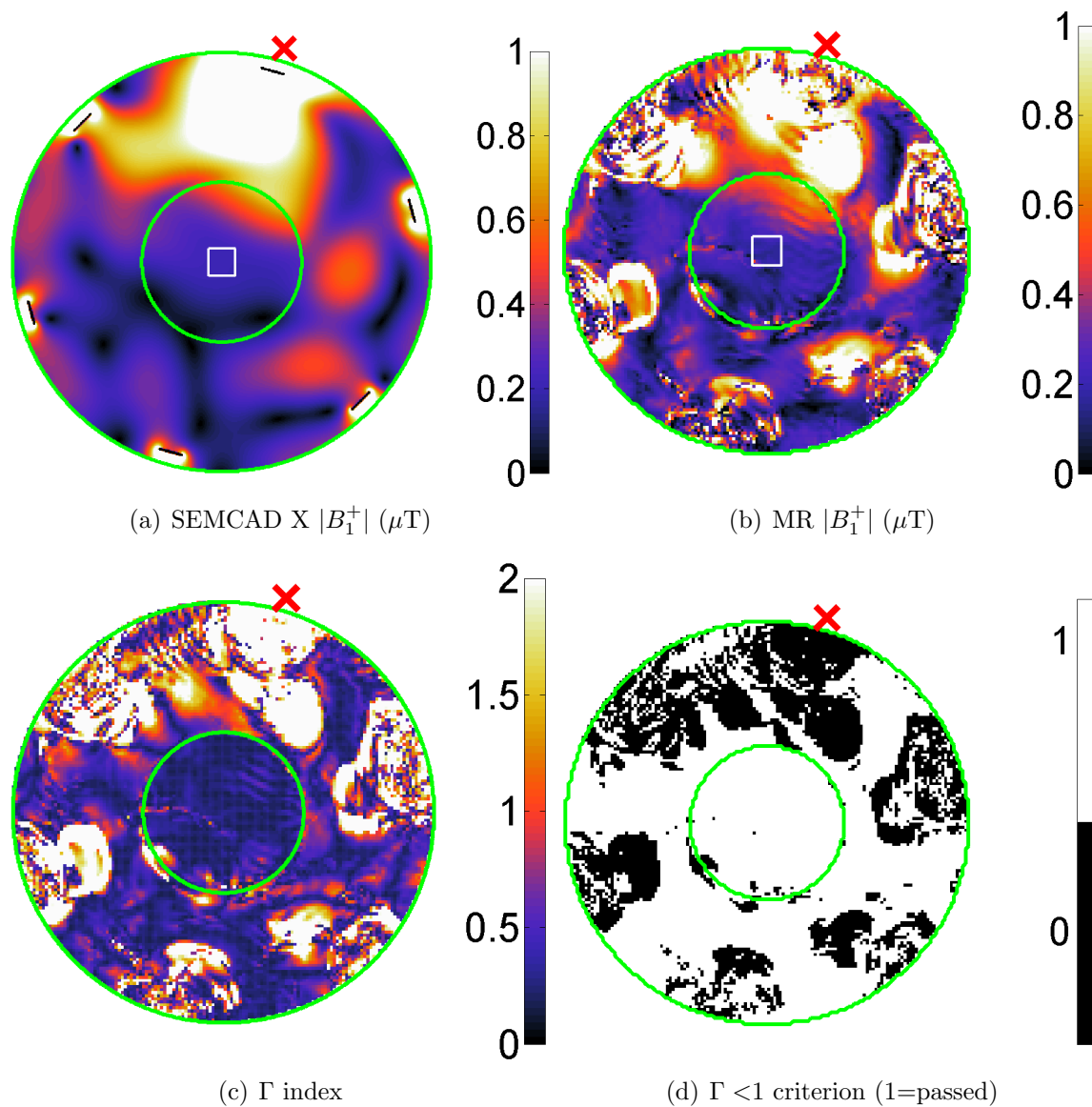


Figure 9.5: Comparison of the predicted (a) and measured (b) B_1^+ maps of antenna one (red cross) in the water and muscle phantom (green circles). The gamma indices for a distance to agreement of 2 mm and a dose difference of 6% are plotted in (c), and the accepted voxels are plotted in (d). The square in the centre of the muscle phantom indicates the area that was used to determine the ratio between the measured and predicted B_1^+ (Table 9.3).

The ICNIRP restriction on $\text{SAR}_{10\text{g,max}}$ is 10 Wkg^{-1} (6 min averaged) for the head and trunk. Hence, for a typical duty-cycle of 5%, a total input power of 665 W is allowed and thus a maximum B_1^+ of $9 \mu\text{T}$ is feasible (B_1^+ scales with the square-root of the power).

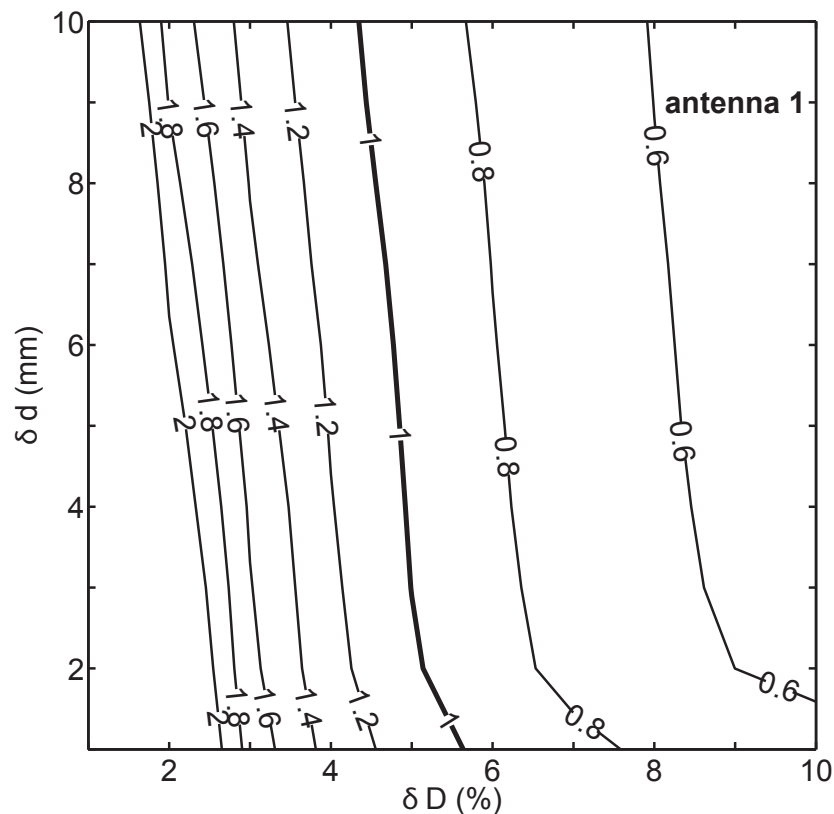


Figure 9.6: Contour plots of the 95th percentile of the Γ index (γ_{95}) as a function of distance to agreement (δd) and dose difference (δD) for antenna one. The bold line is the $\gamma_{95}=1$ contour. In the area where $\gamma_{95} < 1$, the acceptance criteria are met.

9.3.3 B_1^+ optimization in head and neck anatomies

RF field patterns in the human head become complex at ultra-high magnetic field strengths. A bright center and a weak periphery are observed in images obtained with standard volume coils, while surface coils provide strong signal in the periphery¹⁸⁵. These differences in intensity are caused by constructive and destructive interference in the transmitted field patterns and by RF penetration effects. Multi-element transmit coils, i.e. a phased array of antennas, enables controlling these interference patterns, such that the region of interest (ROI) can be imaged effectively.

Figure 9.8 demonstrates that eight channels of the 7T collar can be used effectively to create intense B_1^+ maps at different locations in the head and neck anatomy, e.g. at the larynx or nasopharynx position. 7 μ T (larynx) and 4 μ T (nasopharynx) can be obtained at a typical duty-cycle of 5% and at the ICNIRP $SAR_{10g,max}$ restriction of 10 Wkg^{-1} .

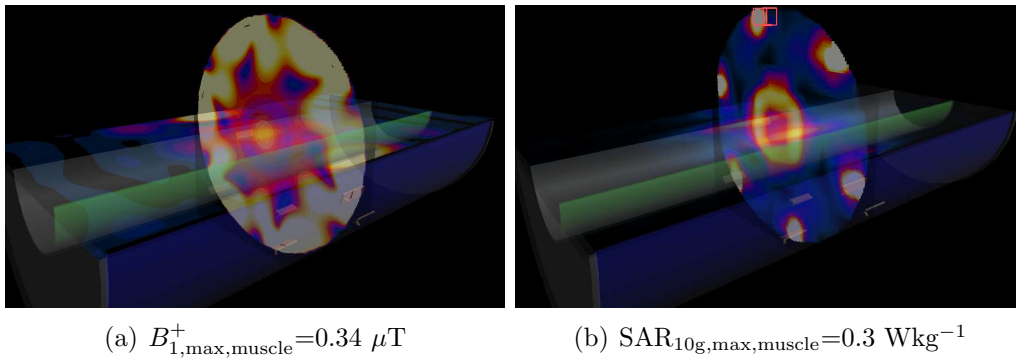


Figure 9.7: B_1^+ and $\text{SAR}_{10\text{g}}$ generated by the *LABproto* applicator at 1 W peak input power and optimized B_1^+ at the center.

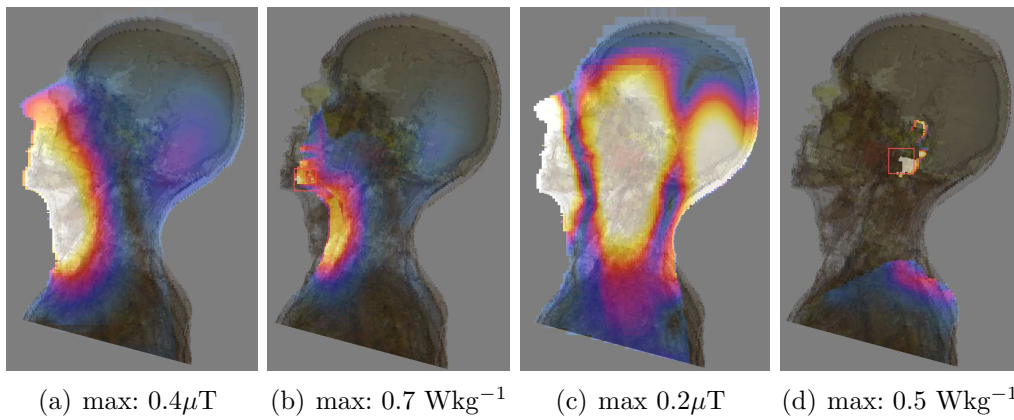


Figure 9.8: B_1^+ and $\text{SAR}_{10\text{g}}$ generated by the *7Tcollar* applicator at 1 W peak input power and optimized B_1^+ at the larynx (a,b) or the nasopharynx (c,d).

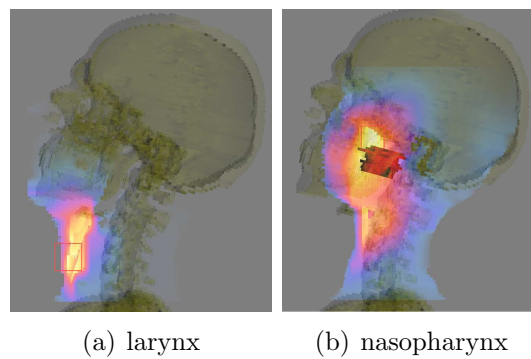


Figure 9.9: $\text{SAR}_{10\text{g}}$ generated by the *7Tcollar* optimized for heating the larynx (a) or nasopharynx tumour (b).

9.3.4 SAR optimization at tumours in the head and neck

To illustrate the potential of an hybrid MR and a 12-channel hyperthermia applicator, we calculated and optimized the SAR distribution in both the larynx and in a nasopharynx tumour. Early experience showed that it is challenging to cover deeply located nasopharynx tumours effectively, i.e. the 25% iso-SAR_{max} coverage¹²⁵ is 58% for the standard HYPERcollar operating at 434 MHz¹⁴⁹.

Figure 9.9 shows that focussed heating is feasible with the hybrid MR and hyperthermia applicator, i.e. the 7Tcollar at 298 MHz. The SAR_{10g,max} is 4.7 Wkg⁻¹ in the larynx and 1.5 Wkg⁻¹ in the nasopharynx tumour, while keeping the SAR_{10g,max} in the spinal cord under 0.2 Wkg⁻¹. The 7Tcollar provides a 25% iso-SAR_{max} coverage of 60% for the nasopharynx tumour, which is in agreement with the standard HYPERcollar at 434 MHz¹⁴⁹ using twelve antennas. For the larynx tumours the coverage is expected to be much better, i.e. a coverage in the range of 85 to 94%¹⁴⁹. Hence, the hybrid MR and hyperthermia applicator can be used effectively to control the heat in head and neck tumours.

9.4 Discussion and conclusions

In this study we found that a 7T MR scanner can be used to validate the qualitative field distributions predicted by hyperthermia treatment planning tools. The 7Tcollar, i.e. a hybrid MR and hyperthermia applicator can be used effectively to both image and heat tumours in the head and neck region.

Redesign of the applicator for 298 MHz We used simulations prior to manufacturing to redesign the dimensions of the patch antennas to match its resonance to the Larmor frequency of 298 MHz. The predicted reflection coefficients were in agreement to the measurements. Hence, the “virtual prototyping” approach allowed avoiding time-intensive and costly experiments

3D validation of RF modelling tools by 7T MRI We found large but linear differences between the predicted and measured B_1^+ values. Therefore, the gamma evaluation is only an exploratory operation and cannot be used to validate the model predictions quantitatively at this stage. After normalization, good agreement was observed inside the muscle phantom: more than 95% of the MR measurement points met the acceptance criteria 2 mm/6%. For comparison, acceptance criteria in the order of 3 mm/3% are commonly considered feasible in radiotherapy⁶⁸. Note further that 2 mm is the maximum achievable distance due to the limited resolution (2 mm) and geometrical distortions (± 2 mm) of the MRI.

More work is required to improve the quantitative value of the B_1^+ . In our experiment, we did not measure the powers during the MR B_1^+ mapping itself, but we estimated the power by repeating the experiment with the RF cables connected to a scope instead of

the LAB*proto* applicator. Hence, the major improvement is to simultaneously measure the forwarded and reflected powers at the output of the amplifiers during the B_1^+ mapping. The second recommendation is to use the highest possible power levels (1 kW instead of 15W) to increase the signal to noise. We used the MR signal received by one channel only. Using the received signals of all channels will provide better SNR's and possibilities to distinct and filter areas outside the detection range, i.e. too low flip angles or clipped values.

B_1^+ optimization for imaging We found that the 12-channel 7T*collar* can generate B_1^+ values in the range of 0.2 (nasopharynx) to 0.5 μT (larynx) per 1 W peak input power. For comparison, Vaughan et al.¹⁹² obtained maximum 0.4 μT in the brain, at a 1 W peak excitation pulse equivalent for a 16-element TEM head coil. It is difficult to compare our results to those obtained with other transceiver “coils”, since we did not use equal phantoms or imaging protocols. However, we do believe that our 7T*collar* is an efficient transmit and receive applicator because the Poynting vector of the antennas is directed towards the imaging target region¹⁵⁶. The main advantage of efficient transmit and receive arrays is that high peak B_1^+ is possible 9.2 enabling imaging sequences that require high bandwidth.

We optimized the B_1^+ by the Target Center Point (TCP) method, which maximizes B_1^+ only in one voxel, leading to areas with bright intensities and a weak periphery. When uniform images are desired, these signal intensity variations can be corrected for using B_1^+ homogenization algorithms. To demonstrate the imaging capabilities of the 7T*collar* we optimized B_1^+ only. However, multi-objective functions, i.e. minimize SAR while maximize B_1^+ , can be used when SAR restrictions¹⁰⁰ limit imaging quality.

We used antennas that are submerged in water, which provides excellent coupling of RF energy into the human anatomy. We do note however, that standard usage of water-filled MR imaging devices might be cumbersome in practice. Using water inside the bore of an MR scanner is only possible if the risk for leakage into sensitive electronics can be avoided. Further, the waterbolus should have a good contact with the human anatomy to avoid air inclusions. This means that site-specific waterboli are required that should not limit patient comfort, i.e. provide sufficient breathing possibilities. However, using waterboli in MR scanners are feasible⁹⁸ and are tolerated by patients in our routine clinical treatments. We do note that the water volume could be reduced substantially for a real clinical device and that the waterbolus could also be used for active skin-cooling.

Comparison of patch antennas and coils We used an array of patch antennas that was originally designed and optimized (SAR) for hyperthermia treatments in the neck region and not specifically for imaging (B_1^+) purposes. For hyperthermia treatments, we rely on SAR predictions from electromagnetic models. These predictions require that the antenna and its feeding network is easy to model. Compared to conventional MR coils, the advantage of the patch antenna in water is that it is already matched to the 50 ohms RF cable without the use of a matching network, such as balancing networks and tuning

capacitors.

Another potential advantage of using an antenna submerged in water, is that the size of the “half-wavelength” antenna is reduced by approximately a factor nine ($\sqrt{\epsilon_{r,water}}$), providing the possibility to place more transmit and receive elements.

SAR optimization for heating tumours Paulides et al.¹⁴³ found that the range of 400 to 600 MHz provides the optimum power absorption distributions, however they also note that the optimum frequency is highly dependent on the size of the target volume. The frequency of the original *HYPERcollar* is higher (434 MHz) than the modified design of the *7Tcollar*. Consequently, the focus diameter in a homogeneous phantom is increased by a factor of approximately 1.5. Providing sufficient tumour coverage is thus easier using the *7Tcollar*. However, we expect that the *7Tcollar* will also heat more normal and critical tissues, which should be quantified further.

Hybrid MRI/HT with a common RF system Combining MR scanners and hyperthermia applicators that can work on the same frequency, i.e. an “hybrid” MR/HT applicator, has several advantages. First, the MR and HT system might share one common RF amplifiers system and RF electronics. Second, special RF heating equipment, shielding and filtering of the different RF signals is avoided, which is an essential part when other than Larmor frequencies are used for heating. Finally, the amplitude and the phase of the MR acquired B_1^+ maps, provide direct control of the applied fields in the patient during the hyperthermia treatment. These maps can be used for example to verify patient-specific field and SAR predictions, but also for quality assurance (QA) in phantoms.

10. Virtual prototyping

Virtual prototyping
of RF and US applicators for
hyperthermia treatment
of breast cancer

This chapter is based on:

JF Bakker, MM Paulides, IM Obdeijn, GC van Rhoon and KW van Dongen.

"An ultrasound cylindrical phased array for deep heating in the breast: theoretical design using heterogeneous models". *Phys Med Biol*, Vol. 54, No. 10, pp. 3201-15, 2009.

Abstract

Purpose: At the Erasmus Medical Center in Rotterdam, an electromagnetic applicator (HYPERcollar) has been developed for hyperthermia treatment of head and neck tumours. The design of this applicator has, in our view also potential for heating tumours in intact breasts. The objective of this pilot study was therefore to explore the heating ability of the HYPERcollar for intact breast tumours and to compare this ability to an earlier optimized ultrasound (US) design. **Materials and methods:** “Virtual prototyping” was applied based on simulations of temperature profiles in breast models that contain a central tumour and an artificial tumour near the thorax. **Results:** The HYPERcollar can generate maximum temperatures of 44 °C in both centrally and deeply located tumours, while keeping the temperature in normal tissues below 41 °C. The average temperature increase is 5.9 °C in the central tumour and 4.0 °C in the deeper located thorax tumour. The earlier US design provides a better penetration and better focussing capabilities, however its temperature focus is too small to cover tumours with diameters larger than 2-3 cm. Hence, scanning of multiple foci is required to heat larger volumes with ultrasound. **Conclusions:** These data provide a strong indication that the HYPERcollar can be used effectively for heating centrally and deeply located tumours in intact breasts. Compared to the US applicator, a larger focus is obtained which reduces the need for focus scanning. Further research must be preceded by an extensive analysis of clinical needs to distinguish the target patient population. This study then enables making an evidence based choice between EM and US technology, and provides the foundation for further steps.

10.1 Introduction

Hyperthermia (HT), an increase of the temperature towards 40 to 44 °C, is a powerful modality to improve the clinical outcome of radiotherapy (RT) and chemotherapy. Several randomized phase III trials have demonstrated this improvement for tumours at various treatment sites^{25,108,188}. Vernon et al.¹⁹⁴ showed the benefit of HT for superficially localized breast cancer as well, i.e. the overall complete response rate in five phase III trials was 41% for RT alone and 59% for the combined treatment (RT+HT). Although the overall results of these studies were positive, the effect of HT was minimal for inoperable tumours in the intact breast. Vernon et al.¹⁹⁴ and Sherar et al.¹⁶⁸ indicate that this minimal effect was caused by insufficient heating at deep locations due to the various electromagnetic (EM) applicators, allowing frequency dependent heating depths of maximum 4 cm at 433 MHz, 2 cm at 915 MHz or 1 cm at 2450 MHz. To the best of the authors knowledge,

adequate heating equipment for HT at deeper located inoperable tumours in the intact breast is still not available.

At the Erasmus Medical Center in Rotterdam, an electromagnetic applicator, i.e. the *HYPERcollar* has been developed for the treatment of tumours in the head and neck region^{6,146}. This applicator has been verified experimentally¹⁴⁷ and is currently being used in the clinic¹⁴⁹. Although the *HYPERcollar* has been designed specifically for tumours in the head and neck region, the applicator design may prove to be useful also for heating in intact breasts. Especially deeply located tumours near the thorax (chest wall) are of interest, since these cannot be heated effectively with commonly used applicators³².

Although only EM radiation is exploited in the clinical phase III trials, in theory ultrasound (US) is of interest for intact breasts, due to the corresponding larger penetration depths and better focusing possibilities. In a previous study⁸, we theoretically designed an US phased array for heating tumours in the breast. The array contains 192 transducers, however using a large amount of electronically controlled transducers is cumbersome in practice and economically unwanted. Consequently, a clinical phased-array ultrasound applicator including a 192 multi-channel RF amplifier system is not available in our hospital. In the past, we developed hyperthermia applicators by trial and error, i.e. an applicator was manufactured, tested, redesigned, manufactured etcetera. The *HYPERcollar* however, was designed based on simulations. Ever since, this “virtual prototyping” approach has become the standard in our research since it avoids time-intensive and costly experimental verifications. In this pilot study, we used basic “virtual prototyping” to investigate the theoretical feasibility if the *HYPERcollar* system could be used for heating tumours in the intact breast. The heating profiles from the *HYPERcollar* are compared to those of the 192 channel ultrasound applicator, optimized in previous work, to investigate which applicator is of interest to mechanically construct and test for heating breast tumours.

10.2 Materials and methods

10.2.1 Approach

We constructed dielectric, acoustic and thermal models of intact breasts. These models were embedded in water, which is used both as a coupling medium and to cool the skin. To investigate the feasibility of inducing hyperthermia in tumours in the intact breast, we calculated the absorption and temperature profiles due to RF exposure from the *HYPERcollar*. The SAR and temperature patterns of the electromagnetic *HYPERcollar* are compared to those obtained with the theoretical ultrasound applicator.

10.2.2 Heterogeneous breast model

An heterogeneous 3D model of the breast anatomy is constructed from an MRI scan of a 39 year old female (Figure 10.1), with a centrally located breast tumour. The breasts are imaged in prone position, i.e. a realistic breast position and shape when inserted in the

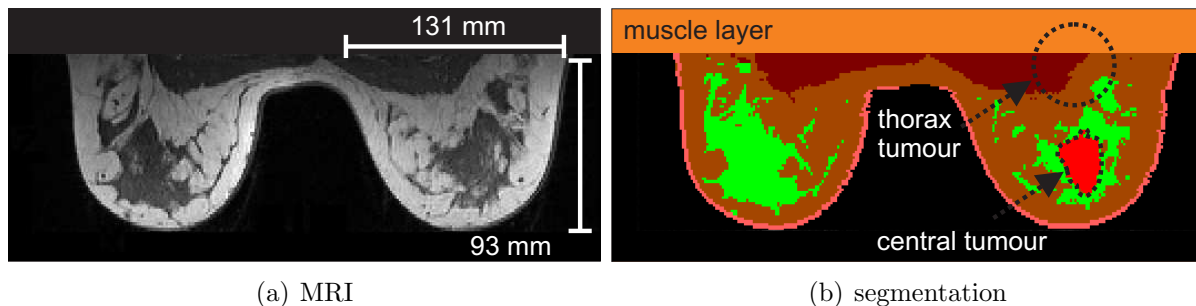


Figure 10.1: Construction of the MRI-based model, that is used in the characterization of SAR and temperature distributions in either the “central tumour” ($\sim 30 \times 20 \times 38 \text{ mm}^3$) or the artificial “thorax tumour” (black dotted sphere with a radius of 25 mm).

Table 10.1: Tissue properties used in the computations. Values between the brackets are the minimum and maximum values found in literature, which is used as input for sensitivity simulations with extreme thermal properties. Ultrasound properties are given in Bakker et al.⁸

Tissue	ρ kg/m ³	EM		Thermal		
		ε_r	σ_{eff} S/m	k_t W/m/K	c_t J/Kg/K	ω_b ml/min/kg
Water	993	78	0.04	0.50	4186	-
Muscle	1040	57	0.8	0.50 (0.39-0.60)	3580 (3500-3698)	27 (18-38)
Fat	950	12	0.08	0.24 (0.20-0.33)	2493 (2300-2973)	25 (19-28)
Skin	1200	49	0.7	0.37 (0.26-0.50)	3496 (3150-3662)	87 (30-120)
Breast	1020	19	0.1	0.50	2493 (2300-2973)	25 (19-28)
Tumour	1000	59	0.9	0.50	3770	330 (140-780)

HYPERcollar. The contrast enhanced MRI was used to delineate the “central tumour” and normal tissues using iSeg¹⁰⁴. By assigning corresponding dielectric, acoustic¹⁷⁰ and thermal¹³⁰ properties (Table 10.1), we obtained the patient models for the computations. Note that the thermal properties of blood are set to $\rho_b c_b = 4052910 \text{ (Jm}^{-3}\text{K}^{-1}\text{)}$, where ρ_b is the blood volume density of mass and c_b is the specific heat of blood.

A brick-shaped muscle layer is placed on top of the breast to mimic the presence of the chest wall, which was not imaged since it was located outside the MR imaging coils. To investigate also the ability to apply HT at depth, we mimicked a “thorax tumour” by placing an artificial sphere (radius 25 mm and 40-90mm from the skin). The breast model was modified by removing the unexposed breast when inserted into an applicator.

The HYPERcollar The HYPERcollar (Figure 1.3c) is currently used for heating tumours in the head and neck region¹⁴⁶. The applicator consists of twelve patch antennas, equidistantly placed in two rings. The antennas are fed by power and phase controlled signals with an operating frequency of 433.92 MHz. Selective tumour heating can be obtained by altering the phases of the radio frequency (RF) signals to generate adaptive interference patterns. The applicator contains a closed waterbolus that surrounds the patient's neck. For the theoretical study on intact breast heating, we replaced the water bolus by a rectangular water layer and placed the applicator on an absorbing bottom-layer (Figure 10.2a).

The choice of the bottom-layer material is of importance since it may influence the field distributions of the applicator.

Electromagnetic fields are simulated using SEMCAD X¹⁶⁷ for each antenna individually and the SAR in the tumour is maximized by altering individual antenna amplitudes and phases according to the procedure of Kohler¹¹⁶ to maximize

$$\overline{\text{SAR}}_{\text{ratio}} = \frac{\overline{\text{SAR}}_{\text{tumour}}}{\overline{\text{SAR}}_{\text{breast}}}, \quad (10.1)$$

where $\overline{\text{SAR}}_{\text{tumour}}$ and $\overline{\text{SAR}}_{\text{breast}}$ are the average SAR in the tumour and the entire breast respectively.

A high SAR-ratio indicates good focussing at the tumour. Lee et al.¹²⁵ found a second indicator for superficial HT that 25% iso-SAR_{max} coverage is a good predictor for clinical outcome, however in this study we take the more conservative 50% to account for model and position errors. The focus (ellipsoid) dimensions are quantified by the major diameters, i.e. the focus width $W_{50\%,\text{SAR}}$ in the transversal (xy) plane and the focus length $L_{50\%,\text{SAR}}$ in the axial (xz) plane. For temperature distributions, the diameters $W_{50\%,\Delta T}$ and $L_{50\%,\Delta T}$ of the 50% iso- ΔT_{max} contours are used, where ΔT_{max} is the maximum temperature increase.

The electromagnetic model of the HYPERcollar is discretized with a maximum element size of $\lambda/15$ and refinements near the antennas ($\lambda/250 < \Delta < \lambda/80$). The computational domain is truncated using absorbing, uni-axial, perfectly-matched layers (UPML) was steady state obtained after ten periods.

Ultrasound applicator The ultrasound applicator consists of 192 transducers operating at a frequency of 100 kHz (Figure 10.2b). The transducers are divided over six rings with a radius of 75 mm. Selective tumour heating is obtained by altering the phases of the signals to generate adaptive interference patterns. A numerical acoustic model is used to predict the complex pressure wave propagation in the heterogeneous breast and to compute the SAR. A detailed description of the ultrasound applicator and the ultrasound simulations can be found in Bakker et al.⁸.

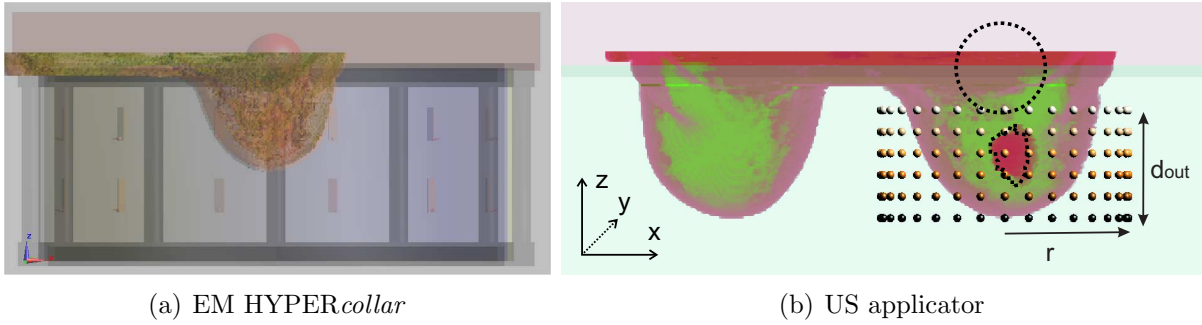


Figure 10.2: Configuration of the electromagnetic (EM) HYPERcollar (a) and the ultrasound (US) applicator (b).

10.2.3 Thermal simulations

Temperature patterns are computed by using a thermal model that describes the heat transfer in tissues. The model is based on Pennes Bio Heat Equation (PBHE)¹⁵¹ and is formulated as,

$$\rho_t c_t \frac{\partial T_t}{\partial t} = \nabla \cdot (k_t \nabla T_t) + \rho_t Q_m + \rho_t \text{SAR} - \rho_b c_b \rho_t \omega_b (T_t - T_b), \quad (10.2)$$

where ρ_t is the volume density of mass, c_t is the specific heat, k_t is the thermal conductivity and T_t is the time and spatial dependent temperature of tissue “t”; c_b , ρ_b and T_b are the spatial dependent specific heat, volume density of mass and temperature (37 °C) of the blood “b”; ω_b is the blood perfusion rate and Q_m is the metabolic heat generation rate (neglected in this work).

Blood perfusion provides an ambiguous effect on the temperature elevation in tissues, i.e. it removes heat from the target area and spreads the heat towards the surrounding tissues. This effect can be described by discrete vessel modelling¹¹⁷, however when information about the vascular anatomy is not available, it is recommended⁵² to combine the PBHE with an effective conductivity model.

The effective conductivity model used in this work is defined as¹⁹⁸

$$k_{eff}(\mathbf{r}) = k_t(\mathbf{r}) \{1 + C\omega_b(\mathbf{r})\}, \quad (10.3)$$

where C is a constant (0.01) obtained experimentally²⁷. The breast is embedded in 30 °C water for which a Dirichlet boundary condition ($T = T_{\text{boundary}}$) is applied is used. The SAR is scaled such that the maximum steady state temperature is 44 °C.

The PBHE, the effective conductivity model and the thermal boundary conditions are discretized and solved with a Finite Difference Time Domain (FDTD) technique¹⁴⁰, which is implemented in SEMCAD X¹⁶⁷.

Table 10.2: SAR and temperature results obtained with either the electromagnetic (EM) *HYPERcollar* or the ultrasound (US) applicator in the central or thorax tumour. SAR_{ratio} is the ratio between the average SAR in the tumour and in the breast, ΔT is the average temperature increase, $W_{50\%}$ is the width and $L_{50\%}$ length of the focus, where 50% indicates the 50%iso-SAR or 50%iso ΔT .

	central		thorax	
	EM	US	EM	US
SAR_{max}	1.5	0.17	0.3	0.11
SAR_{ratio}	12.2	21.7	3.9	7.3
$SAR W_{50\%}$ (mm)	20	5.7	40.0	6.5
$SAR L_{50\%}$ (mm)	56	13.5	63.0	21.5
ΔT_{tumour} ($^{\circ}C$)	5.9	3.0	4.0	2.4
ΔT_{breast} ($^{\circ}C$)	-0.9	-1.4	-0.5	-1.5
$T W_{50\%}$ (mm)	35	19	44	21
$T L_{50\%}$ (mm)	57	21	70	32

10.3 Results

10.3.1 SAR

Figure 10.3 shows the SAR distributions in a central and thorax tumour generated by the electromagnetic *HYPERcollar*. For comparison reasons also the results of our earlier optimized US applicator is given. The SAR focus size of the ultrasound applicator is much smaller and the SAR-ratio is much higher than the electromagnetic applicator (Table 10.2). For the deeply located thorax tumour, strong SAR values at the skin surface are observed for the *HYPERcollar*.

10.3.2 Temperature simulations

The temperature distributions are calculated for the *HYPERcollar* and the ultrasound applicator using optimized focussing at the deeply located thorax tumour. We limited the thermal analysis to the most challenging case, i.e. the deeply located thorax tumour. The water bolus temperature is fixed at 30 $^{\circ}C$ for all configurations. The start temperature of the breast is 37 $^{\circ}C$. Further, input power and SAR are scaled such that the maximum steady state temperature in the tumour is 44 $^{\circ}C$.

Figure 10.4 and Table 10.2 shows that the *HYPERcollar* heats a larger volume of the tumour than the ultrasound applicator. This finding is nicely illustrated by the fact that the area enclosed by the 41 $^{\circ}C$ iso-Temperature surface is smaller for the ultrasound applicator than for the *HYPERcollar*.

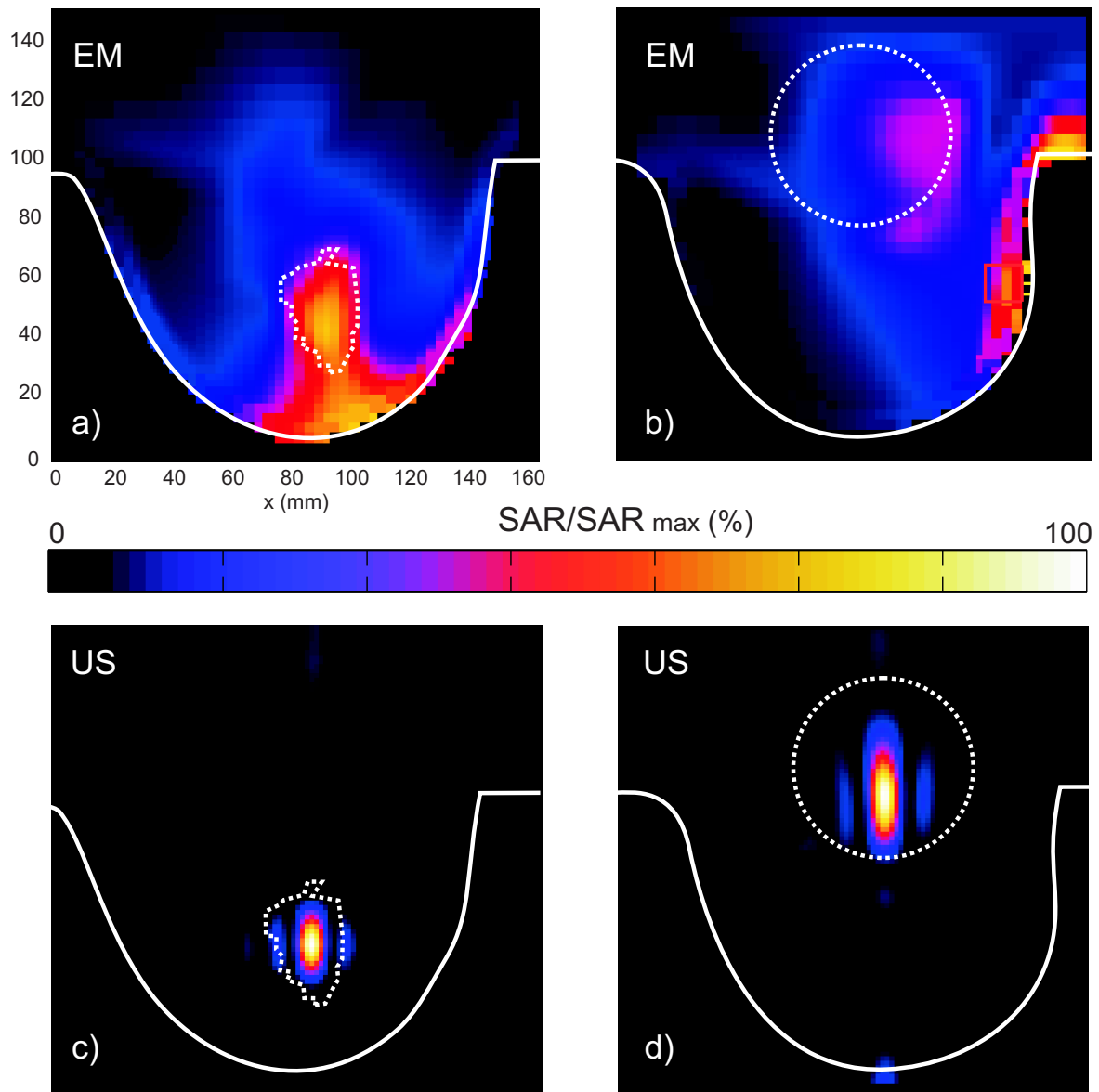


Figure 10.3: SAR distributions in a central (a,c) and thorax (b,d) tumour generated by the ultrasound (US) or electromagnetic (EM) applicator.

Sensitivity study Additional thermal simulations are performed to investigate the sensitivity of the thermal properties (k_t , c_t and ω_b). We studied scenarios using minimum, mean and maximum values of the thermal parameters from literature (Table 10.1) for heating the thorax tumour with the *HYPERcollar*. Figure 10.5 shows that the tumour temperature varies 0.6 °C for the studied thermal tissue values. Table 10.3 shows that extreme thermal parameters lead to changes in the focus width (40-47 mm) and length (62-75 mm).

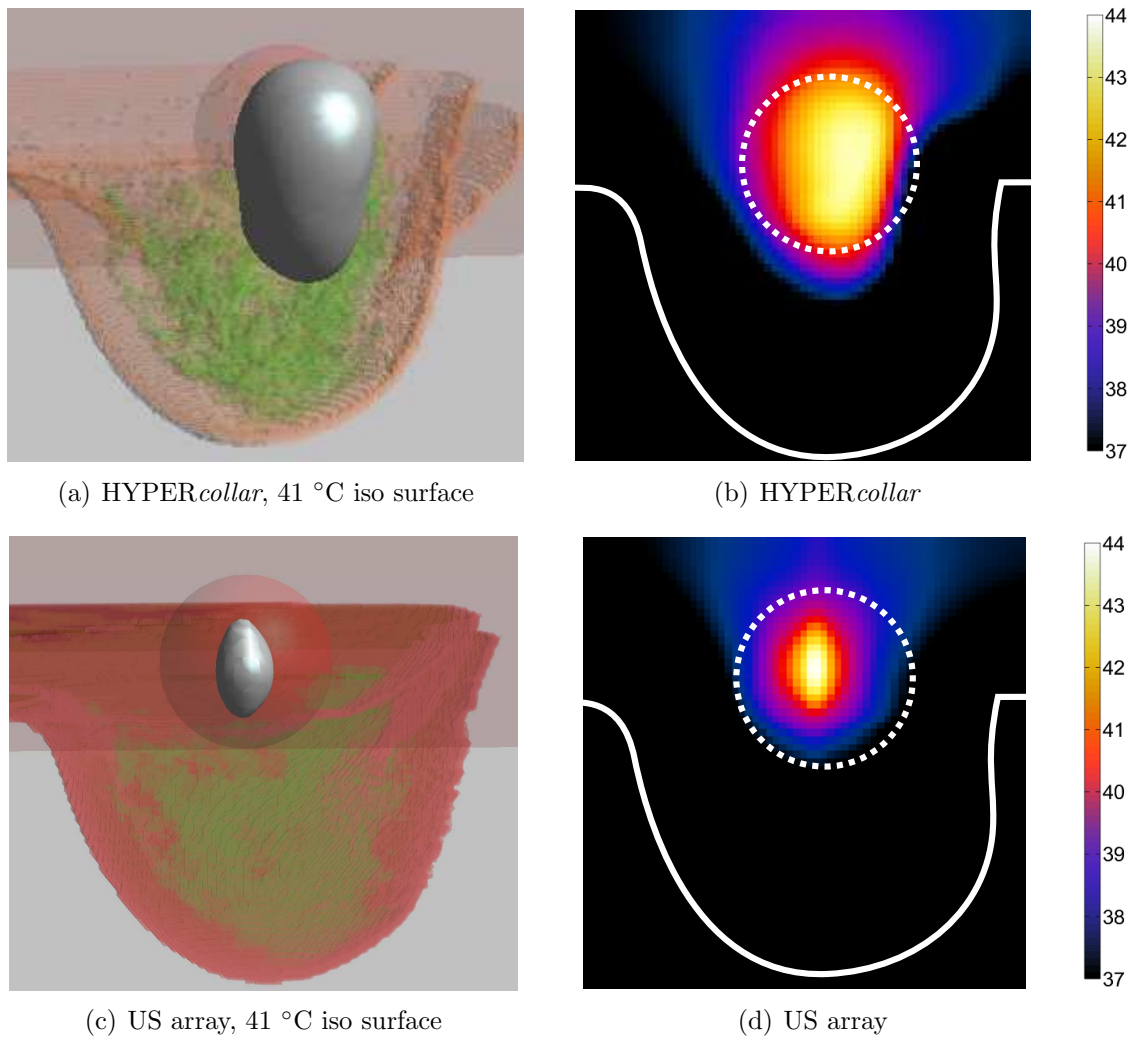


Figure 10.4: Temperature distributions obtained with the electromagnetic HYPERcollar (a and b) and the theoretically designed ultrasound array (c and d) for optimized SAR in the thorax tumour. The distributions are visualized for the xz -plane through the centre of the tumour. Black represents temperatures ≤ 37 °C.

10.4 Discussion

In this study, we used “virtual prototyping” to investigate the potential of using the HYPERcollar to heat tumours in intact breasts. By using simulations, we found maximum temperatures of 44 °C in centrally and deeply located tumours, while keeping the temperature in normal tissues below 41 °C.

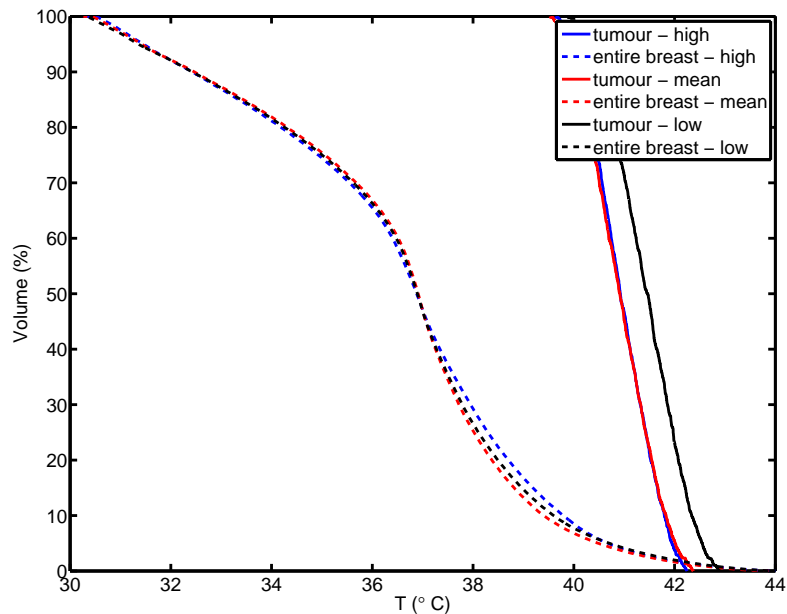


Figure 10.5: Cumulative temperature volume histograms corresponding to low, mean and high values for the effective conductivity k_t , specific heat capacity c_t and blood perfusion rate ω_b obtained with the *HYPERcollar* and steering towards the thorax tumour.

Table 10.3: Sensitivity of the results to extreme thermal parameters (Table 10.1)

	min	mean	max
ΔT_{tumour} (°C)	3.9	4.0	4.4
ΔT_{breast} (°C)	-0.5	-0.5	-0.5
$T W_{50\%}$ (mm)	40	44	47
$T L_{50\%}$ (mm)	62	70	75

Comparison to an ultrasound applicator We compared the results to those of a theoretical design of an ultrasound applicator. We found that the temperature focus of the ultrasound applicator is too small (2-3 cm) to cover the entire tumour. For larger tumours, the electromagnetic *HYPERcollar* is in favour, which is best expressed by the larger average temperature increase, i.e. 5.9 °C versus 3.0 °C for the central tumour and 4.0 °C versus 2.4 °C for the deep tumour. We do note however, that scanning the ultrasound focus can be used to increase the heated volume⁸.

The great advantage of using the *HYPERcollar* instead of the ultrasound applicator is that it has already been manufactured, the electromagnetic applicator model has been verified experimentally and early clinical results in patients are reported¹⁴⁹. We do note

however, that more work is required to adapt the waterbolus of the applicator such that it provides a good contact for intact breasts in prone position.

The heating capabilities are shown by “virtual prototyping” for both applicators. The next step is to define which tumours, in terms of size and location are of interest for hyperthermia treatments.

Comparison to other electromagnetic applicators Wu et al.²⁰⁵ designed and constructed an RF phased array consisting of four electromagnetic antennas operating at 140 MHz. Their applicator can generate a geometric focus at the centre of the breast, which has been verified by electric field measurements in a water tank. Finite-element simulations were evaluated in a simplified breast model that contains a spherical volume located at the breast centre. By simulations they showed that the peak temperature of 44 °C is located outside the tumour and that the deepest part of the tumour is heated to only 39 °C. Heating profiles for deeply located tumours near the chest wall were not provided. Taking into account the required increase in penetration depth, we anticipate that the *HYPERcollar* provides both more effective interference at depth as well as increased degrees of freedom to optimize the heating.

Zastrow et al.²⁰⁹ showed a theoretical design of an RF phase array consisting of 24 antennas. Treatment regions of 1-2 cm in size were achieved by using patient-specific beamformers. They used omnidirectional antennas without a coupling medium, which are too inefficient for a clinical hyperthermia system. Hence, although their results are promising, more work is required to verify the model predictions and to construct a real working clinical device.

Thermal properties We investigated the influence of thermal modelling parameters by repeating the simulations for extreme values found in literature. Maximum 0.5 °C difference in the average temperature of the thorax tumour was found for extreme thermal parameters. These differences are caused by the fact that the effective conductivity is increased for higher perfusion levels.

We used thermal properties under normal conditions, i.e. at the base-line temperature of 37 °C. However, the blood flow in normal tissues and tumours can depend on the local temperature¹⁷¹, potentially leading to altered temperature distributions in hyperthermia applications¹²⁴. The effective conductivity model depends partly on a experimentally determined constant that scales the conductivity with the local perfusion value²⁷. Unfortunately, literature data on such patient-specific and temperature-dependent thermal values in healthy tissues and breast tumours is sparse. In general, self-regulation of healthy tissue by non-linear temperature-dependent blood perfusion, reduces hot spots caused by local maxima of the absorbed electromagnetic fields¹²⁴.

Possibilities for improvements In this pilot study we did not redesign the *HYPERcollar* for breast heating, e.g. we did not obtain the optimum values for the frequency, number of antennas, number of rings and the distance between rings. Consequently, we

expect that improved heating profiles can be obtained for an optimized design of the *HYPERcollar* for the purpose of breast heating.

Although not shown, SAR distributions were also calculated for two breasts inserted in the *HYPERcollar*. Inserting both breasts in the *HYPERcollar* is feasible when the tumour is centrally located. However, when the tumour is located near the chest wall it is not possible to obtain a proper SAR distribution, since high SAR values are generated at the skin, which is too close to the antennas. More work is required to investigate how to insert one breast in the *HYPERcollar* while not exposing the other breast.

The optimum water temperature depends on the depth of the tumour. In our clinic, we use water temperatures of ± 40 °C for superficial (≤ 4 cm depth) tumours and ± 15 °C for deeply located tumours in the pelvic region. In this work, we fixed the water temperature at 30 °C, assuming that the tumours are located semi-deep. A Dirichlet boundary condition is used in the simulations. In practice however, the water will be cooled and circulated and therefore a convection coefficient due to water flow should be included. Further research is thus required to find a set of optimum water temperatures as a function of heating depth.

The vascular system is not included in the breast model. Especially near large blood vessels, inhomogeneities in the temperature distributions can be expected. We used an effective conductivity model instead of a complex vascular network. This model is related to the blood perfusion rate via a constant C , which is determined experimentally for the tongue²⁷. This constant should be obtained for breast tissues as well to improve the reliability of the thermal modelling parameters.

In this work, we optimized the SAR and not directly the temperature. Due to the large differences in thermal properties and cooling effects by the water, we expect that better results can be obtained if temperature optimization is used.

We used a cylindrical shaped applicator, which can effectively create a homogeneous focus in the breast. The width of the focus relates linearly to the wavelength ($\pm \lambda/3$), however the length is limited by the applicator geometry. Increasing the number of elements per ring or the number of rings does not decrease the focus length^{8,148}. Therefore it might be worthwhile to place additional antennas at the bottom surface of the cylinder.

10.5 Conclusions

“Virtual prototyping” using simulations is used to demonstrate that the *HYPERcollar* can heat tumours in the intact breast up to 44 °C while keeping the temperature in normal tissues below 41 °C. Therefore, this pilot study shows that redesigning the *HYPERcollar* may be of interest to enable heating tumours in intact breasts to stimulate radiotherapy or chemotherapy. However, further research must be preceded by an extensive analysis of clinical needs to distinguish the target patient population. This study then enables making an evidence based choice between EM and US technology, and provides the foundation for further steps.

11. RF dosimetry

RF dosimetry in patients and medical staff
during hyperthermia treatments

This chapter is based on:

JF Bakker, RA Canters, E Neufeld, MM Paulides and GC van Rhoon. "EMF dose in patients and medical staff during hyperthermia treatment of cancer". International Symposium on Electromagnetic Compatibility, Rome, Italy, 2012.

JF Bakker, MM Paulides, RA Canters, and GC van Rhoon. "EMF exposure assessment of healthy persons during loco-regional hyperthermia using the BSD-2000 Sigma 60 system". 27th Annual meeting of the European Society for Hyperthermic Oncology (ESHO), Aarhus, Denmark, 2011.

JF Bakker, RA Canters, MM Paulides, and GC van Rhoon. "Hot feet in the BSD Sigma 60: a numerical study of whole-body exposure". 26th Annual meeting of the European Society for Hyperthermic Oncology (ESHO), Rotterdam, The Netherlands, 2010.

Abstract

Purpose: At the Erasmus Medical Center, we apply hyperthermia treatments (HT) of cancer in the pelvic area using an electromagnetic applicator installed in a Faraday shielded treatment room. Consequently, medical staff and accompanying persons are exposed to electromagnetic fields (EMF) during treatment. In the past, procedures were defined based on measurements defining compliant areas where the fields are expected to be below the exposure guidelines. Today, advanced electromagnetic models enable more precise dose assessment in the human anatomy and better evaluation of the procedures. The objective of this study was to investigate theoretically if the exposure of medical staff and accompanying persons is compliant to the guidelines when adhering to the procedures. **Materials and methods:** Hereto, Finite Difference Time Domain (FDTD) modelling was used to assess the whole-body averaged (SAR_{wb}) and spatial-averaged (SAR_{10g}) specific absorption rate in whole-body models of the Virtual Family, mimicking the patient, medical staff and an accompanying person. **Results:** We found that predicted fields can exceed the exposure guidelines ten fold. However, the basic restrictions on SAR_{wb} and SAR_{10g} are not exceeded for workers, but SAR_{wb} can exceed the guideline by a factor of two for accompanying persons that are in close vicinity of the applicator. As side-issue, we found that comfort complaints in the feet reported by some of our patients are related to locally increased SAR_{10g} levels, i.e. up to 50% of those in the main pelvic target area. **Conclusions:** In conclusion, adhering to the procedures defined in the early nineties is effective in keeping the exposure in medical staff and accompanying persons compliant to the exposure guidelines.

11.1 Introduction

Hyperthermia, an increase of the temperature towards 40 to 44°C, is a powerful modality to improve the clinical outcome of radiotherapy and chemotherapy⁶⁷. At the Erasmus Medical Center (The Netherlands), we use the BSD-2000 $\Sigma 60^*$ to heat tumours in the pelvic area. This applicator contains a phased-array consisting of a single ring of eight dipole antennas, operating at radio frequencies (RF) in the range of 70-100 MHz. High power (0.5-1 kW) RF electromagnetic waves are required to increase the temperature in the pelvis within 30 minutes (“heating” phase) to therapeutic temperatures, which is maintained in the 60 minutes “plateau” phase. The system is installed in an air-conditioned Faraday cage for electromagnetic compatibility (EMC).

Clinical application of loco-regional deep HT can be a physiologically stressful treatment.

*BSD medical systems, Salt Lake City, USA

Therefore, medical staff and accompanying persons regularly enter the treatment room to check, relax and improve comfort of the patient (Figure 11.2). Consequently, these persons are exposed to electromagnetic fields for extended periods. Further, the number of patient referrals is increasing and hence the medical staff members are exposed more frequently.

Publications reporting the exposure levels during clinical application of loco-regional deep hyperthermia are scarce. Accurate data on the electromagnetic field exposure levels are clearly required, after activation of the health and safety guidelines addressed by the European Parliament⁵³ and the International Commission on Non-Ionizing Radiation Protection (ICNIRP)⁹⁹.

Therefore, procedures are applied in which compliant areas are defined where radiation levels are below the ICNIRP limit of 10 Wm^{-2} for workers. These procedures are based on an internal report describing the results from isotropic radiation measurements performed in 1993 at 36 prescribed locations around the BSD-2000 $\Sigma 60$ system and for different patients and treatment sessions (Figure 11.1). As a result of the measurements, accompanying persons are asked to sit on a specific chair, at which the fields are compliant to the reference levels for the general public. We do note that the field measurements in the Faraday treatment room were limited to a 2D plane at 1 m above the ground, and that the results are sensitive to the exact position of probe and the person performing the measurements.

Today, advanced numerical electromagnetic models are available, such that also the internal dose in both medical staff and accompanying persons can be assessed. Hence, we can use these models more rigorously to test compliance for various exposure scenarios and to update our working procedures when necessary.

We recently introduced patient-specific treatment planning to optimize the heating profiles in patients in standard clinical practice. Hereto, dielectric patient models are constructed from Computed Tomography (CT) slices from the knees upto mid abdomen (Figure 11.3a). Hence, influences of the legs, arms and head on the specific absorption rate (SAR) distribution are neglected. In clinical practice, comfort complaints at the feet and ankles are reported by our patients (Figure 11.3b). Although it is assumed that body parts outside the applicator are not heated, medical staff respond by using water bags and by applying cold and wet towels as effective measures to cool the feet. These RF power related complaints are decreased after using the water bags and towels.

The objective of this study was to investigate if the exposure of medical staff and accompanying persons are compliant to the guidelines when adhering to the working procedures. As a side-issue, we investigated if reported comfort complaints in the feet of patients are caused by local increased $\text{SAR}_{10\text{g}}$ values.

11.2 Methods

We assessed the electromagnetic fields in the treatment room using simulations. Based on these fields, we calculated the SAR in patients, medical staff and accompanying persons.

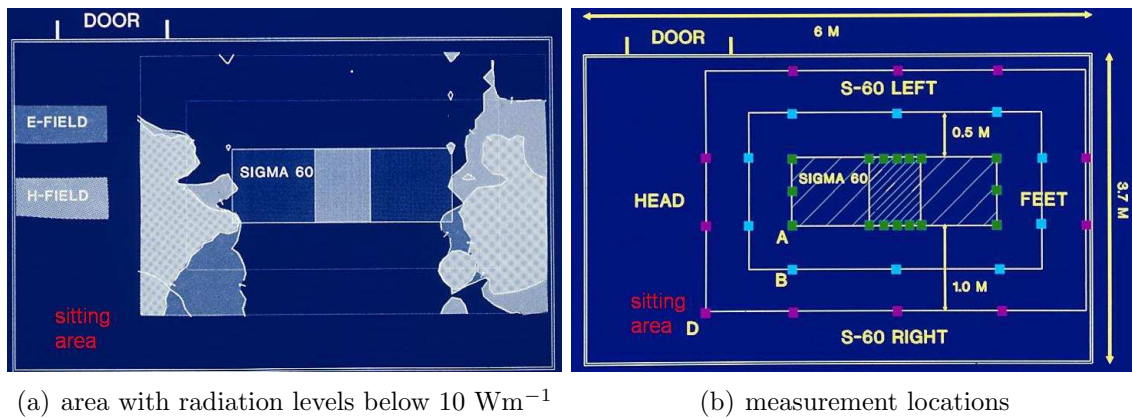


Figure 11.1: Measured radiation levels (a) at predefined locations (b) during a hyperthermia treatment at 90 MHz and 500 W.



Figure 11.2: Example of medical staff and a patient in the BSD-2000 $\Sigma 60$.

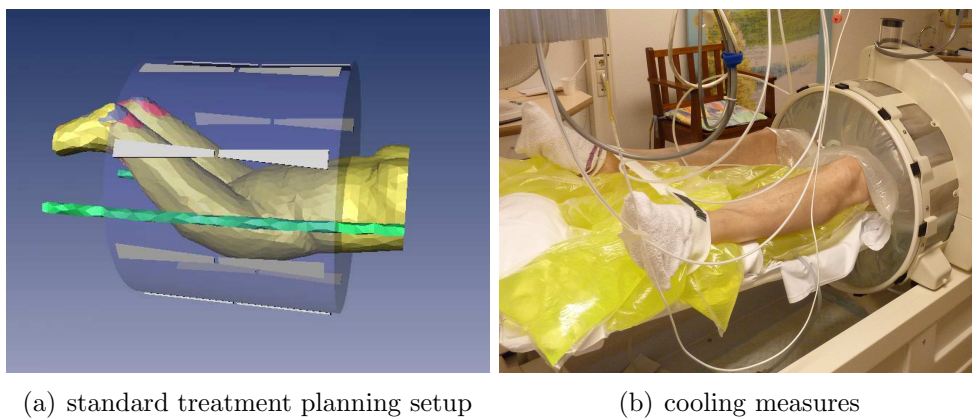


Figure 11.3: CT slices from the knees upto mid abdomen (a) and cold water bags and wet towels to reduce the temperature at the feet (b).

11.2.1 Simulation settings

FDTD modelling¹⁶⁷ was used to compute the incident fields generated by the BSD-2000 $\Sigma 60$ in the treatment room and to compute the SAR_{10g} and SAR_{wb} in the human body at several positions (Figure 11.4). The coaxial feedings of the eight dipole antennas are modelled by placing edge sources at the gap between the two conducting strips. The sources have an electrical impedance of 100 Ω , equal amplitudes and phases and operate at a frequency of 90 MHz. The input power of the sources was 1000 W, i.e. the maximum observed in all treatments. Demineralized water (relative permittivity $\epsilon_r=80$ and effective conductivity $\sigma_{eff}=0.001 \text{ Sm}^{-1}$) is applied between the patient and the cylindrical array for both skin cooling and efficient coupling of the electromagnetic energy into the patient. The dielectric model further included the plastic parts of the BSD-2000 $\Sigma 60$ ($\epsilon_r=2.1$, $\sigma_{eff}=0 \text{ Sm}^{-1}$), wooden cabinets and walls ($\epsilon_r=5$, $\sigma_{eff}=0.1 \text{ Sm}^{-1}$), a linoleum floor ($\epsilon_r=2.1$, $\sigma_{eff}=0.1 \text{ Sm}^{-1}$), and a metal housing of the air-conditioning (perfectly conducting).

11.2.2 Exposure scenarios

The SAR_{10g} and SAR_{wb} were assessed for various scenarios. First, we inserted the whole-body Ella model of the Virtual Family²³ in the BSD-2000 $\Sigma 60$ applicator (Figure 11.4a) to investigate locally increased SAR levels at the feet. By default, the treatment room was assigned as perfectly conducting (PEC) material. To study their influence, we modelled the room also as uni-axial perfectly matched layers (UPML) to investigate the effect of the reflecting Faraday cage on the results.

The exposure in medical staff and accompanying persons were assessed for three scenarios: 1) at 5 cm distance from the applicator at the right side of the patient, 2) near the feet of the patient, and 3) at the default sitting area for the accompanying person, i.e. close to the wall at a distance of approximately 1.5 m from the applicator (Figure 11.4b).

The patient, medical staff and accompanying persons were mimicked using the 26 year old female “Ella” of the Virtual Family²³. The patient and medical staff were in their original straight position. The SEMCAD X poser tool was used to change the posture for the sitting accompanying person. Dielectric properties of the various tissues were assigned according to the 4-Cole-Cole dispersion model of Gabriel^{74,87}.

11.3 Results

11.3.1 Influence of conductive human on field measurements

Figure 11.5 demonstrates that a conducting human affects the electric field distribution in the room in this case locally by a factor five.

11.3.2 EMF dose in medical staff and accompanying persons

Figure 11.6 shows the SAR_{10g} distributions in medical staff that are in close vicinity of the applicator, i.e at the centre of the applicator and at the feet of the patient. Increased SAR values are observed at the ankles, knees and the arms. Both SAR_{wb} (0.15 Wkg^{-1}) and SAR_{10g} (1.8 Wkg^{-1}) are maximum for the centre position. Table 11.1 lists the SAR_{wb} and SAR_{10g} in medical staff and in accompanying persons for various locations in the treatment room. The basic SAR restrictions for “workers” and “general public” are included for comparison.

Medical staff using the BSD-2000 $\Sigma 60$ can be exposed to electromagnetic fields above the ICNIRP guidelines. Basic restrictions on SAR_{wb} and SAR_{10g} are not exceeded for the investigated scenarios. The SAR_{wb} in accompanying persons can exceed the basic restriction by a factor of two when they are in close vicinity of the applicator. Therefore, these persons are instructed to sit on a chair at 1.5 m distance from the applicator during the length of the treatment and thereby reducing their exposure to the acceptable level.

11.3.3 EMF dose in patients

(Figure 11.7) demonstrates increased electric fields near the patients head, shoulders, ankles and feet. We allocate these whole-body resonance effects to the electric fields aligned parallel to the length of the patient body that is approximately half a wavelength in air. Standing modes due to reflections at the metal treatment room, result in areas with low or high field intensities within the chamber. For a perfectly conducting treatment room (PEC), these reflections coincide with the whole-body resonance locations at the head and feet. The observation of increased electric fields at the extremities of the body does not

Table 11.1: Simulated electric fields in air (E_{rms}), whole-body averaged (SAR_{wb}) and peak localized (SAR_{10g}) specific absorption rate in medical staff and accompanying for various positions (centre, head and feet) with respect to the patient. The input power of the applicator is 1000 W. ^{*1} indicates the ICNIRP restriction for the SAR_{10g} in the head or trunk and ^{*2} for those in the extremities.

	E_{rms} Vm^{-1}	SAR_{wb} Wkg^{-1}	SAR_{10g} Wkg^{-1}
<i>ICNIRP guidelines</i>			
general public	28	0.08	$2^{*1}/4^{*2}$
workers	61	0.4	$10^{*1}/20^{*2}$
<i>Simulated values</i>			
centre	190-949	0.15	1.8
head	100-300	0.04	0.98
feet	80-320	0.07	0.80
chair	63	0.01	0.05

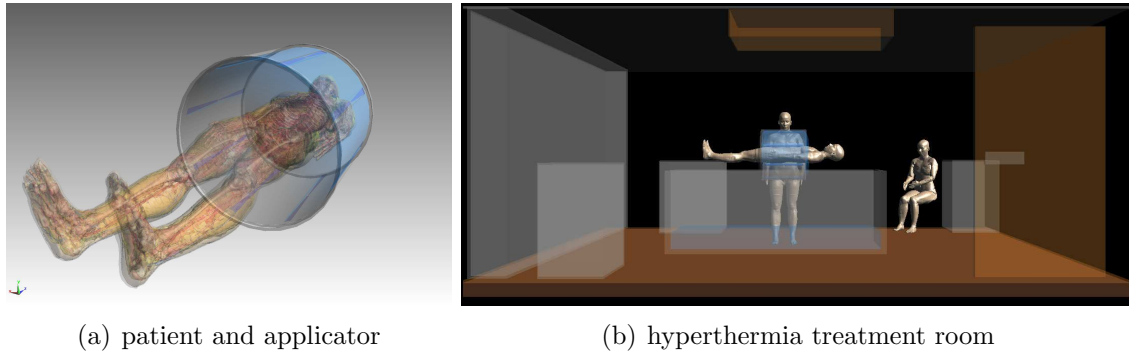


Figure 11.4: Modelled exposure configurations during deep hyperthermia treatments with the BSD-2000 $\Sigma 60$ applicator in the treatment room.

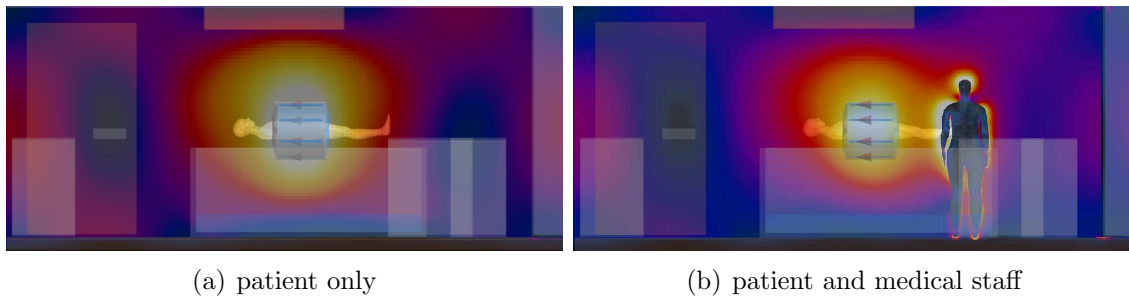


Figure 11.5: Influence of the presence of medical staff on the electric field (E_{rms}) in the treatment room. The colorscale is from black (0%) to white (100%).

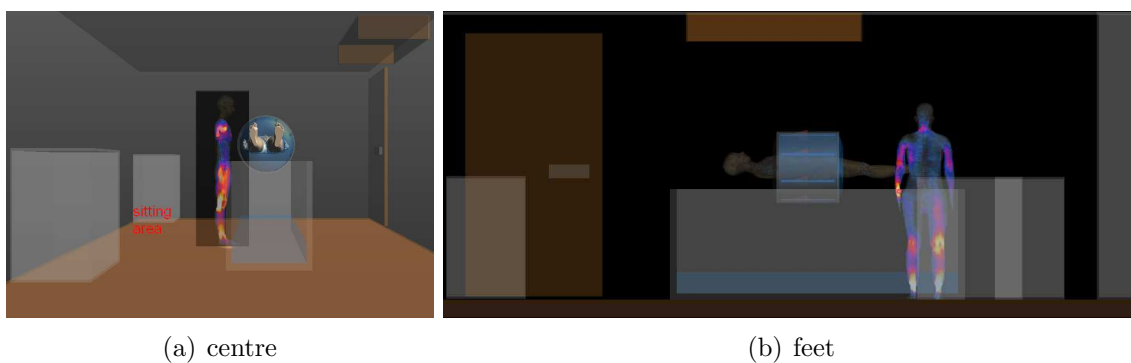


Figure 11.6: Localized specific absorption rate (SAR_{10g}) distributions in medical staff for standing near the centre of the applicator or near the feet of the patient. The colorscale is from black (0%) to white (100%).

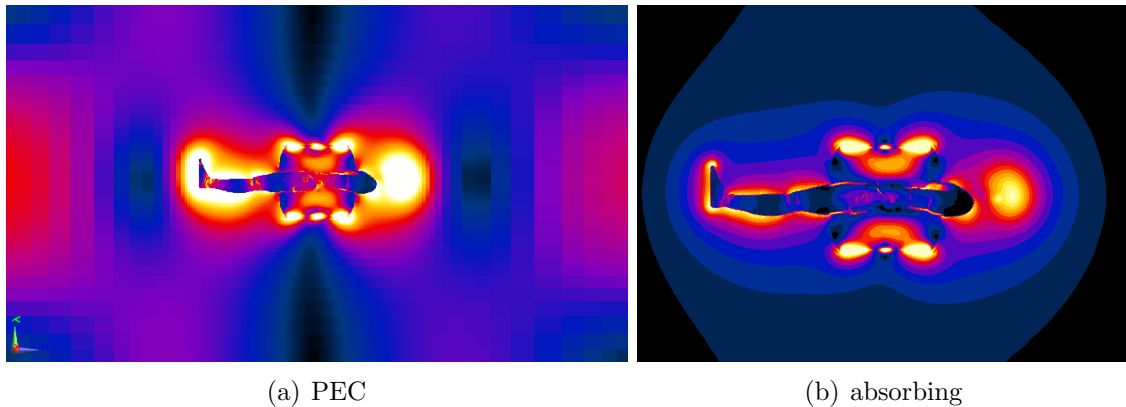


Figure 11.7: Simulated electric fields (E_{rms}) in the treatment room which is modelled either as perfectly electrically conducting (PEC) or absorbing. The colorscale is from black (0%) to white (100%).

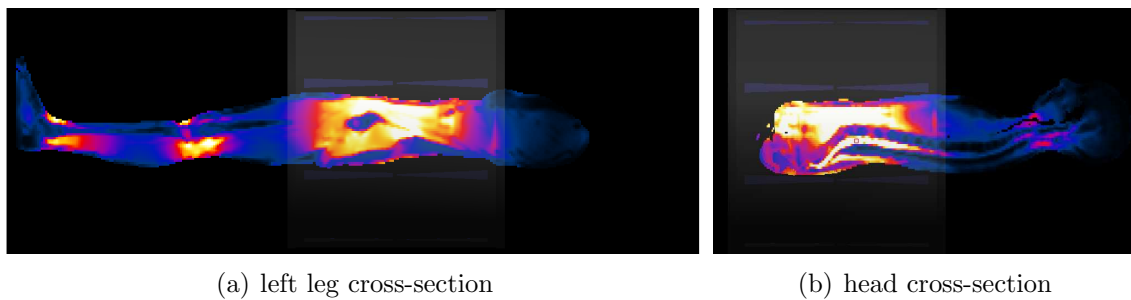


Figure 11.8: Simulated localized specific absorption rate averaged over 10g tissue ($\text{SAR}_{10\text{g}}$) in a patient that is treated using the BSD-2000 $\Sigma 60$ hyperthermia applicator. Note that the treatment room, i.e. a Faraday cage is modelled by perfectly electrically conducting (PEC) boundaries. The colorscale is from black (0%) to white (100%).

automatically lead to strong absorption levels, since the coupling from the water bolus to the body is more efficient than from air. For an absorbing treatment room, the peak $\text{SAR}_{10\text{g}}$ values in the feet are only 10% of those at the target location in the pelvic region. However, for a reflecting treatment room, the peak $\text{SAR}_{10\text{g}}$ values at the feet are up to 50% of SAR_{max} (Figure 11.8).

11.4 Discussion

Advanced electromagnetic modelling tools are extremely useful to study the exposure of patients, medical staff and accompanying persons during hyperthermia treatments in

detail.

Coupling of electromagnetic energy into the standing workers is not maximum, since the electric fields are aligned perpendicular to the main body axis. In addition, equal amplitude and phase settings were used, while these might differ in real treatments. Altered RF signals will lead to different interference patterns in the treatment room and therefore to different SAR distributions in the anatomy of medical staff and accompanying persons. Finally, we investigated only straight and sitting anatomies while other postures can occur in daily treatments. Hence, we investigated a limited amount of typical scenarios and more work is required to assess worst-case exposure conditions.

The simulations show that a conducting human affects the electric field distribution in the treatment room. Hence, for the earlier assessment of the electric fields measured using a hand-held monitor, it is clear that the local fields were strongly affected by the person that performed the measurements. Although the field measurements performed in 1993 provide only an estimate of the order of intensity levels, the derived working procedures are supported by the additional information provided from the detailed simulations.

It is relevant to mention that the treatment room is equipped with a high capacitance of air-conditioning to keep the room temperature below 20 °C. The latter is done to actively cool the patient during loco-regional deep hyperthermia, but is of course also beneficial for medical staff or other persons in the room to regulate body temperature.

Comfort complaints at the feet reported by patients are related to local increased SAR levels, not detected in standard treatment planning using limited CT scans. These increased SAR levels are caused by whole-body resonances due to the fact that the length of the patient is approximately half a wavelength in air. More patient anatomies including different lengths should be simulated to investigate the range of these increased SAR levels as function of anatomy length. For clinical hyperthermia planning, whole-body patient models or model extensions are required to predict complaints that occur far from the treatment region and to include effects on the SAR distribution in the pelvic region. Further, more work is required to investigate the optimum measure that can be taken to minimize the SAR values in the feet and potentially avoid complaints in this region. Furthermore, we recommend to study the effect of neglecting certain body parts in hyperthermia treatment planning on the SAR distributions in the pelvic region.

11.5 Conclusions

The current procedure for medical staff during hyperthermia treatments using the BSD-2000 $\Sigma 60$ result in exposure levels that are compliant to the basic restrictions of the ICNIRP guidelines. For accompanying persons, we allocated a chair at 1.5m distance from the applicator reducing their exposure to a compliant level. Comfort complaints in the feet of patients are caused by local increased SAR values.

12.

Discussion

General discussion and perspectives

12.1 Exposure assessment using numerical simulations

In general, it is difficult to use direct measurements in humans to assess the absorbed dose resulting from exposure to EMF. Therefore, numerical electromagnetic and thermal models are used to predict the complex interaction between EMF and the human anatomy. Validation of these numerical models is usually obtained by comparing its results to 1) analytical solutions of simple geometries or 2) 2D and 3D measurements in homogeneous phantoms.

Medical applications such as hyperthermia treatments provide unique possibilities to verify the applied dose inside the body. Fibre-optic thermometers are placed interstitially to control the temperature in the tumour and in normal tissues. Recent advances in non-invasive MR thermometry offers great future opportunities to obtain 3D data. Hence, these in-vivo patient-specific measurements are of great value for assessing the accuracy of the model predictions.

Furthermore, the applied fields in medical applications are in general orders of magnitude higher than those defined in the guidelines for healthy persons. Potentially, this will lead to established threshold dose levels for e.g. normal and critical tissues, relevant for defining tissue specific safety factors in future guidelines.

12.2 Evaluation of the exposure guidelines

To avoid adverse health effects, exposure limits have been developed using approximated models of the human anatomy^{99,101}. It is assumed that the reference levels are determined for the worst-case situations, such that the maximum permitted internal dose levels will not be exceeded.

In this thesis, a comprehensive assessment of the exposure to different EMF sources is provided for both children and adults. An evaluation is made how the guidelines, based on simple models, translate to the dose in complex anatomies in various population groups.

ELF guidelines: 1 Hz to 100 kHz The ELF guidelines¹⁰¹ are based on established effects in volunteers exposed to low frequency magnetic fields. These effects include muscle and nerve stimulation, and the perceived flickering of light due to the induction of phosphenes in the retina.

The reference levels are adequate for nearly all cases. However, for workers the basic restriction on the permitted internal electric fields (E_i) is occasionally exceeded by maximum 79%. The basic restriction in workers is set without any reduction factor, at the phosphene threshold to avoid disturbing light flickering and brain function effects. Therefore, fine-tuning of the guidelines is required by lowering the reference levels for the magnetic fields at specific frequencies.

ICNIRP recommends contiguous averaging and taking the 99th percentile, to suppress

local peak electric fields due to numerical stair-casing errors and to provide a biologically reasonable averaging distance. However, in this thesis it is shown that these recommendations cause the computational results from various research institutes to depend strongly on the grid discretization and the amount of tissues defined in the anatomical models. It is therefore recommended to investigate if the percentile can be replaced with the peak averaged value of the electric field, under the condition that sufficient oversampling of the anatomy is obtained to avoid errors by numerical artefacts.

RF guidelines: 100 kHz to 300 GHz The basic restrictions⁹⁹ on the whole-body-averaged (SAR_{wb}) and the peak 10g spatial-averaged (SAR_{10g}) specific absorption rate are designed to prevent whole-body heat stress. The restrictions are assumed to keep the whole-body temperature increase under 1 °C during 30 minutes and to prevent excessive localized tissue heating.

The reference levels are adequate for nearly all cases, i.e. the prediction from the early eighties is surprisingly close to those using detailed anatomical models. However, for young children, and therefore also for small individuals, the basic restriction on SAR_{wb} is occasionally exceeded by maximum 45%. A reduction factor of 50 for the general public is applied in the SAR_{wb} limits to assure that threshold dose levels, at which biological effects have been established, are not exceeded. However, it is undesirable that this factor is used to cover the uncertainty margins for worst-case exposure conditions. Therefore, fine-tuning of the guidelines is required by lowering the reference levels for the electromagnetic fields*. The peak SAR_{10g} values remain under the limit for all scenarios studied. However, the observation of peak SAR values in children raised further questions about potentially excessive localized tissue heating. In this thesis it is shown that a local peak temperature increase as high as 1 °C can occur. Thermal tissue damage is not only determined by the absolute temperature but also by the exposure time. Hence, it is recommended to define tissue-specific limits on local peak temperature increase for specified durations of exposure in future guidelines.

Uncertainty A rigorous uncertainty assessment should be included when arguing the consistency of exposure guidelines or predicting the dose in medical applications. It is common practice to test the validity of the numerical code by comparison to analytical solutions of simple problems. However, time-consuming and costly measurements, and a complete uncertainty evaluation of all the modelling parameters are usually not included. In this thesis three different solvers (finite-element ELF, FDTD RF, FDTD thermal) were used, which are validated by both analytical comparisons and 3D measurements. In addition, extensive sensitivity studies and (Monte Carlo) analyses were performed to address the effect on our results due to uncertainties in various modelling parameters such as, (age-dependent) tissue properties, discretization and boundary conditions.

*The Health Council of the Netherlands has adopted this recommendation to lower the reference levels for the electromagnetic fields at specific frequencies⁸⁹

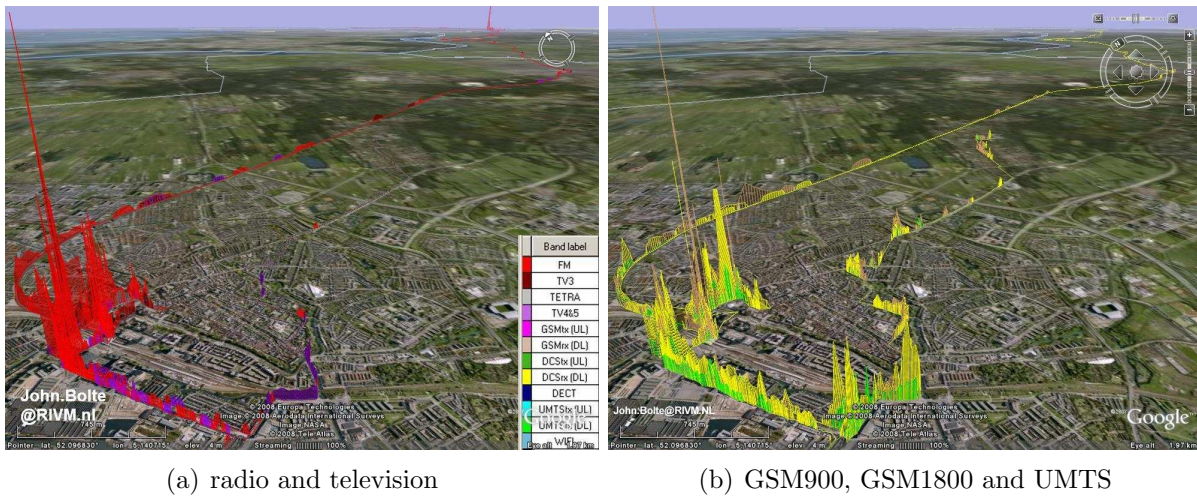


Figure 12.1: Example of personal electric field exposure plots between Bilthoven and Utrecht (The Netherlands) for FM radio (red) and television (purple) broadcasting and for GSM900 (brown), GSM1800 (yellow) and UMTS (green). Pictures are by courtesy of dr. John Bolte, National Institute for Public Health and the Environment (RIVM).



Figure 12.2: Screen-shot of the SAR distribution on top of the CT of a patient during an hyperthermia treatment in VEDO (Visualizer for Electromagnetic Dosimetry and Optimization) .

Exposure levels under daily life conditions In this thesis it is shown that the guidelines are not compliant, i.e. the EMF reference levels are not sufficient to keep the dose under the permitted basic restrictions for all cases. However, this finding does not automatically mean that humans are exposed to hazardous levels under daily life conditions. Daily life exposure levels are characterized both indoors and outdoors (Figure 12.1) by using personal exposure meters that record the field strengths in various frequency bands^{13,15,109,111}. In general, the measured EMF levels in the human environment are much lower (<0.1%) than the permitted reference levels. Hence, it is expected that the recommendation of lowering the reference levels in the RF guidelines has few consequences. Although the daily life field strengths are small compared to the reference levels, it is of great importance to continuously monitor these values for exceptions and to investigate new technologies that emit electromagnetic fields.

12.3 EMF dosimetry for medical applications

2D and 3D validation of hyperthermia planning tools Errors in the SAR and temperature predictions should be minimized, avoiding sub-optimal clinical outcome and safety issues expressed by burns or damage in critical tissues. Hence, quantitative validation of hyperthermia treatment planning systems is essential, followed by quality assurance (QA) by means of hardware calibrations and verification of the heating patterns.

In this thesis, both two (2D) and three (3D) dimensional QA measurements for the clinical head and neck hyperthermia applicator (HYPER*collar*) are shown. Hereto, a laboratory prototype applicator was constructed, i.e. the LAB*proto* in which fibre-optic thermometry, infra-red thermography and Schottky-diode electric-field measurements were performed. It is shown that the SAR focus can be steered in radial and axial direction and that the distributions are well predicted by the simulations.

The 2D measurements cover only a subset of the 3D applicator target volume. Fibre-optic thermometry is accurate but provides only a few 1D tracks. Electric field sheets are easy-to-use but provides low spatial resolution data. IR thermography provides high-resolution images, but requires opening the set-up for each IR picture, leading to long cooling times and decreased accuracies per experiment.

There is thus a need for fast and accurate 3D validation methods for hyperthermia planning models. The 3D SAR profiles of hyperthermia applicators can be measured in homogeneous liquids by using an electric field probe mounted on a robotic arm³¹(Figure 1.2c)[†]. Unfortunately, this system is inappropriate for measurements in solid phantoms or human anatomies.

We therefore explored if 3D Magnetic Resonance Imaging (MRI) scanners can be used to validate the RF excitation fields, i.e. the B_1^+ maps predicted by the hyperthermia planning tools. The gamma evaluation showed a good qualitative agreement between the predicted and measured B_1^+ fields inside the muscle-equivalent phantom of the LAB*proto*.

[†]Dasy5, Schmid & Partner Engineering AG, Switzerland

Quantitative validation is feasible, when accurate power and phase measurements are available during the B_1^+ mapping.

This B_1^+ mapping provides excellent possibilities to validate the electromagnetic models, such as the implementation of the FDTD code. In this case, we could also verify if the applicator model is described correctly. However, for hyperthermia applicators that are not MR compatible, such a validation is of course not feasible. In general, it is recommended to design hyperthermia applicators that can be modelled and validated easily.

The 7Tcollar: a hybrid hyperthermia and MRI applicator In general MRI is of great interest for hyperthermia applications, since it provides high resolution three-dimensional (3D) image data of patient-specific tissue parameters. Electric properties tomography (EPT) and blood perfusion MRI can be used to improve the accuracy of the predicted SAR and temperature distributions. The ultimate goal is to use MR for non-invasive thermometry in the tumour and to detect treatment limiting hot-spots.

The 7Tcollar has a great potential to be used effectively as a hybrid hyperthermia applicator and MR imaging device. Using the same Larmor frequency for both imaging and heating provide major advantages such as sharing one common RF amplifier system, on-line verification of the (predicted) fields and SAR in patients, and 3D QA by using the amplitude and phase of MR B_1^+ maps. However, 7T MR scanners are still state-of-the-art investigational devices which are used mainly for clinical research purposes. Commonly used 1.5T and 3.0T MR scanners generate larger wavelengths which is not suitable for focussed heating in the head and neck. For such scanners, separate amplifier systems are required, which are available⁶ but needs more work to decouple the MR and hyperthermia signals.

Virtual prototyping The 2D and 3D validation measurements showed that the numerical models are reliable in the prediction of the fields generated by the patch antennas. As a result, it is possible to design new applicators using “virtual prototyping”. The HYPERcollar was redesigned for intact breast tumours without actually constructing and testing the electrical and mechanical applicator itself. It is shown that the new design is capable of heating both central and deeply located tumours in the intact breast. Virtual prototyping was used to demonstrate that the 7Tcollar can be used effectively as a hybrid hyperthermia applicator and MR imaging device. Hence, virtual prototyping has become the standard in our research since it avoids time-intensive and costly experimental verifications. Note however, that regular verifications of the predicted SAR and temperature profiles needs to be integrated in QA procedures.

Dosimetry in patients and medical staff Advanced dosimetry software enables to visualize and characterize the exposure in both patients and medical staff. Based on the displayed SAR profiles, crucial decisions are made to improve the applied dose in the patient and to minimize the unwanted exposure of medical staff and accompanying persons. In this thesis, the exposure assessments are limited to hyperthermia treatments

with the BSD $\Sigma 60$ applicator. However, the exposure for superficial and head and neck treatments is now being evaluated. Exposure assessments for the medical staff can be extended from hyperthermia treatments to MR scanners and electrical surgery devices.

12.4 Future work and perspectives

Improved model input parameters The term “garbage in garbage out” (GIGO) is used in the field of computer science to indicate that powerful computers can produce large amounts of erroneous information in a short time. The results and its estimated uncertainties depend heavily on the availability and quality of the model input parameters, such as the tissue dielectric and thermal properties.

Useful data on living human tissues is sparse and therefore most of the data is based on post-mortal samples. It is therefore recommended to extend existing knowledge on human data. Special attention should be given to fill the existing gaps for the dielectric properties at frequencies below 1 MHz and for temperature-dependent blood perfusion levels. Fortunately, recent advances in MR electrical properties tomography (EPT) and non-invasive MR thermometry (MRT) provide great possibilities to investigate heterogeneities, anisotropies, and temperature dependent tissue properties in various anatomies. We strongly encourage to obtain such valuable inter- and intra-individual human data and make it publicly available[‡], such that other research groups can use the mean and spread of the values in assessing the uncertainty contribution to their modelling results.

Dosimetry for health risk characterization For defining conservative reference levels that are compliant with the basic restrictions it is essential to use a representative group of anatomies in the exposure evaluations. Although a great number of exposure scenarios using detailed models of six children and two adults in straight position are analysed, these few models do not represent the entire human population. We did not investigate postures including electrical loops potentially leading to locally increased fields. Therefore, it is recommended to extend the evaluation using a sufficient set of different anatomies (i.e. Asian, elderly, obese, pregnant woman, babies) including other than standing postures, to assess the worst-case envelope of the entire population.

In this thesis the analysis was restricted to uniform waves with various incidences and polarizations, such that the results are generic and can be used for a widespread of applications. There are a lot of applications however, where the anatomy is in the near field of non uniform radiating antennas. Detailed modelling of the emitting source and the position of the anatomy is then required to correctly predict if basic restrictions are exceeded. Although not shown in this thesis, research partner IT'IS Foundation performed near-field assessments within the scope of the ZonMw project[§], i.e. for mobile and DECT phones, induction cookers and for wireless devices worn or operated on the body. In parallel, other

[‡]online database of tissue properties <http://www.itis.ethz.ch/database>

[§]The Netherlands Organization for Health Research and Development (ZonMw)

studies have examined Wi-Fi stations, laptops and electronic article surveillance (EAS). There will be a continuous need for exposure assessments of specific devices, as there is an ongoing development of new wireless applications and technologies.

Dosimetry in medical applications The recent introduction of parallel computing by GPUs[¶] has led to substantial improvements in accuracy and speed of electromagnetic computations. Therefore, it has become possible to introduce patient-specific dosimetry planning for hyperthermia treatments, providing the medical staff a clear picture of the actual SAR distributions on top of the CT scan of a patient (Figure 12.2). The fast computer models enable maximizing treatment quality while minimizing unwanted exposure of medical staff. Furthermore, these models are used as efficient “virtual prototyping” tools for the design of improved medical devices, avoiding time-intensive experiments before constructing a real working clinical applicator.

The next technological step for hyperthermia treatments in the Erasmus MC, is to join the existing knowledge on hyperthermia and MR devices into a hybrid temperature imaging and heating device for various treatment sites of the human body. Together with online complaint-adaptive treatment planning, this will enable great possibilities to characterize and optimize the heat delivery for individual patients.

Dosimetry for biological and epidemiological studies The analysis in this thesis was restricted to macroscopic, i.e. tissue-specific exposure assessments. Frequently, only the fields external to Petri-dishes are reported in biological cell exposure studies. However, to identify the biological interaction with EMF, it is crucial to report also the induced internal, local field strengths, current densities, absorbed energy, and temperature increase. Similar dosimetric identifications are required for future epidemiological studies on possible effects caused by EMF.

[¶]Graphical Processor Units

Summary

Electromagnetic fields (EMF) are present everywhere in our environment but are usually invisible to the human eye. EMF for example generated by mobile phones and 50 Hz power lines, can cause electric fields, currents and tissue heating in the human body. In the past, exposure limits were developed to avoid adverse health effects. These limits were derived from dose assessments using simple models which for example approximate the human by homogeneous spheroids. Nowadays, state-of-the-art electromagnetic models enable to predict and visualize the propagation of electromagnetic waves in the human anatomy. This thesis shows that these models can provide detailed information on the exposure of the general public in daily life situations (**Part I**), and those of patients and staff in medical applications such as hyperthermia treatments of cancer (**Part II**). The common ground of these two parts is the assessment of the internal dose in the human anatomy upon exposure to external EMF.

Chapter 1 starts with a general introduction on the interaction of EMF with the human anatomy and on the topics addressed in this thesis. The three-dimensional (3D) anatomical models of adults and children are described in **Chapter 2**.

Part I: Exposure in daily life

Chapter 3 describes the ICNIRP^{||} guidelines, which recommend limits for the internal dose and maximum EMF reference levels. **Chapter 4** provides various examples of sources that emit EMF, in the near and far-field, and at extremely low (ELF) or radio frequencies (RF).

Chapter 5 shows the induced electric fields in children and adults that are exposed to uniform ELF magnetic fields at the maximum permitted field strengths. The electric

^{||}International Commission on Non-Ionizing Radiation Protection

fields are within the ICNIRP restrictions in nearly all cases, however they are occasionally exceeded by maximum 79% for workers. Therefore, fine-tuning of the guidelines is required by lowering the reference levels. The guidelines recommend an averaging method to suppress local peak electric fields caused by numerical artefacts. However, this method depends strongly on the grid discretization and the number of tissues in the anatomical models. Therefore, alternative routines should be considered, leading to consistent suppression of peak values.

In **Chapter 6**, the specific absorption rate (SAR) is assessed in children and adults that are exposed to RF electromagnetic plane waves. The limits for localized absorption (SAR_{10g}), designed to restrict temperature increase, are not exceeded for the scenarios studied. However, the restriction on whole-body averaged absorption (SAR_{wb}) is occasionally exceeded by maximum 45% in small children. Hence, fine-tuning of the guidelines is required by lowering the EMF reference levels. In 2011, the Health Council of the Netherlands has adopted this recommendation in their report on the influence of RF telecommunication signals on children's brains.

The peak SAR values in children raise further questions about the maximum tissue heating. Therefore, the peak temperature increase is assessed for worst-case exposure scenarios in **Chapter 7**. A local temperature increase as high as 1 °C can occur. Thermal tissue damage is determined by both temperature and exposure time. Therefore, limits on temperature increase for specified durations of exposure should be defined in future guidelines.

Part II: Exposure in medical applications

Focussed EMF are used in hyperthermia treatments to heat tumours in patients. In the last few years, accuracy and speed of electromagnetic modelling has improved substantially. Therefore, these models enable patient-specific treatment planning to target the EMF such that the absorption and temperature in the tumour is maximized. The same models can be used to minimize unwanted exposure of the medical staff, but also for the design of new medical equipment. However, quantitative model validation is mandatory to avoid a reduced clinical outcome or safety issues such as burns.

Chapter 8 describes the experiments performed to verify the model predictions for hyperthermia treatments in the head and neck region. A laboratory prototype head and neck applicator, i.e. the *LABcollar* is used to generate SAR patterns in a muscle-equivalent phantom. 2D measurements using electric field sensors, infra-red (IR) thermography and fibre-optic thermometry show that the SAR distributions are well predicted by the simulations.

The *LABcollar* is a cylindrical-symmetric configuration such that the 2D measurements

can be understood as semi 3D results. However, this method is not suited for 3D validation of asymmetric configurations. In general, MRI** is of great interest for hyperthermia applications since it provides high resolution 3D image data of patient-specific tissue parameters. Therefore a hybrid hyperthermia applicator and MR scanner has a great potential to be used effectively for both imaging and heating at various locations in the head and neck. Therefore, in **Chapter 9** it is explored if a hybrid hyperthermia applicator and 7T MR scanner can be used for 3D model validation and for heating tumours in the head and neck region. Experiments using a prototype applicator in a 7T MR scanner (*7Tcollar*) show a good qualitative agreement between the predicted and measured B_1^+ RF excitation patterns in a muscle phantom, expressed by less than 6% dose difference at a distance of 2 mm. Simulations show promising SAR and B_1^+ patterns for larynx and nasopharynx tumours.

Electromagnetic models can be used also for “virtual prototyping” of new medical equipment, avoiding time-intensive and costly experiments. In **Chapter 10** it is explored if an existing clinical applicator for head and neck tumours, i.e. the *HYPERcollar*, can be used also for intact breast tumours. Simulations show that the applicator can generate maximum 44 °C in both centrally and deeply located tumours, while keeping the temperature in normal tissues below 41 °C.

Chapter 11 demonstrates that electromagnetic models can be used to better understand the complex interaction of EMF with both patients and medical staff. At the Erasmus MC, hyperthermia treatments of pelvic tumours are applied using an electromagnetic applicator (BSD-2000 $\Sigma 60$), which is installed in an electrically conducting (Faraday) chamber. Medical staff and accompanying persons that enter this treatment room are exposed to EMF that exceed the ICNIRP reference levels. The SAR_{wb} and SAR_{10g} limits for medical staff are not exceeded for the investigated scenarios. The SAR_{wb} can exceed the basic restriction in accompanying persons by a factor of two when they are in close vicinity of the applicator. Therefore, these persons are instructed to sit on a chair and thereby reducing their exposure to the recommended level.

Some patients report complaints during the treatment. In the standard treatment planning, a patient model is constructed from a Computer Tomography (CT) scan that is limited to the pelvic area. Therefore, complaints outside this region are not predicted. Simulations using whole-body models show that these complaints could be due to high local SAR values at the feet, caused by resonance effects in the body and by reflections from the Faraday chamber.

**Magnetic Resonance Imaging

Samenvatting

Elektromagnetische velden (EMV) zijn overal in onze omgeving aanwezig, maar ze zijn meestal onzichtbaar voor het menselijk oog. EMV van bijvoorbeeld mobiele telefoons en hoogspanningsmasten, veroorzaken elektrische velden, stromen en opwarming in het menselijke lichaam. Om ongunstige gezondheidseffecten te voorkomen, zijn er in het verleden limieten voor de blootstelling aan EMV opgesteld. Deze limieten zijn afgeleid van berekeningen met simpele modellen die bijvoorbeeld de anatomie vereenvoudigen door een homogene ellipsoïde. Tegenwoordig zijn geavanceerde elektromagnetische modellen beschikbaar om de voortplanting van elektromagnetische golven in het menselijke lichaam te voorspellen en te visualiseren.

Dit proefschrift laat zien dat deze modellen gedetailleerde informatie kunnen geven over de blootstelling van de bevolking in het dagelijks leven (**Deel I**), en over die van patiënten en personeel in medische toepassingen zoals hyperthermie behandelingen bij kanker (**Deel II**). De overeenkomst tussen de twee delen in dit proefschrift is de bepaling van de interne dosis in de anatomie van de mens bij blootstelling aan externe EMV.

Hoofdstuk 1 begint met een algemene inleiding over EMV en over de onderwerpen in dit proefschrift. **Hoofdstuk 2** beschrijft de drie-dimensionale (3D) anatomische modellen van volwassenen en kinderen die gebruikt zijn in de dosisbepaling.

Deel I: Blootstelling in het dagelijkse leven

Hoofdstuk 3 beschrijft de ICNIRP^{††} richtlijnen, waarin limieten voor de interne dosis en maximale referentieniveaus voor externe EMV voorgesteld worden. **Hoofdstuk 4** geeft een aantal voorbeelden van apparaten die EMV produceren, in het nabije en verre stralingsveld, en met extreem lage (ELF) of radio frequenties (RF).

^{††}International Commission on Non-Ionizing Radiation Protection

Hoofdstuk 5 laat de geïnduceerde elektrische velden zien in kinderen en volwassenen die worden blootgesteld aan uniforme ELF magnetische velden bij de maximaal toegestane waarden. In bijna alle gevallen blijven de elektrische velden in het lichaam binnen de ICNIRP limieten, maar voor werknemers worden deze overschreden met maximaal 79%. De referentieniveaus voor EMV moeten dus worden verlaagd. In de richtlijnen wordt een methode aanbevolen om lokale piek elektrische velden te onderdrukken. Echter, deze methode blijkt sterk afhankelijk te zijn van de grid discretisatie en het aantal weefsels in de anatomische modellen. Daarom moeten alternatieve methodes overwogen worden voor een consistente onderdrukking van de piekwaarden.

In **Hoofdstuk 6** wordt de specifieke energie-absorptie-tempo (Specific Absorption Rate, SAR) bepaald in kinderen en volwassenen die worden blootgesteld aan RF elektromagnetische vlakke golven. De limieten voor de lokale absorptie (SAR_{10g}), bedoeld om de toename in lokale temperatuur te beperken, worden niet overschreden voor de bestudeerde scenario's. Echter, de limiet op lichaam gemiddelde absorptie (SAR_{wb}) wordt met maximaal 45% overschreden voor kleine kinderen. Daarom moeten de referentieniveaus in de richtlijnen worden verlaagd. In 2011 heeft de Nederlandse Gezondheidsraad deze aanbeveling overgenomen in hun rapport over de invloed van radiofrequentie telecommunicatie signalen op de hersenen bij kinderen.

De hoge lokale SAR waarden in kinderen roepen vragen op over de maximale weefsel verwarming. Daarom wordt in **Hoofdstuk 7** de piek temperatuurstijging bepaald voor worst-case blootstelling scenario's. Lokale temperatuurstijgingen van maximaal 1 °C zijn mogelijk. Weefschade wordt bepaald door de temperatuur en de blootstellingsduur. Er moeten dus limieten voor de lokale temperatuurstijging en de blootstellingsduur worden gedefinieerd in de richtlijnen.

Deel II: Blootstelling bij medische toepassingen

Bij hyperthermie behandelingen worden EMV gefocuseerd om tumoren in patiënten te verwarmen. De nauwkeurigheid en snelheid van het berekenen van de voortplanting van EMV is de afgelopen jaren aanzienlijk verbeterd. Deze verbetering maakt patiënt-specifieke behandelplanning mogelijk, waarbij de EMV zodanig gestuurd worden dat de absorptie en de temperatuur in de tumor maximaal is. Dezelfde modellen kunnen worden gebruikt om de ongewenste blootstelling van medische staf te bepalen en te verminderen, maar ook om nieuwe apparatuur te ontwerpen. Echter, kwantitatieve validatie van de gebruikte modellen is noodzakelijk om sub-optimale klinische resultaten en veiligheidsrisico's zoals brandwonden te voorkomen.

Hoofdstuk 8 beschrijft de experimenten die zijn uitgevoerd om de model voorspellingen voor hoofd-hals hyperthermie te verifiëren. Een laboratorium prototype hoofd-hals applicator (de *LABcollar*) is gebruikt om SAR patronen te maken in een spier-equivalent

fantoom. 2D metingen met elektrische veld sensoren, infrarood (IR) thermografie en glasvezel thermometers tonen aan dat deze SAR patronen correct voorspeld worden door de model simulaties.

De LAB*collar* is een cylinder symmetrische opstelling waardoor de 2D metingen als semi 3D geïnterpreteerd kunnen worden. Echter, voor 3D validatie van asymmetrische configuraties is deze methode niet geschikt. Het combineren van hyperthermie en MRI^{‡‡} heeft een groot potentieel voor het effectief verwarmen van tumoren, door de gedetailleerde informatie over patiënt-specifieke weefsel eigenschappen, zoals bijvoorbeeld de doorbloeding. In **Hoofdstuk 9** wordt daarom verkend of een hybride hoofd-hals hyperthermie en 7T MR scanner (7T*collar*) gebruikt kan worden voor 3D model validatie en voor het verwarmen van tumoren in het hoofd-hals gebied. Experimenten met een prototype (7T*proto*) en een 7T MRI scanner laten een goede overeenkomst (minder dan 6% verschil binnen een afstand van 2 mm) zien tussen de gemeten en voorspelde B_1^+ RF excitatie-velden in een spier fantoom. Simulaties tonen veelbelovende SAR en B_1^+ verdelingen voor larynx en nasopharynx tumoren.

Elektromagnetische modellen kunnen ook gebruikt worden in “virtual prototyping”, oftewel het efficiënt ontwerpen van nieuwe medische apparaten. Hierdoor worden tijdrovende en kostbare experimenten vermeden voordat de apparaten gefabriceerd worden. In **Hoofdstuk 10** wordt onderzocht of een bestaande klinische applicator voor hoofd-hals tumoren (de HYPER*collar*) kan worden ingezet voor het verwarmen van tumoren in de borst. Simulaties laten zien dat deze applicator maximaal 44 °C kan genereren in zowel centraal als diep gelegen tumoren, terwijl de temperatuur in normale weefsels onder de 41 °C blijft.

Hoofdstuk 11 laat zien dat de elektromagnetische modellen bijdragen aan een beter begrip van de complexe interactie van EMV met zowel patiënten als met medisch personeel. In het Erasmus MC worden tumoren in het bekkengebied verwarmd met een applicator (BSD-2000 Σ60) die is geïnstalleerd in een elektrisch geleidende (Faraday) ruimte. Medische staf en begeleiders die deze ruimte betreden, worden blootgesteld aan EMV die de maximaal toelaatbare niveaus overschrijden. De SAR_{wb} en SAR_{10g} limieten voor het medisch personeel worden niet overschreden voor de onderzochte scenario's. De SAR_{wb} kan de limiet voor begeleiders met een factor twee overschrijden, wanneer zij dichtbij de applicator zijn. Daarom worden begeleiders van patiënt worden geïnstrueerd om op een stoel op enige afstand te zitten, waardoor de blootstelling tijdens de behandeling minder dan de toegestane limiet is.

Sommige patiënten rapporteren klachten in de voeten tijdens de behandeling. Door de beperkte Computed Tomography (CT) scan van het bekkengebied worden deze klachten niet voorspeld door de behandelplanning. Simulaties met volledige patiënt modellen tonen aan dat de klachten in de voeten van patiënten verklaard kunnen worden door hoge

^{‡‡}Magnetic Resonance Imaging

lokale SAR waarden, veroorzaakt door resonanties in het lichaam en door reflecties van de Faraday kooi.

PhD portfolio

Courses

2012 Photoshop and Illustrator CS5, Erasmus MC

2009 Biomedical English writing and communication, Erasmus MC

2008 Biomedical Research Techniques, Erasmus MC

2005 Advanced programming in MATLAB, Mathworks

Educational activities

Supervision of Master's and Bachelor's projects:

2011 Thyrsa Jagt. Applied Mathematics at Delft University of Technology

2010 Roel Roskam. Integrated Product Design at Delft University of Technology

2010 Margit de Kever. Applied Mathematics at Delft University of Technology

2009 Boudewijn Slager. Applied Physics at The Hague University of Applied Sciences

2007 Pim Hoek. Applied Physics at The Hague University of Applied Sciences

2005 Koos Goekoop. Applied Physics at The Hague University of Applied Sciences

2004 Wouter den Haan. Applied Physics at The Hague University of Applied Sciences

Other teaching activities:

Open door days Radiation oncology department, Radiotherapy symposium, various excursions for Delft University of Technology, Eindhoven University of Technology and The Hague University of Applied Sciences. Various teaching sessions to hyperthermia technicians

Advisory reports

EMF dosimetry and SAR calculations for the Dutch Health Council. Invloed van radiofrequente telecommunicatiesignalen op kinders Hersenen. Den Haag: Gezondheidsraad, 2011; publicatienr. 2011/20. ISBN 978-90-5549-853-6

<http://www.gezondheidsraad.nl/sites/default/files/201120.pdf>

Reviews

Reviewer for grant proposals and full papers of the Dutch Cancer Society (KWF), Physics in Medicine and Biology, International Journal of Hyperthermia, IEEE Transactions on Biomedical Engineering, Radiation Research, Journal of Electromagnetic Waves and Applications and Progress in Electromagnetic Research.

Books

MM Paulides, JF Bakker, J van der Zee, and GC van Rhoon. Contouring for targeted head and neck hyperthermia, in “Contouring in head and neck cancer: P Levendag, A Al-Mamgani and D Teguh, Elsevier GmbH, 2009”

Honors

Featured article from IOP Journals. JF Bakker, MM Paulides, E Neufeld, A Christ, N Kuster, and GC van Rhoon. Children and adults exposed to electromagnetic fields at the ICNIRP reference levels: theoretical assessment of the induced peak temperature increase. *Phys Med Biol*, 57:1815–1829, 2012

Travel grant for the 33th annual meeting of the Bioelectromagnetic Society (BEMS), Halifax, Canada, 2011

Roberts Prize for the best paper published in 2010 in Physics in Medicine and Biology. MM Paulides, JF Bakker, M Linthorst, J van der Zee, Z Rijnen, E Neufeld, PMT Pattynama,

PP Jansen, PC Levendag and GC van Rhoon. The clinical feasibility of deep hyperthermia treatment in the head and neck: new challenges for positioning and temperature measurement. *Phys Med Biol*, 55:2456–2480, 2010

Winner of the “New Investigator Award” at the European Society of Hyperthermia Oncology Meeting 2007. MM Paulides, JF Bakker, E Neufeld, J van der Zee, PP Jansen, PC Levendag, and GC van Rhoon. The HYPERcollar: a novel applicator for hyperthermia in the head and neck. *Int J Hyperthermia*, 23(7):567-76, 2007

International journal publications

JF Bakker, MM Paulides, E Neufeld, A Christ, XL Chen, N Kuster, and GC van Rhoon. Children and adults exposed to low frequency magnetic fields at the ICNIRP reference levels: theoretical assessment of the induced electric fields. *Phys Med Biol*, 57:1815–1829 2012.

JF Bakker, MM Paulides, E Neufeld, A Christ, N Kuster, and GC van Rhoon. Children and adults exposed to electromagnetic fields at the ICNIRP reference levels: theoretical assessment of the induced peak temperature increase. *Phys Med Biol*, 56:4967–4989, 2011

JF Bakker, MM Paulides, A Christ, N Kuster, and GC van Rhoon. Assessment of induced SAR in children exposed to electromagnetic plane waves between 10 MHz and 5.6 GHz (corrigendum).” *Phys Med Biol*, 2856–2883, 2011.

JF Bakker, MM Paulides, A Christ, N Kuster, and GC van Rhoon. Assessment of induced SAR in children exposed to electromagnetic plane waves between 10 MHz and 5.6 GHz. *Phys Med Biol*, 55:3115–3130, 2010.

JF Bakker, MM Paulides, AH Westra, H Schippers, and GC van Rhoon. Design and test of a 434 MHz multi-channel amplifier system for targeted hyperthermia applicators. *Int J Hyperthermia*, 26:158–170, 2010.

JF Bakker, MM Paulides, IM Obdeijn, GC van Rhoon, and KWA van Dongen. An ultrasound cylindrical phased array for deep heating in the breast: theoretical design using heterogeneous models. *Phys Med Biol*, 54:3201–3215, 2009.

A Christ, R Guldimann, B Bühlmann, M Zefferer, JF Bakker, GC van Rhoon and N Kuster. Exposure of the human body to professional and domestic induction cooktops compared to the basic restrictions, *Bioelectromagnetics*, 2012.

MM Paulides, JF Bakker, M Linthorst, J van der Zee, Z Rijnen, E Neufeld, PM Pattynama, PP Jansen, PC Levendag, and GC van Rhoon. The clinical feasibility of deep

hyperthermia treatment in the head and neck: new challenges for positioning and temperature measurement. *Phys Med Biol*, 55:2465–2480, 2010.

RA Canters, P Wust, JF Bakker, and GC van Rhoon. A literature survey on indicators for characterisation and optimisation of SAR distributions in deep hyperthermia, a plea for standardisation. *Int J Hyperthermia*, 25:593–608, 2009.

MM Paulides, JF Bakker, E Neufeld, J van der Zee, PP Jansen, PC Levendag, and GC van Rhoon. Winner of the “New Investigator Award” at the European Society of Hyperthermia Oncology Meeting 2007. The HYPERcollar: a novel applicator for hyperthermia in the head and neck. *Int J Hyperthermia*, 23:567–576, 2007.

MM Paulides, JF Bakker, N Chavannes, and GC van Rhoon. A patch antenna design for application in a phased-array head and neck hyperthermia applicator. *IEEE Trans Biomed Eng*, 54:2057–2063, 2007.

MM Paulides, JF Bakker, AP Zwamborn, and GC van Rhoon. A head and neck hyperthermia applicator: theoretical antenna array design. *Int J Hyperthermia*, 23:59–67, 2007.

MM Paulides, JF Bakker, and GC van Rhoon. Electromagnetic head-and-neck hyperthermia applicator: experimental phantom verification and FDTD model. *Int. J. Radiat. Oncol. Biol. Phys.*, 68:612–620, 2007.

M de Bruijne, T Samaras, JF Bakker, and GC van Rhoon. Effects of waterbolus size, shape and configuration on the SAR distribution pattern of the Lucite cone applicator. *Int J Hyperthermia*, 22:15–28, 2006.

Publications at conferences

JF Bakker, RA Canters, MM Paulides and GC van Rhoon. EMF dose in patients and medical staff during hyperthermia treatment of cancer. *EMC Europe, Rome, Italy*, 2012.

JF Bakker, MM Paulides, E Neufeld, A Christ, N Kuster, and GC van Rhoon. Assessment of the induced SAR and peak temperature increase in children exposed to electromagnetic fields at the ICNIRP reference levels. *33th Annual meeting of the Bioelectromagnetic Society (BEMS), Halifax, Canada*, 2011.

JF Bakker, MM Paulides, RA Canters, and GC van Rhoon. EMF exposure assessment of healthy persons during loco-regional hyperthermia using the BSD-2000 Sigma 60 system. *27th Annual meeting of the European Society for Hyperthermic Oncology (ESHO), Aarhus*,

Denmark, 2011.

JF Bakker, MM Paulides, E Neufeld, A Christ, N Kuster, and GC van Rhoon. Children exposed to radio frequency fields: numerical assessment of induced absorption and temperature increase. *3rd Dutch Bio-Medical Engineering Conference, Egmond aan Zee, The Netherlands*, 2011.

JF Bakker, MM Paulides, E Neufeld, A Christ, N Kuster, and GC van Rhoon. Interaction of electromagnetic fields and the human body: tools for predicting induced absorption, currents and temperature Rise. *3rd Dutch Bio-Medical Engineering Conference, Egmond aan Zee, The Netherlands*, 2011.

JF Bakker, RA Canters, MM Paulides, and GC van Rhoon. Hot feet in the BSD Sigma 60: a numerical study of whole-body exposure. *26th Annual meeting of the European Society for Hyperthermic Oncology (ESHO), Rotterdam, The Netherlands*, 2010.

JF Bakker, MM Paulides, T Drizdal, and RA Canters, GC van Rhoon. Clinical hyperthermia: improving quality through treatment planning. *Book of abstracts of the 2nd Dutch Conference on Bio-Medical Engineering, Egmond aan Zee, The Netherlands*, 2009.

JF Bakker, KWA van Dongen, MM Paulides, and GC van Rhoon. Heating breast tumors with an ultrasound or electromagnetic cylindrical phased-array. *10th International Congress on Hyperthermic Oncology (ICHO), Munich, Germany*, 2008.

JF Bakker, MM Paulides, and GC van Rhoon. A phased array head and neck applicator: measurements of the SAR distributions in a cylindrical muscle phantom. *24th Annual meeting of the European Society for Hyperthermic Oncology (ESHO), Prague, Czech Republic*, 2007.

JF Bakker, MM Paulides, GC van Rhoon, H Schippers, and T ter Meer. Development of a gain & phase detector for a head & neck electromagnetic hyperthermia applicator. *Proceedings of joint 9th International Conference on Electromagnetics in Advanced Applications ICEAA'05 and 11th European Electromagnetic Structures Conference EESC'05, Torino, Italy*, 2005.

CAT van den Berg, JJ Bluemink, ALHMW van Lier, MM Paulides, JF Bakker, RF Verhaart, JJW Lagendijk, FFJ Simonis and A Raaijmakers. MR and Hyperthermia: Exploiting similarities for mutual benefit, *European Microwave Week, Amsterdam, The Netherlands*, 2012.

MM Paulides, Z Rijnen, JF Bakker, P Togni, PC Levendag and GC van Rhoon. Treatment planning guided RF hyperthermia, *European Microwave Week, Amsterdam, The Netherlands*, 2012.

MM Paulides, Z Rijnen, JF Bakker, GM van de Velde, PC Levendag and GC van Rhoon. Planning guided hyperthermia treatment of head and neck cancer, *The 11th International Congress of Hyperthermic Oncology (ICHO), Kyoto, Japan, 2012.*

RF Verhaart, JF Bakker, JJ Bluemink, P. Togni, CAT van den Berg and MM Paulides. Hybrid head and neck hyperthermia and 7T MR imaging: a pilot study, *The 11th International Congress of Hyperthermic Oncology (ICHO), Kyoto, Japan, 2012.*

LW Hofstetter, WCM Numan, JF Bakker, G Kotek, EW Fiveland, GC Houston, G Kudeilka, GC van Rhoon, MM Paulides and DTB Yeo. Evaluation of MR thermometry techniques for RF hyperthermia. *9th Interventional MRI Symposium, Boston, USA, 2012.*

WC Numan, LW Hofstetter, JF Bakker, EW Fiveland, G Kotek, GC Houston, GC van Rhoon, DTB Yeo and MM Paulides. "MR Thermometry for head and neck hyperthermia: experimental verification of simulations for guiding setup design". *29th Annual Scientific Meeting of the European Society for Magnetic Resonance in Medicine and Biology, Lisbon, Portugal, 2012.*

RF Verhaart, JJ Bluemink, JF Bakker, P Togni, AJ Raaijmakers, GC van Rhoon, CAT van den Berg and MM Paulides. "Validation of the predicted B1+ of a radiofrequency hyperthermia applicator using a 7T MR scanner". *29th Annual Scientific Meeting of the European Society for Magnetic Resonance in Medicine and Biology, Lisbon, Portugal, 2012.*

F Adibzadeh, JF Bakker, MM Paulides and GC van Rhoon. The impact of anatomical differences on absorbed energy from exposure to mobile phone at different regions in the brain. *34th Annual Meeting of the Bioelectromagnetics Society (BEMS), Brisbane, Australia, 2012*

MM Paulides, JF Bakker, Z Rijnen, P Togni, PC Levendag and GC van Rhoon. Complaint-adaptive steering in head and neck hyperthermia: implementation and early analysis of clinical benefit. *29th Annual Society for Thermal Medicine (STM) meeting, Portland, USA, 2012.*

GC van Rhoon, JF Bakker, RA Canters, and MM Paulides. EMF exposure assessment of healthy persons during loco-regional hyperthermia using the BSD-2000 Sigma 60 system. *33th Annual meeting of the Bioelectromagnetic Society (BEMS), Halifax, Canada, 2011.*

Z Rijnen, JF Bakker, M de Keiver, RA Canters, MM Paulides, and GC van Rhoon. VEDO: a software tool for standardization of planning-guided deep hyperthermia in the clinic. *27th Annual meeting of the European Society for Hyperthermic Oncology (ESHO), Aarhus, Denmark, 2011.*

MM Paulides, P Togni, Z Rijnen, JF Bakker, and GC van Rhoon. Dealing with setup uncertainties in planning-guided application of head and neck deep hyperthermia. *28th Annual Meeting of the Society for Thermal Medicine (STM), New Orleans, United States of America, 2011.*

MM Paulides, JF Bakker, and GC van Rhoon. A patch antenna design for a phased-array applicator for hyperthermia treatment of head and neck tumours. *Proceedings of the 3rd European Medical and Biological Conference, IFMBE European Conference on Biomedical Engineering (EMBEC), Prague, Czech Republic, 2005.*

MM Paulides, JF Bakker, and GC van Rhoon. A head and neck hyperthermia applicator: theoretical antenna array design. *23rd Annual meeting of the European Society for Hyperthermic Oncology (ESHO), Berlin, Germany, 2006.*

MM Paulides, JF Bakker, P Jansen, PC Levendag, J van der Zee, and GC van Rhoon. Innovations in technology to targeted heating in head and neck hyperthermia. *28th Annual meeting of the International Clinical Hyperthermia Society (ICHS), Mumbai, India, 2007.*

MM Paulides, JF Bakker, P Jansen, PC Levendag, J van der Zee, and GC van Rhoon. A novel head and neck applicator for targeted hyperthermia. *International meeting on innovative approaches in head and neck oncology (EHNS - ESTRO), Barcelona, Spain, 2007.*

MM Paulides, JF Bakker, and GC van Rhoon. A patch antenna design for a head and neck hyperthermia applicator. *The 23rd International Review of Progress in Applied Computational Electromagnetics (ACES), Verona, Italy, 2007.*

MM Paulides, JF Bakker, P Jansen, PC Levendag, J van der Zee, and GC van Rhoon. The HYPERcollar: a novel head and neck applicator for targeted hyperthermia. *8th International meeting on progress in radio-oncology ICRO / OGRO, Salzburg, Austria, 2007.*

MM Paulides, JF Bakker, P Jansen, PC Levendag, J van der Zee, and GC van Rhoon. Innovations in technology to target heating in head and neck hyperthermia. *World Conference on Interventional Oncology and Society of Thermal Medicine, Washington DC, USA, 2007.*

MM Paulides, JF Bakker, P Jansen, PC Levendag, J van der Zee, and GC van Rhoon. Innovations in technology to target heating in head and neck hyperthermia. *World Conference on Interventional Oncology and Society of Thermal Medicine, Washington DC, USA, 2007.*

MM Paulides, JF Bakker, E Neufeld, P Jansen, PC Levendag, J van der Zee, and G. van Rhoon. The HYPERcollar: a novel phased-array applicator for hyperthermia treatment

in the neck. *24th Annual meeting of the European Society for Hyperthermic Oncology (ESHO), Prague, Czech Republic, 2007.*

MM Paulides, JF Bakker, N Chavannes, and GC van Rhoon. A patch antenna element for the HYPERcollar applicator: design and characterization. *24th Annual meeting of the European Society for Hyperthermic Oncology (ESHO), Prague, Czech Republic, 2007.*

MM Paulides, JF Bakker, E Neufeld, P Jansen, PC Levendag, J van der Zee, and GC van Rhoon. Application of hyperthermia in the head and neck using the HYPERcollar. *10th International Congress on Hyperthermic Oncology (ICHO), Munich, Germany, 2008.*

GC van Rhoon, MM Paulides, JF Bakker, N Kuster, E Neufeld, J van der Zee, and PC Levendag. Hyperthermia treatment planning targets heating to the tumor. *27th Annual Congress of the European Society for Therapeutic Radiology and Oncology (ESTRO), Goteborg, Sweden, 2008.*

KWA van Dongen, JF Bakker, MM Paulides, I Obdeijn, and GC van Rhoon. Design of an ultrasound cylindrical phased-array for hyperthermia breast cancer treatment. *NAG/DAGA, International Conference on Acoustics, Rotterdam, NL, 2009.*

MM Paulides, JF Bakker, M Linthorst, Z Rijnen, P Jansen, PC Levendag, J van der Zee, and GC van Rhoon. Hyperthermia in head and neck tumors: the Rotterdam experience. *25th Annual meeting of the European Society for Hyperthermic Oncology (ESHO), Verona, Italy, 2009.*

MM Paulides, Z Rijnen, JF Bakker, E Neufeld, M Linthorst, J van der Zee, PC Levendag, and GC van Rhoon. Integration of technology into the clinic to facilitate focused treatment of advanced head and neck tumours. *26th Annual meeting of the European Society for Hyperthermic Oncology (ESHO), Rotterdam, The Netherlands, 2010.*

MM Paulides, Z Rijnen, JF Bakker, E Neufeld, M Linthorst, J van der Zee, PC Levendag, and GC van Rhoon. Hyperthermia treatment of advanced head and neck cancer: integration of technology into the clinic. *Annual Meeting of the Society for Thermal Medicine (STM), Clearwater FL, USA., 2010.*

Invited presentations

JF Bakker, MM Paulides, RF Verhaart, P Togni and GC van Rhoon. MRI bij Hyperthermie. *MRI symposium Parkstad, Heerlen, The Netherlands, 2012.*

JF Bakker, MM Paulides and GC van Rhoon. Blootstelling van volwassenen en kinderen aan elektromagnetische velden: dosisbepaling met metingen en simulaties, 6e bijeenkomst

klankbordgroep EMV van het kennisplatform Electromagnetische velden en Gezondheid. 's-Hertogenbosch, 2011

JF Bakker, MC Gosselin, A Christ, GC van Rhoon, N Kuster, APM Zwamborn and PC Levendag. Assessment of the cumulative exposure of children to electromagnetic fields, begeleidingscommissie ZonMw programma elektromagnetische velden en gezondheid. Utrecht, 2011.

JF Bakker, M Lequin, G Kotek, P Wielopolski, MM Paulides GC van Rhoon and PC Levendag. Post-mortem MR scans for the development of anatomical whole-body models of children, Grand Round, Erasmus MC-Sophia Rotterdam, 2010.

JF Bakker, A Christ, GC van Rhoon, N Kuster, APM Zwamborn and PC Levendag. Assessment of the cumulative exposure of children to electromagnetic fields, begeleidingscommissie ZonMw programma elektromagnetische velden en gezondheid. Utrecht, 2010.

JF Bakker, A Christ, GC van Rhoon, N Kuster, APM Zwamborn and PC Levendag. Assessment of the cumulative exposure of children to electromagnetic fields, begeleidingscommissie ZonMw programma elektromagnetische velden en gezondheid. Den Haag, 2009.

JF Bakker, A Christ, GC van Rhoon, N Kuster, APM Zwamborn and PC Levendag. Assessment of the cumulative exposure of children to electromagnetic fields. Dutch Cancer Society (KWF) working party Hyperthermia, AMC Amsterdam, 2009.

JF Bakker, A Christ, GC van Rhoon, N Kuster, APM Zwamborn and PC Levendag. Assessment of the cumulative exposure of children to electromagnetic fields. begeleidingscommissie ZonMw programma elektromagnetische velden en gezondheid, Den Haag, 2008.

JF Bakker, MM Paulides and GC van Rhoon. A phased-array hyperthermia applicator for head and neck cancer treatment. Workshop vibration control and structural integration of antennas, National Aerospace Laboratory (NLR), Amsterdam, 2007.

JF Bakker, MM Paulides, C van der Zee, GC van Rhoon, "The HYPERcollar". Dutch Cancer Society (KWF) working party Hyperthermia, Erasmus MC Rotterdam, 2006.

MM Paulides, JF Bakker, C van der Zee, GC van Rhoon. "Towards a novel applicator for hyperthermia treatment of head and neck carcinomas. Dutch Cancer Society (KWF) working party Hyperthermia, AMC Amsterdam, 2005.

Curriculum Vitae

Jurriaan Fokke Bakker was born on March 20th, 1979 in Schagen, The Netherlands

1983-1991 Primary school, de Ark, Schagen

1991-1997 Secondary school, Murmellius Gymnasium, Alkmaar

1997-1999 Civil Engineering & Applied Physics, Delft University of Technology

1999-2003 Bachelor of Engineering degree in Engineering Physics, Rijswijk University of Professional Technical Education. Thesis: "Effects of water bolus size and shape on the SAR distribution in muscle equivalent tissue"

2003-2008 Master of Science degree in Applied Physics, Delft University of Technology. Thesis: "Heating breast tumors with an ultrasound or electromagnetic cylindrical phased-array"

2003-2008 Research Physicist assistant at Erasmus MC - Daniel den Hoed Cancer Center, Rotterdam. Dutch Cancer Society (KWF) project: "Development, construction and clinical testing of a novel electromagnetic applicator for Hyperthermia of advanced Head and Neck carcinoma"

2008-2012 PhD student at Erasmus MC - Daniel den Hoed Cancer Center, Rotterdam. The Netherlands Organisation for Health Research and Development (ZonMw) project: "Assessment of the cumulative exposure of children to electromagnetic fields"

Dankwoord

Het is een voorrecht om te mogen promoveren op een fascinerend onderwerp. Het steeds beter begrijpen van het elektromagnetisch spektakel in het menselijke lichaam, biedt veel voordelen voor zowel de gewone sterveling als voor de patiënt. Het direct kunnen toepassen van verse kennis in de kliniek is voor mij de grootste drijfveer achter deze promotie geweest. Maar promoveren is meer dan nieuwe technologieën ontwikkelen. De bevindingen moeten ook publiek gemaakt worden, en dat betekent schrijven, schrijven, ... Promoveren doe je niet alleen. Bewust en onbewust hebben vele fantastische mensen een bijdrage geleverd aan dit proefschrift. Daarom zeg ik tegen al deze mensen: bedankt!

Prof. Gerard van Rhoon, de onuitputtelijke ideeën generator. Jouw positieve energie weet iedereen te stimuleren, tot een hoogte van maar liefst 1912m (Mont-Ventoux). Bedankt voor jou onvoorwaardelijke steun en vertrouwen, maar ook voor de aanvoer van Franse wijnen, verpakt per zes.

Dr. Maarten P, de paper-dokter. Samen bouwden we als eerste ter wereld de “magnetron” voor hoofd-hals tumoren. Ik heb bij jou als grote broer en fijne collega, de kunst van het promoveren kunnen afkijken. Bedankt voor je grote bijdrage en feedback bij het helder opschrijven van de resultaten. De continue aanwas van nieuwe gemotiveerde onderzoekers binnen de unit hyperthermie en het waarborgen van de hoogst haalbare wetenschappelijke kwaliteit is bij jou in de beste handen!

Prof. Peter Levendag. U bent het levende bewijs dat een radiotherapeut zich niet zomaar laat afschepen als een natuurkundige begint te vertellen over niet-ioniserende electromagnetische velden. Met grote bewondering heb ik kunnen genieten van uw enorme expertise als radiotherapeut en bedank ik u voor het vertrouwen in “ons techneuten” tijdens het verwarmen van tumoren in het zo kritische hoofd-hals gebied.

Dr. Maarten B, de kwaliteits-agent. Als mijn eerste begeleider bij hyperthermie, fietste ik

dagelijks in jouw kielzog van Delft naar Rotterdam en weer terug. De eerste MATLAB scripts werden onder jouw toezicht gemaakt. Jouw enorme inzet voor kwaliteit in de kliniek, “alles voor de patiënt”, is mij altijd bijgebleven. Bedankt!

De fijne samenwerking met de artsen en laboranten maken het werk relevant en stimulerend. De koffie momenten met mede-onderzoekers vormen de ideale basis om nieuwe ideeën te toetsen. Ook na het werk gaat het onderzoeken verder, weliswaar op andere aandachtsgebieden: “German chocolat” en “Swiss beer” zijn toch echt niet lekker. Onderzoek en kliniek draaiende houden doen we samen met de geweldige ondersteuning van technische medewerkers en secretaresses. Alle hyperthermie collega’s, bedankt!

Het ontwikkelen van nieuwe hyperthermie apparatuur kan niet zonder de enorme hulp en vaardigheid van onze fijn-mechanische instrumentmakers. De *HYPERcollar* en de *LABproto* zijn slechts enkele voorbeelden die gebruikt zijn in dit proefschrift. Mannen bedankt!

I have really appreciated the cooperation with our research partner IT’IS/SPEAG. Especially the software training sessions and experiments in Zürich were essential for the success of our ZonMw and Dutch Cancer Society projects. Big thanks to the entire team for their support.

De goede samenwerking met het UMC Utrecht, het AMC Amsterdam, TNO, en het Nationaal Lucht en Ruimtevaartlaboratorium (NLR) is van groot belang voor een goede kennisuitwisseling binnen Nederland. Grote dank voor de gezamenlijke experimenten en de ontwikkeling van de onmisbare hardware en software.

De samenwerking met de technische universiteiten uit Delft en Eindhoven is uniek te noemen. Koen en Martin, bedankt voor het bijbrengen van het modelleren van geluidsgolven. Met Prof. Anton Tjihuis en Prof. Peter Zwamborn, kan ik mij geen betere sparring partners bedenken voor het modelleren en meten van elektromagnetische velden. Bedankt!

Vele familieleden en vrienden hebben mij geholpen om tijdens het promoveren niet te verwilderen tot een afgezonderde onderzoeker. Thuis op het vertrouwde nest met mijn ouders en broer, op een zeilboot, de fiets, of in een afgesloten ski-lift met Bart & Ingmar. Bedankt!

Heel stoer als je een boek over elektromagnetische velden in de kast hebt staan, maar zo’n sprekende voorkant is natuurlijk helemaal spannend! Karin, zonder jouw gekke inspiratie en vormgeving was dit boekje natuurlijk heel saai gebleven. BKCR DTP is top!

Sommigen lezen alles. Daarom zijn de laatste woorden van dit proefschrift voor jou. Lieve Andrea, we hebben het samen geflikt: dit proefschrift is af. “Mede mogelijk gemaakt door BKCR Consulting”. Bedankt voor jouw eindeloze geduld, oppeppers, energie, humor en onvoorwaardelijke vertrouwen. Ik hou van jou!

References

1. JW Adams, HE Taggart, M Kanda, and J Shafer. Electromagnetic interference (EMI) radiative measurements for automotive applications. Boulder, Colorado: U.S. Technical report, Department of commerce, national bureau of standards, 1979.
2. R Anderson, V Croft and RL McIntosh. SAR versus S(inc): What is the appropriate RF exposure metric in the range 1-10 GHz? Part I: Using planar body models. *Bioelectromagnetics*, 31(6):454–466, 2010.
3. K Arunachalam, P Maccarini, T Juang, C Gaeta, and PR Stauffer. Performance evaluation of a conformal thermal monitoring sheet sensor array for measurement of surface temperature distributions during superficial hyperthermia treatments. *Int J Hyperthermia*, 24:313–325, 2008.
4. A Bahr, T Bolz, and C Hennes. Numerical dosimetry ELF: accuracy of the method, variability of models and parameters, and the implication for quantifying guidelines. *Health Phys*, 92:521–530, 2007.
5. JF Bakker, MM Paulides, A Christ, N Kuster, and GC Van Rhoon. Assessment of induced SAR in children exposed to electromagnetic plane waves between 10 MHz and 5.6 GHz. *Phys Med Biol*, 55:3115–3130, 2010.
6. JF Bakker, MM Paulides, AH Westra, H Schippers, and GC Van Rhoon. Design and test of a 434 MHz multi-channel amplifier system for targeted hyperthermia applicators. *Int J Hyperthermia*, 26:158–170, 2010.
7. JF Bakker, MM Paulides, E Neufeld, A Christ, N Kuster, and GC Van Rhoon. Children and adults exposed to electromagnetic fields at the ICNIRP reference levels: theoretical assessment of the induced peak temperature increase. *Phys Med Biol*, 56:4967–4989, 2011.

8. JF Bakker, MM Paulides, IM Obdeijn, GC Van Rhoon, and KW Van Dongen. An ultrasound cylindrical phased array for deep heating in the breast: theoretical design using heterogeneous models. *Phys Med Biol*, 54:3201–3215, 2009.
9. Q Balzano, O Garay, and T Manning. RF energy in cars from window-mounted antennas. *Conference record of the 36th Annual Conference, IEEE Vehicular Technology Group, Dallas, Texas*, pages 32–40, 1986.
10. P Bernardi, M Cavagnaro, S Pisa, and E Piuizzi. Specific absorption rate and temperature elevation in a subject exposed in the far-field of radio-frequency sources operating in the 10-900-MHz range. *Biomedical Engineering, IEEE Transactions on*, 50(3):295–304, 2003.
11. A Bhattacharya and RL Mahajan. Temperature dependence of thermal conductivity of biological tissues. *Physiol Meas*, 24:769–783, 2003.
12. National Radiological Protection Board. ELF electromagnetic fields and the risk of cancer, report of an advisory group on non-ionising radiation, Chilton, Didcot, Oxon OX11 0RQ. Technical report, NRPB, 2001.
13. JF Bolte and T Eikelboom. Personal radiofrequency electromagnetic field measurements in the Netherlands: exposure level and variability for everyday activities, times of day and types of area. *submitted to Env Internat*, 2012.
14. JF Bolte and MJM Pruppers. Gezondheidseffecten van blootstelling aan radiofrequente elektromagnetische velden - Probleemanalyse niet-ioniserende straling. Technical report, RIVM, 2004.
15. JF Bolte, G Van der Zande, and J Kamer. Calibration and uncertainties in personal exposure measurements of radiofrequency electromagnetic fields. *Bioelectromagnetics*, 32:652–663, 2011.
16. BSD Medical Corporation. *Sigma eye applicator operator manual*. BSD Medical Corporation, 1995.
17. EC Burdette, PG Friederich, RL Seaman, and LE Larsen. In situ permittivity of canine brain: regional variations and postmortem changes. *IEEE Transactions on Microwave Theory and Techniques*, 34(1):38–50, 1986.
18. RA Canters, P Wust, JF Bakker, and GC Van Rhoon. A literature survey on indicators for characterisation and optimisation of SAR distributions in deep hyperthermia, a plea for standardisation. *Int J Hyperthermia*, 25(7):593–608, 2009.
19. K Caputa, M Okoniewski, and MA Stuchly. An algorithm for computations of the power deposition in humantissue. *IEEE Antennas and Propagation Magazine*, 41(4):102–107, 1999.

-
20. XL Chen. Analysis of the human body exposure of low frequency magnetic fields using high resolution anatomical models of adults and children. *submitted to BEMS*, 2011.
 21. A Christ and N Kuster. Differences in RF energy absorption in the heads of adults and children. *Bioelectromagnetics*, Suppl 7:31–44, 2005.
 22. A Christ, G Schmid, R Djafarzadeh, R Überbacher, S Cecil, M Zefferer, E Neufeld, M Lichtsteiner, M Bouterfas, and N Kuster. Numerische bestimmung der spezifischen absorptionsrate bei ganzkörperexposition von kindern: abschlussbericht. techreport, IT'IS Foundation, ETH Zurich, 2009.
 23. A Christ, W Kainz, EG Hahn, K Honegger, M Zefferer, E Neufeld, W Rascher, R Janka, W Bautz, J Chen, B Kiefer, P Schmitt, HP Hollenbach, J Shen, M Oberle, D Szczerba, A Kam, J W Guag, and N Kuster. The Virtual Family-development of surface-based anatomical models of two adults and two children for dosimetric simulations. *Phys Med Biol*, 55:N23–N38, 2010.
 24. RF Cleveland and ED Mantiplly. Measurements of environmental electromagnetic fields at amateur radio stations. FCC: Washington, Washington DC, VS, FCC/OET ASD-9601. Technical report, Federal Communications Commission, 1996.
 25. R Colombo, LF Da Pozzo, A Salonia, P Rigatti, Z Leib, J Baniel, E Caldarera, and M Pavone-Macaluso. Multicentric study comparing intravesical chemotherapy alone and with local microwave hyperthermia for prophylaxis of recurrence of superficial transitional cell carcinoma. *J Clin Oncol*, 21:4270–4276, 2003.
 26. E Conil, A Hadjem, F Lacroux, MF Wong, and J Wiart. Variability analysis of SAR from 20 MHz to 2.4 GHz for different adult and child models using finite-difference time-domain. *Phys Med Biol*, 53:1511–1525, 2008.
 27. J Crezee and JJ Legendijk. Experimental verification of bioheat transfer theories: Measurement of temperature profiles around large artificial vessels in perfused tissue. *Phys Med Biol*, 35:905923, 1990.
 28. DASY52. Dosimetric and near-field Assessment SYstem, Schmid & Partner Engineering AG, Switzerland, <http://www.speag.com>, 2012.
 29. TW Dawson, K Caputa, and MA Stuchly. High-resolution organ dosimetry for human exposure to low-frequency electric fields. *IEEE Transactions on Power Delivery*, 13(2):366–373, 1998.
 30. M De Bruijne, T Samaras, E Neufeld, and GC Van Rhoon. Effectiveness of FDTD in predicting SAR distributions from the lucite cone applicator. In *Abstracts of the 22nd Annual Meeting of the ESHO, Graz, Austria (ESHO-05)*, 2005.

31. M de Bruijne, T Samaras, N Chavannes, and GC Van Rhoon. Quantitative validation of the 3D SAR profile of hyperthermia applicators using the gamma method. *Phys Med Biol*, 52:3075–3088, 2007.
32. M de Bruijne, B Van der Holt, GC Van Rhoon, and J Van der Zee. Evaluation of CEM43 degrees CT90 thermal dose in superficial hyperthermia: a retrospective analysis. *Strahlenther Onkol*, 186:436–443, Aug 2010.
33. PJ Dimbylow. FDTD calculations of the whole-body averaged SAR in an anatomically realistic voxel model of the human body from 1 MHz to 1 GHz. *Phys Med Biol*, 42:479–490, 1997.
34. PJ Dimbylow. Induced current densities from low-frequency magnetic fields in a 2 mm resolution, anatomically realistic model of the body. *Phys Med Biol*, 43:221–230, 1998.
35. PJ Dimbylow. Fine resolution calculations of SAR in the human body for frequencies up to 3 GHz. *Phys Med Biol*, 47:2835–2846, 2002.
36. PJ Dimbylow. Resonance behaviour of whole-body averaged specific energy absorption rate (SAR) in the female voxel model, NAOMI. *Phys Med Biol*, 50:4053–4063, 2005.
37. PJ Dimbylow. Development of the female voxel phantom, naomi, and its application to calculations of induced current densities and electric fields from applied low frequency magnetic and electric fields. *Phys Med Biol*, 50(6):1047–1070, 2005.
38. PJ Dimbylow. Development of pregnant female, hybrid voxel-mathematical models and their application to the dosimetry of applied magnetic and electric fields at 50 Hz. *Phys Med Biol*, 51(10):2383–2394, 2006.
39. PJ Dimbylow. Quandaries in the application of the icnirp low frequency basic restriction on current density. *Phys Med Biol*, 53(1):133–145, 2008.
40. PJ Dimbylow and W Bolch. Whole-body-averaged SAR from 50 MHz to 4 GHz in the University of Florida child voxel phantoms. *Phys Med Biol*, 52:6639–6649, 2007.
41. PJ Dimbylow and R Findlay. The effects of body posture, anatomy, age and pregnancy on the calculation of induced current densities at 50 Hz. *Radiat Prot Dosimetry*, 139:532–538, 2010.
42. PJ Dimbylow, A Hirata, and T Nagaoka. Intercomparison of whole-body averaged SAR in European and Japanese voxel phantoms. *Phys Med Biol*, 53:5883–5897, 2008.
43. PJ Dimbylow, W Bolch, and C Lee. SAR calculations from 20 MHz to 6 GHz in the University of Florida newborn voxel phantom and their implications for dosimetry. *Phys Med Biol*, 55:1519–1530, 2010.

-
44. FA Duck. *Physical Properties of Tissue*. Academic Press Inc, 1990. ISBN 978-0122228001.
 45. CH Durney. Electromagnetic dosimetry for models of humans and animals: A review of theoretical and numerical techniques. *Proceedings of the IEEE*, 68(1):33–40, 1980.
 46. CH Durney. *Basic Introduction to Bioelectromagnetics*. CRC Press, 1999. ISBN 0-8493-1198-5.
 47. Dutch Antenna Register. Information from website <http://www.antenneregister.nl>, April 2003.
 48. Dutch Telecom Agency. Voorwaarden gebruik draadloze dataverbindingen (Radio-LANs) in de 2.4 en 5 GHz banden. Telecom nieuwsbrief 04-03 FIS, April 2003.
 49. S El-Sayed and N Nelson. Adjuvant and adjunctive chemotherapy in the management of squamous cell carcinoma of the head and neck region: A meta-analysis of prospective and randomized trials. *J Clin Oncol*, 14:838–847, 1996.
 50. EPA. Radiofrequency radiation measurement survey, Honolulu, Hawaii May 14-25, 1984. Las Vegas, Nevada. Technical report, United States Environmental Protection Agency, 1985.
 51. EPA. Electric magnetic fields in your environment. Technical report, United States Environmental Protection Agency, 1992.
 52. ESHO Taskgroup Committee. *Treatment planning and modelling in hyperthermia, a task group report of the European Society for Hyperthermic Oncology*. Tor Vergata, Rome, Italy, 1992.
 53. European Parliament. Directive 2004/40/ec of the european parliament and of the council of 29 april 2004 on the minimum health and safety requirements regarding the exposure of workers to the risks arising from physical agents (electromagnetic fields) (18th individual directive within the meaning of article 16(1) of directive 89/391/eec), 2004.
 54. D Fatehi and GC Van Rhoon. SAR characteristics of the Sigma-60-Ellipse applicator. *Int J Hyperthermia*, 24:347–356, 2008.
 55. D Fiala, KJ Lomas, and M Stohrer. A computer model of human thermoregulation for a wide range of environmental conditions: the passive system. *J Appl Physiol*, 87:1957–1972, 1999.
 56. D Fiala, KJ Lomas, and M Stohrer. Computer prediction of human thermoregulatory and temperature responses to a wide range of environmental conditions. *Int J Biometeorol*, 45:143–159, 2001.

57. RP Findlay and PJ Dimbylow. Effects of posture on FDTD calculations of specific absorption rate in a voxel model of the human body. *Phys Med Biol*, 50:3825–3835, 2005.
58. RP Findlay and PJ Dimbylow. Variations in calculated SAR with distance to the perfectly matched layer boundary for a human voxel model. *Phys Med Biol*, 51: N411–415, 2006.
59. RP Findlay and PJ Dimbylow. Calculated SAR distributions in a human voxel phantom due to the reflection of electromagnetic fields from a ground plane between 65 MHz and 2 GHz. *Phys Med Biol*, 53:2277–2289, 2008.
60. RP Findlay, AK Lee, and PJ Dimbylow. FDTD calculations of SAR for child voxel models in different postures between 10 MHz and 3 GHz. *Radiat Prot Dosimetry*, 135:226–231, 2009.
61. B Floderus, C Stenlund, and F Carlgren. Occupational exposures to high frequency electromagnetic fields in the intermediate range (300Hz to 10MHz). *Bioelectromagnetics*, 23:568–577, 2002.
62. VM Flyckt, BW Raaymakers, and JJ Lagendijk. Modelling the impact of blood flow on the temperature distribution in the human eye and the orbit: fixed heat transfer coefficients versus the Pennes bioheat model versus discrete blood vessels. *Phys Med Biol*, 51:5007–5021, 2006.
63. VM Flyckt, BW Raaymakers, H Kroeze, and JJ Lagendijk. Calculation of SAR and temperature rise in a high-resolution vascularized model of the human eye and orbit when exposed to a dipole antenna at 900, 1500 and 1800 MHz. *Phys Med Biol*, 52: 2691–2701, 2007.
64. KR Foster and JJ Morrissey. Thermal aspects of exposure to radiofrequency energy: Report of a workshop. *International Journal of Hyperthermia*, 27(4):307–319, 2011.
65. M Franckena, LJ Stalpers, PC Koper, RG Wiggeraad, WJ Hoogenraad, JD Van Dijk, CC Warlam-Rodenhuis, JJ Jobsen, GC Van Rhoon, and J Van der Zee. Long-term improvement in treatment outcome after radiotherapy and hyperthermia in locoregionally advanced cervix cancer: an update of the Dutch Deep Hyperthermia Trial. *Int J Radiat Oncol Biol Phys*, 70:1176–1182, 2008.
66. M Franckena, D Fatehi, M de Bruijne, RA Canters, Y Van Norden, JW Mens, GC Van Rhoon, and J Van der Zee. Hyperthermia dose-effect relationship in 420 patients with cervical cancer treated with combined radiotherapy and hyperthermia. *Eur J Cancer*, 45:1969–1978, 2009.
67. M Franckena, RA Canters, F Termorshuizen, J Van der Zee, and GC Van Rhoon. Clinical implementation of hyperthermia treatment planning guided steering: A cross

-
- over trial to assess its current contribution to treatment quality. *Int J Hyperthermia*, 26(2):145–157, 2010.
68. E. M. Franken, J C J. de Boer, and B J M. Heijmen. A novel approach to accurate portal dosimetry using ccd-camera based epids. *Med Phys*, 33(4):888–903, Apr 2006.
 69. C Gabriel. Dielectric properties of biological tissue: variation with age. *Bioelectromagnetics*, Suppl 7:S12–18, 2005.
 70. C Gabriel and A Peyman. Dielectric measurement: error analysis and assessment of uncertainty. *Phys Med Biol*, 51:6033–6046, 2006.
 71. C Gabriel, S Gabriel, and E Corthout. The dielectric properties of biological tissues: I. Literature survey. *Phys Med Biol*, 41:2231–2249, 1996.
 72. C Gabriel, A Peyman, and EH Grant. Electrical conductivity of tissue at frequencies below 1 MHz. *Phys Med Biol*, 54:4863–4878, 2009.
 73. S Gabriel, RW Lau, and C Gabriel. The dielectric properties of biological tissues: II. Measurements in the frequency range 10 Hz to 20 GHz. *Phys Med Biol*, 41: 2251–2269, 1996.
 74. S Gabriel, RW Lau, and C Gabriel. The dielectric properties of biological tissues: III. Parametric models for the dielectric spectrum of tissues. *Phys Med Biol*, 41: 2271–2293, 1996.
 75. OP Gandhi. State of the knowledge for electromagnetic absorbed dose in man and animals. *Proceedings of the IEEE*, 68(1):24–32, 1980.
 76. OP Gandhi and G Kang. Calculation of induced current densities for humans by magnetic fields from electronic article surveillance devices. *Phys Med Biol*, 46:2759–2771, 2001.
 77. JR Gauger. Household appliance magnetic field survey. *IEEE Transactions on Power Apparatus and Systems*, 104:2436–2444, 1985.
 78. J Gellermann, W Wlodarczyk, H Ganter, J Nadobny, H Faehling, M Seebass, R Felix, and P Wust. A practical approach to thermography in a hyperthermia/magnetic resonance hybrid system: validation in a heterogeneous phantom. *Int J Radiat Oncol Biol Phys*, 61:267–277, 2005.
 79. J Gellermann, H Faehling, M Mielec, CH Cho, V Budach, and P Wust. Image artifacts during MRT hybrid hyperthermia—causes and elimination. *Int J Hyperthermia*, 24:327–335, 2008.
 80. RG Gordon, RB Roemer, and SM Horvath. A mathematical model of the human temperature regulatory system—transient cold exposure response. *IEEE Trans Biomed Eng*, 23:434–444, 1976.

81. Guy and Chou. Hazard analysis: "low frequency through medium frequency range". Brooks Air Force Base, TX: U.S. Technical report, Air Force School of Aerospace Medicine, 1982.
82. JW Hand, JJ Lagendijk, Bach Andersen J, and JC Bolomey. Quality assurance guidelines for ESHO protocols. *Int J Hyperthermia*, 5:421–428, 1989.
83. JW Hand, JJ Lagendijk, JV Hajnal, RW Lau, and IR Young. SAR and temperature changes in the leg due to an RF decoupling coil at frequencies between 64 and 213 MHz. *J Magn Reson Imaging*, 12:68–74, 2000.
84. JW Hand, Y Li, and JV Hajnal. Numerical study of RF exposure and the resulting temperature rise in the foetus during a magnetic resonance procedure. *Phys Med Biol*, 55:913–930, 2010.
85. NN Hankin. The radiofrequency radiation environment: environmental exposure levels and RF radiation emitting sources. Washington DC. 520/1-85-014. Technical report, United States Environmental Protection Agency Office of Radiation and Indoor Air, 1986.
86. C Harris, W Boivin, S Boyd, J Coletta, L Kerr, K Kempa, and S Aranow. Electromagnetic field strengths levels surrounding electronic article surveillance (EAS) systems. *Health Physics*, 78(1):21–27, 2000.
87. PA Hasgall, E Neufeld, MC Gosselin, A Klingenberg, and N Kuster. IT'IS Database for thermal and electromagnetic parameters of biological tissues. www.itis.ethz.ch/database, 2011.
88. EE Hatch, MS Linet, RA Kleinerman, RE Tarone, RK Severson, CT Hartsock, C Haines, WT Kaune, D Friedman, LL Robison, and S Wacholder. Association between childhood acute lymphoblastic leukemia and use of electrical appliances during pregnancy and childhood. *Epidemiology*, 9(3):234–245, 1998.
89. Health Council of the Netherlands. Influence of radiofrequency telecommunication signals on children's brains. publication no. 2011/20E, 2011.
90. A Hirata, K Caputa, TW Dawson, and MA Stuchly. Dosimetry in models of child and adult for low-frequency electric field. *IEEE Trans Biomed Eng*, 48:1007–1012, 2001.
91. A Hirata, M Fujimoto, T Asano, J Wang, O Fujiwara, and T Shiozawa. Correlation between maximum temperature increase and peak SAR with different average schemes and masses. *IEEE Transactions on Electromagnetic Compatibility*, 48(3): 569–578, 2006.

-
92. A Hirata, S Kodera, J Wang, and O Fujiwara. Dominant factors influencing whole-body average SAR due to far-field exposure in whole-body resonance frequency and GHz regions. *Bioelectromagnetics*, 28:484–487, 2007.
 93. A Hirata, S Watanabe, O Fujiwara, M Kojima, K Sasaki, and T Shiozawa. Temperature elevation in the eye of anatomically based human head models for plane-wave exposures. *Phys Med Biol*, 52:6389–6399, 2007.
 94. A Hirata, T Asano, and O Fujiwara. FDTD analysis of body-core temperature elevation in children and adults for whole-body exposure. *Phys Med Biol*, 53:5223–5238, 2008.
 95. A Hirata, N Ito, and O Fujiwara. Influence of electromagnetic polarization on the whole-body averaged SAR in children for plane-wave exposures. *Phys Med Biol*, 54:59–65, 2009.
 96. A Hirata, K Wake, S Watanabe, and M Taki. In-situ electric field and current density in Japanese male and female models for uniform magnetic field exposures. *Radiat Prot Dosimetry*, 135:272–275, 2009.
 97. NG Huilgol. A phase I study to study arsenic trioxide with radiation and hyperthermia in advanced head and neck cancer. *Int J Hyperthermia*, 22:391–397, 2006.
 98. Hybrid hyperthermia system BSD 2000-3D MRI. Dr. Sennewald MedizinTechnik GMBH, 2012.
 99. ICNIRP. International Commission on Non-Ionizing Radiation Protection, Guidelines for limiting exposure to time-varying electric, magnetic, and electromagnetic fields (up to 300 GHz). *Health Phys*, 74:494–522, 1998.
 100. ICNIRP. International Commission on Non-Ionizing Radiation Protection, Medical magnetic resonance (MR) procedures: protection of patients. *Health Phys*, 87:197–216, 2004.
 101. ICNIRP. International Commission on Non-Ionizing Radiation Protection, Guidelines for limiting exposure to time-varying electric and magnetic fields (1 Hz to 100 kHz). *Health Phys*, 99(6):818–836, 2010.
 102. IEEE. Std c95.3 recommended practice for measurements and computations of radio frequency electromagnetic fields with respect to human exposure to such fields, 100 kHz–300 GHz, 2002.
 103. IEEE. Standard for safety levels with respect to human exposure to radio frequency electromagnetic fields, 3 kHz to 300 GHz, Std C95.1, 2005.
 104. iSeg. Medical image segmentation tool, Zurich Med Tech, Switzerland, 2012.

105. ISO/IEC. Guide 98-3:2008 - uncertainty of measurement – part 3: Guide to the expression of uncertainty in measurement (gum:1995), 2008.
106. K Ito, K Furuya, Y Okano, and L Hamada. Development and characteristics of a biological tissue-equivalent phantom for microwaves. *Electronics and Communications in Japan (Part I: Communications)*, 84:67–77, 2001.
107. JD Jackson. *Classical Electrodynamics Third Edition*. Wiley, 1998. ISBN 047130932X.
108. E Jones, D Thrall, MW Dewhurst, and Z Vujaskovic. Prospective thermal dosimetry: the key to hyperthermia’s future. *Int J Hyperthermia*, 22:247–253, 2006.
109. W Joseph, G Vermeeren, L Verloock, MM Heredia, and L Martens. Characterization of personal RF electromagnetic field exposure and actual absorption for the general public. *Health Phys*, 95:317–330, Sep 2008.
110. W Joseph, Verloock L, and Martens L. General public exposure by ELF Fields of 150-36/11 kV substations in urban environment. *IEEE Transactions on Power Delivery*, pages 642–649, 2009.
111. W Joseph, G Vermeeren, L Verloock, and L Martens. Estimation of whole-body SAR from electromagnetic fields using personal exposure meters. *Bioelectromagnetics*, 31: 286–295, 2010.
112. W Joseph, G Vermeeren, L Verloock, and F Goeminne. In-situ magnetic field exposure and icnirp based safety distances for electronic article surveillance systems. *Radiat Prot Dosimetry*, May 2011.
113. RSJP Kaatee and GC Van Rhoon. An electric field measurement system, using a two-dimensional array of diodes. *Int J Hyperthermia*, 15:441–454, 1999.
114. MH Kalos and PA Whitlock. *Monte Carlo Methods*. John Wiley and Sons, 1986. ISBN 0-471-89839-2.
115. J Kelfkens and MJM Pruppers. Extreem-laagfrequente elektrische en magnetische velden van huishoudelijke apparatuur. Technical report, RIVM, 2005.
116. T Kohler, P Maass, P Wust, and M Seebass. A fast algorithm to find optimal controls of multiantenna applicators in regional hyperthermia. *Phys Med Biol*, 46:2503–2514, 2001.
117. AN Kotte, GM Van Leeuwen, and JJ Lagendijk. Modelling the thermal impact of a discrete vessel tree. *Phys Med Biol*, 44(1):57–74, 1999.
118. H Kroeze, JB Van de Kamer, AAC De Leeuw, and JJ Lagendijk. Regional hyperthermia applicator design using FDTD modelling. *Phys Med Biol*, 46:1919–1935, 2001.

-
119. S Kuhn, W Jennings, A Christ, and N Kuster. Assessment of induced radio-frequency electromagnetic fields in various anatomical human body models. *Phys Med Biol*, 54:875–890, 2009.
 120. I Laakso. Assessment of the computational uncertainty of temperature rise and SAR in the eyes and brain under far-field exposure from 1 to 10 GHz. *Phys Med Biol*, 54:3393–3404, 2009.
 121. JJ Lagendijk. A mathematical model to calculate temperature distributions in human and rabbit eyes during hyperthermic treatment. *Phys Med Biol*, 27:1301–1311, 1982.
 122. JJ Lagendijk, GC Van Rhoon, SN Hornsleth, P Wust, AC De Leeuw, CJ Schneider, JD Van Dijk, J Van der Zee, R Van Heek-Romanowski, SA Rahman, and C Gromoll. Esho quality assurance guidelines for regional hyperthermia. *Int J Hyperthermia*, 14:125–133, 1998.
 123. DL Lambdin. An investigation of energy densities in the vicinity of vehicles with mobile communications equipment and near a handheld walkie talkie. Las Vegas, Nevada. EPA ORP/EAD 79-2. Technical report, U.S. Environmental Protection Agency, 1979.
 124. J Lang, B Erdmann, and M Seebass. Impact of nonlinear heat transfer on temperature control in regional hyperthermia. *IEEE Trans Biomed Eng*, 46:1129–1138, 1999.
 125. HK Lee, AG Antell, CA Perez, WL Straube, G Ramachandran, RJ Myerson, B Emami, EP Molmenti, A Buckner, and MA Lockett. Superficial hyperthermia and irradiation for recurrent breast carcinoma of the chest wall: prognostic factors in 196 tumors. *Int J Radiat Oncol Biol Phys*, 40:365–375, 1998.
 126. Q Li and OP Gandhi. Thermal implications of the new relaxed IEEE RF safety standard for head exposures to cellular telephones at 835 and 1900 MHz. *IEEE Transactions on Microwave Theory and Techniques*, 54(7):3146 – 3154, 2006.
 127. JC Lin. SAR and temperature distributions in canonical head models exposed to near- and far-field electromagnetic radiation at different frequencies. *Electromagnetic Biology and Medicine*, 24(3):405–421, 2005.
 128. ED Mantiply, KR Pohl, SW Popell, and JA Murphy. Summary of Measured Radiofrequency Electric and Magnetic Fields (10 kHz to 30 GHz) in the General and Work Environment. *Bioelectromagnetics*, 18:563–577, 1997.
 129. M Martinez-Burdalo, A Sanchis, A Martin, and R Villar. Comparison of SAR and induced current densities in adults and children exposed to electromagnetic fields from electronic article surveillance devices. *Phys Med Biol*, 55:1041–1055, 2010.

130. RL McIntosh and V Anderson. BIOEM2009, joint meeting of the Bioelectromagnetics Society and the European BioElectromagnetics Association: A comprehensive tissue properties database provided for the thermal assessment of a human at rest, 2009.
131. RL McIntosh and V Anderson. SAR versus S(inc): What is the appropriate RF exposure metric in the range 1-10 GHz? Part II: Using complex human body models. *Bioelectromagnetics*, 31(6):467–478, 2010.
132. DE Merewether, R Fisher, and FW Smith. On implementing a numeric Huygen's source scheme in a Finite Difference program to illuminate scattering bodies. *IEEE Transactions on Nuclear Science*, 27(6):1829–1833, 1980.
133. KH Mild and KG Lovstrand. Environmental and professionally encountered electromagnetic fields, 1990.
134. JP Muccioli and SS Awad. The electromagnetic environment of an automobile electronic system. *IEEE Trans Electromag Compatibility*, 29:245–251, 1987.
135. J Nadobny, W Wlodarczyk, L Westhoff, J Gellermann, B Rau, G Monich, and P Wust. Development and evaluation of a three-dimensional hyperthermia applicator with Water-COated Antennas (WACOA). *Int J Hyperthermia*, 30:2052–2064, 2003.
136. T Nagaoka, S Watanabe, K Sakurai, E Kunieda, S Watanabe, M Taki, and Y Yamana. Development of realistic high-resolution whole-body voxel models of Japanese adult males and females of average height and weight, and application of models to radio-frequency electromagnetic-field dosimetry. *Phys Med Biol*, 49:1–15, 2004.
137. T Nagaoka, E Kunieda, and S Watanabe. Proportion-corrected scaled voxel models for Japanese children and their application to the numerical dosimetry of specific absorption rate for frequencies from 30 MHz to 3 GHz. *Phys Med Biol*, 53:6695–6711, 2008.
138. K Nehrke and P Bornert. Improved b1-mapping for multi rf transmit systems. In *Proc Intl Soc Mag Reson Med*, page 353, 2008.
139. SM Neuder. Electromagnetic fields in biological media: part 2. The SCAT program, multilayered spheres, theory and applications HEW Publication (FDA), 1979.
140. E Neufeld, N Chavannes, T Samaras, and N Kuster. Novel conformal technique to reduce staircasing artifacts at material boundaries for FDTD modeling of the bioheat equation. *Phys Med Biol*, 52:4371–4381, 2007.
141. E Neufeld, S Khn, G Szekely, and N Kuster. Measurement, simulation and uncertainty assessment of implant heating during mri. *Phys Med Biol*, 54(13):4151–4169, Jul 2009.

-
142. National Institute of Environmental Health Sciences. Electric and magnetic fields associated with the use of electric power. Technical report, NIEHS, 2002.
 143. MM Paulides, SHJA Vossen, APM Zwamborn, and GC Van Rhoon. Theoretical investigation into the feasibility to deposit RF energy centrally in the head and neck region. *Int Rad Onc Biol Phys*, 63:634–642, 2005.
 144. MM Paulides, DHM Wielheesen, J Van der Zee, and GC Van Rhoon. Assessment of the local SAR distortion by major anatomical structures in a cylindrical neck phantom. *Int J Hyperthermia*, 21:382–400, 2005.
 145. MM Paulides, JF Bakker, N Chavannes, and GC Van Rhoon. A patch antenna design for a phased-array head and neck hyperthermia applicator. *IEEE Trans Biom Eng*, 54:2057–2063, 2007.
 146. MM Paulides, JF Bakker, E Neufeld, J Van der Zee, PP Jansen, PC Levendag, and GC Van Rhoon. Winner of the "New Investigator Award" at the European Society of Hyperthermia Oncology Meeting 2007. The HYPERcollar: a novel applicator for hyperthermia in the head and neck. *Int J Hyperthermia*, 23:567–576, 2007.
 147. MM Paulides, JF Bakker, and GC Van Rhoon. Electromagnetic head-and-neck hyperthermia applicator: experimental phantom verification and FDTD model. *Int J Radiat Oncol Biol Phys*, 68:612–620, 2007.
 148. MM Paulides, JF Bakker, APM Zwamborn, and GC Van Rhoon. A head and neck hyperthermia applicator: theoretical antenna array design. *Int J Hyperthermia*, 23:59–67, 2007.
 149. MM Paulides, JF Bakker, M Linthorst, J Van der Zee, Z Rijnen, E Neufeld, PMT Pattynama, PP Jansen, Levendag PC, and Van Rhoon GC. The clinical feasibility of deep hyperthermia treatment in the head and neck: new challenges for positioning and temperature measurement. *Phys Med Biol*, 55(9):2465–2480, 2010.
 150. KD Paulsen, S Geimer, J Tang, and WE Boyse. Optimisation of pelvic heating rate distributions with electromagnetic phased arrays. *Int J Hyperthermia*, 15:157–186, 1999.
 151. HH Pennes. Analysis of tissue and arterial blood temperatures in the resting human forearm. *J Appl Physiol*, 1:93–122, 1948.
 152. A Peyman and C Gabriel. Cole-Cole parameters for the dielectric properties of porcine tissues as a function of age at microwave frequencies. *Phys Med Biol*, 55: N413–419, 2010.
 153. A Peyman, C Gabriel, EH Grant, G Vermeeren, and L Martens. Variation of the dielectric properties of tissues with age: the effect on the values of SAR in children when exposed to walkie-talkie devices. *Phys Med Biol*, 54:227–241, 2009.

154. A Peyman, C Gabriel, HR Benedickter, and J Frohlich. Dielectric properties of human placenta, umbilical cord and amniotic fluid. *Phys Med Biol*, 56:N93–98, 2011.
155. JP Pignon, J Bourhis, C Domenge, and L Designe. Chemotherapy added to locoregional treatment for head and neck squamous-cell carcinoma: three meta-analyses of updated individual data. *Lancet*, 355:949–955, 2000.
156. AJ Raaijmakers, O Ipek, DW Klomp, C Possanzini, PR Harvey, JJ Lagendijk, and CAT van den Berg. Design of a radiative surface coil array element at 7 T: the single-side adapted dipole antenna. *Magn Reson Med*, 66(5):1488–1497, 2011.
157. A Razmadze, L Shoshiashvili, D Kakulia, R Zaridze, G Bit-Babik, and A Faraone. Influence of specific absorption rate averaging schemes on correlation between mass-averaged specific absorption rate and temperature rise. *Electromagnetics*, 29:77–90, 2009.
158. PS Ruggerra. Near field measurements of RF fields: "Symposium on biological effects and measurements of radio frequency/microwaves. Rockville, Maryland. Technical report, U.S. Department of Health and Human Services, Bureau of Radiological Health, 1977.
159. T Samaras, PJM Rietveld, and GC Van Rhoon. Effectiveness of FDTD in predicting SAR distributions from the lucite cone applicator. *IEEE Trans Micr Theor Tech*, 48:2059–2063, 2000.
160. T Samaras, GC Van Rhoon, and JN Sahalos. Theoretical investigation of measurement procedures for the quality assurance of superficial hyperthermia applicators. *Int J Hyperthermia*, 18:416–425, 2002.
161. T Samaras, A Christ, and N Kuster. Effects of geometry discretization aspects on the numerical solution of the bioheat transfer equation with the fdtd technique. *Phys Med Biol*, 51(11):N221–N229, 2006.
162. L Sandrini, A Vaccari, C Malacarne, L Cristoforetti, and R Pontalti. RF dosimetry: a comparison between power absorption of female and male numerical models from 0.1 to 4 ghz. *Phys Med Biol*, 49:5185–5201, 2004.
163. G Schmid and R Uberbacher. Age dependence of dielectric properties of bovine brain and ocular tissues in the frequency range of 400 MHz to 18 GHz. *Phys Med Biol*, 50:4711–4720, 2005.
164. G Schmid, G Neubauer, UM Illievich, and F Alesch. Dielectric properties of porcine brain tissue in the transition from life to death at frequencies from 800 to 1900 MHz. *Bioelectromagnetics*, 24:413–422, 2003.

-
165. TW Sederberg and SR Parry. Free-form deformation of solid geometric models. *SIGGRAPH Comput. Graph.*, 20:151–160, 1986.
 166. M Seebass, R Beck, J Gellerman, J Nadobny, and P Wust. Electromagnetic phased arrays for regional hyperthermia: Optimal frequency and antenna arrangement. *Int J Hyperthermia*, 17:321–336, 2001.
 167. SEMCAD X. Simulation platform for electromagnetic and thermal dosimetry, Schmid & Partner Engineering AG, Switzerland, 2012.
 168. M Sherar, FF Liu, M Pintilie, W Levin, J Hunt, R Hill, J Hand, C Vernon, G Van Rhoon, J Van der Zee, DG Gonzalez, J Van Dijk, J Whaley, and D Machin. Relationship between thermal dose and outcome in thermoradiotherapy treatments for superficial recurrences of breast cancer: data from a phase III trial. *Int J Radiat Oncol Biol Phys*, 39:371–380, 1997.
 169. N Siauve, L Nicolas, C Vollaire, and C Marchal. Optimization of the sources in local hyperthermia using a combined finite element-genetic algorithm method. *Int J Hyperthermia*, 20:815–833, 2004.
 170. B Sohrab, G Farzan, B Ashkan, and J Amin. Ultrasound thermotherapy of breast: Theoretical design of transducer and numerical simulation of procedure. *Japanese Journal of Applied Physics*, 45:1856–1863, 2006.
 171. CW Song, A Lokshina, JG Rhee, M Patten, and HL Seymour. Implication of blood flow in hyperthermic treatment of tumors. *IEEE Transactions on Biomedical Engineering*, BME-31:9–16, 1984.
 172. PR Stauffer. Evolving technology for thermal therapy of cancer. *Int J Hyperthermia*, 21:731–744, 2005. Review.
 173. A Stogryn. Equations for calculating the dielectric constant of saline water (correspondence). *IEEE Trans Micr Theor Tech*, 19:733–376, 1971.
 174. JA Stolwijk. Responses to the thermal environment. *Fed. Proc.*, 36:1655–1658, 1977.
 175. MA Stuchly and TW Dawson. Interaction of low-frequency electric and magnetic fields with the human body. *Proceedings of the IEEE*, 88(5):643–664, 2000.
 176. A Taflove and SC Hagness. *Computational Electrodynamics: The Finite-Difference Time-Domain Method*. Artech House, 685 Canton Street, Norwood, MA 02062, 3rd edition, 2005. ISBN 1-580-53832-0.
 177. BN Taylor and CE Kuyatt. *Guidelines for evaluating and expressing the uncertainty of NIST measurement results*, *NIST Technical Note 1297*. NIST Technical Note 1297, 1994.

178. RA Tell, ED Mantiplay, P Wagner, and RF Cleveland. Radiofrequency electromagnetic fields and induced currents in the spokane, Washington Area. Las Vegas, Nevada. EPA/520/6-88/008. Technical report, United States Environmental Protection Agency, 1988.
179. A Trotti. Toxicity in head and neck cancer: a review of trends and issues. *Int J Rad Oncol Biol Phys*, 47:1–12, 2000.
180. PF Turner and T Schaeffermeyer. BSD-2000 approach for deep local and regional hyperthermia. *Strahlentherapie und Oncologie*, 165:738–741, 1989.
181. JL Ulcek and RF Cleveland Jr. Evaluating Compliance with FCC Guidelines for Human Exposure to Radiofrequency Electromagnetic Fields. FCC Washington, Washington DC, VS, January 1997; Supplement B (Edition 97-01) tot OET Bulletin 65 (Edition 97-01). Technical report, FCC, 1997.
182. T Uusitupa, I Laakso, S Ilvonen, and K Nikoskinen. SAR variation study from 300 to 5000 MHz for 15 voxel models including different postures. *Phys Med Biol*, 55: 1157–1176, 2010.
183. R Valdagni and M Amichetti. Report of long-term follow-up in a randomized trial comparing radiation therapy and radiation therapy plus hyperthermia to metastatic lymph nodes in stage IV head and neck patients. *Int J Rad Oncol Biol Phys*, 28: 163–169, 1993.
184. R Valdagni, F-F Liu, and S Kapp. Important prognostic factors influencing outcome of combined radiation and hyperthermia. *Int J Rad Oncol Biol Phys*, 15:959–972, 1988.
185. P Van de Moortele, C Akgun, G Adriany, S Moeller, J Ritter, CM Collins, MB Smith, JT Vaughan, and K Ugurbil. B1 destructive interferences and spatial phase patterns at 7 t with a head transceiver array coil. *Magnetic Resonance in Medicine*, 54(6): 1503–1518, 2005.
186. CAT Van den Berg, LW Bartels, AA De Leeuw, JJ Lagendijk, and JB Van de Kamer. Experimental validation of hyperthermia SAR treatment planning using MR B1+ imaging. *Phys Med Biol*, 49:5029–5042, 2004.
187. E Van der Wal, M Franckena, DH Wielheesen, J Van der Zee, and GC Van Rhoon. Steering in locoregional deep hyperthermia: evaluation of common practice with 3D-planning. *Int J Hyperthermia*, 24:682–693, 2008.
188. J Van der Zee, D Gonzalez Gonzalez, GC Van Rhoon, JD Van Dijk, WL Van Putten, and AA Hart. Comparison of radiotherapy alone with radiotherapy plus hyperthermia in locally advanced pelvic tumours: a prospective, randomised, multicentre trial. Dutch Deep Hyperthermia Group. *Lancet*, 355:1119–1125, 2000.

-
189. GC Van Rhoon, A Ameziane, WM Lee, DJ Van der Heuvel, HJ Klinkhamer, C Barendrecht, K Volenec, and PJ Rietveld. Accuracy of electrical field measurement using the flexible Schottky diode sheet at 433 MHz. *Int J Hyperthermia*, 19:134–144, 2003.
190. GC Van Rhoon, DJ Van Der Heuvel, A Ameziane, PJ Rietveld, K Volenec, and J Van der Zee. Characterization of the SAR-distribution of the Sigma-60 applicator for regional hyperthermia using a Schottky diode sheet. *Int J Hyperthermia*, 19:642–654, 2003.
191. GC Van Rhoon, A Aleman, G Kelfkens, H Kromhout, FE Van Leeuwen, HF Savelkoul, WJ Wadman, RD Van de Weerd, AP Zwamborn, and E Van Rongen. Health Council of The Netherlands: no need to change from SAR to time-temperature relation in electromagnetic fields exposure limits. *Int J Hyperthermia*, 27:399–404, 2011.
192. JT Vaughan, M Garwood, CM Collins, W Liu, L DelaBarre, G Adriany, P Andersen, H Merkle, R Goebel, MB Smith, and K Ugurbil. 7T vs. 4T: RF power, homogeneity, and signal-to-noise comparison in head images. *Magn Reson Med*, 46:24–30, 2001.
193. G Vermeeren, MC Gosselin, S Kuhn, V Kellerman, A Hadjem, A Gati, W Joseph, J Wiart, F Meyer, N Kuster, and L Martens. The influence of the reflective environment on the absorption of a human male exposed to representative base station antennas from 300 MHz to 5 GHz. *Phys Med Biol*, 55:5541–5555, 2010.
194. CC Vernon, JW Hand, SB Field, D Machin, JB Whaley, J Van der Zee, WL Van Putten, GC Van Rhoon, JD Van Dijk, D Gonzalez Gonzalez, FF Liu, P Goodman, and M Sherar. Radiotherapy with or without hyperthermia in the treatment of superficial localized breast cancer: results from five randomized controlled trials. International Collaborative Hyperthermia Group. *Int J Radiat Oncol Biol Phys*, 35:731–744, 1996.
195. PR Wainwright. The relationship of temperature rise to specific absorption rate and current in the human leg for exposure to electromagnetic radiation in the high frequency band. *Phys Med Biol*, 48:3143–3155, 2003.
196. PR Wainwright. Computational modelling of temperature rises in the eye in the near field of radiofrequency sources at 380, 900 and 1800 MHz. *Phys Med Biol*, 52:3335–3350, 2007.
197. J Wang, O Fujiwara, S Kodera, and S Watanabe. FDTD calculation of whole-body average SAR in adult and child models for frequencies from 30 MHz to 3 GHz. *Phys Med Biol*, 51:4119–4127, 2006.
198. S Weinbaum and LM Jiji. A new simplified bioheat equation for the effect of blood flow on local average tissue temperature. *J Biomech Eng*, 107(2):131–9, 1985.

199. WHO. World Health Organization, Environmental Health Criteria 137 - Electromagnetic Fields (300 Hz to 300 GHz), 1993.
200. WHO. World Health Organization, Research Agenda for Radio Frequency Fields, 2006.
201. WHO. World Health Organization, Research Agenda for Extremely Low Frequency Fields, 2007.
202. WHO. World Health Organization, Environmental Health Criteria 238 - Extremely Low Frequency Fields, 2007.
203. WHO. World Health Organization, Research Agenda for Radio Frequency Fields, 2010.
204. B Witvliet and B Bogaard. Veldsterktemetingen Trintelhaven, AM middengolf 1395 kHz, 2002.
205. L Wu, RJ McGough, OA Arabe, and TV Samulski. An RF phased array applicator designed for hyperthermia breast cancer treatments. *Phys Med Biol*, 51:1–20, 2006.
206. P Wust, M Seebas, J Nadobny, P Deuffhard, G Mönich, and R Felix. Simulation studies promote technological development of radiofrequency phased array hyperthermia. *Int J Hyperthermia*, 12:477–498, 1996.
207. PS Yarmolenko, EJ Moon, C Landon, A Manzoor, DW Hochman, BL Viglianti, and MW Dewhirst. Thresholds for thermal damage to normal tissues: an update. *Int J Hyperthermia*, 27:320–343, 2011.
208. VL Yarnykh. Actual flip-angle imaging in the pulsed steady state: a method for rapid three-dimensional mapping of the transmitted radiofrequency field. *Magn Reson Med*, 57(1):192–200, 2007.
209. E Zastrow, SC Hagness, and BD Van Veen. 3D computational study of non-invasive patient-specific microwave hyperthermia treatment of breast cancer. *Phys Med Biol*, 55:3611–3629, 2010.

ISBN 978-90-8891-457-7